Light-sensitive nanocarriers for drug delivery in photodynamic therapy

Beatriz Rodríguez Amigo

UNIVERSITAT RAMON LLULL

DOCTORAL THESIS

Title	**Light-sensitive nanocarriers for drug delivery in photodynamic therapy**
Presented by	**Beatriz Rodríguez Amigo**
Centre	**IQS School of Engineering**
Department	**Analytical and Applied Chemistry**
Directed by	**Prof. Dr. Santi Nonell Marrugat**

You do not need to be great to start,
but you need to start to become great

Zig Ziglar

To my mother, father and sister
To Pol

ACKOWLEDGMENTS

Financial support for this research has been provided by the Spanish Ministerio de Economía y Competitividad through grants No. **CTQ2013-48767-C3-1-R** and **CTQ2016-78454-C2-1-R**.

I would like to thank Interquim, laboratorios Ferrer for my predoctoral fellowship. Additional financial support from Institut Químic de Sarrià has been received for extend my predoctoral fellowship. Moreover, financial support from the Erasmus+ grant for visiting the Università degli Studi di Parma and from the European Society for Photobiology (ESP) for attending the 16th Congress of the ESP are also gratefully acknowledged.

Ultimately, thank everybody who has been involved in my daily work over this four-year period, especially to the FotoQ team and my computational girl. Thanks to my supervisor S. Nonell and my "host" supervisors C. Viappini and S. Abbruzzetti during my abroad stage. Moreover, I would like to thanks M. Mora and M.L. Sagristà for all the support given and their understanding. I would also like to thank M. Agut for the microbiological support.

However, none of this would have been possible without the unconditional support of my parents, sister and Pol.

ABSTRACT

This thesis reports the study of nanocarriers as drug delivery systems for photosensitisers in photodynamic therapy. Proteins and liposomes are the two nanovehicles of different nature used for this purpose.

Beginning with the proteins, the complexes formed between hypericin and the proteins apomyoglobin and β-lactoglobulin have been explored. The physicochemical and photophysical properties have been studied, as also assessing their photoantibacterial activity against Gram-positive and Gram-negative bacteria. In both protein scaffolds the photosensitiser is found mainly in monomeric form, preserving its fluorescence and singlet oxygen photosensitising properties and yielding a stable complex. In the case of β-lactoglobulin, the complex formation has also been tested with the addition of a 20% DMSO as a co-solvent, which improves the photophysical properties but surprisingly, worsens its antimicrobial activity. Both protein complexes are effective against Gram-positive but not against Gram-negative bacteria. Moreover, it has been proved that hypericin, inside the apomyoglobin cavity, can perform STED microscopy through which its localization in bacteria can be monitored. Additionally, the suitability of β-lactoglobulin as a dual carrier for hypericin and acid retinoic has also been exploited. In this last multi-component system, the photophysical properties have been evaluated to confirm the formation and complex stability.

Secondly, a nanocarrier for its use in combined therapy has been developed, in which conventional chemotherapeutic drugs are combined with photosensitising agents to overcome resistance and improve the effectiveness of the individual treatments. For this purpose, two different liposome formulations have been designed and studied with a common photosensitiser but different anti tumour drugs. The bimodal formulations with both agents entrapped and their unimodal counterparts, having each drug loaded in separate liposomes, have been evaluated. The physicochemical, photophysical and photobiological properties of bimodal and unimodal suspensions have been studied. The subcellular localization shows different organelle accumulation by each agent, triggering different key signals transduction pathways, eluding the cellular resistance mechanisms. The treatment *in vitro* of these multi-component liposomes with cancer cells has a promising effect, since at least an additive outcome is observed when compared with the individual treatments. Finally, we have explored the potential of active targeting strategies by covalently linking a monoclonal antibody to the surface, leading to slightly greater outcomes for one of the liposomal formulations.

RESUMEN

Esta tesis profundiza en el estudio de nanotransportadores como sistema de vehiculización y en algunos casos, liberación de fotosensibilizadores empleados en terapia fotodinámica. Se emplean dos nanotransportadores de naturaleza distinta: proteínas y liposomas.

En primer lugar se han investigado los complejos formados entre hipericina y las proteínas apomioglobina y β-lactoglobulina. Se han estudiado las características fisicoquímicas y fotofísicas, evaluando la actividad antimicrobiana frente bacterias gram-positivas y gram-negativas. En ambas matrices proteicas el fotosensibilizador se encuentra mayoritariamente en forma monomérica, preservando sus propiedades fotofísicas y formando un complejo estable. En el caso de la β-lactoglobulina se estudia además, la formación del complejo con la adición del 20% de DMSO como co-solvente, lo que mejora las propiedades físicas pero sorprendentemente, empeora la capacidad antimicrobiana. Ambos complejos proteicos son efectivos contra bacterias gram-positivas, pero no contra gram-negativas. Además, se demuestra que la hipericina en la cavidad de la apomioglobina es capaz de realizar microscopía de super-resolución STED, mediante la cual se puede monitorizar los sitios de unión a las bacterias. Asimismo, se ha estudiado la β-lactoglobulina como portador dual de hipericina y ácido retinoico. En este último sistema multi-componente se evalúan las propiedades fotofísicas para verificar la formación y estabilidad del complejo.

En segundo lugar, se desarrolla un nanovehículo para su uso en terapia combinada en el que se incorpora fármacos quimioterapéuticos convencionales con agentes fotosensibilizantes, para superar las resistencias y mejorar la eficacia de los tratamientos individuales. Con este objetivo, se han diseñado y estudiado dos formulaciones liposomales diferentes, ambas con el mismo fotosensibilizador, pero con diferentes agentes quimioterapéuticos. Se preparan las formulaciones bimodales con ambos agentes en el mismo vehículo además de sus homólogos unimodales, con la incorporación única de uno de los dos agentes. Se han evaluado las características fisicoquímicas, fotofísicas y fotobiológicas de las suspensiones bimodales y unimodales. La localización subcelular demuestra que cada principio activo se localiza en orgánulos diferentes desencadenando rutas de señalización celular diferentes, eludiendo los posibles mecanismos de resistencia. El tratamiento *in vitro* en células cancerígenas de estos sistemas tiene un efecto prometedor siendo al menos aditivo en comparación con los tratamientos individuales. Finalmente, se ha evaluado el potencial de la vehiculización activa mediante la unión covalente de un anticuerpo monoclonal en la superficie, lo que lleva a resultados ligeramente superiores para una de las dos formulaciones.

RESUM

Aquesta tesi aprofundeix en l'estudi de nanotransportadors com a sistemes de vehiculització i en alguns casos, alliberació de fotosensibilitzadors emprats en teràpia fotodinàmica. S'han fet servir dos nanotransportadors de naturalesa diferent: proteïnes i liposomes.

En primer lloc s'ha investigat els complexos formats entre la hipericina i les proteïnes apomioglobina i β-lactoglobulina. S'han estudiat les característiques fisicoquímiques i fotofísiques, avaluant l'activitat antimicrobiana en front a bacteris gram-positius i gram-negatius. En ambdues matrius proteiques el fotosensibilitzador es troba majoritàriament en forma monomèrica, preservant les seves propietats fotofísiques i formant un complex estable. En el cas de la β-lactoglobulina s'estudia a més, la formació del complex amb l'adició d'un 20% de DMSO com a co-solvent, fet que millora les propietats fotofísiques en detriment de la capacitat antimicrobiana. Ambdós complexos proteics son efectius contra bacteris gram-positius però no contra gram-negatius. Per altra banda, es demostra que la hipericina incorporada a la cavitat de l'apomioglobina pot ser utilitzada en microscòpia de super-resolució STED. Amb aquesta tècnica es pot monitoritzar els llocs d'unió del fotosensibilitzador a la membrana dels bacteris. Així mateix, s'estudia l'ús de la β-lactoglobulina com a portador dual d'hipericina i àcid retinoic. En aquest últim sistema multi-component s'avaluen les propietats fotofísiques per a verificar la formació i estabilitat del complex.

En segon lloc, es desenvolupa un nanovehicle per la seva aplicació en teràpia combinada en el qual s'incorporen fàrmacs quimioterapèutics convencionals amb agents fotosensibilitzants, per superar resistències i millorar l'eficàcia dels tractaments individuals. Amb aquest objectiu, s'han dissenyat i estudiat dues formulacions liposomals diferents, ambdues amb el mateix fotosensibilitzador però encapsulant diferents agents quimioterapèutics. Es preparen formulacions bimodals on s'incorporen els dos agents al mateix vehicle i els seus homòlegs unimodals, amb la incorporació única d'un dels dos agents. S'han avaluat les característiques fisicoquímiques, fotofísiques i fotobiològiques de les suspensions bimodals i unimodals. La lozalització subcel·lular demostra que cada principi actiu es localitza a orgànuls diferents desencadenant rutes de senyalització cel·lular diferents, eludint els possibles mecanismes de resistència. El tractament *in vitro* en cèl·lules cancerígenes amb aquests sistemes tenen un efecte prometedor, ja que com a mínim presenten un comportament additiu respecte els tractaments individuals. Finalment, s'ha avaluat el potencial de la vehiculització activa mitjançant la unió covalent d'un anticòs monoclonal a la superfície, el que millora lleugerament els resultats per una de les dues formulacions.

TABLE OF CONTENTS

1. INTRODUCTION

1.1. Photodynamic therapy: general aspects 3
1.1.1. Jablonski diagram: the photosensitisation process and mechanisms of action 4
1.1.2. Photosensitisers: general considerations 6
1.1.3. Cell death mechanisms 8
1.1.4. Clinical applications 10
1.2. Photodynamic therapy for antimicrobial purposes 12
1.2.1. Differences between gram-positive and gram-negative bacteria in their cellular structure 13
1.2.2. The photosensitiser: hypericin 14
1.3. Photodynamic therapy for cancer purposes 14
1.3.1. Mechanisms whereby PDT induces tumour damage 15
1.3.2. The photosensitiser: protoporphyrin IX 16
1.4. Drug delivery systems in photodynamic therapy 17
1.4.1. Targeted drug delivery systems 20
1.4.2. Proteins as drug delivery systems 22
1.4.3. Liposomes as drug delivery systems 25
1.5. Combining PDT with conventional treatments 28
1.5.1. Combining PDT with conventional antimicrobial treatments 28
1.5.2. Combining PDT with conventional cancer drugs 29
1.6. Theranostics 32
1.7. Objectives 34
1.8. References 35

2. GENERAL TECHNIQUES AND METHODS

2.1. Steady-state optical techniques 45
2.1.1. Absorbance 45
2.1.2. Fluorescence 45
2.2. Time-resolved optical techniques 45
2.2.1. Time-correlated single photon counting (TCSPC) 46
2.2.2. Time-resolved NIR phosphorescence detection (TRPD) 47
2.2.3. UV-vis nanosecond laser flash photolysis 49
2.3. Fluorescence microscopy 50
2.3.1. Wide field 50
2.3.2. Confocal 51
2.3.3. Stimulated Emission Depletion (STED) 51
2.4. References 53

3. HYPERICIN@APOMYOGLOBIN

3.1. Introduction 57
3.2. Experimental section 57
3.2.1. Materials 57
3.2.2. Apomyoglobin preparation 58
3.2.3. Binding isotherm 58

3.2.4.Modelling studies 59
3.2.5.Microbial growth and photoinactivation process 59
3.3. Results and discussion 60
3.3.1.Complex characterisation and photophysical properties 60
3.3.2.Bacteria photodynamic inactivation 65
3.3.3.Hyp-apoMb as a fluorescence probe for super-resolution Stimulated Emission Depletion 68
3.4. Conclusions 72
3.5. References 74

4. HYPERICIN@β-LACTOGLOBULIN
4.1. Introduction 79
4.2. Experimental section 81
4.2.1.Materials 81
4.2.2.Binding isotherm 81
4.2.3.Modelling studies 82
4.2.4.Microbial growth and photoinactivation process 84
4.3. Results and discussion 84
4.3.1.Complex characterisation in PBS 84
4.3.2.Photophysical properties with and without DMSO – tuning the solvation surface 87
4.3.3.Bacteria photodynamic inactivation 93
4.3.4.Incorporation of retinoic acid to the Hyp-2βLG complex. Study of this multimodal system 98
4.4. Conclusions 112
4.5. References 113

5. LIPOSOMES WITH PROTOPORPHYRIN IX AND CPT-11 AS A DRUG DELIVERY SYSTEM WITH DUAL THERAPEUTIC ACTIVITY IN CANCER
5.1. Introduction 119
5.2. Experimental section 120
5.2.1.Materials 120
5.2.2.Preparation of unimodal and bimodal liposomes 121
5.2.3.Liposome characterisation 122
5.2.4.Cell cultures 124
5.2.5.Preparation of trastuzumab-conjugated bimodal liposomes 125
5.3. Results and discussion 126
5.3.1.Physicochemical characterisation 126
5.3.2.Spectroscopic and photophysical properties 134
5.3.3.Cell viability studies 139
5.3.4.Subcellular localisation and morphological changes 140
5.3.5.Active targeting with Herceptin® 144
5.4. Conclusions 148
5.5. References 150

6. LIPOSOMES WITH PROTOPORPHYRIN IX AND DOXORUBICIN AS A DRUG DELIVERY SYSTEM WITH DUAL THERAPEUTIC ACTIVITY IN CANCER

6.1. Introduction 157
6.2. Experimental section 158
6.2.1.Materials 158
6.2.2.Preparation of unimodal and bimodal liposomes 158
6.2.3.Liposome characterisation 159
6.2.4.Cell cultures 160
6.2.5.Preparation of trastuzumab-conjugated bimodal liposomes 162
6.3. Results and discussion 163
6.3.1.Physicochemical characterisation 163
6.3.2.Spectroscopic and photophysical properties 170
6.3.3.Cell viability studies 175
6.3.4.Subcellular localisation and morphological changes 177
6.3.5.Active targeting with Herceptin® 179
6.4. Conclusions 184
6.5. References 187

7. GENERAL DISCUSSION

7.1. General discussion and future perspectives 193
7.2. References 198

8. CONCLUSIONS 203

9. List of abbreviations 205

10. List of publications 207

CHAPTER 1

Introduction

A general introduction to the subject of the thesis is given in this chapter, as well as the main objectives of this work. The basis of photodynamic therapy as an anticancer and antimicrobial tool are reviewed, together with the state of art of drug delivery systems applied to this treatment modality, especially centred in proteins and liposomes. Moreover, some updates on the state of combined therapy are also presented.

1.1. Photodynamic therapy: general aspects

Photodynamic therapy (PDT) is a clinically approved therapeutic modality for the treatment of malignant and non-malignant diseases as well as pathogenic infections. It consists of the administration of a photoactive drug, called photosensitiser (PS), followed by light exposure in the presence of oxygen. These three components are not harmful or cytotoxic *per se*, but combined leads to the production of reactive oxygen species (ROS), which oxidize intracellular molecules and thereby destroy cells (Figure 1.1).[1–3]

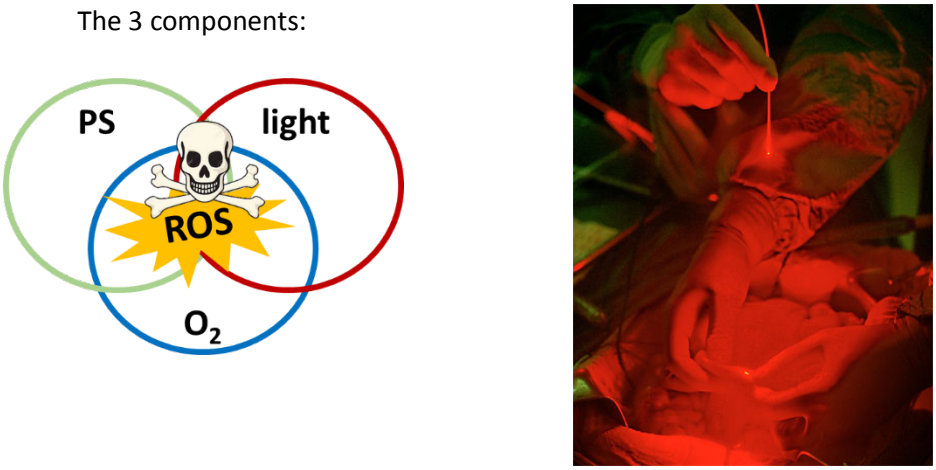

Figure 1.1. PDT is a therapeutic modality based on the combination of the PS, light and oxygen to generate ROS which exerts cellular damage. The image shows a PDT scenario where a patient who has already taken the PS is illuminated under a beam of light through a fiber optic directly focused to the tumor site. Photograph was taken by John Crawford (National Cancer Institute) and licensed in Wikimedia Commons.

PDT comprises two stages: first the PS administration to the patient either systematically or locally, in the absence of light, which is left to accumulate in the malignant tissue for a certain time. Secondly, once the ratio between PS concentration in malignant tissue respect to that in healthy tissue is maximum, light of appropriate wavelength and dose is delivered to the specific tumour or infected area.[4] This therapy has the advantage over other treatments of dual selectivity: the PS is targeted or is accumulated specifically to the tumour or other lesion and the light can also be accurately delivered in a spatially confined and focused manner.[5]

Ultimately, the cell death is caused via apoptosis, necrosis or autophagy, by the generation of ROS, which have a high and unspecific reactivity. Due to its multi-target mode of action, the scope of PDT expands from the treatment of cancer cells, with the approval of several PSs for clinical use and several others undergoing clinical trials, to the treatment of microbial infections.[6] However, PDT has side effects including the inherent broad reactivity of ROS makes that during PDT therapy both healthy and unhealthy cells will be damaged equally unless a precise localisation of the PS or light is achieved. Since light can diffuse through tissues, it is critical to assure the PS location with respect to the healthy tissue to achieve more selective in

PDT treatments. Another limitation of this approach is the importance that PSs absorb in the optical therapeutic window (650-900 nm) to ensure the maximum penetration depth of light and avoid the long-lasting skin photosensitivity. Therefore, new methodologies in order to enhance the selectivity of this therapy are urgently needed and some of these improvements will be addressed in the following sections.

1.1.1. Jablonski diagram: the photosensitisation process and mechanisms of action

Production of singlet molecular oxygen ($^1O_2$) by photosensitisation remains the most common and convenient means of producing this non-radical yet highly-ROS. The process starts when the PS in its singlet ground state (^{1}PS) absorbs light of an appropriate wavelength, usually in the visible (VIS) and near-infrared range (NIR). This results in the excitation of a single electron of the PS from the highest occupied molecular orbital (HOMO) to the lowest unoccupied molecular orbital (LUMO), while the spin remains unchanged during the process. The excited state, known as the excited singlet state (^{1}PS*), is relatively short lived, few nanoseconds at most. In this stage, several photophysical and photochemical processes can occur (Kasha's rule) to lose the excitation energy. The PS can return to its ground state emitting light (fluorescence) or internally converts the energy to heat by a radiationless relaxation. Both transitions are, according to spin selection rules, allowed since the spin number is preserved. On the other hand, the excited electron can also reserve its spin, thus undergoing intersystem crossing (ISC) and populating the first excited triplet state (^{3}PS*), less energetic than the first excited singlet state (S_1). Despite being a forbidden transition and therefore a relatively slow process (up to 1 s) for most organic compounds in solution, it can still occur with a certain probability as a consequence of spin-orbit coupling (i.e., interaction with the electron's magnetic momentum and its spin-motion magnetic momentum).[7,8]

The ^{3}PS* ultimately decays to the ground state, either by a radiative process (phosphorescence) or by internal conversion. Nevertheless, the long-lived ^{3}PS* can also react in two distinctly different photochemical processes. **Type I** pathway involves an **electron or hydrogen transfer** reaction between the ^{3}PS* and a substrate, initiating a cascade of radical reactions which, in the presence of molecular oxygen ($^3O_2$), culminate in the formation of various types of ROS, including hydroxyl radical ($^{\bullet}$OH), superoxide radical anion ($O_2^{\bullet-}$) or hydrogen peroxide (H_2O_2) (Figure 1.2). Specifically, electron transfer from a substrate to ^{3}PS* yields a radical anion ($PS^{\bullet-}$), which reacts further with $^3O_2$ to yield $O_2^{\bullet-}$. This primary ROS is not highly reactive in biological systems, but can be reduced further to produce H_2O_2 that can easily cross biological membranes.

Moreover, H_2O_2 can react with $O_2^{\bullet-}$ to form $^{\bullet}OH$, whose high redox potential of E_0=1.35 V allows it to oxidize most molecules within the cell.

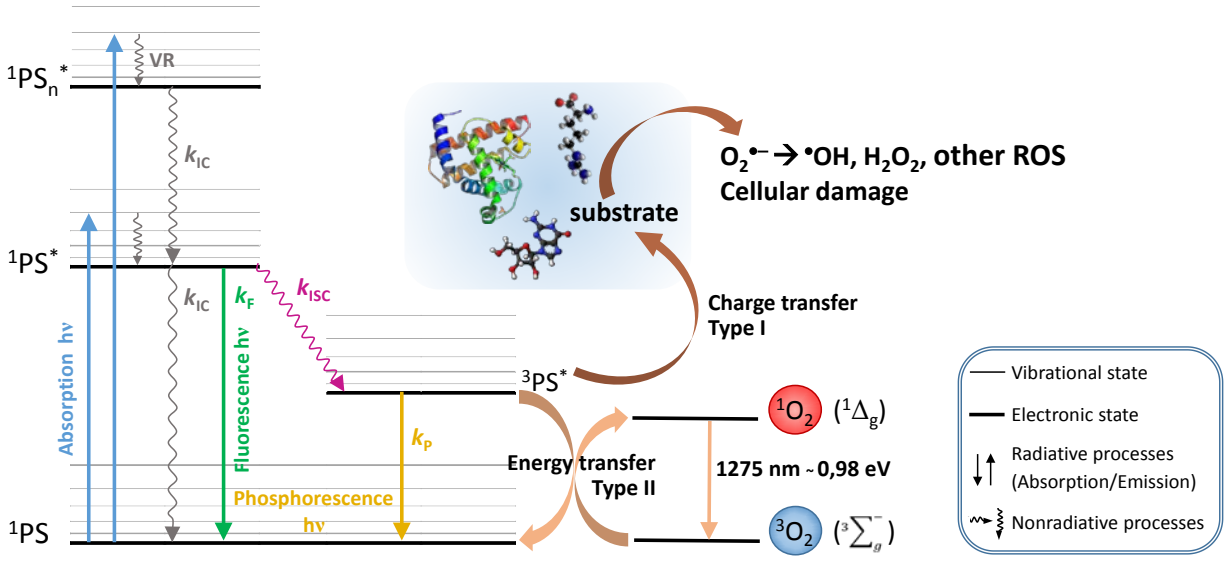

Figure 1.2. Jablonski diagram representing the energetic states of a PS; the photophysical processes occurring upon light absorption and type I and type II reactions. IC: internal conversion, ISC: intersystem crossing and VR: vibrational relaxation.

The **type II** pathway involves an **energy transfer** reaction from the ^{3}PS* to oxygen, yielding the transient and highly reactive $^1O_2$ (Figure 1.2). This reaction is spin-restricted because oxygen in its ground state is also a triplet ($^3O_2$)[8] and triplets reacting with triplets have a 1/9th probability to yield two singlets ($^1O_2$ and ^{1}PS).

PS act as a catalytic molecule since one molecule may account for many "PDT cycles", involving many oxygen molecules, many photons and many substrate molecules. Indeed, it has been estimated that the turnover rate can be as high as 10^6 or 10^7 cycles per second per molecule of PS.[9] Nevertheless, a photoexcited PS molecule can react with other molecules present in the system leading to photobleaching or photodegradation and is related to the photostability of the PS that will be mention in the next section.

$^1O_2$ is kinetically far more reactive than $^3O_2$ due to its particular spin multiplicity. Unlike $^3O_2$, which cannot oxidize organic molecules because of the spin angular momentum conservation rules, $^1O_2$ has the right spin to carry out the oxidation of organic compounds. Thus, the highly reactive $^1O_2$ subsequently reacts towards a broad variety of molecules and biomolecules, particularly proteins, lipids, and nucleic acids of microbial and malignant cells (Figure 1.3).[7,10,11]

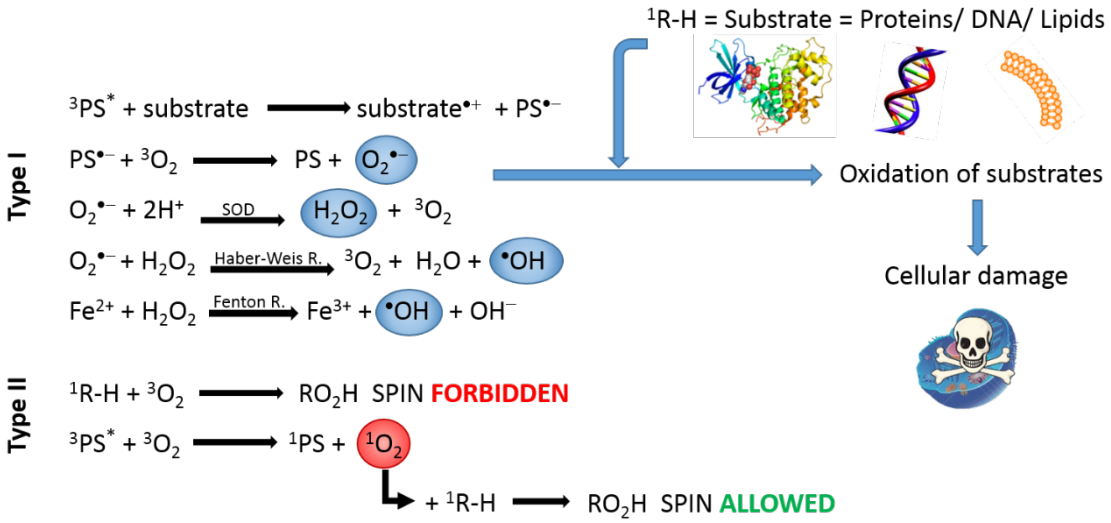

Figure 1.3. Possible photochemical reactions during PDT.

The lifetime of $^1O_2$ is very dependent on the solvent or its environment.[12,13] In neat H_2O, the lifetime is 3.5 µs, in D_2O it is 68 µs, in organic solvents it is in the range 10–100 µs, and in lipids it is 50–100 µs.[14] It decreases dramatically (to ~0.2 µs) inside cells due to reactions with biological substances, which limits the $^1O_2$ diffusion in cells.[8] Thus, PDT treatments are spatially localised at the point of $^1O_2$ generation and primary cell damage will be localized within its vicinity, which is approximately about 10 nm in diameter, 30 nm at much (thickness of a cell membrane).[15]

Type I and type II processes may occur simultaneously, and the ratio depends on several factors, particularly the properties of the PS used and the oxygen concentration. For many PSs, type II is regarded as the dominant process in PDT.

1.1.2. Photosensitisers: general considerations

PDT efficiency broadly depends on three factors, namely the light (source type dose, and delivery regime), the concentration of oxygen, and the PS. Moreover, since the diffusion constant of singlet oxygen is D= 1.4 x 10^{-5} $cm^2 \cdot s^{-1}$,[8] rather low, $^1O_2$ has a low sphere of action and therefore the intracellular localisation of the PS greatly determines the site of primary cellular damage.

PSs are commonly organic planar molecules with highly delocalised π-orbitals. They can be synthetic or natural molecules with some preferable characteristics: 1) low levels of dark toxicity and low incidence of administration toxicity (i.e., hypotension or allergic reaction); 2) capable of absorbing light in the so-called optical therapeutic window in order to penetrate tissue and reduce skin photosensitivity; 3) their triplet state must have sufficient energy to allow an efficient energy transfer to $^3O_2$ (E_T > 94 $KJ \cdot mol^{-1}$; 22.5 $kcal \cdot mol^{-1}$); 4) endowed with high triplet quantum yields and long triplet state lifetimes.[10,16] Other desirable photophysical and

photochemical properties are: 5) relatively high extinction coefficients at the light excitation wavelength to minimize the light fluences needed; 6) high photostability; 7) solubility in biological environments and 8) a rapid clearance from the body.[6,10,17]

According to the previous requisites, we can currently find a large number of dye families capable of acting as PDT photosensitisers (Figure 1.5). The following classification is based on their chemical structures:

Porphyrin-based photosensitisers. A vast majority of PSs are derivatives of the cyclic tetrapyrrole structure named porphin.[4] This macrocycle core consists of 18-π conjugated electrons with four pyrrolic subunits linked on opposing sides (α-positions, Figure 1.4) through four methine (CH) bridges, known as the *meso*-carbon positions.[18] Some of them are naturally occurring pigments active in many biological processes and include the metallopigments haem (i.e., the prosthetic group of proteins like haemoglobin, cytochromes, catalase, etc.).[19] However, most efficient porphyrin-based PSs used in PDT are synthetic and have substituents in the *meso*- or β-positions. Some well-known tetrapyrrolic PSs are porphyrins, chlorins, bacteriochlorins, phthalocyanines or porphycenes.

The first approved PS belong to this category was a mixture of porphyrin oligomers, called Photofrin®, a purified version of hematoporphyrin derivative (HpD).[20]

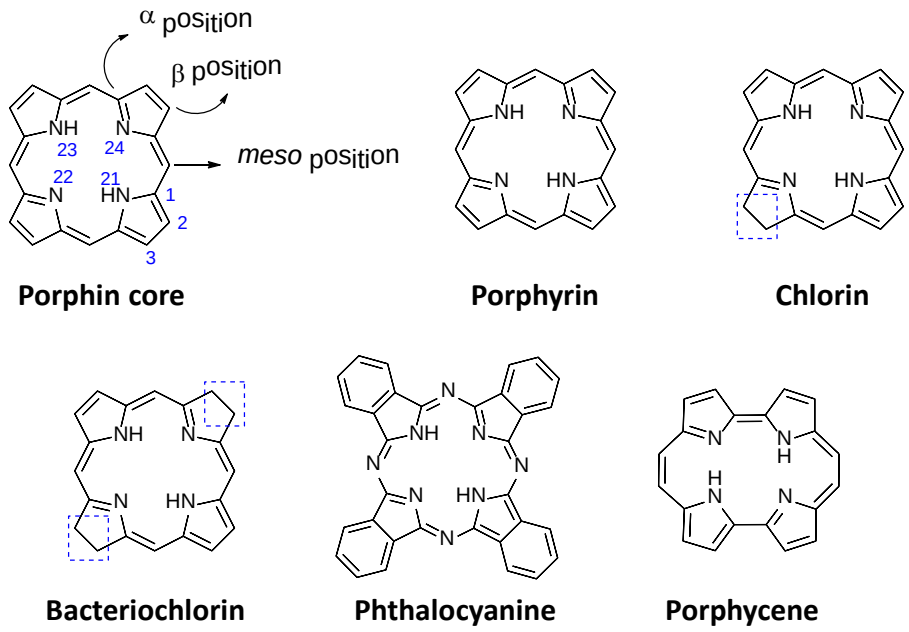

Figure 1.4. Structure of some of the existing cyclic tetrapyrrolic PSs.

Non-porphyrin-based photosensitisers. Inside this group, the most used PSs are: polynuclear aromatic hydrocarbons; aromatic ketones (anthraquinones, perylenequinones), aromatic heterocycles (psolarens, coumarins, flavins, xanthenes, rhodamines, fluoresceins, acridines, phenazines or phenothiazines); carbon nanoforms; or coordinate compounds of many transition metals, mainly Ru(II).[17,20,21]

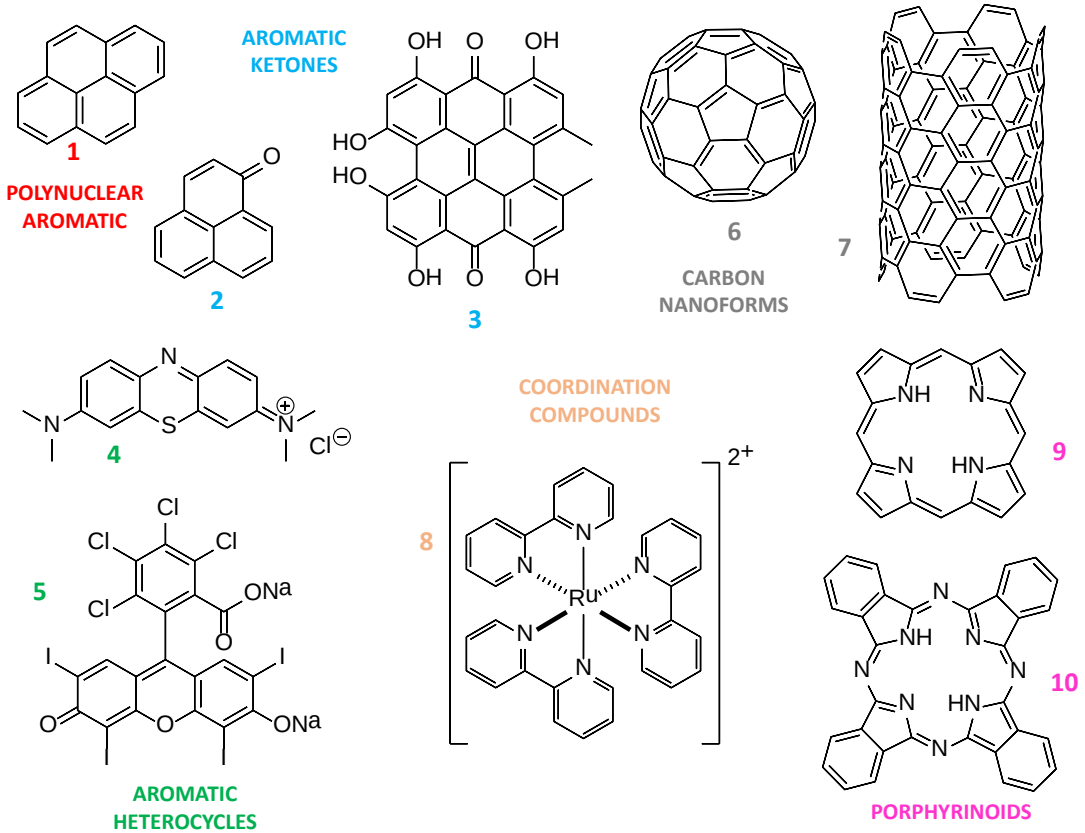

Figure 1.5. Structures of some of the most common PSs: 1) pyrene; 2) phenalenone; 3) hypericin; 4) methylene blue; 5) rose bengal; 6) fullerene- C_{60}; 7) carbon nanotube; 8) tris(bipyridine)ruthenium (II); 9) porphyrin and 10) phthalocyanine;

Each particular type of PSs finds application in different areas, basically depending on their photostability and their optical window.

1.1.3. Cell death mechanisms

As already mentioned, the production of ROS lead to an irreparable cellular damage which triggers tumour cell death by any of the four pathways- apoptosis, necrosis, autophagy or paraptosis.[22] The type of mechanism involved in cell death depends on several factors, for instance treatment dose, cell line, mode and dose of irradiation or subcellular localisation of the PS.[23] The latest plays a key role in PDT since the $^1O_2$ will diffuse just in the close vicinity of its production and the cellular response depends on which organelles are photochemically damaged. Most of the subcellular organelles, such as mitochondria, lysosomes, nucleus, plasma membrane, endoplasmic reticulum (ER) or Golgi apparatus, can become targets for PSs.

Apoptosis is a very complex, multi-step, multi-pathway (i.e., can be triggered by external or internal signals) cell death that is genetically encoded in every cell of the body and is a common modality in cells treated with PDT.[24] Apoptotic cells are characterised by some morphological features, including chromatin condensation, nuclear fragmentation, cell shrinkage and plasma membrane blebbing. Cells are ultimately fragmented into multiple membrane vesicles, called apoptotic bodies. Apoptotic bodies are engulfed by phagocytes *in vivo*, which prevents inflammation and tissue destruction. Regarding the biochemical level, oxidation of cellular components by ROS initiates a stress response which elicits a cascade of signalling events commonly involving activation of caspase, mitochondria damage or cytochrome c release, among many others. Mitochondria plays a key role in regulating pro-apoptotic signals and triggering the apoptosis mechanism as a response, although some recent investigators indicate that other organelles such as lysosomes, Golgi apparatus or ER may be important in prompting pro-apoptotic signalling cascades.[25,26]

On the other hand, **necrosis** has traditionally been thought as a passive, not regulated cell death, although recent reports have remarked that some form of necrosis may also occur in a regulated manner.[27,28] Excessive chemical or physical injury to the cell results in this violent and quick cell death modality. Necrotic cells are characterised by cytoplasm swelling and vacuolisation, destruction of organelles and uncontrolled rupture of the plasma membrane, leading to the release if intracellular contents and pro-inflammatory molecules, which result in an acute inflammatory response and at the end membrane blebbing.[23]

Photochemical damage of cells can also lead to cell death by **autophagy**. Autophagy is a catabolic process that allows the cell to maintain a balance between the synthesis, degradation and recycling of cellular products. In this process, a portion of the cytosol, usually containing cellular organelles, is sequestered by a double membrane forming the autophagosome, which ultimately fuses with a lysosome, yielding the autophagolysosome.[24] This cell death modality is, in fact, a cytoprotective mechanism to preserve cellular homeostasis but it can also promote cell death in response to excessive stress signals including oxidative stress caused by PDT.[1] Recent studies show that autophagy could both have a pro-death or preservation role after PDT treatment.[29,30] Kessel *et al.* claim that when mitochondria is the target, autophagy plays a protecting role, whereas if the target is the lysosome then, autophagy does not provide any protection, being indeed more effective cell death mechanism.[31]

Kessel *et al.* have described a new mode of cell death, which is called **paraptosis**.[32] Unlike apoptosis, this is a mode of non-caspase-mediated cellular death associated with ER stress. It is

characterised by mitochondrial swelling and extensive cytoplasmic vacuolisation, with exceptionally large vacuoles derived from the ER, which could be labelled with an ER stain. It seems that somehow lysosome photodamage promotes and activates paraptosis. During the process, the nuclei remain intact but the cells died from a process that is still under investigation and it cannot yet be estimate the extent to which paraptosis contributes to PDT-mediated cell death. Kessel has also demonstrated that ER photodamage can lead to paraptosis, whereas lysosomal photodamage results only in apoptosis.[32]

Although these cell death mechanisms are directly related to eukaryotic cells, several studies indicate that some features of programmed cell death such as apoptosis are conserved in bacteria. Some reports suggests that proteins like CidA and LrgA, originally found in *S. aureus* but widely conserved in other bacteria, possess functions analogous to the pro-apoptotic effector of the Bcl-2 protein family. In response to toxic agents, antibiotics, oxidation stress or certain environment conditions these proteins cause membrane disruption and lead to the activation of peptidoglycan hydrolases that ultimately induce a cellular disassembly.[33] Moreover, in most cases bacterial cell death involves ROS generation follows by DNA fragmentation, chromosomal condensation and membrane depolarization.[34]

Bacterial infection elicits a diverse array of host protective and stress responses, including the cell death and proliferative responses, inflammatory response, and innate immune response. Ultimately, the host cell death response critically influences the fate of bacterial infection, the integrity of the host innate defence barrier, innate and acquired immunity, and disease outcome.[35] Bacteria-triggered cell death results in various modes of cell death that greatly vary with the host cell type, stage of infection, infectious dosage, physiological condition of the cell, bacterial factors, and experimental setting.

1.1.4. Clinical applications

The current era of PDT can be considered to begin in 1960 when R. Lipson and S. Schwartz observed that injection of crude preparation of hematoporphyrin led to fluorescence of neoplastic lesions visualised during surgery. Schwartz further purified the hematoporphyrin crude and obtained a more phototoxic version that he called hematoporphyrin (HpD), which was used by Lipson *et al.* for further investigations.[36] In 1978, Dougherty *et al.* conducted the first clinical trial combining HpD and red light and obtained partial or complete tumour eradication in almost all lesions treated.[37] Importantly, they further purified HpD up to the launching of the first clinically approved PS known as Photofrin®,[38] which nowadays is still one of the most clinically used PSs.[1] However, Photofrin® has several drawbacks: it consists of a

mixture of many compounds so it is difficult to reproduce its composition, it is not very tumour selective and causes long-lasting cutaneous photosensitivity, as it is absorbed by the skin.[11]

Since then, significant efforts have been invested in the development of new PSs and establish better protocols for PDT treatments. Up to now, there are many PSs approved by the Regulatory Agencies for numerous cancers including lung cancer, gastrointestinal tract, the head and neck region, bladder, prostate, and nonmelanoma skin cancers and actinic keratosis.[39] Some of these approved PSs are δ-aminolevulinic acid (ALA, Levulan®) or 5-aminolevulinate (MAL, Metvix®), both precursors to endogenous protoporphyrin IX (PpIX), for actinic keratosis; hexaminolevulinate (Cysview®) for colon and bladder cancer diagnosis; temoporfin (m-THPC, Foscan®) for head and neck cancers or Photosens® just approved in Russia for various cancers.[6]

On the other hand, antimicrobial PDT (aPDT) may find widespread application for a variety of infectious diseases, its current clinical use is mostly restricted to dentistry and dermatological applications.[40,41] Unlike cancer PDT, the dyes used in aPDT were originally approved for other applications, but their photosensitising ability is being exploited for aPDT. Not surprisingly, they belong to widely diverse chemical families (e.g., xanthenes such as Rose Bengal (RB), perylenequinones such as hypericin, phenothiazinium salts such as Methylene Blue (MB) or Toluidine Blue O (TBO) and cyanines such as Indocyanine Green (ICG), as well as their derivatives and a number of additional dyes from other families (e.g., curcuminoids, tetrapyrroles or fullerenes).[42,43] MB, TBO and ICG are the only PSs clinically approved for antimicrobial applications, besides ALA and MAL that are as well approved for dermatologic indications.[44–47] Most of the previous PSs are in clinical trials for applications like onychomycosis, oral candidiasis, psoriasis, acne, atopic dermatitis, foot ulcers or periodontitis.

Although oncological applications have been the main driving force behind PDT, extension to non-oncological conditions has long been pursued. For instance, Visudyne™ (verteporfin; QLT Phototherapeutics, Inc., Vancouver, BC, Canada) obtained FDA approval in 1999 for the treatment of the wet form of age-related macular degeneration (AMD).[48] Purlytin™ has already finished phase III studies for AMD, and motexafin lutetium, under its commercial name of Optrin®, is also being tested for the loss of vision due to retina damage.[6]

In the field of dermatology, PhotoCure ASA completed the studies for Allumera®, a methyl aminolevulinate (MAL)-based product for skin rejuvenation that was released in the USA in 2011, and has finished phase II tests for the use of Visonac® for the treatment of acne vulgaris.[49]

Although originally PDT was developed as a cancer treatment, nowadays it also has successful uses in the treatment of non-cancerous diseases. Some examples are already mentioned like in

the ophthalmology or dermatology field, but has also been used in rheumatology for arthritis or for vascular diseases such as atherosclerosis. However, PDT is gaining importance in what were its origins in microbiology for a large variety of localised infections or against local viral diseases such as herpes.[42]

1.2. Photodynamic therapy for antimicrobial purposes

Light has been used in therapy for more than three thousand years. Ancient Egyptian, Indian and Chinese civilisations used light to treat various diseases, including psoriasis, vitiligo or skin cancer. Yet it was not until 1900 that a medical student Oscar Raab and his professor Hermann von Tappeiner reported that certain wavelengths were lethal to microorganisms such as paramecia in the presence of acridine.[50]

Despite having several applications for killing pathogenic microorganisms *in vitro* or in animal models, its uses to treat infections in patients still has not many applications. Although this seems to be changing since the emergence of antibiotic resistance due to, among other things, the inappropriate prescription of antibiotics, the failure of some patients to complete their treatment or due to the dramatically low effectiveness of antibiotics to treat bacteria as a biofilm. Therefore, the situation has led to a major research effort to find alternatives like antimicrobial photodynamic therapy (aPDT) to antibiotics treatments since just some evidences have been found of microbial viability recovery and resistance mechanisms against it.[51] aPDT also has a broad spectrum action, since can kill different microorganisms (e.g., bacteria, fungi, yeasts or parasitic protozoa), its efficacy is not significantly dependent of the strain or the antibiotic resistance pattern and has a small probability to promote the onset of mutagenicity. Contrary to PDT for cancer where the PS is generally delivered systemically, in aPDT the PS will be locally administered into the infected area by methods such as topical application, instillation, interstitial injection or aerosol delivery. Thus, the therapy lead to an extensive reduction in pathogen population either by means of damage DNA or cytoplasmic membrane, with very limited damage to the host tissue.[52] aPDT is certainly a suitable therapy to overcome the antibiotic resistance problem, now that for instance methicillin-resistant *Staphylococcus aureus* (MRSA), vancomycin-resistant E*nterococcus faecalis* (VRE) or some new strains of *Escherichia coli* are causing much concern these days.[53]

However, there are always some limitations that make this treatment had not been established as a standard therapy with antimicrobial purposes. One of the greatest limitations is the different susceptibility to PDT between gram-positive and gram-negative bacteria. It is known that gram-negative are much less susceptible to PDT with many commonly used PS that, even

so, caused a great phototoxicity in gram-positive. It was found that, in general, neutral or anionic PS molecules are efficiently bound to and photodynamically inactivate gram-positive bacteria, whereas they are bound, to a greater or lesser extent, only to the outer membrane of gram-negative bacterial cells, but do not inactivate them after illumination.[54]

Another important issue to be addressed in order to promote aPDT as the standard therapy is the selectivity for the microbes over mammalian cells. It is imperative to be reducing the disease-causing pathogens while the surrounding host cells of the patient are not receiving any PDT damage.[7]

1.2.1. Differences between gram-positive and gram-negative bacteria in their cellular structure

The higher susceptibility of gram-positive bacteria is explained by their physiology, cellular structure and organisation. Both gram-positive and gram-negative bacteria present an outer cell wall. In particular, in gram-positive species the outer wall (15- 80 nm thick) contains up to 100 peptidoglycan layers, which are associated with lipoteichoic and negatively charges teichuronic acids. This wall instead of representing an effective permeability barrier, displays a quite high porosity degree, enabling various macromolecules to diffuse into the inner plasma membrane (Figure 1.6).[55]

On the contrary, the outer wall of gram-negative species is endowed with an additional 10- 15 nm thick element, external to the peptidoglycan network.[51,52] This outer membrane is a bilamellar membrane composed of porin proteins, lipopolysaccharide trimers and lipoproteins that constitutes a physical and functional barrier between the cell and its environment (Figure 1.6).[56]

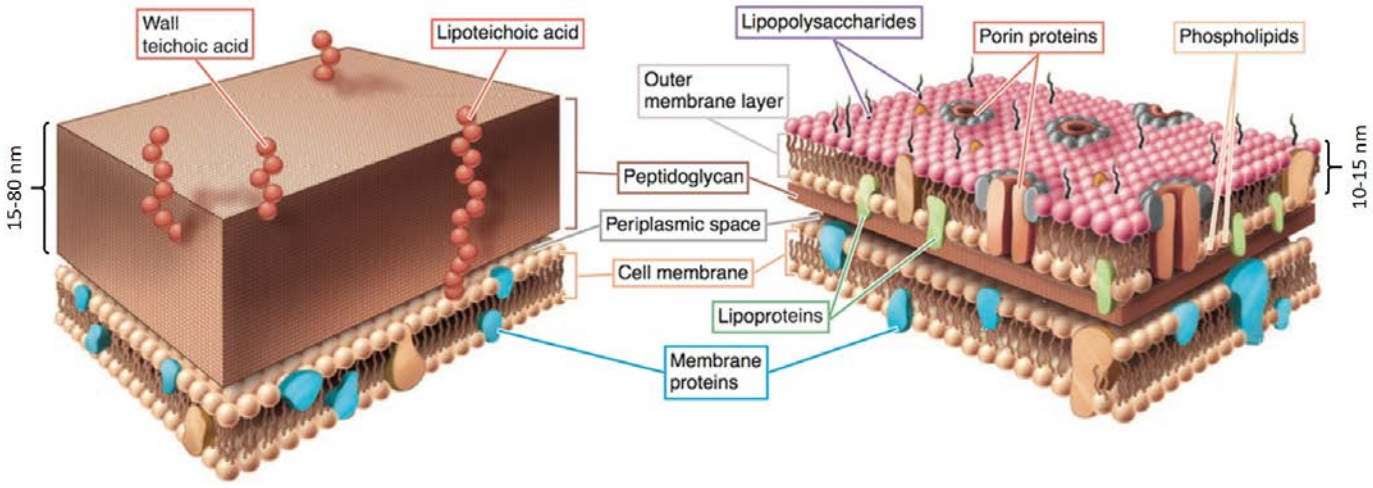

Figure 1.6. Comparison of gram-positive and gram-negative bacterial cell walls. Image adapted from: *http://microbioenergetica.squarespace.com.*

1.2.2. The photosensitiser: hypericin

As has been pointed out, cationic PSs such as methylene blue or toluidine blue are the only ones which can bind and penetrate through the gram-negative membrane. However, gram-positive bacteria could be killed independently of the PS's charge. Then it is important to reach an equilibrium between the charge and the hydrophobic character of the PS that let it reach the inner membrane of the cell.[7]

Usually, lipophilic PSs such as hypericin (Hyp, see Figure 1.5) are incorporated into the cellular membrane through a passive transport by diffusion. Hyp is a neutral and water insoluble perylenequinone isolated from St John's wort and is possibly one of the most powerful PSs present in nature. The pentacyclic conjugated chromophore provides good absorption bands in the red range with a peak around 595 nm.[53] Hyp has a quite high quantum yield of $^1O_2$ formation ($\Phi_\Delta \approx 0.32$ in ethanol) and it is a both type I and II PS. In cells, Hyp is particularly accumulated in the membranes of the ER and Golgi complex, causing the cell death by the ER stress leading to apoptosis but ultimately activating the host immune system.[57] Moreover, Hyp may cause cell death by paraptosis according to Kessel *et al.* in three different cell lines, A549, 1c1c7 and WSU12, likely caused by the ER photodamage (data shown in the 17th Congress of the European Society for Photobiology).

Although Hyp has been known as a medicinal plant with antidepressant properties for many years, recently has been tested clinically for several cancer indications because of the multiple pathways that are activated with Hyp-PDT.[58] Hyp is also receiving much attention for the detection of bladder cancer, due to its fluorescence quantum yield ($\Phi_F \approx 0.35$).[59,60] Moreover, it has also been scrutinized for its antiviral, anti-fungal and antibiotic properties.[55]

1.3. Photodynamic therapy for cancer purposes

Cancer is a major cause of morbidity and mortality, with approximately 14 million new cases and 8 million cancer-related deaths in 2012.[61] Therefore, it is not surprising that much effort is made to overcome this worldwide burden. Although the conventional cancer treatment options are chemotherapy, radiotherapy or surgery, among others, PDT is an alternative approach since in 1972 appeared the first reports of the anticancer PDT by Lipson and Baldes. They first used HpD combined with red light to treat bladder cancer in animals and in humans. Since then, PDT has been mostly developed as an anticancer therapy for tumours of the skin and mucous membranes, for tumours of hollow organs accessible by endoscope, and recently for deep solid tumours where light can be delivered by interstitial fibers inserted into the tumor.[7]

PDT, although still emerging, is already a successful and clinically approved therapeutic modality, that was to become the first drug-device combination approved by the US Food and Drug Administration (FDA). However, is still many things to do because, since the approval of Photofrin® in 1993, the number of clinically approved drugs for PDT is disappointingly low.

The demand for the precision, efficacy and selectivity of the treatments is increasing every day. In PDT, selectivity is one of the best qualities, but the highly localised nature of the PS could be a problem to treat metastatic lesions. In order to overcome this, a deeper understanding of which are the mechanisms activated by PDT could be decisive. It has been shown that induce a systemic immune response could propagate the damage to some extent.[1]

On the other hand, one of the limitations of PDT turns out to be a desirable feature. Specifically, the photobleaching of the PS (i.e., the dye destruction over illumination) would make light dosimetry less critical because overtreatment would be avoided.

Some reports suggest changes in the traditional protocols of cancer PDT, which could improve the control of the procedure, depending on cancer to be treated. For instance, reducing the interval between drug administration and irradiation, giving light when the PS is still in the blood vessels could increase the vascular damage (explained in 1.3.1).

1.3.1. Mechanisms whereby PDT induces tumour damage

PDT induces tumour damage via direct cellular, vascular and immunological mechanisms. Intracellular cytotoxic mechanisms include stress response, apoptotic, paraptotic, necrotic, and/or autophagic cell death, most of them already explained.

Direct cytotoxic effects do not explain the PDT strong antitumour activity, thus there are triggered in most cases other indirect mechanisms that contribute to the high effectiveness of the treatment.

Direct cell damage. The intracellular explosive generation of high reactive ROS are responsible for the direct cell damage, which ultimately leads to, the above mentioned, apoptosis, necrosis or autophagy cell death. Some indications suggest that PSs localised in mitochondria or ER promotes an apoptosis response, although this last can cause autophagy as well, whereas those which targeted plasma membrane or lysosomes promote necrosis.[24,62]

Vascular damage. ROS may also damage the tumour-associated vasculature, causing damage to the endothelial cells and ultimately blocking the blood flow in the vessels.[63] Evidences of vascular-targeted PDT alterations include thrombus formation, blood vessel occlusion and

vascular function shutdown; these events result in disruption/blocking of the channels, which supply oxygen and nutrients to the tumour. Both are capital necessities for the growth of the tumour mass and progression of cancer to other parts of the body (i.e., metastasis tumours).[64,65] Occlusion of blood vessels and hypoxia can occur few minutes after beginning the PDT treatment, as it was previously mentioned. PSs that can cause cell death by targeting the vascular space or blood vessels are gaining much importance due to its great results. Moreover, vascular damage can stimulate the immune response in the host system.

Inflammatory and immune damage. PDT can induce an immune response in the host tissue in response to a PDT-induced oxidative stress.[66] This fact *per se* is not surprising since other approaches such as surgery, chemotherapy and ionizing radiation also activate an immune response. However, whereas the previous develop immunosuppression, PDT has shown immunostimulation, which makes it an advantage for cancer treatment.

The onset of PDT-induced inflammatory is marked by dramatic changes in the tumour vasculature, which becomes permeable for blood proteins and pro-adhesive for inflammatory cells. Thus, after PDT, a concomitant inflammatory response occurs inducing the release of immunomodulators, such as cytokines and growth factors. This activity response of the host is reported to have implications in further destruction of remaining tumour cells and preventing tumour recurrence and metastasis.[65]

1.3.2. The photosensitiser: protoporphyrin IX

The large aromatic conjugation of its core endows porphyrins with very intense absorption bands at about 400 nm (named B or Soret band) and series of lower-intensity bands in the green-red spectral region (500-650 nm; Q bands).[17] Thus, free-base porphyrins are generally deeply red or purple colored and barely fluorescent ($\Phi_F > 0.2$) but with high intersystem crossing and triplet quantum yields. Moreover, they possess low energy triplet excited states whose energy is really close to that of the $^1O_2 \leftarrow O_2$ transition ($E_T \approx 150$ kJ·mol^{-1}; $E_\Delta \approx 94$ kJ·mol^{-1}) and their triplets are easily trapped by molecular oxygen before they decay ($f_{T,\Delta}\, O_2 \approx 1$, fraction of T_1 quenched by $^3O_2$).

Given their ubiquitous presence in biological systems and their promising photophysical and photosensitising properties, porphyrins have been largely explored as PSs for the production of above all $^1O_2$, in biological media.[67]

PpIX is a naturally occurring precursor of haem, which represents the prosthetic group of several proteins, such as haemoglobin. PpIX is produced in the haem pathway in mitochondria starting with the ALA precursor. However, PpIX can also be administered exogenously.

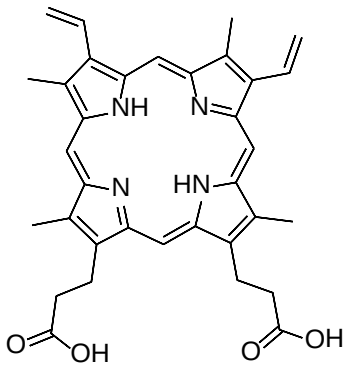

Figure 1.7. PpIX chemical structure.

Authors have reported that PpIX accumulation in tumours is facilitated by the particular porphyrin metabolism in malignant tissues that are characterised by high cellular turnover.[62] Although PpIX is most efficiently photoactivated at the Soret band, about 405 nm, the presence of Q-bands, with the absorption peaks at 510, 545, 580 and 630 nm, allows to also use red light to activate it *in vivo*.

1.4. Drug delivery systems in photodynamic therapy

Over the last decade, pharmaceutical companies are experiencing a big economic challenge due to the high costs of drug discovery and development and the extensive time needed for getting the approval from Regulatory Agencies. One possible strategy in order to overcome these hurdles is potentiating drugs that already have been approved or used for specific diseases, tailoring them in a drug delivery system (DDS).

Over the past two decades, nanotechnology and its application in medicine has experienced a rapid diversification and a remarkable progress has been made in the development and application, above all in cancer treatment. Nanoparticles (NPs) began being scrutinised as vehicles for PDT in order to solve the aforementioned disadvantages, thereby leading to a higher efficacy of the drug with a decrease overall toxicity. Since most PSs with promising photophysical properties are very hydrophobic, hindering their systemic administration and provoking the loss of their photophysical properties in aqueous medium, these DDSs can supply an anchor or a core milieu where the PS can be well accommodated. Therefore, the nanovehicle renders a water compatible and stable system, preventing from aggregation or premature degradation of the PS.[68]

Moreover, NPs allow the encapsulation of high PS payloads, improved photoactivity and appropriately timed release and activation of therapeutic agents.[2] NPs also have the exquisite ability of being retained in tumour tissues and improve its biodistribution thanks to the enhanced and permeability retention effect (EPR, explained in section 1.4.1), phenomenon known as passive targeting and which clearly potentiates localisation of NPs at the site of action, increasing treatment tolerability.[69]

A vast array of nanodelivery systems have been studied for PDT, including liposomes,[70–72] proteins,[73] organic polymeric NPs, micelles or dendrimers[74,75] such as those of poly-(acrylamide) or poly-(lactic-co-glycolic) acid (PLGA).[76] On the other hand, nanovehicles made of inorganic materials such as silica[77], gold,[78,79] or even systems which are PSs *per se*, such as fullerenes, quantum dots, upconversion NPs or TiO_2 NPs.[80,81]

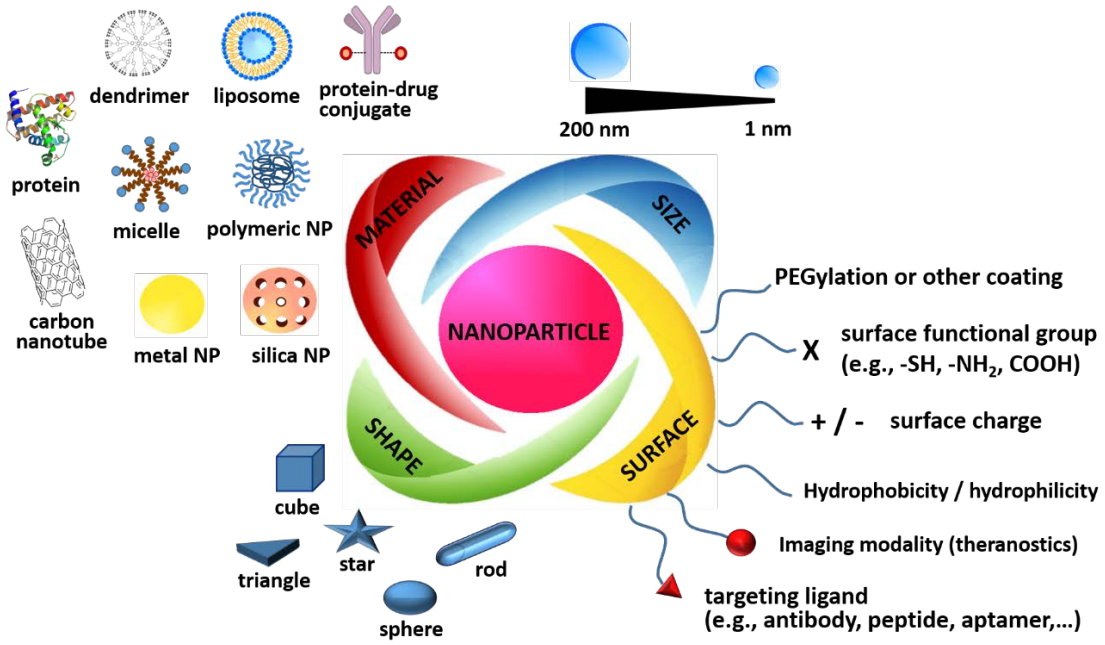

Figure 1.8. Schematic diagram of the main four biophysicochemical properties of a NP that could be tailored or modulated in order to obtain the ideal DDS.

Shape, size, material and surface nature of the NPs govern their biological interactions such as intracellular uptake, blood circulation times, or their clearance through reticuloendothelial system. The surface modification is gaining importance due to the several characteristics that can bestow to the carrier. One example is the surface modification with certain polymers such as chitosan or poly-(ethylene glycol) (PEG) which improve their biodistribution and pharmacokinetics. Additionally, targeting ligands (e.g., small organic molecules, peptides, antibodies or nucleic acids) can be added to the surface to specifically target cancerous cells through selective binding to the receptors overexpressed on their surface.[82] The study and

optimisation of these parameters during synthetic procedures can result in promising DDSs (Figure 1.8).

A nanocarrier should meet a series of characteristics. The ideal DDS should be biodegradable and biocompatible, have a small size and high loading capacity, be stable, non-immunogenic and non-toxic, have a prolonged circulation in the body after the administration, and selectively accumulate in the target area. Additionally, it was traditionally believed that the PS should be incorporated into the vehicle without alteration of its photophysical properties in order to be ready to generate ROS once reaches the cell.[83] Although this holds true for some PSs in certain carriers due to the improved solubility of the PS in the local environment of the nanocarrier, in other cases the photosensitising ability of the PS becomes reduced due to the high local concentration of the PS itself.[84] The phenomenon might actually be valuable in terms of preventing systemic phototoxicity to the patient before the nanocarrier reaches its target.

Biodegradable DDSs such as liposomes, proteins or polymeric NPs have gathered special attention as nanocarriers particularly because of their biocompatibility and biodegradability. Normally they suffer an enzymatic or hydrolytic degradation and thereby are excreted out, minimizing long-term accumulation of carriers in biological system. **Non-biodegradable carriers** such ceramic or metal-based NPs have not been traditionally used as DDSs due to their inability to degrade in biological systems. Nevertheless, these systems have shown promise in PDT since the action mechanism in this therapy relies on the production and diffusion of $^1O_2$ to reach the cellular components. Therefore, non-biodegradable NPs may be suitable nanocarriers of PSs as long as they enable $^1O_2$ diffusion out of the carrier.[85] Although their main disadvantage is that their possible long-term toxicity has not yet evaluated, and this is the reason why almost all the approved DDSs in clinical belong to the first group of NPs.

One of the big benefits, not aforementioned, is the design as a multifunctional nanoplatforms to carry multiple components together with the PSs, such as imaging agents or chemotherapeutic drugs; or be design as a theranostics platforms (see section 1.5 and 1.6).[85]

Despite a general improvement of PDT when NPs are used, there are some issues that need to be addressed, including their instability during blood circulation or low renal clearance.[82] Moreover, a higher selectivity is still pursued for cell targeting, since healthy peritumoural cells frequently experience the same phototoxic effects due to unfortunate PS uptake. It is becoming more evident that the PS needs to be activated once internalised inside the target cells in order to achieve a more selective treatment, either by internal stimuli such as pH or temperature,[86]

by an external stimulus such as light[87] or through recovery of the photophysical activity by specific enzymes at the target site.[88]

On the other hand, nanotechnology in aPDT has also been used as an attractive approach for enhancing the delivery of the PS, due to the optimum PS encapsulation or the enhanced uptake within microbial cells.[89] However, most of the advantages aforementioned can be extrapolated for aPDT as well, such as the passive- or active-targeting that enhances the selectivity or the non-immunogenicity of the carriers. The typical NPs used for aPDT purposes are liposomes, PLGA and cyclodextrins.[7] Although there are several DDSs approved for microbial or fungal infections, such as Abelcet®, AmBisome® or Amphotec®, there are still not approval nanocarriers for aPDT.[90] However, due to the great quantity of patents on this topic, we should not wait much until the first approval.[91]

1.4.1. Targeted drug delivery systems

Intravenous injection represents the most commonly used route for the administration of NP-based therapeutics. Upon injection, the size, shape and surface properties of the NP can strongly affect their behaviour with respect to targeting and clearance. Generally, NPs with a size smaller than 6 nm will be rapidly filtered out by the kidneys, while NPs larger will either accumulate in a lesion or be cleared by the phagocyte system. The surface charge also affects dramatically in the NP's fate inside the body. A positive surface will lead to high systemic toxicity because of hemolysis and platelet aggregation, and the NPs tend to be quickly cleared from the blood. On the other hand, negative surface charge has longer circulation half-life. Although complete clearance is desired when the treatment is finished, generally a long circulation time is preferred to allow them a proper accumulation in the target tissue.[82]

Once NPs are in the circulatory system, they need to go through the vascular walls into the target lesion and then release the cargo. Unlike small molecules, NPs cannot cross the tight junctions between endothelial cells on normal vascular linings, owing to their relatively large sizes. However, the vessels inside a tumour region are well-known for their leaky walls, allowing NPs with the right sizes go through efficiently. Together with the absent or disrupted lymphatic system results in a preferential accumulation of NPs in the tumour tissue.[92] Other tumour characteristics are the high proliferation rate of cancer cells, upregulated expression of low-density lipoproteins (LDL) receptors, decreased intratumoral pH and the presence of tumour-associated macrophages.[7] These differences between a healthy and the tumour microenvironment are the basis for a **passive tumour targeting**, and it is known as enhanced permeability and retention (EPR) effect. Depending on the tumour type, the gaps in the tumour

vasculature are typically in the size range of 100- 800 nm, therefore NPs smaller than this range could preferentially accumulate by EPR effect (Figure 1.9). Nevertheless, NPs with a size between 30- 200 nm show a most effective EPR.[82]

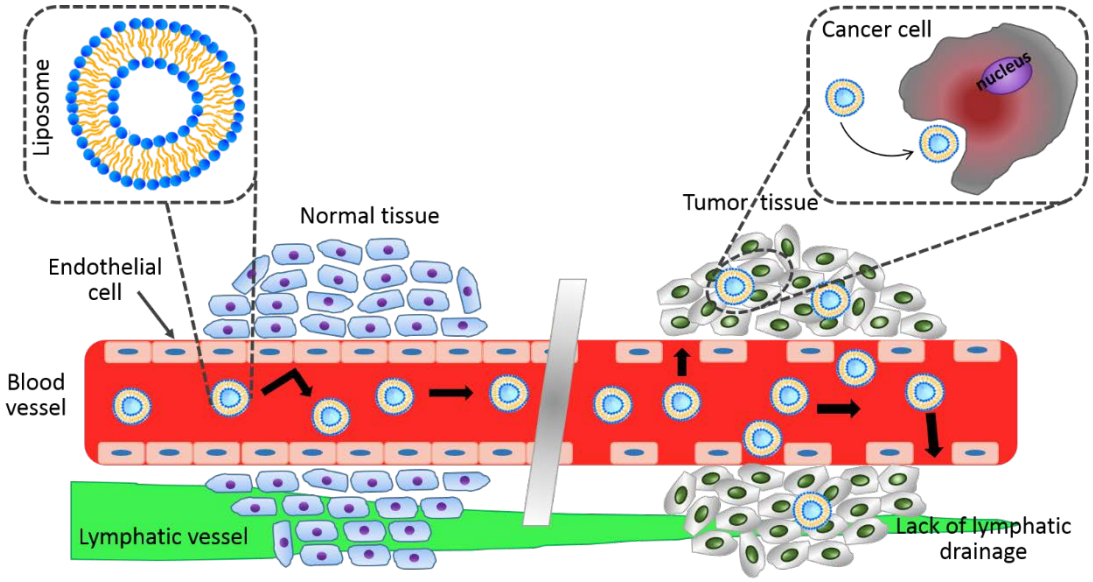

Figure 1.9. Schematic representation of the role of a passive tumour targeting known as EPR. Unlike in normal tissue, liposomes or other DDSs with the right size can extravasate into the tumour cells through the gaps between endothelial cells and accumulate there due to poor lymphatic drainage.

Notwithstanding its widespread use in the clinic, passive targeting strategy has many limitations as the vessels formed through angiogenesis or the permeability are not homogenous throughout the tumour.

Active targeting could be the alternative to help overcoming all the limitations of passive targeting. The bases of this alternative are the molecular recognition, in which ligand –receptor binding allows the NP to selectively and strongly bind to the surface of a specific type of cells. Ligands such as small molecules (e.g., sugars, folic acid), peptides, lectins, proteins (e.g., transferrin), antibodies or antibodies fragments, and nucleic acids (e.g., aptamers) are added to the surface of NPs (Figure 1.10).[92] The linking of the PS must be performed so that interaction with the receptor is not altered.

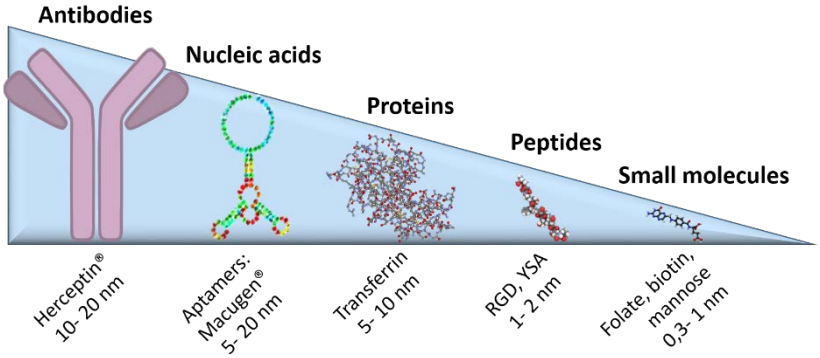

Figure 1.10. Classification by type of ligand and size of bioactive targeting moieties.

In the past few years, monoclonal antibodies (mAb), protein molecules made in the laboratory by recombinant DNA technology, have remained the preferred and most extensively used and investigated type of targeting moieties, due to the high affinity and specificity they render to the NPs. This potential of the application of mAb in targeted cancer therapy led to the approval of a large number of these macromolecules for clinical use, including rituximab, cetuximab and trastuzumab.[82] This last mAb, trastuzumab (Herceptin®), is a monoclonal antibody approved in 1998, that interferes with the human epidermal growth factor receptor 2 (HER2), is now routinely used to treat early-stage and metastatic breast cancer.[93]

It has been shown that active targeting enhances the internalisation, which is dominated by receptor-mediated endocytosis. However, it is still under debate whether the introduction of an active targeting ligand results in an improvement in tumour accumulation or not. It is believed that the accumulation of NPs in tumour tissue is dominated by the passive process, which is time-dependent and requires a long circulation half-life. Therefore, active targeting ligands can help achieve a higher intracellular drug concentration once the passive process has already played its role and the NPs have crossed the vasculature.[82] This lack of accumulation in the vasculature has led to an active vascular targeting as a promising alternative, where the NPs accumulation in the tumour tissue is no longer determined by the EPR effect.

1.4.2. Proteins as drug delivery systems

The use of natural materials is attractive because of their abundance, good biocompatibility, non-immunogenic and their easy recognition and metabolically process. In addition, they could be modified through chemical/biochemical reactions. One clear example of natural carriers are proteins since they clearly have a carrier function in biological systems.[94] Proteins as vehicles are able to interact with a molecule (ligand) at a specific binding site, with a binding equilibrium constant that is often modulated according to the environment. Some of the proteins employed are naturally self-assembled protein subunits of the same protein or a combination of proteins that make up a complete system. Moreover, proteins have the advantage of being non-toxic, low-cost, water-soluble and easily prepared.

A number of proteins have long been used as DDSs, including ferritin/apoferritin, viral capsids, soy and whey proteins, collagen, and gelatin.[95] More recently, serum proteins such as transferrin, albumin, and low-density lipoproteins (LDL) are being used for PDT treatments taking advantage of their accumulation in tumour tissues.[96–98] The selective uptake in solid tumours could be due to the increased metabolic activity, an enhanced vascular permeability of

tumour blood vessels for circulating macromolecules, and a lack of a functional lymphatic drainage system in tumour tissue.[96]

Probably the most well-known carrier proteins are albumins, the most abundant plasma protein. Human serum albumin (HSA) is a potential candidate for site-directed drug delivery due to simplicity in ligand attachment to the surface of the protein.[99] Indeed, for the treatment of metastatic breast cancer, a novel HSA NPs have achieved the FDA approval, under the trade name of Abraxane®.[85] For PDT purposes, several reports have been published, for instance Kuan Chen *et al.* prepared a DDS using HSA to deliver pheophorbide a (Pheo) to Jurkat cells and found that Pheo-HSA NPs caused a much higher phototoxicity than the free PS due to the different uptake mechanism and possibly different site of accumulation, although the amount of the cellular Pheo uptake was equivalent.[100] In a series of papers on HSA NPs loaded with tetra(m-hydroxyphenyl)chlorin (mTHPC or Foscans) or tetra(m-hydroxyphenyl)porphyrin (mTHPP), it was demonstrated that the photophysical properties of the encapsulated PS depends mainly on the loading ratio and also on the degree of protein crosslinking.[101,102] A key aspect of the successful use of proteins as DDS is the binding affinity of the PS to the protein pocket(s). This was demonstrated by Guo-Yu Jiang *et al.*, who enhanced the binding affinity of tetraphenylporphyrin towards BSA by linking it to Phenol Red, which efficiently binds to BSA on its own.[103]

However, the present thesis is focused on another two big families of proteins: globins and lipocalins. **Globins**, like haemoglobin or myoglobin (Mb), are ubiquitous carrier proteins whose primary function concerns the storage and transport of gaseous ligands like O_2 or NO. The binding of these gases occurs at the metal center of the prosthetic haem group, which is based on a tetrapyrrole ring structure. The easy protocol to remove and replace the prosthetic group is the basis of many applications, such as that proposed by Hayashi *et al*. showing an iron porphycene-apomyoglobin complex with a high oxygen affinity.[104]

The apomyoglobin (apoMb) (i.e., the protein without the haem group) is a small globular protein (~17 kDa) characterised by the typical eight α-helix strands folding of globins that wraps a main hydrophobic pocket able to accommodate the haem. Mb is an abundant cytoplasmic protein found in the cardiac and skeletal muscles of all vertebrates.[105] Its primary function is to facilitate O_2 diffusion; even if a more complex allosteric functionality and a role in NO scavenging have been proposed.[106]

Proteins belonging to the family of **lipocalins** are another example of widespread diversified proteins able to bind and carry small hydrophobic ligands like retinoids or lipids. β-lactoglobulin

(βLG) is the major protein from bovine milk, and although it is present in other animals' milk, this protein is absent in humans' milk. This lipocalin is also recognised as a versatile carrier for small bioactive molecules, although its biological function still remains unclear. Some of these ligands are mainly placed in the middle of the structure inside the β-barrel, such as vitamin D, cholesterol, curcumin, fatty acids and their derivatives or catechins.[107] By chance, βLG was shown in 1972 to bind vitamin A (retinol) with an apparent association constant similar to that of retinol-binding protein (RBP) but the details of the binding have been controversial. The binding constants for some of these compounds vary widely, from as little as 1.5 x 10^2 M^{-1} for 2-heptanone to 6.8 x 10^5 M^{-1} for palmitate and 5 x 10^7 M^{-1} for retinol.[108]

Regarding its structure, βLG comprises 162 amino acid residues with one free cysteine residue not exposed and two disulphide bridges, with a molecular mass of 18.4 kDa.[109] There are several genetic variants but A and B variants are the most common and very similar to each other that differ by only two amino acids.[110] The secondary structure is composed of 15% α-helix, 50% β-sheet, and 15-20% reverse turn (Figure 1.11). The secondary and tertiary structures are largely preserved from below pH < 2 to higher than pH 8. The quaternary structure over this pH range is reported to be predominantly dimeric at moderate ionic strength (e.g., 100 mM NaCl) and temperatures above 20ºC, whereas at low pH and very low ionic strength (pH < 3 and ionic strength < 10 mM), bovine βLG is predominantly monomeric.[110]

Figure 1.11. Molecular structure of the monomeric assembly of bovine β-lactoglobulin (code 1beb).

βLG has been intensively studied in the food industry because of its nutritional and functional effects on various biological processes. There are just a few examples of its applicability as nanocarrier for PDT, one of them is the complex formed with riboflavin reported by Diarrassouba *et al*. in 2013.[111]

1.4.3. Liposomes as drug delivery systems

Liposomes are the earliest and most widely studied DDSs to be applied in medicine, cosmetic or antimicrobial fields due to their unique properties. Up to now, there are more than 10 liposomal formulations approved for clinical use today such as Doxil®, the first liposomal formulation to be approved by the FDA in 1995, DaunoXome® or ThermoDox®.

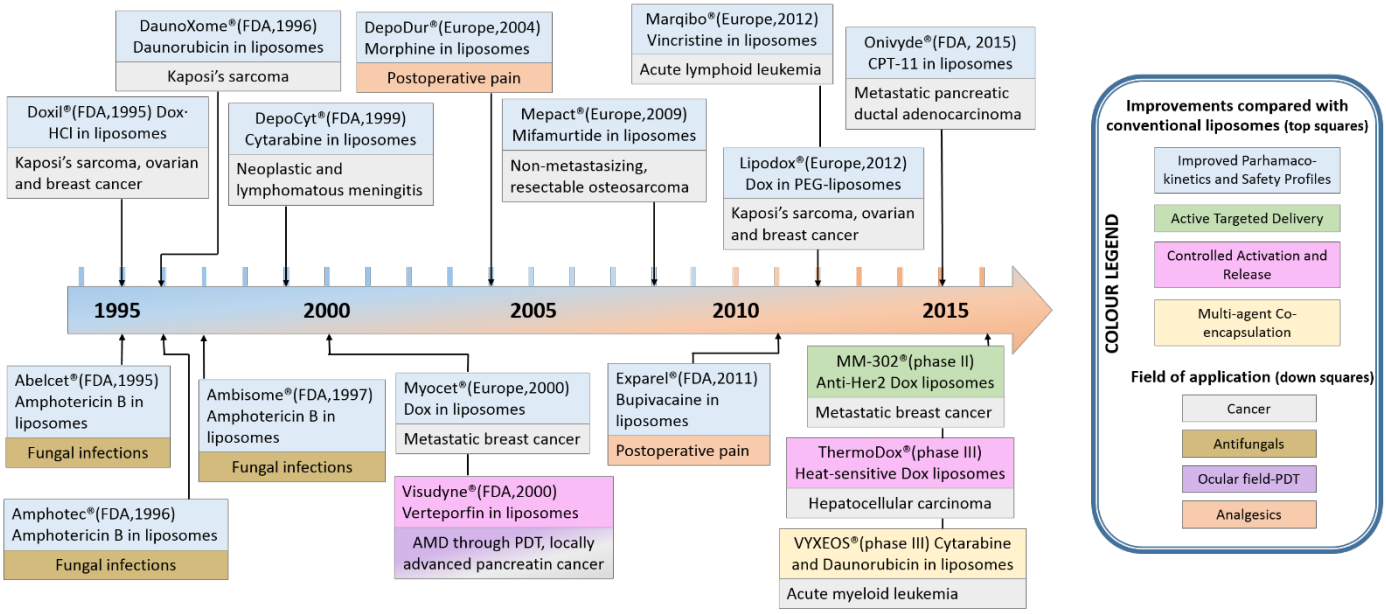

Figure. 1.12. Timeline of some of the last twenty-two years approvals and clinical trials of liposomes as DDSs for the improvement of the pharmacokinetics, safety profiles, the efficiency and selectivity of the treatment. Each DDS has been represented by two squares: top square show the improvement made compared with conventional liposomes and the down square indicates the field of application. Visudyne® is still the only DDS approved in the PDT field. Liposomes for gene therapy are not included.[90]

One in three patents related to nanotechnology are with liposomes.[2] However, there is just one formulation approved in 2000 in the PDT field, which is Visudyne® for the treatment of wet AMD.

Figure 1.12 represents a timeline of all the liposomal formulations approvals and in clinical trials. Looking carefully it could be noticed how science, that means nanotechnology, cancer treatment or PDT, progresses in the same direction, tailoring the nanocarriers to achieve more selective delivery and in the end obtaining more controllable systems.

Conventional liposomes are highly biocompatible and biodegradable nanocarriers composed of a unilamellar or multilamellar phospholipid bilayers surrounding an aqueous inner core (Figure 1.13). Their ability to contain a wide variety of molecules either hydrophilic drugs in their aqueous core or hydrophobic agents in its bilayer, constitute them as excellent nanocarriers. Furthermore, liposomes are biologically inert, non-toxic, relatively immunogenic and provide a large drug payload per particle, protecting the encapsulated agents from metabolic processes.

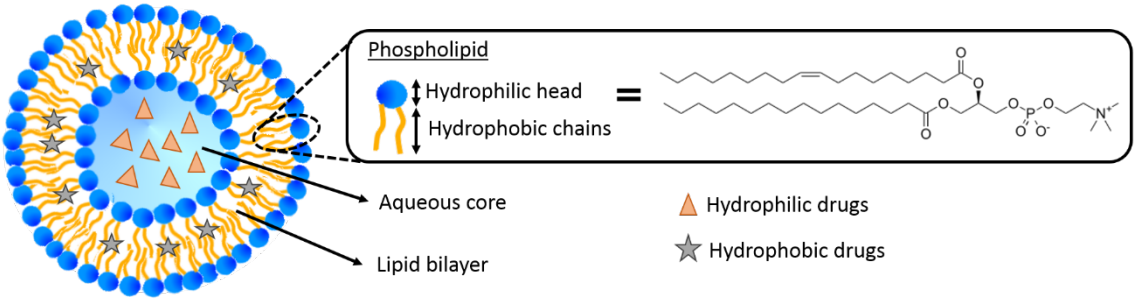

Figure 1.13. Liposome scheme.

There are various preparation methods available depending on the size and lamellarity desired, and the PS nature (e.g., hydrophobicity, charge) should also be taken into account. Thin-film hydration is the most widely used preparation method for liposomes, in which lipid components with or without a drug are dissolved in an organic solvent, usually chloroform. The solvent will be evaporated by rotary evaporation followed by rehydration of the film in an aqueous solvent. The other methods include reverse-phase evaporation, freeze-drying and ethanol injection.[112] Ultrasound induced cavitation and membrane extrusion are common methods for unilamellar vesicles preparation. High-energy sonication is usually used to synthesize small unilamellar vesicles (SUV; <100nm). Extrusion methods are used either for the synthesis of SUV or large unilamellar vesicles (LUV; 100-1000 nm). If instead of this, once the film is hydrated it is performed several freeze-thaw cycles the result is the formation of multilamellar vesicles (MLVs; 500-5000 nm).[87]

The choice of phospholipids, either natural or synthetics, and other lipids or molecules that will constitute the bilayer is crucial for physical and chemical characterisation of liposomes, such as size, zeta potential, surface charge density, and membrane packing constraints, etc. The broad range includes molecules with neutral, anionic or zwitterionic head groups. FDA-approved systems commonly use phosphatidylcholine (PC), phosphatidylethanolamine (PE) and sphingomyelin.[113] These lipids or phospholipids include a charged or hydrophilic domain (head) and two fatty acyl chains (tails) typically 14-18 carbons in length. Usually, the lipid bilayer has a thickness of 3-6 nm. The fluidity and permeability of the liposome bilayer depends on the lipid phase transition temperature (T_c or T_m). Above this temperature, the bilayer turns disordered and very fluid, whereas when the temperature is below the transition temperature liposomes exhibit a well-ordered or gel phase. The T_m will change depending on the length, degree of unsaturation and charge of the (phospho)lipids comprising the bilayer.[114] Typically, saturated lipids offer higher stability in terms of oxidation but, since they have a higher T_m, yield a much rigid and rather impermeable bilayer compared with their unsaturated counterparts, which give more permeable and less stable bilayers.[115]

Moreover, most of the liposomes include cholesterol to modify the rigidity of the bilayer membrane, reducing the rotational freedom (by increasing the orientation order) of the phospholipid hydrocarbon chains, that causes an increased retention of the drug inside the liposome.[85] The incorporation of cholesterol and/or saturated phospholipids reduces liposomal uptake by cells of the MPS (mononuclear phagocyte system), solving to some extent the problem of the small circulation half-life. In this context, charged liposomes and/or large-size liposomes are cleared from the systemic circulation more rapidly than neutral and/or small-size liposomes.[116,117]

Charged liposome have some advantages compared with neutral ones. For example, the presence of a surface charge induces electrostatic repulsion among liposomes by creating a sensitive ζ-potential that prevents aggregation or flocculation processes in solution. Although negatively-charged liposomes show a quick clearance from the body, they undergo faster cellular uptake by endocytosis and to a greater extent than neutral liposomes. On the contrary, cationic liposomes normally show a nonspecific cellular uptake and tend to aggregate with proteins in serum, which are negatively charged. Some of these serum proteins may potentially activate the MPS, causing the clearance from the body.[114,118] For the aforementioned reasons, negatively charged lipid particles are the most common FDA-approved liposomal formulations.

Liposomes fate after their administration. During their circulation in the bloodstream, liposomes interact with plasma proteins, such as opsonins, high-density lipoproteins (HDLs), and low-density lipoproteins (LDLs). Once liposomes encounter a cell, four possible routes can be triggered. A first mechanism consists of liposomes' adsorption onto the cell membrane, where the liposomes bilayer is degraded by mechanical strain or by the action of enzymes. The cargo will be released into the extracellular fluid, where it will diffuse through the cell membrane and the cytoplasm. A second way, much rare, consists of the fusion of the liposomal membrane with the plasma membrane of the target cell, with the release of liposomal content directly into the cytoplasm.[115] The third way is receptor-mediated endocytosis, a frequent process for vesicles with a maximum diameter of 150 nm. Eventually, liposomes are accumulated in the lysosomes inside the cell where they are degraded by the enzymes' action. Finally, phagocytosis can also occur but involves mainly liposomes larger than 150 nm that are phagocytosed by specialised cells of the immune system, such as macrophages or monocytes.[118]

The benefits of liposome-encapsulated or linked drugs/PSs include an improved solubility of lipophilic and amphiphilic drugs; a sustained drug release from the liposomes, both systemically

or locally administered; site-specific targeting; passive targeting to the tumour or inflamed tissue due to EPR effect; and improved penetration into tissues.

Some of the major drawbacks of conventional liposomes are their trend to fuse or aggregate with each other or their rapid systemic clearance via their uptake by the MPS cells, such as macrophages and monocytes.[116] It is known that phagocytosis has been one of the major problems of these carriers. However, many surface-modification strategies have been carried out to overcome these limitations. The recurrent solution is the coating with PEG, an inert, non-toxic and biocompatible hydrophilic polymer. PEGylated liposomes are not opsonized (i.e., opsonisation process consists of the adsorption of opsonins, various plasma proteins, onto the phospholipid membrane) and are able to escape the capture by the cells' phagocytic systems by rendering the nanocarriers invisible to macrophages (stealth liposomes).[118] Thus, they are able to improve the stability and blood-circulation time, giving more opportunities to accumulate in the target tissue through a passive targeting.[82]

During the last years, the lack of selectivity for cancer cells has led to the conjugation of the liposomes with some active targeting molecules. Another development has been the introduction of multi-functionality within the same liposome. For instance, multicomponent liposomes have been designed for the delivery of drug combinations or for the stimuli-responsive assembly/disassembly processes to control drug release.[82,118] In this thesis, liposomes have been developed that enable the delivery of combined therapies, specifically both PSs and chemotherapeutic drugs, as well as targeting and imaging capabilities for theranostics purposes.

1.5. Combining PDT with conventional treatments

1.5.1. Combining PDT with conventional antimicrobial treatments

The low selectivity of the drugs and the widespread emergence of resistance, which limits the effectiveness, affect also the treatment of microbial infections, the second leading cause of death worldwide. It is feared that the emergence of resistance to antibiotics can lead to a situation similar to the pre-antibiotic era. In the field of antimicrobials and antifungals, there are only a few reports on the combination of traditional treatments with aPDT. Unfortunately, little is known about the protocols used.

Junior *et al.*[135] reported better results of a methylene blue-PDT in combination with fluconazole compared to either isolated approaches. Although they do not confirm the mechanism, they suggested that permeabilisation of the fungal cell membrane by PDT makes the cells more

susceptible to fluconazole action. Furthermore, it has been reported that the use of azoles can increase the oxidation stress promoted by PDT by contributing to ROS formation themselves. Morton *et al.*[136] showed the activity of rose Bengal-PDT treatment after 72 h incubation with traditional antifungal drugs. According to the authors, the combined therapies may allow for a reduction in treatment times and costs as well as improve patient compliance.

1.5.2. Combining PDT with conventional cancer drugs

Despite extraordinary advances over the last decade, conventional cancer treatments, including chemotherapy, radiation therapy and surgical intervention, still have two major limitations: the low selectivity of the drugs, leading to serious side effects, and the emergence of resistance, which limits the effectiveness of the drugs.[82] Chemotherapy often requires multiple doses to be effective, resulting in increasingly severe systemic toxicity, while a single PDT treatment is usually sufficient. In contrast, curative radiation therapy normally requires daily radiation for 6–7 weeks, while chemotherapy courses can last for months and surgery requires hospitalisation for days to weeks.[119,120] Moreover, the standard procedures are substantially invasive for patients for the aforementioned reasons. Because such limitations affect increasingly larger segments of the population as it grows older, alternative approaches and strategies must be sought that could positively impact on these issues.

On the other hand, PDT has certain inherent advantages comparing with these conventional therapies, including minimal normal tissue (i.e., host or healthy tissue) toxicity, no long-term systemic toxicity such as immunosuppression, lack of drug resistance mechanisms, and favourable cosmetic outcomes.[121] There are currently several PSs approved for the treatment of various cancers such as head, neck tumours, basal-cell carcinoma, cervical, endobronchial, esophageal, bladder or gastric cancer.

Therefore, PDT in combination with conventional and approved antineoplastic drugs may overcome some of these potential limitations, without overlapping toxicities. The advantages of combining both modalities are that they target different key signals transduction pathways and should be more efficient in destroying cancer cells, eluding the cellular resistance mechanisms. Indeed, few reports and preclinical studies show that the combined treatment allow the reduction of the dosage of individual drugs and consequently the lessening of important side effects, while the overall efficacy is preserved or even increased.[122–126] However, combination protocols are far from being established as the final therapeutic outcome, even *in vitro*, it appears to depend on assorted.[62]

PDT can directly damage tumour cells through apoptosis and necrosis and through anti-tumour vasculature effects as it has been previously described. However, tumour cells that survive PDT can lead to regrowth of tumour cells and tumour vessels. Introduction of chemotherapeutics concurrently can further damage tumour cells, preventing regrowth because of the damage in multiple organelles. Since none of the clinically approved PSs accumulates in cell nuclei, the chemotherapeutic drug will be the one which induces this DNA damage.[1] Additionally, anti-cancer drug themselves may generate oxidative stress, generating hydroxyl radicals which, when combined with PDT may be sufficient to induce cell cycle arrest and subsequent cytotoxic death of cancer cells.[121]

The recent advances in nanotechnology enable the incorporation of various pharmaceutical components in a single nanoplatform. Thus, key to this thesis is the use of enabling nanotechnologies in order to develop nanodevices for the enhanced tumour accumulation and the selective delivery of a drug and a PS agent to the same cell and with an optimum ratio.

Doxorubicin (Dox), mitomycin, and cisplatin have been most frequently studied in combination with PDT in preclinical studies.[121] Irinotecan (CPT-11) and its active metabolite, SN-38 are also included for study in this thesis.

Doxorubicin (Dox) is an anthracycline antibiotic used clinically for a wide range of solid tumours and haematological malignancies, including advanced breast cancer, small cell lung cancer, AIDS-related Kaposi's sarcoma, acute leukaemia, and lymphomas and myeloma (Figure 1.14).

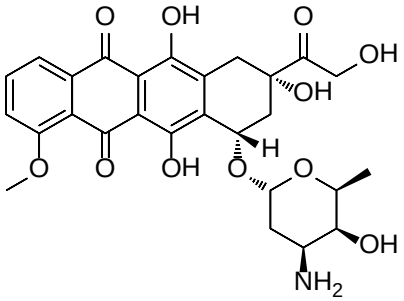

Figure 1.14. Dox chemical structure.

Dox functions in several ways including inhibiting DNA synthesis via intercalation, inhibition of topoisomerase II, free radical formation, and lipid peroxidation. Dox is considered one of the most potent anti-cancer drugs, cardiotoxicity being its main side effect. Casas *et al.* first evaluated the interaction between ALA/PDT and doxorubicin in mice bearing transplantable mammary adenocarcinomas.[127] The authors assigned the observed enhancement of PDT to the weakening of cellular defence mechanisms by the pre-treatment involving free radical generation by doxorubicin. Kirveliene *et al.* studied the cytotoxic and antitumour effect of Dox

in combination with a second-generation chlorin PS have been studied *in vitro* and *in vivo*.[128] Recently, an amphiphilic block copolymer micelle bearing a $^1O_2$-sensitive linker has been reported that releases Dox in a controlled fashion upon exposure of a chlorin PS to light.[129] Moreover, another study with Dox and chlorin e6 successfully demonstrated that a dual-effect liposome could lower the tumour growth rate *in vivo*.[130]

Irinotecan and **SN-38** are antineoplastic agents belonging to the camptothecins' family with strong antitumor activity. They inhibit topoisomerase I, thereby arresting the synthesis of DNA. CPT-11 is converted to its metabolite SN-38 by a human carboxylesterase, primarily in the liver but also in tumours, with a reported at least 100-fold higher antitumoral activity (Figure 1.15).[131]

CPT-11 is a first-line drug approved for the treatment of a variety of human tumours, including colorectal, pancreatic, lung and gynaecological cancers.[132] However, their severe side effects, such as myelosuppression and gastrointestinal disorders, impose some restrictions for camptothecin therapies and additional considerations to develop suitable pharmaceutical formulations for clinical purposes.[133] Other drawbacks for their clinical applications are the chemical instability of the lactone ring, which opens to the inactive carboxylate form at physiological pH and, in the case of SN-38, the great insolubility in almost all the solvents that could be used to formulate this drug.[132]

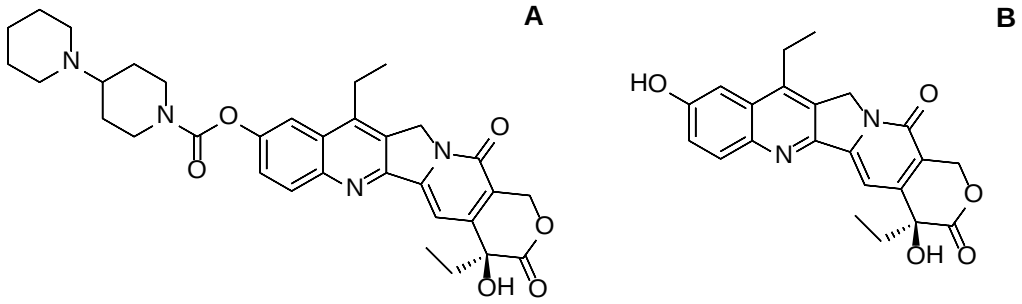

Figure 1.15. Chemical structure of A) irinotecan or CPT-11, and its active metabolite B) SN-38.

In 2016, Yue *et al.* evaluated the activity of a mitochondrial-targeting amphiphilic block polymer with a ROS-cleavable thioketal linker, in which ROS production contributes both to the release of camptothecin and to the PDT treatment.[134] On the other hand, Huang *et al.* showed a synergistically combination of PDT and CPT-11 in liposomes that enhanced tumour growth inhibition.[126]

1.6. Theranostics

Theranostics is based on the combination of a diagnostic imaging agent with a therapeutic drug on the same multifunctional platform. This is indeed the case of PDT drugs that produce cytotoxic ROS upon light absorption and whose fluorescence is also used for molecular imaging, locating many diseases and photodiagnosis.

Table 1.1. Clinically approved PSs with their excitation wavelength, maximum emission wavelength, fluorescent quantum yield, $^1O_2$ quantum yield and its main subcellular location.

Class	Photosensitiser (INN Name – trade name)	λ_{exc} / nm	$\lambda_{max\ em}$ / nm	Φ_F	Φ_Δ[a]	Subcellular localisation
Hematoporphyrin	Hematoporphyrin (HpD) - Photofrin	630	690	NA	0.89	Golgi apparatus, plasma membrane
Protoporphyrin prodrugs	δ-Aminolevulinic acid HCl (ALA) - Levulan	635	635	0.05	0.56	Mit, cytosol, cytosolic membranes, cell membranes
	5-Aminolevulinate (MAL) - Metvix	635	635	0.05	0.56	Mit, cytosol, cytosolic membranes, cell membranes
	Hexamino-levulinate HCl (HAL) - Cysview or Hexvix	375-450	635	0.05	0.56	Mit, cytosol, cytosolic membranes, cell membranes
Chlorins	Meta-tetra (hydroxyphenyl) chlorin or temoporfin (m-THPC) - Foscan	652	652	0.22	0.01 / 0.30 (EtOH)	ER, Mit
	Talaporfin sodium, N-aspartyl chlorin e6, or LS11 (NPe6) - Laserphyrin	664	670	0.003	0.77	Lysosome, endosome
	Chlorin e6 (Ce6-PVP) - Photolon	660-665	675	0.18	0.64	Lysosomes
	Chlorin e6, chlorin p6 and purpurins - Photoditazin	660-662	~700	0.05	0.6	Lysosomes
	Chlorin e6, chlorin p6 and purpurins - Radachlorin	662	668	0.04	0.75	Lysosomes
Porphycenes	9-Acetoxy-2,7,12,17-tetrakis-(β-methoxyethyl) - ATMPn	638	~650	0.27	0.38	Mit, lysosomes, ER, plasma membrane
Phthalocyanines	Mixture of chloroaluminium sulphonic phthalocyanines (AlPcS4) - Photosens	675	689	0.559	0.38	Mit
Psoralens	8-methoxypsoralen, methoxsalen (8-MOP) -Uvadex	303	505	0.003	0.004 (C_6H_6)	Nuclei

[a] Most are given in phosphate buffer pH~7.4 or in a mixture of phosphate buffer with 1% Triton X-100. NA: not available. ER: Endoplasmic reticulum; Mit: mitochondria

Therefore, PDT is inherently an ideal theranostic modality, since obtaining a fluorescence image of the PS in the target tissue can give rise to image-guided dosimetry and aid surgical resection as well as monitoring of the treatment response.[137] In fact, PDT is nowadays being routinely used for the detection and diagnosis of bladder cancer and fluorescence-guided resection in surgical operations.[138] Photophysical and photochemical properties of the approved PSs for cancer treatments are collected in Table 1.1.

When performing a surgical procedure with the goal of completely removing a tumour, it is critical to finely differentiate the tumour margins. Moreover, it is also of great interest to have tools to quantify the *in situ* production of ROS, thereby yielding tools to clinicians to assess the end of the treatment.

As it has been pointed out previously, the first-line treatment for the vast majority of solid tumours involves surgery followed by several sessions of chemotherapy and/or radiotherapy. In a typical surgical procedure, the surgeon, aided with computer tomography and magnetic resonance imaging (MRI) recorded previously, removes all the malignant tissue and sends it to the pathologist for analysis. The standard pathology report normally takes several days to be obtained, while the patient is recovering from the operation. If the pathologic report indicates the presence of positive tumour margins, then the patient is often asked to go through another surgical procedure, which is neither convenient nor practical. In contrast, a more desirable strategy would be to provide the surgeon with tools to intra-operatively discern the malignant tissue and, especially, eliminate the possible tumour margins left after resection. The combination of PDT with fluorescence image-guided surgery procedures would allow solving the previous inconveniences.

Some examples of this novel technology are the PLGA-DSPE-folate micelles of Tian *et al.* loaded with the activatable PS selenium-rubyrin.[139] Its photophysical activity and fluorescence is quenched at basic or neutral pH, but are restored at acidic pH, which provokes activation of the PS only when internalised in lysosomes through folate-receptor endocytosis. Additionally, Jin *et al.* demonstrated that fluorescence imaging of folate-targeted activatable porphysomes intravenously injected in KB xenograft bearing mice could guide the treatment protocol. They also studied the time window for best PDT, which was 24 h after injection.[140]

1.7. Objectives

The main goal of this thesis is to design and study biodegradable and biocompatible nanocarriers for photodynamic therapy and evaluate their activity for antimicrobial or anticancer purposes. In this last direction, the main novelty will be the co-encapsulation of a chemotherapeutic agent and a PS in the same nanovehicle. The main goal is broken down into the following specific objectives:

- Development of a self-assembled nanocarrier with photosensitising properties based on apomyoglobin and hypericin. Evaluation of its physicochemical and photophysical properties and of its photodynamic activity *in vitro* against bacteria.
- Development of a biodegradable nanodelivery complex with photosensitising properties based on β-lactoglobulin and hypericin. Evaluation of its physicochemical and photophysical properties and of its photodynamic activity *in vitro* against bacteria.
- Study of β-lactoglobulin as dual nanocarrier for hypericin and retinoic acid. Evaluation of its physicochemical and photophysical properties.
- Development of a multi-component liposomal formulation for the co-encapsulation of PpIX and irinotecan. Evaluation of its physicochemical and photophysical properties and its photodynamic activity *in vitro* against cancer cells. Analysis of synergistic or additive effects comparing both modalities alone and the effect of targeting surface ligands.
- Development of a multi-component liposomal formulation for the co-encapsulation of PpIX and doxorubicin. Evaluation of its physicochemical and photophysical properties and its photodynamic activity *in vitro* against cancer cells. Analysis of synergistic or additive effects comparing both modalities alone and the effect of targeting surface ligands.

1.8. References

(1) Agostinis, P.; Berg, K.; Cengel, K. A.; Foster, T. H.; Girotti, A. W.; Gollnick, S. O.; Hahn, S. M.; Hamblin, M. R.; Juzeniene, A.; Kessel, D.; *et al.* Photodynamic Therapy of Cancer: An Update. *CA. Cancer J. Clin.* **2011**, *61*, 250–281.

(2) Obaid, G.; Broekgaarden, M.; Bulin, A.-L.; Huang, H.-C.; Kuriakose, J.; Liu, J.; Hasan, T. Photonanomedicine: A Convergence of Photodynamic Therapy and Nanotechnology. *Nanoscale,* **2016**, *8*, 12471–12503.

(3) Wainwright, M.; Maisch, T.; Nonell, S.; Plaetzer, K.; Almeida, A.; Tegos, G. P.; Hamblin, M. R. Photoantimicrobials—are We Afraid of the Light? *Lancet Infect. Dis.* **2017**, *17*, 49–55.

(4) Josefsen, L. B.; Boyle, R. W. Photodynamic Therapy and the Development of Metal-Based Photosensitisers. *Met. Based. Drugs,* **2007**, *2008*, 1–23.

(5) McCaughan, J. S. Photodynamic Therapy. *Drugs Aging,* **1999**, *15*, 49–68.

(6) Rodríguez-Amigo, B.; Planas, O.; Bresolí-Obach, R.; Torra, J.; Ruiz-González, R.; Nonell, S. Photosensitisers for Photodynamic Therapy: State of the Art and Perspectives. In *Photodynamic Medicine: From Bench to Clinic*; Kostron, H.; Hasan, T., The Royal Society of Chemistry, **2016**; 23–62.

(7) Sharma, S. K.; Mroz, P.; Dai, T.; Huang, Y.; Tyler, G. Photodynamic Therapy for Cancer and for Infections : What Is the Difference. *Isr. J. Chem.* **2013**, *52*, 691–705.

(8) Plaetzer, K.; Krammer, B.; Berlanda, J.; Berr, F.; Kiesslich, T. Photophysics and Photochemistry of Photodynamic Therapy: Fundamental Aspects. *Lasers Med. Sci.* **2009**, *24*, 259–268.

(9) Brown, J. E.; Brown, S. B.; Vernon, D. I. Photosensitising Drugs- Their Potential in Oncology. *Expert Opin Investig Drugs,* **1999**, *8*, 1967–1979.

(10) Castano, A. P.; Demidova, T. N.; Hamblin, M. R. Mechanisms in Photodynamic Therapy: Part One - Photosensitizers, Photochemistry and Cellular Localization. *Photodiagnosis Photodyn. Ther.* **2004**, *1*, 279–293.

(11) Dolmans, D. E. J. G. J.; Fukumura, D.; Jain, R. K. Photodynamic Therapy for Cancer. *Nat Rev Cancer,* **2003**, *3*, 380–387.

(12) Jiménez-Banzo, A.; Sagristà, M. L.; Mora, M.; Nonell, S. Kinetics of Singlet Oxygen Photosensitization in Human Skin Fibroblasts. *Free Radic. Biol. Med.* **2008**, *44*, 1926–1934.

(13) Ragàs, X.; Agut, M.; Nonell, S. Singlet Oxygen in Escherichia Coli: New Insights for Antimicrobial Photodynamic Therapy. *Free Radic. Biol. Med.* **2010**, *49*, 770–776.

(14) Boix-Garriga, E.; Rodríguez-Amigo, B.; Planas, O.; Nonell, S. Properties of Singlet Oxygen. In *Singlet Oxygen: Applications in Biosciences and Nanosciences*; Nonell, S.; Flors, C., Royal Society of Chemistry, **2016**; 23–46.

(15) Macdonald, I. J.; Dougherty, T. J. Basic Principles of Photodynamic Therapy. *J. Porphyrins Phthalocyanines,* **2001**, *5*, 105–129.

(16) DeRosa, M. C.; Crutchley, R. J. Photosensitized Singlet Oxygen and Its Applications. *Coord. Chem. Rev.* **2002**, *233–234*, 351–371.

(17) Abrahamse, H.; Hamblin, M. R. New Photosensitizers for Photodynamic Therapy. *Biochem. J* **2016**, *473*, 347–364.

(18) Aramendia, P. F.; Redmond, R. W.; Braslavsky, S. E.; Schaffner, K.; Vogel, E.; Nonell, S. The Photophysical Properties of Porphycenes: Potential Photodynamic Therapy Agents. *Photochem. Photobiol.* **1986**, *44*, 555–559.

(19) Battersby, A. R. Tetrapyrroles: The Pigments of Life. *Nat. Prod. Rep.* **2000**, *17*, 507–526.

(20) Kuznetsova, N. *Photosensitizers in Medicine, Environment, and Security*; Nyokong, T.; Ahsen, V., Springer, Netherlands: Dordrecht, **2012**.

(21) Ormond, A. B.; Freeman, H. S. Dye Sensitizers for Photodynamic Therapy. *Materials (Basel).* **2013**, *6*, 817–840.

(22) Kiesslich, T.; Tortik, N.; Pichler, M.; Neureiter, D.; Plaetzer, K. Apoptosis in Cancer Cells Induced by Photodynamic Treatment: A Methodological Approach. *J. Porphyr. Phthalocyanines,* **2013**, *17*, 197–209.

(23) Castano, A. P.; Demidova, T. N.; Hamblin, M. R. Mechanisms in Photodynamic Therapy: Part Two: Cellular Signaling, Cell Metabolism and Modes of Cell Death. *Photodiagnosis and photodynamic therapy*, **2005**, *2*, 1–23.

(24) Mroz, P.; Yaroslavsky, A.; Kharkwal, G. B.; Hamblin, M. R. Cell Death Pathways in Photodynamic Therapy of Cancer. *Cancers (Basel),* **2011**, *3*, 2516–2539.

(25) Liu, L.; Zhang, Z.; Xing, D. Cell Death via Mitochondrial Apoptotic Pathway due to Activation of Bax by Lysosomal Photodamage. *Free Radic. Biol. Med.* **2011**, *51*, 53–68.

(26) Moserova, I.; Kralova, J. Role of ER Stress Response in Photodynamic Therapy: ROS Generated in Different Subcellular Compartments Trigger Diverse Cell Death Pathways. *PLoS One,* **2012**, *7*, e32972.

(27) Galluzzi, L.; Bravo-San Pedro, J. M.; Kroemer, G. Organelle-Specific Initiation of Cell Death. *Nat. Cell Biol.* **2014**, *16*, 728–736.

(28) Coupienne, I.; Fettweis, G.; Rubio, N.; Agostinis, P.; Piette, J. 5-ALA-PDT Induces RIP3-Dependent Necrosis in Glioblastoma. *Photochem. Photobiol. Sci.* **2011**, *10*, 1868–1878.

(29) Dewaele, M.; Maes, H.; Agostinis, P. ROS-Mediated Mechanisms of Autophagy Stimulation and Their Relevance in Cancer Therapy. *Autophagy,* **2010**, *6*, 838–854.

(30) Reiners, J. J.; Agostinis, P.; Berg, K.; Oleinick, N. L.; Kessel, D. Assessing Autophagy in the Context of Photodynamic Therapy. *Autophagy,* **2010**, *6*, 7–18.

(31) Shirakabe, A.; Zhai, P.; Ikeda, Y.; Saito, T.; Maejima, Y.; Hsu, C.-P.; Nomura, M.; Egashira, K.; Levine, B.; Sadoshima, J. Drp1-Dependent Mitochondrial Autophagy Plays a Protective Role Against Pressure Overload–Induced Mitochondrial Dysfunction and Heart Failure. *Circulation,* **2016**, *133*, 1249–1263.

(32) Kessel, D.; Reiners, J. J. Effects of Combined Lysosomal and Mitochondrial Photodamage in a Non-Small-Cell Lung Cancer Cell Line: The Role of Paraptosis. *Photochem. Photobiol.* **2017**.

(33) Bayles, K. W. Bacterial Programmed Cell Death: Making Sense of a Paradox. *Nat. Rev. Microbiol.* **2014**, *12*, 63–69.

(34) Dwyer, D. J.; Camacho, D. M.; Kohanski, M. A.; Callura, J. M.; Collins, J. J. Antibiotic-Induced Bacterial Cell Death Exhibits Physiological and Biochemical Hallmarks of Apoptosis. *Mol. Cell.* **2012**, *46*, 561–572.

(35) Ashida, H.; Mimuro, H.; Ogawa, M.; Kobayashi, T.; Sanada, T.; Kim, M.; Sasakawa, C. Cell Death and Infection: A Double-Edged Sword for Host and Pathogen Survival. *J. Cell Biol.* **2011**, *195*, 931–942.

(36) Lipson, R. L.; Baldes, E. J. The Photodynamic Properties of a Particular Hematoporphyrin Derivative. *Arch. Dermatol.* **1960**, *82*, 508–516.

(37) Dougherty, T. J.; Kaufman, J. E.; Goldfarb, A.; Weishaupt, K. R.; Boyle, D.; Mittleman, A. Photoradiation Therapy for the Treatment of Malignant Tumors. *Cancer Res.* **1978**, *38*, 2628–2635.

(38) Dougherty, T. J.; Gomer, C. J.; Henderson, B. W.; Jori, G.; Kessel, D.; Korbelik, M.; Moan, J.; Peng, Q. Photodynamic Therapy. *J. Natl. Cancer Inst.* **1998**, *90*, 889–905.

(39) Michael R. Detty, Scott L. Gibson, and S. J. W. Current Clinical and Preclinical Photosensitizers for Use in Photodynamic Therapy. *J. Med. Chem.* **2004**, *47*, 3897–3915.

(40) Konopka, K.; Goslinski, T. Photodynamic Therapy in Dentistry. *J. Dent. Res.* **2007**, *86*, 694–707.

(41) Kharkwal, G. B.; Sharma, S. K.; Huang, Y. Y.; Dai, T.; Hamblin, M. R. Photodynamic Therapy for Infections: Clinical Applications. *Lasers Surg. Med.* **2011**, *43*, 755–767.

(42) Hamblin, M. R.; Hasan, T. Photodynamic Therapy: A New Antimicrobial Approach to Infectious Disease? *Photochem. Photobiol. Sci.* **2004**, *3*, 436–450.

(43) Javed, F.; Samaranayake, L. P.; Romanos, G. E. Treatment of Oral Fungal Infections Using Antimicrobial Photodynamic Therapy: A Systematic Review of Currently Available Evidence. *Photochem. Photobiol. Sci.* **2014**, *13*, 726–734.

(44) Sharma, S. K.; Dai, T.; Kharkwal, G. B.; Huang, Y.-Y.; Huang, L.; De Arce, V. J. B.; Tegos, G. P.; Hamblin, M. R. Drug Discovery of Antimicrobial Photosensitizers Using Animal Models. *Curr. Pharm. Des.* **2011**, *17*, 1303–1319.

(45) Dai, T.; Huang, Y. Y.; Hamblin, M. R. Photodynamic Therapy for Localized Infections- State of the Art. *Photodiagnosis Photodyn. Ther.* **2009**, *6*, 170–188.

(46) Parker, S. The Use of Diffuse Laser Photonic Energy and Indocyanine Green Photosensitiser as an Adjunct to Periodontal Therapy. *Br Dent J,* **2013**, *215*, 167–171.

(47) Lin, J.; Wan, M. T. Current Evidence and Applications of Photodynamic Therapy in Dermatology. *Clin. Cosmet. Investig. Dermatol.* **2014**, *30*, 145.

(48) Huggett, M. T.; Jermyn, M.; Gillams, A.; Illing, R.; Mosse, S.; Novelli, M.; Kent, E.; Bown, S. G.; Hasan, T.; Pogue, B. W.; *et al.* Phase I/II Study of Verteporfin Photodynamic Therapy in Locally Advanced Pancreatic Cancer. *Br. J. Cancer,* **2014**, *110*, 1698–1704.

(49) Photocure Annual Report. Cevira and Lumacan. Photocure Annual Report. Cevira and Lumacan.

(50) Lee, Y.; Baron, E. D. Photodynamic Therapy: Current Evidence and Applications in Dermatology. *Semin. Cutan. Med. Surg.* **2011**, *30*, 199–209.

(51) Sperandio, F. F.; Huang, Y.-Y.; Hamblin, M. R. Antimicrobial Photodynamic Therapy to Kill Gram-Negative Bacteria. *Recent Pat. Antiinfect. Drug Discov.* **2013**, *8*, 108–120.

(52) Fu, X.-J.; Fang, Y.; Yao, M. Antimicrobial Photodynamic Therapy for Methicillin-Resistant Staphylococcus Aureus Infection. *Biomed Res. Int.* **2013**, *2013*, 159157.

(53) Yin, R.; Hamblin, M. Antimicrobial Photosensitizers: Drug Discovery under the Spotlight. *Curr. Med. Chem.* **2015**, *22*, 2159–2185.

(54) Ragàs, X.; Sánchez-García, D.; Ruiz-González, R.; Dai, T.; Agut, M.; Hamblin, M. R.; Nonell, S. Cationic Porphycenes as Potential Photosensitizers for Antimicrobial Photodynamic Therapy. *J. Med. Chem.* **2010**, *53*, 7796–7803.

(55) Liu, Y.; Qin, R.; Zaat, S. A. J.; Breukink, E.; Heger, M. Antibacterial Photodynamic Therapy: Overview of a Promising Approach to Fight Antibiotic-Resistant Bacterial Infections. *J. Clin. Transl. Res.* **2015**, *1*, 140–167.

(56) Jori, G.; Fabris, C.; Soncin, M.; Ferro, S.; Coppellotti, O.; Dei, D.; Fantetti, L.; Chiti, G.; Roncucci, G. Photodynamic Therapy in the Treatment of Microbial Infections: Basic Principles and Perspective Applications. *Lasers Surg. Med.* **2006**, *38*, 468–481.

(57) Zheng, Y.; Yin, G.; Le, V.; Zhang, A.; Chen, S. Y.; Liang, X.; Liu, J. W. Photodynamic-Therapy Activates Immune Response by Disrupting Immunity Homeostasis of Tumor Cells, Which Generates Vaccine for Cancer Therapy. *Int. J. Biol. Sci.* **2016**, *12*, 120–132.

(58) Agostinis, P.; Vantieghem, A.; Merlevede, W.; De Witte, P. A. M. Hypericin in Cancer Treatment: More Light on the Way. *Int. J. Biochem. Cell Biol.* **2002**, *34*, 221–241.

(59) Delcanale, P.; Pennacchietti, F.; Maestrini, G.; Rodríguez-Amigo, B.; Bianchini, P.; Diaspro, A.; Iagatti, A.; Patrizi, B.; Foggi, P.; Agut, M.; *et al.* Subdiffraction Localization of a Nanostructured Photosensitizer in Bacterial Cells. *Sci. Rep.* **2015**, *5*, 15564.

(60) López-Chicón, P.; Paz-Cristobal, M. P.; Rezusta, A.; Aspiroz, C.; Royo-Cañas, M.; Andres-Ciriano, E.; Gilaberte, Y.; Agut, M.; Nonell, S. On the Mechanism of Candida Spp. Photoinactivation by Hypericin. *Photochem. Photobiol. Sci.* **2012**, *11*, 1099–1107.

(61) Stewart, B. W.; Wild, C. P. *World Cancer Report 2014*; **2014**.

(62) Chiaviello, A.; Postiglione, I.; Palumbo, G. Targets and Mechanisms of Photodynamic Therapy in Lung Cancer Cells: A Brief Overview. *Cancers (Basel).* **2011**, *3*, 1014–1041.

(63) Chen, B.; Pogue, B. W.; Luna, J. M.; Hardman, R. L.; Hoopes, P. J.; Hasan, T. Tumor Vascular Permeabilization by Vascular-Targeting Photosensitization: Effects, Mechanism, and Therapeutic Implications. *Clin. Cancer Res.* **2006**, *12*, 917–923.

(64) Weiss, A.; den Bergh, H. van; Griffioen, A. W.; Nowak-Sliwinska, P. Angiogenesis Inhibition for the Improvement of Photodynamic Therapy: The Revival of a Promising Idea. *Biochimica et Biophysica Acta -Reviews on Cancer*, **2012**, *1826*, 53–70.

(65) Dąbrowski, J. M.; Arnaut, L. G. Photodynamic Therapy (PDT) of Cancer: From Local to Systemic Treatment. *Photochem. Photobiol. Sci.* **2015**, *14*, 1765–1780.

(66) Yamamoto, N.; Homma, S.; Sery, T. W.; Donoso, L. A.; Hoober, J. K. Photodynamic Immunopotentiation: In Vitro Activation of Macrophages by Treatment of Mouse Peritoneal Cells with Haematoporphyrin Derivative and Light. *Eur. J. Cancer* **1991**, *27*, 467–471.

(67) Bonnett, R. Photosensitizers of the Porphyrin and Phthalocyanine Series for Photodynamic Therapy. *Chem. Soc. Rev.* **1995**, *24*, 19–33.

(68) Bechet, D.; Couleaud, P.; Frochot, C.; Viriot, M.-L. L.; Guillemin, F.; Barberi-Heyob, M. Nanoparticles as Vehicles for Delivery of Photodynamic Therapy Agents. *Trends Biotechnol.* **2008**, *26*, 612–621.

(69) Torchilin, V. Tumor Delivery of Macromolecular Drugs Based on the EPR Effect. *Adv. Drug Deliv. Rev.* **2011**, *63*, 131–135.

(70) Postigo, F.; Mora, M.; de Madariaga, M. A.; Nonell, S.; Sagrista, M. L. Incorporation of Hydrophobic Porphyrins into Liposomes: Characterization and Structural Requirements. *Int. J. Pharm.* **2004**, *278*, 239–254.

(71) García-Díaz, M.; Nonell, S.; Villanueva, A.; Stockert, J. C.; Cañete, M.; Casadó, A.; Mora, M.; Sagristá, M. L. Do Folate-Receptor Targeted Liposomal Photosensitizers Enhance Photodynamic Therapy Selectivity? *Biochim. Biophys. Acta,* **2011**, *1808*, 1063–1071.

(72) Toledano, H.; Edrei, R.; Kimel, S. Photodynamic Damage by Liposome-Bound Porphycenes: Comparison between in Vitro and in Vivo Models. *J. Photochem. Photobiol. B,* **1998**, *42*, 20–27.

(73) Comas-Barceló, J.; Rodríguez-Amigo, B.; Abbruzzetti, S.; Rey-Puech, P. del; Agut, M.; Nonell, S.; Viappiani, C. A Self-Assembled Nanostructured Material with Photosensitising Properties. *RSC Adv.* **2013**, *3*, 17874–17879.

(74) Kuruppuarachchi, M.; Savoie, H.; Lowry, A.; Alonso, C.; Boyle, R. W. Polyacrylamide Nanoparticles as a Delivery System in Photodynamic Therapy. *Mol. Pharm.* **2011**, *8*, 920–931.

(75) Gao, D.; Xu, H.; Philbert, M. A.; Kopelman, R. Ultrafine Hydrogel Nanoparticles: Synthetic Approach and Therapeutic Application in Living Cells. *Angew. Chem. Int. Ed. Engl.* **2007**, *46*, 2224–2227.

(76) Boix-Garriga, E.; Acedo, P.; Casadó, A.; Villanueva, A.; Stockert, J. C.; Cañete, M.; Mora, M.; Sagristá, M. L.; Nonell, S. Poly(D, L-Lactide-Co-Glycolide) Nanoparticles as Delivery Agents for Photodynamic Therapy: Enhancing Singlet Oxygen Release and Phototoxicity by Surface PEG Coating. *Nanotechnology,* **2015**, *26*, 365104.

(77) Planas, O.; Bresolí-Obach, R.; Nos, J.; Gallavardin, T.; Ruiz-González, R.; Agut, M.; Nonell, S. Synthesis, Photophysical Characterization, and Photoinduced Antibacterial Activity of Methylene Blue-Loaded Amino- and Mannose-Targeted Mesoporous Silica Nanoparticles. *Molecules,* **2015**, *20*, 6284–6298.

(78) Khaing Oo, M. K.; Yang, Y.; Hu, Y.; Gomez, M.; Du, H.; Wang, H. Gold Nanoparticle-Enhanced and Size-Dependent Generation of Reactive Oxygen Species from Protoporphyrin IX. *ACS Nano,* **2012**, *6*, 1939–1947.

(79) Planas, O.; Macia, N.; Agut, M.; Nonell, S.; Heyne, B. Distance-Dependent Plasmon-Enhanced Singlet Oxygen Production and Emission for Bacterial Inactivation. *J. Am. Chem. Soc.* **2016**, *138*, 2762–2768.

(80) Tegos, G. P.; Demidova, T. N.; Arcila-Lopez, D.; Lee, H.; Wharton, T.; Gali, H.; Hamblin, M. R. Cationic Fullerenes Are Effective and Selective Antimicrobial Photosensitizers. *Chem. Biol.* **2005**, *12*, 1127–1135.

(81) Lim, S. F.; Austin, R. H. *Upconverting Nanoparticle-Based Multi-Functional Nanoplatform for Enhanced Photodynamic Therapy: Promises and Perils*; Hamblin, M. R.; Avci, P.; Elsevier, **2015**.

(82) Sun, T.; Zhang, Y. S.; Pang, B.; Hyun, D. C.; Yang, M.; Xia, Y. Engineered Nanoparticles for Drug Delivery in Cancer Therapy. *Angew. Chemie - Int. Ed.* **2014**, *53*, 12320–12364.

(83) Konan, Y. N.; Gurny, R.; Allémann, E. State of the Art in the Delivery of Photosensitizers for Photodynamic Therapy. *J. Photochem. Photobiol. B.* **2002**, *66*, 89–106.

(84) Vargas, A.; Lange, N.; Arvinte, T.; Cerny, R.; Gurny, R.; Delie, F. Toward the Understanding of the Photodynamic Activity of M-THPP Encapsulated in PLGA Nanoparticles: Correlation between Nanoparticle Properties and in Vivo Activity. *J. Drug Target.* **2009**, *17*, 599–609.

(85) Lucky, S. S.; Soo, K. C.; Zhang, Y. Nanoparticles in Photodynamic Therapy. *Chem. Rev.* **2015**, *115*, 1990–2042.

(86) Li, X.-S.; Ke, M.-R.; Huang, W.; Ye, C.-H.; Huang, J.-D. A pH-Responsive Layered Double Hydroxide (LDH)-Phthalocyanine Nanohybrid for Efficient Photodynamic Therapy. *Chem. Eur. J.* **2015**, *21*, 3310–3317.

(87) Jin, C. S.; Zheng, G. Liposomal Nanostructures for Photosensitizer Delivery. *Lasers Surg. Med.* **2011**, *43*, 734–748.

(88) Lovell, J. F.; Liu, T. W. B.; Chen, J.; Zheng, G. Activatable Photosensitizers for Imaging and Therapy. *Chem. Rev.* **2010**, *110*, 2839–2857.

(89) Kashef, N.; Huang, Y.-Y.; Hamblin, M. R. Advances in Antimicrobial Photodynamic Inactivation at the Nanoscale. *Nanophotonics,* **2017**, *0*, 1–27.

(90) Bulbake, U.; Doppalapudi, S.; Kommineni, N.; Khan, W. Liposomal Formulations in Clinical Use: An Updated Review. *Pharmaceutics,* **2017**, *9*, 1–33.

(91) Chen, C.-T.; Chen, C.-P.; Yang, J.-C.; Tsai, T. Liposome-Encapsulated Photosensitizers against Bacteria. *Recent Pat. Antiinfect. Drug Discov.* **2013**, *8*, 100–107.

(92) Thanou, M. *Theranostics and Image Guided Drug Delivery*; Chemistry, Royal Society of Chemistry, **2017**.

(93) Quinteros, D. A.; Bermudez, J. M.; Ravetti, S.; Cid, A.; Allemandi, D. A.; Palma, S. D. Therapeutic Use of Monoclonal Antibodies: General Aspects and Challenges for Drug Delivery. In *Nanostructures for Drug Delivery*; Andronescu, E.; Mihai Grumezescu, A., Elsevier, **2017**, 807–834.

(94) Cáceres, J.; Robinson-Duggon, J.; Tapia, A.; Paiva, C.; Gómez, M.; Bohne, C.; Fuentealba, D. Photochemical Behavior of Biosupramolecular Assemblies of Photosensitizers, Cucurbit[n]urils and Albumins. *Phys. Chem. Chem. Phys.* **2017**, *19*, 2574–2582.

(95) MaHam, A.; Tang, Z.; Wu, H.; Wang, J.; Lin, Y. Protein-Based Nanomedicine Platforms for Drug Delivery. *Small,* **2009**, *5*, 1706–1721.

(96) Kratz, F.; Beyer, U. Serum Proteins as Drug Carriers of Anticancer Agents: A Review. *Drug Deliv.* **1998**, *5*, 281–299.

(97) Gbur, P.; Dedic, R.; Chorvat Jr, D.; Miskovsky, P.; Hala, J.; Jancura, D. Time-Resolved Luminiscence and Singlet Oxygen Formation Alter Illumination of the Hypericin-Low-Density Lipoprotein Complex. *Photochem. Photobiol.* **2009**, *85*, 816–823.

(98) Ng, K. K.; Lovell, J. F.; Zheng, G. Lipoprotein-Inspired Nanoparticles for Cancer Theranostics. *Acc. Chem. Res.* **2011**, *44*, 1105–1113.

(99) Debele, T. A.; Peng, S.; Tsai, H. C. *Drug Carrier for Photodynamic Cancer Therapy*, **2015**, 16.

(100) Chen, K.; Preuß, A.; Hackbarth, S.; Wacker, M.; Langer, K.; Röder, B. Novel Photosensitizer-Protein Nanoparticles for Photodynamic Therapy: Photophysical Characterization and in Vitro Investigations. *J. Photochem. Photobiol. B Biol.* **2009**, *96*, 66–74.

(101) Chen, K.; Wacker, M.; Hackbarth, S.; Ludwig, C.; Langer, K.; Röder, B. Photophysical Evaluation of mTHPC-Loaded HSA Nanoparticles as Novel PDT Delivery Systems. *J. Photochem. Photobiol. B,* **2010**, *101*, 340–347.

(102) Preuss, A.; Chen, K.; Hackbarth, S.; Wacker, M.; Langer, K.; Röder, B. Photosensitizer Loaded HSA Nanoparticles II: In Vitro Investigations. *Int. J. Pharm.* **2011**, *404*, 308–316.

(103) Jiang, G.-Y.; Lei, W.-H.; Zhou, Q.-X.; Hou, Y.-J.; Wang, X.-S.; Zhang, B.-W. A New Phenol Red-Modified Porphyrin as Efficient Protein Photocleaving Agent. *Phys. Chem. Chem. Phys.* **2010**, *12*, 12229–12236.

(104) Hayashi, T.; Dejima, H.; Matsuo, T.; Sato, H.; Murata, D.; Hisaeda, Y. Blue Myoglobin Reconstituted with an Iron Porphycene Shows Extremely High Oxygen Affinity. *J. Am. Chem. Soc.* **2002**, *124*, 11226–11227.

(105) Ordway, G. A.; Garry, D. J. Myoglobin: An Essential Hemoprotein in Striated Muscle. *J. Exp. Biol.* **2004**, *207*, 3441–3446.

(106) Frauenfelder, H.; McMahon, B. H.; Austin, R. H.; Chu, K.; Groves, J. T. The Role of Structure, Energy Landscape, Dynamics, and Allostery in the Enzymatic Function of Myoglobin. *Proc. Natl. Acad. Sci. U. S. A.* **2001**, *98*, 2370–2374.

(107) Le Maux, S.; Bouhallab, S.; Giblin, L.; Brodkorb, A.; Croguennec, T. Bovine β-Lactoglobulin/fatty Acid Complexes: Binding, Structural, and Biological Properties. *Dairy Sci. Technol.* **2014**, *94*, 409–426.

(108) O'Neill, T. E.; Kinsella, J. E. Binding of Alkanone Flavors to β-Lactoglobulin: Effects of Conformational and Chemical Modification. *J. Agric. Food Chem.* **1987**, *35*, 770–774.

(109) Kontopidis, G.; Holt, C.; Sawyer, L. The Ligand-Binding Site of Bovine β-Lactoglobulin: Evidence for a Function? *J. Mol. Biol.* **2002**, *318*, 1043–1055.

(110) Mercadante, D.; Melton, L. D.; Norris, G. E.; Loo, T. S.; Williams, M. A. K.; Dobson, R. C. J.; Jameson, G. B. Bovine β-Lactoglobulin Is Dimeric under Imitative Physiological Conditions: Dissociation Equilibrium and Rate Constants over the pH Range of 2.5-7.5. *Biophys. J.* **2012**, *103*, 303–312.

(111) Diarrassouba, F.; Liang, L.; Remondetto, G.; Subirade, M. Nanocomplex Formation between Riboflavin and β-Lactoglobulin: Spectroscopic Investigation and Biological Characterization. *Food Res. Int.* **2013**, *52*, 557–567.

(112) Torchilin, V. P.; Weissig, V. *Liposomes: A Practical Approach*; Torchilin, V.; Weissig, V., 2nd Edition; Oxford University Press, **2007**.

(113) An, X.; Gui, R. Stimuli-Responsive Liposome and Control Release Drug. In *Nanostructures for Drug Delivery*; Andronescu, E.; Grumezescu, A. M., **2017**, 887–918.

(114) Kraft, J. C.; Freeling, J. P.; Wang, Z.; Ho, R. J. Y. Emerging Research and Clinical Development Trends of Liposome and Lipid Nanoparticle Drug Delivery Systems. *J Pharm Sci.* **2014**, *103*, 29–52.

(115) Akbarzadeh, A.; Rezaei-Sadabady, R.; Davaran, S.; Joo, S. W.; Zarghami, N.; Hanifehpour, Y.; Samiei, M.; Kouhi, M.; Nejati-Koshki, K. Liposome: Classification, Preparation, and Applications. *Nanoscale Res. Lett.* **2013**, *8*, 1.

(116) Selim, A.; Lila, A.; Ishida, T. Liposomal Delivery Systems: Design Optimization and Current Applications. *Biol. Pharm. Bull.* **2017**, *40*, 1–10.

(117) Hillaireau, H.; Couvreur, P. Nanocarriers' Entry into the Cell: Relevance to Drug Delivery. *Cell. Mol. Life Sci.* **2009**, *66*, 2873–2896.

(118) Lombardo, D.; Calandra, P.; Barreca, D.; Magazù, S.; Kiselev, M. A. Soft Interaction in Liposome Nanocarriers for Therapeutic Drug Delivery. *Nanomater. (Basel, Switzerland),* **2016**, *6*.

(119) Brown, S. B.; Brown, E. A.; Walker, I. The Present and Future Role of Photodynamic Therapy in Cancer Treatment. *Lancet Oncol.* **2004**, *5*, 497–508.

(120) Allison, R. R.; Bagnato, V. S.; Cuenca, R.; Downie, G. H.; Sibata, C. H. The Future of Photodynamic Therapy in Oncology. *Futur. Oncol.* **2006**, *2*, 53–71.

(121) Luo, D.; Carter, K. A.; Miranda, D.; Lovell, J. F. Chemophototherapy: An Emerging Treatment Option for Solid Tumors. *Adv. Sci.* **2017**, *4*, 1–24.

(122) Marise De Freitas, L.; Serafim, R. B.; Ferreira De Sousa, J.; Moreira, T. F.; Tavares, C.; Santos, D.; Baviera, A. M.; Valente, V.; Soares, C. P.; Fontana, C. R. Photodynamic Therapy Combined to Cisplatin Potentiates Cell Death Responses of Cervical Cancer Cells. *BMC Cancer,* **2017**, *17*, 1–12.

(123) Zhou, L.; Wei, S.; Ge, X.; Zhou, J.; Jiang, H.; Li, F.; Shen, J. Combination of Chemotherapy and Photodynamic Therapy Using Graphene Oxide as Drug Delivery System. *J. Photochem. Photobiol. B,* **2014**, *135*, 7–16.

(124) Ke, M.-R.; Chen, S.-F.; Peng, X.-H.; Zheng, Q.-F.; Zheng, B.-Y.; Yeh, C.-K.; Huang, J.-D. A Tumor-Targeted Activatable Phthalocyanine-Tetrapeptide-Doxorubicin Conjugate for Synergistic Chemo-Photodynamic Therapy. *Eur. J. Med. Chem.* **2017**, *127*, 200–209.

(125) Ruiz-González, R.; Milán, P.; Bresolí-Obach, R.; Stockert, J.; Villanueva, A.; Cañete, M.; Nonell, S. Photodynamic Synergistic Effect of Pheophorbide a and Doxorubicin in Combined Treatment against Tumoral Cells. *Cancers (Basel),* **2017**, *9*, 18.

(126) Huang, H. C.; Mallidi, S.; Liu, J.; Chiang, C. Te; Mai, Z.; Goldschmidt, R.; Ebrahim-Zadeh, N.; Rizvi, I.; Hasan, T. Photodynamic Therapy Synergizes with Irinotecan to Overcome Compensatory Mechanisms and Improve Treatment Outcomes in Pancreatic Cancer. *Cancer Res.* **2016**, *76*, 1066–1077.

(127) Casas, A.; Fukuda, H.; Riley, P.; del C Batlle, A. M.; Caro, R.; Straight, R.; Kopecek, J.; Funayama, Y.; Ogasawara, H.; Ohiro, T.; *et al.* Enhancement of Aminolevulinic Acid Based Photodynamic Therapy by Adriamycin. *Cancer Lett.* **1997**, *121*, 105–113.

(128) Kirveliene, V.; Grazeliene, G.; Dabkeviciene, D.; Micke, I.; Kirvelis, D.; Juodka, B.; Didziapetriene, J. Schedule-Dependent Interaction between Doxorubicin and mTHPC-Mediated Photodynamic Therapy in Murine Hepatoma in Vitro and in Vivo. *Cancer Chemother. Pharmacol.* **2006**, *57*, 65–72.

(129) Saravanakumar, G.; Lee, J.; Kim, J.; Kim, W. J. Visible Light-Induced Singlet Oxygen-Mediated Intracellular Disassembly of Polymeric Micelles Co-Loaded with a Photosensitizer and an Anticancer Drug for Enhanced Photodynamic Therapy. *Chem. Commun.* **2015**, *51*, 9995–9998.

(130) Peng, P. C.; Hong, R. L.; Tsai, Y. J.; Li, P. T.; Tsai, T.; Chen, C. T. Dual-Effect Liposomes Encapsulated with Doxorubicin and Chlorin e6 Augment the Therapeutic Effect of Tumor Treatment. *Lasers Surg. Med.* **2015**, *47*, 77–87.

(131) Chabot, G. G. Clinical Pharmacology and Pharmacodynamics of Irinotecan: A Review. *Ann. N. Y. Acad. Sci.* **1996**, *803*, 164–172.

(132) Roy, B.; Duy, S. V.; Puy, J.-Y.; Martin, C.; Guitton, J.; Dumontet, C.; Périgaud, C.; Lefebvre-Tournier, I. Synthesis and Evaluation of a Molecularly Imprinted Polymer for Selective Solid-Phase Extraction of Irinotecan from Human Serum Samples. *J. Funct. Biomater.* **2012**, *3*, 131–142.

(133) Casadó, A.; Giuffrida, M. C.; Sagrist??, M. L.; Castelli, F.; Pujol, M.; Alsina, M. A.; Mora, M. Langmuir Monolayers and Differential Scanning Calorimetry for the Study of the Interactions between Camptothecin Drugs and Biomembrane Models. *Biochim. Biophys. Acta - Biomembr.* **2016**, *1858*, 422–433.

(134) Yue, C.; Yang, Y.; Zhang, C.; Alfranca, G.; Cheng, S.; Ma, L.; Liu, Y.; Zhi, X.; Ni, J.; Jiang, W.; *et al.* ROS-Responsive Mitochondria-Targeting Blended Nanoparticles: Chemo- and Photodynamic Synergistic Therapy for Lung Cancer with on-Demand Drug Release upon Irradiation with a Single Light Source. *Theranostics,* **2016**, *6*, 2352–2366.

(135) Chibebe Junior, C.; Sabino, C. P.; Tan, X.; Junqueira, J. C.; Wang, Y.; Fuchs, B. B.; Jorge, A. O.; Tegos, G. P.; Hamblin, M. R.; Mylonakis, E.; *et al.* Selective Photoinactivation of Candida Albicans in the Non- Vertebrate Host Infection Model Galleria Mellonella Selective Photoinactivation of Candida Albicans in the Non-Vertebrate Host Infection Model Galleria Mellonella. *BMC Microbiol.* **2013**, *13*, 1471–2180.

(136) Morton, C. O.; Chau, M.; Stack, C. In Vitro Combination Therapy Using Low Dose Clotrimazole and Photodynamic Therapy Leads to Enhanced Killing of the Dermatophyte Trichophyton Rubrum. *BMC Mcrobiology,* **2014**, *14*, 1471–2180.

(137) Huang, P.; Lin, J.; Wang, X.; Wang, Z.; Zhang, C.; He, M.; Wang, K.; Chen, F.; Li, Z.; Shen, G.; *et al.* Light-Triggered Theranostics Based on Photosensitizer-Conjugated Carbon Dots for Simultaneous Enhanced-Fluorescence Imaging and Photodynamic Therapy. *Adv. Mater.* **2012**, *24*, 5104–5110.

(138) Rai, P.; Mallidi, S.; Zheng, X.; Rahmanzadeh, R.; Mir, Y.; Elrington, S.; Khurshid, A.; Hasan, T. Development and Applications of Photo-Triggered Theranostic Agents. *Adv. Drug Deliv. Rev.* **2010**, *62*, 1094–1124.

(139) Tian, J.; Ding, L.; Xu, H. J.; Shen, Z.; Ju, H.; Jia, L.; Bao, L.; Yu, J. S. Cell-Specific and pH - Activatable Rubyrin-Loaded Nanoparticles for Highly Selective Near-Infrared Photodynamic Therapy against Cancer. *J. Am. Chem. Soc.* **2013**, *135*, 18850–18858.

(140) Jin, C. S.; Cui, L.; Wang, F.; Chen, J.; Zheng, G. Targeting-Triggered Porphysome Nanostructure Disruption for Activatable Photodynamic Therapy. *Adv. Healthc. Mater.* **2014**, *3*, 1240–1249.

CHAPTER 2

General techniques and methods

This chapter described the common photophysical techniques and methods that have been employed over this work. Specific details about the methodology used for preparation and characterisation of protein and liposomes, the general protocols of *in vitro* cell culture and photoinactivation procedures will be described in the experimental section of each corresponding chapter.

2.1. Steady state optical techniques

2.1.1. Absorbance

Absorption spectra were recorded on a double beam Cary 6000i UV-Vis-NIR spectrophotometer (Agilent Technologies, Santa Clara, CA, USA). In order to remove the scattering baseline when measuring the absorption spectra of PS or drugs entrapped in liposomes, a spectrum of a suspension of blank liposomes of the same dilution was subsequently recorded. Both spectra were mathematically subtracted to yield the baseline corrected absorption spectrum or scattering subtraction spectrum of the PS/drug.

2.1.2. Fluorescence

Fluorescence spectra were recorded in a Fluoromax 4 spectrofluorometer (Horiba Jobin Yvon, Edison, NJ, USA) exciting at the appropriate wavelength according to the PS.

Fluorescence quantum yields (Φ_F) were determined by the comparative method.[1] Fluorescence emission spectra (F) were collected for a set of sample and reference solutions of increasing absorbance values and the area under the spectrum (AUC) was plotted against the absorption factor ($1- 10^{-A}$). According to equation 2.1, a linear plot should be obtained the slope of which is proportional to Φ_F:

$$F = \left[\frac{\kappa}{n_r^2} I_0 \Phi_F\right] \times (1 - 10^{-A}) \qquad \text{Eq. 2.1}$$

κ is an instrumental factor, I_0 is the radiant power of the excitation beam, and n_r is the solvent's refractive index. Thus, Φ_F for PS-loaded in the nanocarrier was determined from the ratio of slopes measured for the nano-suspensions and the proper reference, as in equation 2.2.

$$\Phi_{F,S} = \frac{F_{slope,S} \cdot n_S^2}{F_{slope,ref} \cdot n_{ref}^2} \times \Phi_{F,ref} \qquad \text{Eq. 2.2}$$

in which the subscript s stands for sample and ref for reference, F_{slope} is the slope from the graph aforementioned and n is the refractive index of the solvent used in each case.

2.2. Time-resolved optical techniques

Time-resolved optical techniques enable the detection of excited states or intermediate species upon pulsed irradiation of a sample. These species formed upon light absorption can be monitored through changes in the signal intensity of an analysing beam (for absorption spectroscopy) or through photon emission (in the case of fluorescence or phosphorescence spectroscopy), in all cases the detection being temporally resolved.

Nowadays these techniques are usually coupled to photon counting detectors due to their better time resolution, better sensitivity and lower interference from sensitizer luminescence or scattered laser light compared to analog detectors. Photomultiplier tubes (PMTs) are detectors the response of which is based on the initiation and amplification of a pulse of electrical current when a photon strikes their surface. This principle has inspired the photon counting mode and therefore the detectors employed are commonly photomultiplier tubes (PMTs). Of the three photon counting techniques existing, namely gated photon counting (GPC), multichannel scaling (MCS) and time-correlated single photon counting (TCSPC), only the last two have been employed for the herein described experiments.[2]

2.2.1. Time-correlated single photon counting (TCSPC)

This method is common for time-resolved fluorescence measurements and it is based on the precisely timed registration of the first single photon arrival to the detector from the emitting sample. The reference for time registration is the excitation pulse. The cumulative signal obtained from repetitive cycles is a histogram of photon arrivals per time bin which represents the time decay one would have obtained from the observation of a single excitation-emission cycle (Figure 2.1).

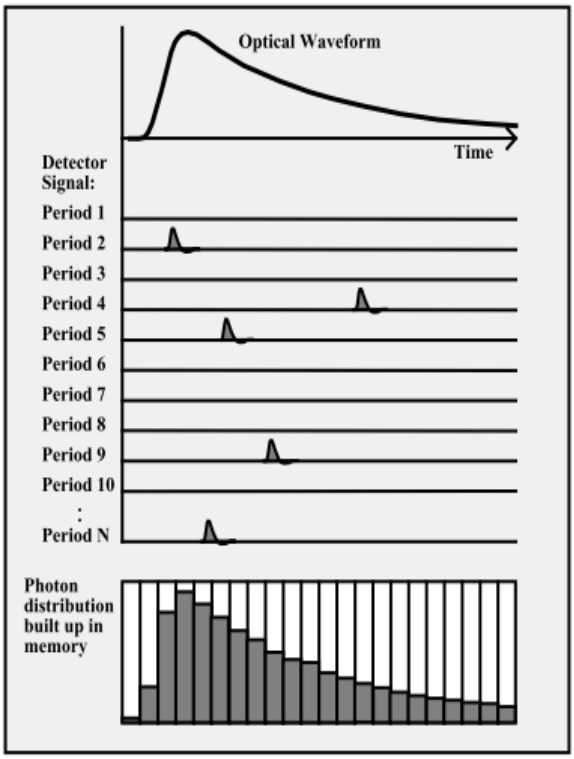

Figure 2.1. Principle of classic TCSPC acquisition. From [3].

It is a prerequisite of this technique to keep the probability of registering more than one photon per cycle low, which can be accomplished by attenuating the light level arriving at the sample,

or in other words, to keep the count rate at the detector equal or below 1% of the excitation rate. It must be taken into account that the measured fluorescence decay is the convolution of the "real" fluorescence decay with the instrumental response factor (IRF). Measurement of the IRF is achieved by placing some scattering medium at the sample compartment, thus no fluorescence but only some scattered excitation light will reach the detector. In order to obtain the real fluorescence decay, deconvolution by data analysis software with the measured fluorescence decay and the IRF needs to be performed.[3]

Time-resolved fluorescence decays were recorded at a specific wavelength, selected by a monochromator grating, using a time-correlated single photon counting system (Fluotime 200, PicoQuant GmbH, Berlin, Germany) with a pulsed LED source emitting at 280 or 502 nm, or 375 nm picosecond diode laser working at 10 MHz repetition rate (depending on the study) for excitation. Decays were analyzed using the PicoQuant FluoFit 4.5.3 data analysis software. Absorbance of the samples was kept below 0.1 at the excitation wavelength in all cases and the photon counting rate was kept below 1%. The IRF signal was measured by placing a cuvette with a suspension of Ludox® in water.

2.2.2. Time-resolved NIR phosphorescence detection (TRPD)

This method is the most commonly employed to directly observe and monitor $^1O_2$ formation and decay and subsequently to measure its lifetime (τ_Δ). It is based on the time-resolved detection of its weak phosphorescence centred at 1275 nm (Figure 2.2). In this case, the photon-counting method is MCS, in which all detected photons are counted and sorted out in the different positions of a board memory, thus the time distribution of the detected photons is obtained at once.

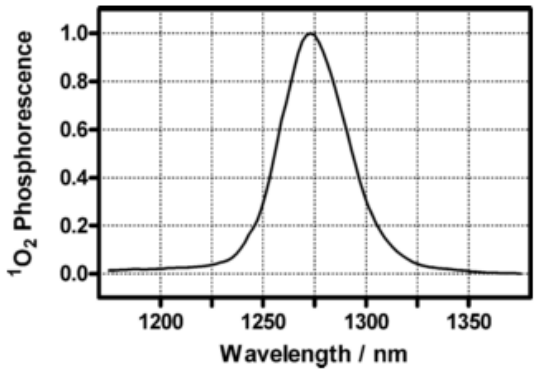

Figure 2.2. Near-infrared spectrum of $^1O_2$ phosphorescence. From [2].

$^1O_2$ phosphorescence was detected using a customized PicoQuant Fluotime 200 system described elsewhere.[2] Briefly, a diode-pumped pulsed Nd:YAG laser (FTSS355-Q, Crystal Laser, Berlin, Germany) working at 10 or 1 kHz repetition rate at 355 nm (5 mW, 0.5 μJ per pulse) or

532 nm (10 mW, 1 μJ per pulse) was used for excitation. A 1064 nm rugate notch filter (Edmund Optics, York, UK) was placed at the exit port of the laser to remove any residual component of its fundamental emission in the NIR region. The luminescence exiting from the side of the cuvette was filtered by a cold mirror and a bandpass filter of the appropriate wavelength-1220, 1275 or 1325 nm (Spectrogon AB, Täby, Sweden). A thermoelectric-cooled near-infrared sensitive photomultiplier tube assembly (H9170-45, Hamamatsu Photonics), sensitive from 950 to 1400 nm, was used to detect NIR luminescence. The detector was operated in photon counting mode and its output sent to a multichannel scaler (PicoQuant Nanoharp 250). Photon histograms were analysed using the PicoQuant FluoFit 4.5.3 data analysis software. For temperature-dependent measurements in the case of the proteins, an Ultraterm 6000383 (JP¡ Selecta S.A., Abrera, Spain) thermostat was used in order to control the temperature.

The temporal profile of the time-resolved $^1O_2$ phosphorescence signals (S_t) is typically a rise-and decay function that can be fitted with the following mathematical model (Eq. 2.3):[4]

$$S_t = \sum_i S_{0_i} \times \frac{\tau_{\Delta_i}}{\tau_{\Delta_i} - \tau_{T_i}} \times (e^{-t/\tau_{\Delta i}} - e^{-t/\tau_{T i}}) + y_o \qquad \text{Eq. 2.3}$$

The subscript i refers to the number of independent $^1O_2$ populations in the sample. S_0 is a quantity proportional to the concentration of $^1O_2$ created by the laser pulse, y_o is an offset due to instrument dark counts and τ_Δ and τ_T are the lifetimes of $^1O_2$ and ^{3}PS*, respectively.

The photosensitizer's triplet lifetime was determined, whenever possible, by fitting with equation 2.4 to the signal obtained at a wavelength where the triplet state of the photosensitizer emits, typically at 1110 nm:

$$I_t = \sum_i A_i \times e^{-t/\tau_{T_i}} \qquad \text{Eq. 2.4}$$

A_i is proportional to the concentration of excited triplet states of the photosensitizer and τ_T is the actual triplet state lifetime of the photosensitizer.

S_0 is a quantity proportional to Φ_Δ as shown in equation 2.5 where κ is a proportionality constant, which includes electronic and geometric factors, k_r is the $^1O_2$ radiative rate constant, E is the incident laser energy, and A is the sample absorbance at 355 or 532 nm.

$$S_0 = \kappa k_r \Phi_\Delta E(1 - 10^{-A}) \qquad \text{Eq. 2.5}$$

The procedure for determining Φ_Δ in liposomal suspensions involved measuring S_0 value for a series of solutions of increasing absorbance and then plotting S_0 versus the sample absorption factor ($1-10^{-A}$), which yielded linear plots. Then Φ_Δ was obtained by comparison of the slopes

of such plots for a suitable reference and the sample, using equation 2.6, in which the subscript s stands for sample and ref for reference.

$$\Phi_{\Delta,s} = \frac{Slope_s}{Slope_{ref}} \times \Phi_{\Delta,ref} \qquad \text{Eq. 2.6}$$

However, in proteins with Hyp usually the Φ_Δ was determined by comparing the S_0 values of optically matched solutions of the complex and the reference at 532 nm as described by equation 2.7.

$$\Phi_{\Delta,s} = \frac{S_{0,s}}{S_{0,ref}} \times \Phi_{\Delta,ref} \qquad \text{Eq. 2.7}$$

2.2.3. UV-Vis nanosecond laser flash photolysis

This technique is employed to examine the absorption or emission with temporal resolution of triplet states or other photochemically generated intermediate species. In this study, it served to determine the PS triplet state kinetics by triplet-triplet absorption when information obtained from the observation of its time-resolved phosphorescence was insufficient. Several setups exist for the detection of triplet-triplet absorption, but most of them have two features in common (Figure 2.3). Firstly, any setup comprises an excitation source to produce triplet states, commonly a pulsed laser. Second, a "monitoring" light source, in this case a Xe lamp, probes the changes in absorbance at the sample.

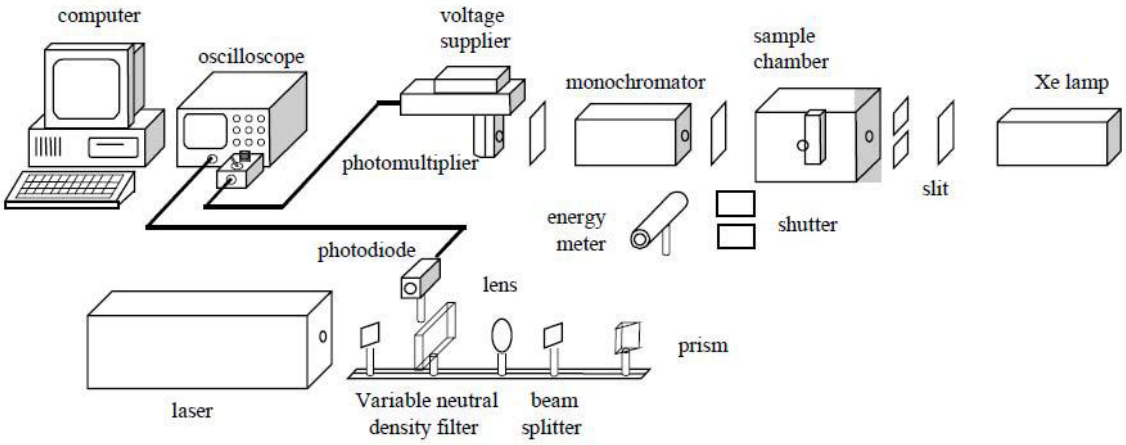

Figure 2.3. Experimental setup for UV-visible nanosecond laser flash photolysis. Adapted from [4].

Transient absorption experiments in the UV–visible (UV–vis) region were carried out using a home-built nanosecond laser flash photolysis system. In this instrument, the 2nd harmonic (532 nm) of a Continuum Surelite I-10 Nd:YAG laser (10 Hz, 5 ns pulsewidth, 0.05-1 mJ per pulse) was directed onto the sample. Changes in the sample absorbance were detected by a Hamamatsu R928 photomultiplier in order to monitor the intensity variations of an analysing beam produced by a 75W short arc Xe lamp (USHIO) and spectral discrimination was provided by a PTI 101

monochromator. The signal was fed to a Lecroy Wavesurfer 454 oscilloscope for digitizing (1 shot, typically) and finally transferred through a GPIB interface (National Instruments) to a PC computer for data storage and analysis. The TTL sync output of the laser was used to trigger the oscilloscope. The energy of the laser pulse was varied by controlling the Q-switch delay and measured with a pyroelectric energy meter (RJP 735 and RJ 7610) from Laser Precision Corp. The system was controlled by the in house-developed LKS software (LabView, National Instruments).

2.3. Fluorescence microscopy

Optical or light microscopy is a key tool in modern cell biology. Light microscopy has several features that make it ideally suited for imaging biology in living cells: the resolution is well-matched to the sizes of subcellular structures, a diverse range of available fluorescent probes makes it possible to mark proteins, organelles, and other structures for imaging. Most broadly, optical microscopy can be divided into two categories: brightfield and fluorescence.

2.3.1. Wide field

Most cell biology imaging is done with wide field microscopy, in which the microscope simply forms an image of the sample on the camera, without any additional optical manipulation. Briefly, optical filters are used in order to select the wavelength of excitation light (coming from mercury or xenon lamp, giving out pure white light) that is directed to the sample via a dichroic mirror and fluorescent light detected by a camera (usually a CCD camera). Thus both the illumination and detection of light covering the whole visual field of the chosen microscope objective is achieved simultaneously. However, the light emitted from out-of-focus regions cannot be distinguished from the light emitted from the in-focus light. Therefore, the image will be a combination of a sharp, focused image of the in-focus plane with a blurred, unsharp image of the out-of-focus light.[5]

Live cells are most commonly imaged on an inverted epifluorescence microscope. In such a microscope, the objective images the sample from below. Inverted microscopes are popular for cell biological imaging because they allow imaging through a glass coverslip to see cells grown above. This means that cells can be grown in coverslip bottom Petri dishes or multiwell plates containing growth media, which can be left open at the top.[6]

Morphological changes of liposomes were observed (bright field and fluorescence) with an Olympus BX61 epifluorescence microscope equipped with an Olympus DP50 digital camera (Olympus, USA), and processed using the Photoshop CS5 software (Adobe Systems, USA).

Some other images were made with an Olympus BX63 automated epifluorescence microscope equipped with a CoolLED's pE-300 light source and an Olympus DP74 digital camera, and processed using the same software.

2.3.2. Confocal

The sample is illuminated by a focused laser beam at a single point in the sample focal plane. Light from this point is detected after passage through a pinhole, such that only light emitted from the focal plane makes it through the pinhole and is recorded on the detector. Light from out-of-focus planes is blocked by the pinhole, and so the confocal only records light from the focal plane of the sample. Scanning mirrors are used to raster the laser spot across the sample, building up an image point by point. Therefore with this microscopy the resolution in z axe is widely improved (> 700 nm).

The co-localization of both PS and drug was made with a multispectral Leica TCS SP8 confocal microscope with a 3X STED module for super- resolution, exciting with a 405 nm laser for CPT-11; with a 488 nm laser for Dox and with a 500 nm laser for PpIX. Images were processed using the Photoshop CS5 software (Adobe Systems, USA).

2.3.3. Stimulated Emission Depletion (STED)

STED is a super-resolution microscopy technic that overcomes the diffraction limit resolution of confocal microscopes using two synchronised laser pulses. In a typical STED setup, molecules excited by a first laser pulse with an ordinary diffraction-limited focus. Immediately, it is followed by the depletion or STED beam, which is red-shifted in frequency and its pulse is spatially arranged in a doughnut-shape using specially designed phase plates. Therefore, this second STED beam instantly sent the excited molecules back to the electronic ground state, quenching via stimulated emission (laser intensity of 10-30 $MW \cdot cm^{-2}$). This occurs except in the focal center, where the STED laser intensity is zero, leaving the fluorescence remains unaffected and hence detected.

This technique needs that the dyes go efficiently under stimulated emission before spontaneous fluorescence emission takes place and without an excessive bleaching. This fact requires that an excited-state molecule encounters a photon that matches the energy difference between the ground and excited state. Moreover, the fluorophore should have a long-lived singlet excited state in order to give enough time to first deactivated (i.e., switching off) by stimulated emission.

The STED nanoscopy has been performed using a custom made setup equipped with a supercontinuum pulsed laser source (ALP-710-745-SC, Fianium LTD, Southampton, UK). The

excitation wavelength is selected by means of an acusto-optic tunable filter (AOTF), while the STED wavelength is predefined by the laser outputs. The laser has a repetition frequency of 20 MHz and a pulse width of about 100 ps. In all the reported experiments, a 566 nm wavelength is used for pulsed excitation and and the emission is collected between 605 and 670 nm at increasing power of the STED beam at 715 nm. The doughnut shape of the STED beam is realized by a vortex phase plate (RPC photonics inc., Rochester, NY, USA). The beams are scanned on the sample by galvanometer mirrors (Till-photonics, FEI Munich GmbH, Germany), focused by a HCX PL APO CS 100x 1.4NA oil (Leica Microsystems, Mannheim, Germany) objective. Fluorescence is collected by an avalanche photodiode (SPCM-AQRH-13- FC, Excelitas Technologies, Vaudreuil-Dorion, Quebec, Canada) in the spectral window 670 – 640 nm.[7]

2.4. References

(1) Brouwer, A. M. Standards for Photoluminescence Quantum Yield Measurements in Solution (IUPAC Technical Report). *Pure Appl. Chem.* **2011**, *83*, 2213–2228.

(2) Jiménez-Banzo, A.; Ragàs, X.; Kapusta, P.; Nonell, S. Time-Resolved Methods in Biophysics. 7. Photon Counting vs. Analog Time-Resolved Singlet Oxygen Phosphorescence Detection. *Photochem. Photobiol. Sci.* **2008**, *7*, 1003–1010.

(3) Becker, W.; Bergmann, A.; Biscotti, G.; Rück, A. Advanced Time-Correlated Single Photon Counting Technique for Spectroscopy and Imaging in Biomedical Systems. *Springer,* **2004**, *5340*, 1–9.

(4) Nonell, S.; Braslavsky, S. E. Time-Resolved Singlet Oxygen Detection. *Methods Enzymol.* ***2000,*** 319, 37–49.

(5) Thorn, K. A Quick Guide to Light Microscopy in Cell Biology. *Mol. Biol. Cell,* **2016**, *27*, 219–222.

(6) Combs, C. A. Fluorescence Microscopy: A Concise Guide to Current Imaging Methods. *Curr. Protoc. Neurosci.,* Crawley, **2010**.

(7) Bianchini, P.; Peres, C.; Oneto, M.; Galiani, S.; Vicidomini, G.; Diaspro, A. STED Nanoscopy: A Glimpse into the Future. *Cell Tissue Res.* **2015**, *360*, 143–150.

CHAPTER 3

Hypericin@Apomyoglobin

The use of drug delivery systems for PSs to improve their solubility in aqueous medium and reduce their inherent toxicity in dark conditions is being extensively explored. Proteins are favourable nanocarriers thanks to their biocompatible and biodegradable properties. One such protein is apomyoglobin (ApoMb), i.e. the proteic portion of myoglobin, a small globular protein which binds different hydrophobic molecules in their binding site. In this chapter, we describe the design, construction, and characterisation of ApoMb-Hyp complexes that preserve the fluorescence and photosensitising properties of the natural dye Hyp.

The work described in this chapter has been carried out in collaboration with the group of Dipartimento di Scienze Matematiche, Fisiche e Informatiche from the University of Parma (Italy).

3.1. Introduction

Although proteins have been always considered good bio-friendly carriers for drugs, recently they have not been extensively studied as exogenously PSs carriers for PDT. This is surprising because their use would minimise problems such as PS solubility, biocompatibility and subcellular localisation, thereby offering a greater control on intracellular $^1O_2$ generation.[1] Other advantages are their simplicity and the relatively facile preparation.

Natural or synthetic proteins have been used indistinctly to encapsulate different types of PSs into the pockets, cavities and clefs of the proteins to form a DDS that release the PS at the target sites.[2–6] The number of PS molecules bound to a single protein and the strength of binding is dictated by the properties of the protein and of the PS. Some of the proteins employed are naturally self-assembled protein subunits of the same protein or a combination of proteins that make up a complete system. This is the case for the system presented herein, where hypericin (Hyp) is bound to apomyoglobin (apoMb), forming a complex driven mainly by hydrophobic interactions. Hyp is found in plants from the genus Hypericum (St. John's wort) and has been considered in the treatment of many cancers, and as an antiviral, antibacterial and antifungal agent. While Hyp is largely insoluble in water, it dissolves readily in ethanol or other polar organic solvents, where it displays a bright red colour due to its absorption properties and an intense orange-red fluorescence emission.

The aim of this chapter is to evaluate the binding constant of Hyp to apoMb (i.e., the affinity with which Hyp is bound to the protein) and the spectroscopic and photophysical properties and its ability to photosensitising $^1O_2$. Moreover, the photoinactivation on gram-positive and gram-negative bacteria and its possible used as a theranostic agent were evaluated.

3.2. Experimental section

3.2.1. Materials

The photoactive molecules rose bengal (RB) and 5,10,15,20-tetrakis(1-methyl-4-pyridinium) porphine tetra(p-toluene-sulfonate) (TMPyP) were purchased from Sigma-Aldrich. The photosensitiser Hyp was purchased from HWI Analytik GmbH. Myoglobin from horse heart and Dulbecco's phosphate-buffered saline (PBS x1) were acquired from Sigma Aldrich. All other chemicals were commercially available reagents of at least analytical grade. Milli-Q water (Millipore Bedford, Massachusetts system, resistivity of 18 MΩ cm) was used.

Once the complex PS-protein is prepared it is stored in the fridge kept in the dark. The dialysis tubing cellulose membrane with a cut-off of 12 kDa was bought in Sigma Aldrich. For the microbiological cultures the Tryptic Soy Broth, the Brain Heart Infusion Broth (BHI broth) and the agar-agar were also acquired from Sigma Aldrich.

3.2.2. Apomyoglobin preparation

ApoMb was prepared from the holoprotein using standard biochemical procedures: haem was removed by cold (− 30 °C) acid acetone method of extraction from horse heart myoglobin. The sample was washed with cold acetone and centrifuged several times, dried with pure nitrogen, and suspended in PBS buffer at pH 7.4. The suspension was then centrifuged, and after dialyzing against PBS buffer, the supernatant was spectroscopically checked to assess sample purity. The concentration of the apoMb stock was calculated from the absorption at 280 nm (ε = 15 800 cm^{-1} M^{-1}) and haem contamination was estimated from the absorption at 408 nm (ε = 179 000 cm^{-1} M^{-1}). In all the preparations, haem contamination was typically 0.5% of the total protein content.

3.2.3. Binding isotherm

The binding of Hyp to a protein-based structure was monitored in an experiment where a Hyp solution in buffer was titrated with increasing protein concentration, obtained adding small aliquots of a concentrated protein solution in the same buffer under constant experimental conditions and fixed temperature. For each concentration, a fluorescence emission spectrum was collected and the values of the integrated fluorescence emission, corrected by the dilution factor, are reported as a function of the protein concentration (binding isotherm). Assuming that unbound Hyp in the aqueous buffer is negligibly fluorescent, the observed fluorescence emission is proportional to the amount of complex Hyp-protein. The values of the association K_a or dissociation K_d constant for the complex formation were retrieved by a fitting of the binding isotherm curve with a model considering the chemical equilibrium:

$$Hyp + apoMb \rightleftarrows apoMb - Hyp$$

The equilibrium binding constant or the association constant is defined as:

$$K_a = \frac{[apoMb - Hyp]}{[apoMb]\,[Hyp]} \qquad \text{(Eq. 3.1)}$$

considering that:

$$[apoMb]_{tot} = [apoMb]_{free} + [apoMb - Hyp]$$

$$[Hyp]_{tot} = [Hyp]_{free} + [apoMb - Hyp]$$

The concentrations of free and protein bound Hyp can be derived:

$$[apoMb - Hyp] \; or \; [complex] = \frac{Ka[apoMb][Hyp]_{tot}}{(1 + K_a[apoMb])} \qquad \text{(Eq. 3.2)}$$

$$[Hyp]_{free} = [Hyp]_{tot}\left(1 - \frac{Ka[apoMb]}{1 + Ka[apoMb]}\right) \qquad \text{(Eq. 3.3)}$$

The total emitted fluorescence is the sum of the fluorescence emission from free and from protein bound Hyp which are in turn proportional to the concentrations of these two species:

$$F^{Hyp,tot} = F^{Hyp,free}[Hyp]_{free} + F^{Hyp,complex}[apoMb - Hyp] \qquad \text{(Eq. 3.4)}$$

$$F^{Hyp,tot} = F^{Hyp}[Hyp]_{tot}\left(1 - \frac{Ka[apoMb]}{1 + Ka[apoMb]}\right) + F^{Hyp,complex}\frac{Ka[apoMb][Hyp]_{tot}}{(1 + K_a[apoMb])}$$

where F^{Hyp} and $F^{Hyp\text{-}complex}$ are scaling factors proportional to fluorescence quantum yields of the two species.

Under the simplifying assumption that the total concentration of apoMb, $[apoMb]_{tot}$, is larger than the concentration of bound Hyp, [apoMb-Hyp], the concentration of free protein, [apoMb], can be well approximated by $[apoMb]_{tot}$. Moreover, since the unbound Hyp is negligibly fluorescent the term of F^{Hyp} could be neglected. Hence, the above expression can be written as:

$$F^{Hyp,tot} = F^{Hyp,complex}\frac{Ka[apoMb]_{tot}[Hyp]_{Tot}}{(1 + K_a[apoMb]_{tot})} \qquad \text{(Eq. 3.5)}$$

3.2.4. Modelling studies

Formation of the apoMb–Hyp complex was modelled by the AutoDock software by the group of Prof. F. Javier Luque at the University of Barcelona. A Lamarckian algorithm was used to search the different conformations with a semi empiric force field for the energy estimation (10 iterations).

3.2.5. Microbial growth and photoinactivation process

Three bacterial strains were used in this work: *E. coli* CECT101 and *S. aureus* CECT239 both obtained from the Spanish Type Culture Collection (CECT) and *B. subtilis* 168WT, received from Prof. Cristiano Viappiani's group in Parma (Italy). Vegetative bacterial cells were grown in sterile Tryptic Soy Broth (*E. coli* and *S. aureus*) or in Brain Heart Infusion broth (*B. subtilis*) at 37°C until an optical density at 600 nm corresponding to 0.4 (*E. coli* and *S. aureus*) or 0.5 (*B. subtilis*). After the incubation period, the cell suspension was washed three times in sterile PBS by means of

centrifugation and resuspension and then incubated in the dark with the photosensitising agent for 30 min at room temperature (*E. coli* and *S. aureus*) or for 90 min at 37°C (*B. subtilis*). Spectroscopic measurements were carried out immediately after the incubation period. Photoinactivation experiments were performed after the incubation period, placing 300 µL of the suspensions in 96-well plates. Irradiation was carried out with Sorisa Photocare LED source (Barcelona, Spain) of a wavelength range of 521 ± 19 nm. The plates were illuminated from the top by use green light for 15 or 30 min (18 and 37 $J \cdot cm^{-2}$, respectively) and serially diluted until 10^{-6} times the original concentration. The diluted samples were seeded on Tryptic Soy (or Brain Heart Infusion) agar and the colony forming units (CFUs) were counted after ~24 h incubation in the dark at 37°C in order to calculate the survival fraction. Experiments were carried out in duplicate.

3.3. Results and discussion

3.3.1. Complex characterisation and photophysical properties

Photophysical properties of Hyp in solution. While Hyp is largely insoluble in water, it dissolves readily in ethanol or other polar organic solvents, where it displays a bright red colour due to its absorption properties and an intense orange-red fluorescence emission (Figure 3.1, B).

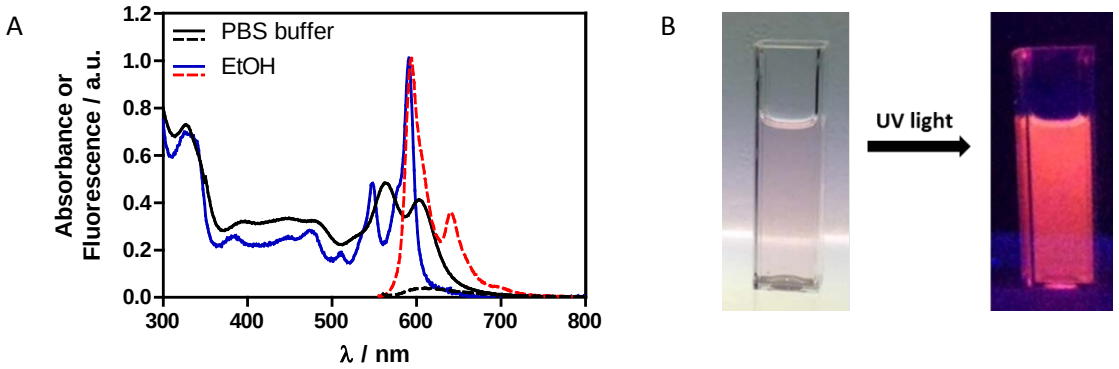

Figure 3.1. A) Absorption spectra of a 2 µM solutions of Hyp in PBS buffer (black solid) and in ethanol (blue solid). It is also shown the fluorescence emission spectra for Hyp in ethanol (red dashed) and in PBS buffer (black dashed). B) Cuvette containing the natural extract from the *Hypericum* plant in ethanol. Under UV light, a bright orange fluorescence is observed.

The absorption spectrum of Hyp in ethanol is characterised by several structured bands with the peak of the lowest-energy electronic transition located at 591 nm (Figure 3.1, A). The fluorescence emission spectrum is also quite structured (two distinct bands are found at 594 nm and 641 nm, and a shoulder at ~695 nm).[7] In DMSO, Hyp also show this well-structured spectrum typically from the monomeric Hyp, but with absorbance and fluorescence maxima (at 599 and 604 nm, respectively) slightly shifted to the red because it is a polar aprotic solvent. In most cases, DMSO was used as a solvent for the Hyp stock because it is fully miscible with water, has

a boiling point high enough to avoid fast evaporations and is relatively well-tolerated by some proteins and biosystems. On the other hand, when Hyp is dissolved in water tends to form aggregates. This result in a broadening of the bands in the absorption spectrum, and in a much weaker, broad and structureless fluorescence emission with a maximum at 608 nm (Figure 3.1). The sensitivity to the microenvironment has been exploited to image the subcellular location of hypericin in cells.[8]

Modelling studies. Mainly driven by hydrophobic interactions, Hyp spontaneously binds to hydrophobic supramolecular structures. Therefore, the presence of hydrophobic binding sites within a protein structure may, therefore, lead to stable Hyp–protein complexes. Such is the case of apoMb, i.e. the protein portion of Mb, that hosts a large hydrophobic cavity which was shown to bind a variety of cofactors, including, e.g., biliverdin,[9] pyranine,[10] and nile red.[11] The theoretical feasibility of fitting Hyp into the apoMb hydrophobic cavity was assessed through computational macromolecular docking software. As shown in Figure 3.2 binding of Hyp to apoMb is expected to occur with a free energy of binding of -9.89 kcal·mol^{-1}. The location and orientation of Hyp in the cavity is very similar to that of haem (Figure 3.2 A), which is not too surprising given the similarities between the size, molecular symmetry, and hydrophobic character of these two ligands.

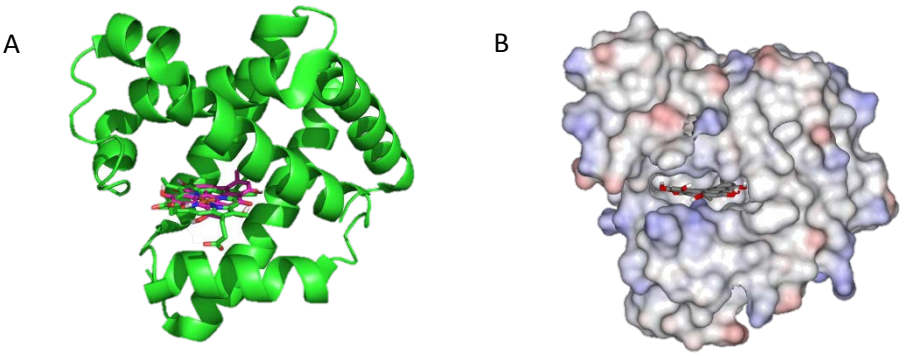

Figure 3.2. A) Crystal structure of horse Mb (PDB 1WLA, the protein is shown as a green cartoon, the haem in green capped sticks) showing also the representative docking of Hyp (magenta capped sticks) into the apoMb structure, obtained using the Lamarckian algorithm. B) Interaction of Hyp with the apoMb cavity showing the solvent-accessible surface of the protein.

Complex formation. As predicted, binding of Hyp to apoMb could be easily realised taking advantage of the well-defined hydrophobic pocket which is present inside the protein. The changes in absorption and fluorescence spectra were indicative of polarity environment changes of Hyp when apoMb was introduced in PBS buffer. Indeed, Hyp absorbance in PBS buffer (black) was recovered forming a more structured and better-defined spectrum (red, Figure 3.3 left panel). Thus indicates that Hyp is protected from aqueous solvent. However, through fluorescence emission more information could be extracted. Fluorescence emission was

exploited to monitor the binding process since the Hyp emission in presence of apoMb increased and the spectrum became more structured, closely resembling that observed in ethanol or DMSO, although a slight red shifted could be clearly noticed (Figure 3.3 right panel). These facts indicate that Hyp is located in a substantially less-polar environment than water, in all probability as a result of binding to the protein. The natural host for the dye appears to be the haem cavity in the holoprotein, which has been reported to be less polar than water.[12,13] Importantly, when fluorescence was recorded in the presence of 50 mM Mb rather than apoMb, the emission intensity was similar to that in PBS buffer. This is strong evidence that, when the binding site is unavailable because already occupied by haem, the binding of Hyp is strongly inhibited.

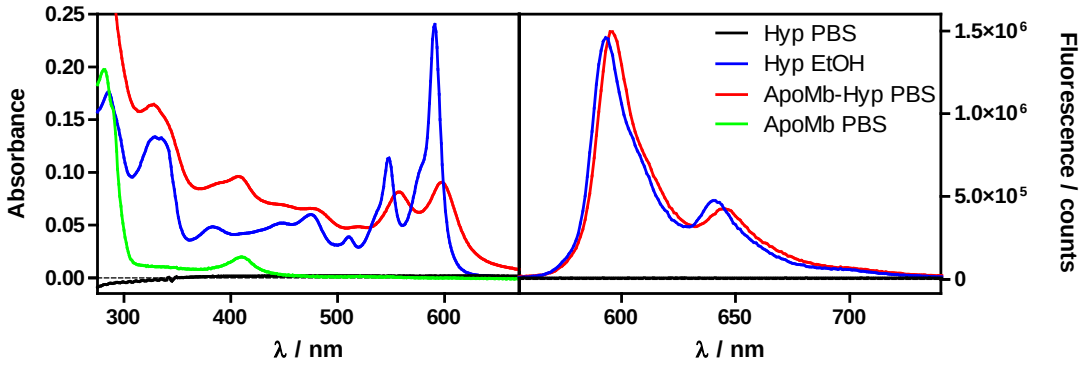

Figure 3.3. Absorbance (left panel) and fluorescence emission (right panel) spectra of Hyp 0.6 µM in PBS (black), ethanol (blue), in PBS in the presence of 30 µM apoMb (red) and the apoMb alone (green).

Figure 3.4 shows the fluorescence emission decay measured by collecting the emission at 600 nm, under pulsed 375 nm excitation. While fluorescence emission decays with a monoexponential relaxation in ethanol (Table 3.1), the decay in PBS is a complex multiexponential process with a dominant, short-lived component, indicative of strong quenching of the excited state, because of the aggregates' presence. When the fluorescence emission decay was measured in the presence of apoMb the contribution of the longer-lived decay components increased and accounted for most of the decay kinetics. This finding is again consistent with Hyp being shielded from the aqueous solvent. The observation of two relatively-long lifetimes in the decay (Table 3.1) likely reflects the coexistence of different Hyp conformers inside the cavity.

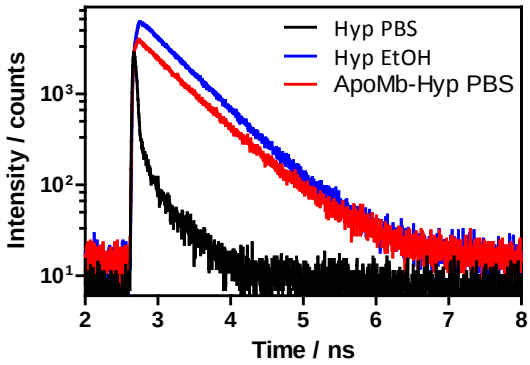

Figure 3.4. Fluorescence emission decay of Hyp 0.6 µM in PBS (black), ethanol (blue) and in PBS in the presence of 30 µM apoMb (red). Excitation at 375 nm, detection at 600 nm.

Table 3.1. Fluorescence emission lifetimes with their amplitudes and fluorescence quantum yield (Φ_F) of Hyp in different environments.

Solvent	τ_1 / ns	τ_2 / ns	τ_3 / ns	Φ_F
EtOH	5.5 ± 0.1 (100%)			0.27 ± 0.02
DMSO	5.5 ± 0.1 (100%)			0.35 ± 0.02
PBS	0.01 ± 0.01 (94%)	2.3 ± 0.1 (4%)	6.5 ± 0.1 (2%)	≈ 0.001
PBS + apoMb	0.01 ± 0.01 (7%)	4.0 ± 0.1 (25%)	6.4 ± 0.1 (68%)	0.14 ± 0.02

Further evidences were provided by steady-state fluorescence anisotropy, measured in Parma by the group of Prof. Cristiano Viappiani (Figure 3.5). While Hyp dissolved in DMSO shows a zero anisotropy, in the presence of apoMb the anisotropy is non-zero, meaning that Hyp rotation is much slower and the molecules hold a preferential orientation within its lifetime of fluorescence emission.

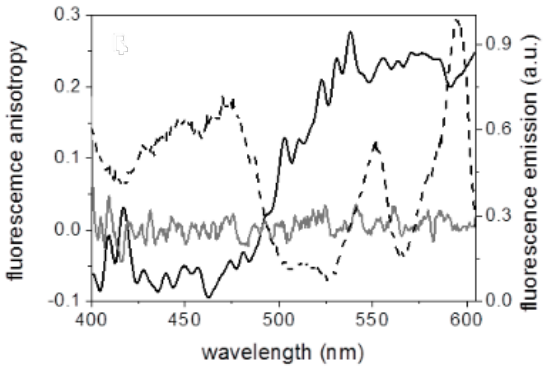

Figure 3.5. Fluorescence excitation anisotropy spectra of apoMb-Hyp in PBS solution (black solid, λ_{em} = 620 nm) and of Hyp in DMSO (grey solid, λ_{em} = 620 nm). The fluorescence excitation spectrum of apoMb-Hyp in PBS solution (black dotted, λ_{em} = 620 nm) is reported for reference. The ratio apoMb: Hyp is 5: 1.

ApoMb-Hyp binding isotherm. The change in the fluorescence emission properties of Hyp upon binding to apoMb was exploited to determine the affinity of the dye for the protein. Since the emission arising from unbound aggregated Hyp is negligibly weak, the fluorescence is emitted only by the bound species. The increase in the emission intensity (Figure 3.6 A) was found to correlate with the increase in total protein concentration (Figure 3.6 B). The equilibrium binding

constant K_a was determined by fitting the total fluorescence emission F to the experimental data using Eq. 3.5.

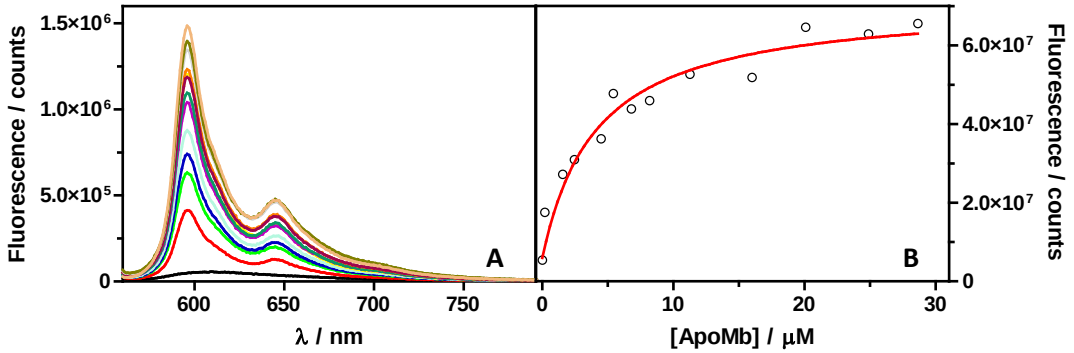

Figure 3.6. (A) Fluorescence emission spectra excited at 550 nm at increasing apoMb concentrations. (B) Integrated fluorescence emission as a function of total protein concentration. The red solid line is the result of a fit to the observed emission using a model derived from the binding equilibrium (Eq 3.5).

After the fitting, the value $K_a = (2.4 \pm 0.5) \times 10^5\ M^{-1}$ was estimated, which results in a dissociation constant $K_d = 4.2 \pm 0.8\ \mu M$. The value is consistent with the assumption that the fraction of Hyp bound to apoMb is low at low apoMb concentrations.

A functional nanostructure: photophysical properties are preserved. The fluorescence experiments suggest that the photoproperties of Hyp are preserved in the apoMb–Hyp complex. Of particular interest is the question whether Hyp retains the ability to photosensitise the production of $^1O_2$. The measured signal shows the typical rise and decay trend that is well fitted with a bi-exponential model characterised by the two lifetimes τ_T and τ_Δ.

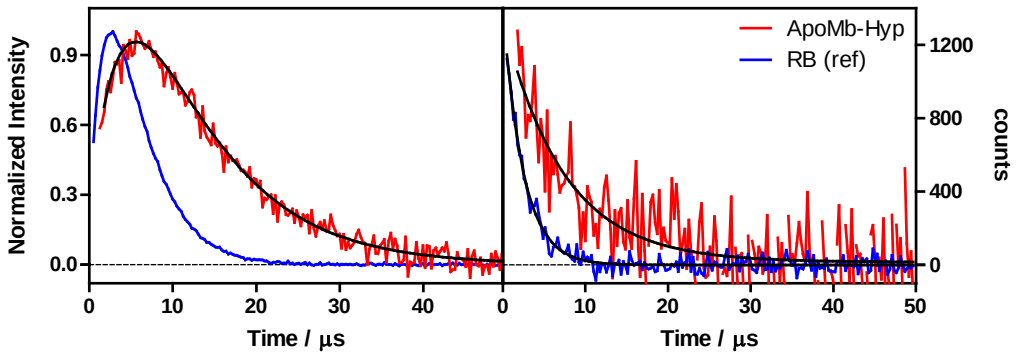

Figure 3.7. Normalised near-infrared phosphorescence emission at 1275 nm (left panel) and 1110 nm (right panel) for air equilibrated aqueous solutions of RB (blue) and the apoMb–Hyp complex (red). Excitation 532 nm, both signals were in PBS buffer pH 7.4.

Figure 3.7 A compares the time course of the near-infrared emission by solutions of apoMb–Hyp and the reference compound RB in PBS. The kinetic data obtained by fitting Eq. 2.3 are collected in Table 3.2. In order to assign the two lifetimes to τ_T and τ_Δ, an additional experiment was carried out observing the luminescence at 1110 nm, where only the triplet PS emits (Fig 3.7 B). In this case, we observed monoexponential decays corresponding to τ_T.

Table 3.2. Time constants of $^1O_2$ phosphorescence (1275 nm) and ^{3}Hyp* phosphorescence (1110 nm) of Hyp in different environments. The lifetimes of RB and TMPyP are given for comparison as references.

Sample	τ_T / ns	τ_Δ / ns	Φ_Δ
Hyp DMSO	1.6 ± 0.1	5.5 ± 0.1	0.28 ± 0.05 0.33[14]
apoMb-Hyp air-saturated	11.1 ± 0.4	2.4 ± 0.4	0.14 ± 0.03
apoMb-Hyp O_2-saturated	5.0 ± 0.4	2.6 ± 0.4	0.19 ± 0.03
RB / TMPyP	2.3 ± 0.1	3.6 ± 0.1	0.76 ± 0.01

Additionally, the solutions were bubbled with oxygen, a triplet quencher, and found that the longest lifetime (11.1 μs) decreased to 5.0 μs, confirming the assignment to the Hyp triplet state. The Φ_Δ of apoMb–Hyp was obtained by comparing the S_0 values for apoMb–Hyp and the references RB and TMPyP, which produce $^1O_2$ with Φ_Δ = 0.76.[15] A respectable value of 0.14 was observed for apoMb–Hyp in air-saturated solutions, which increased to 0.19 upon oxygen bubbling. Taken together, the results indicate that the apoMb scaffold shields Hyp from oxygen to some extent, although not enough to preclude the formation of $^1O_2$. This observation is relevant because, since $^1O_2$ is produced inside the protein, it could be quenched by the protein's aminoacids on its journey to the external medium. This was assessed by Lepeshkevich et al.[16] in a very elegant piece of work, in which the haem in myoglobin was replaced by Zn-protoporphyrin IX (ZnPP). They found that, on average, six out of ten $^1O_2$ molecules succeeded in escaping from the protein matrix into the external medium. The observation that τ_Δ corresponds to the lifetime of $^1O_2$ in water indicates that the majority of $^1O_2$ is indeed capable of escaping into the external aqueous phase.

3.3.2. Bacteria photodynamic inactivation.

To assess the corresponding effects of the apoMb–Hyp complex, photodynamic inactivation tests were carried out on different bacteria, two gram-positive bacteria (*S. aureus* and *B. subtilis*) and one gram-negative (*E. coli*). The results were compared with those for free Hyp under the same experimental conditions and in all the cases, the necessary controls of cells and just the apoMb were always included. An excess of apoMb was added in order to ensure that the bactericidal effect was due to bound rather than free Hyp in solution.

In the case of the inactivation of *S. aureus*, two different proteins: Hyp ratios were tested but maintaining the same Hyp concentration (10 μM). Figure 3.8 shows that higher inactivation is achieved with 1:2 rather than with 1:5 Hyp: protein ratio, when the concentration of the free apoprotein is lower. This result suggests that the excess of the protein alone detracts from the photodynamic activity of the complex. Therefore, the complex 1:2 is capable to reduce the CFUs by 5 logs with the lower green light dose used (18 J·cm^{-2}). Interestingly, although survival

fractions are higher after treatment with the complex than with free Hyp at equal concentrations, dark toxicity is higher for the latter, which is a strong positive point for the use of this protein complex.

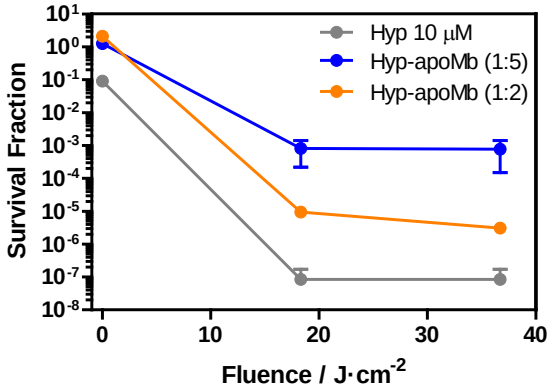

Figure 3.8. Fluence and Hyp-apoMb ratio effects on *S. aureus* photoinactivation. The Hyp concentration in all cases was 10 μM.

In another experiment, after the incubation of the complex with cells, the sample was analysed in order to know whether the Hyp had been taken up by cells and hence it had been released from the protein. For this purpose, the fluorescence spectra before and after the incubation with cells were recorded. Moreover, the samples after the incubation were centrifuged at 1550xg 15 min, extracting the supernatant and resuspended the pellet in the same volume pre-centrifuge, measuring also the spectra of both portions.

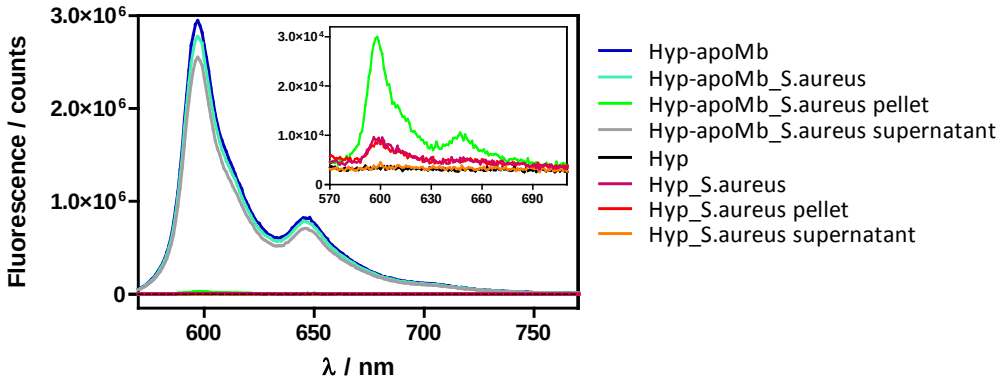

Figure 3.9. Fluorescence emission of free Hyp (8 μM) and Hyp-apoMb complex ([Hyp]= 8 μM and [apoMb]= 40 μM) in PBS buffer before and after the incubation with *S. aureus*. In all the samples the Hyp concentration is kept equal. The samples after the incubation with cells were centrifuged in order to separate the cells fraction, remaining at the bottom (pellet) from the rest of the sample (supernatant). The pellet was suspended in the same PBS amount that had before the centrifugation.

Figure 3.9 shows that the initial fluorescence of the complex Hyp-apoMb previously (dark blue) and after (light blue) the incubation with *S. aureus* is only recovered in the supernatant after the centrifugation (light green). This is an indication that the greater amount of Hyp remains inside the protein cavity, hindering its escape to the cell wall. In the pellet, where the cells were collected, there is a minimum signal of Hyp fluorescence (dark green). Different options can

explain this fact: 1) the low portion of free Hyp present in the sample, 2) the low amount of Hyp that can escape from the protein matrix and be internalised in the cell wall or 3) due to a human error in the separation of the supernatant from the pellet. A completely different scenario is shown for free Hyp, since no fluorescence is seen until the PS molecules reach the cell wall, where a little fluorescence compared with the complex is recorded (see red and magenta signals). This could be indicative of there is only a little monomeric fraction inside or in contact with the cell wall and the greater part of Hyp is found aggregate. For this reason, just in the pellet (red) is registered a low fluorescence signal, whereas in the supernatant (orange) there is no fluorescence.

Figure 3.10 shows the analogous experiment but measuring $^1O_2$ transients. After 30 min of apoMb-Hyp incubation with *S. aureus*, $^1O_2$ was measured in the suspension (light green), then the suspension was centrifuged at 1550g for 15 min, the supernatant was discarded, the pellet was resuspended in PBS back to the original volume, and $^1O_2$ was measured again (dark green).

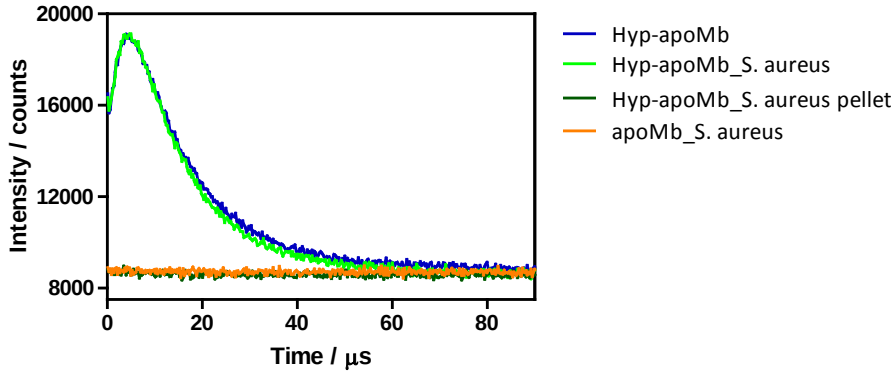

Figure 3.10. Time-resolved phosphorescence decay at 1275 nm for Hyp-apoMb complex ([Hyp]= 8 µM and [apoMb]= 40 µM) in PBS buffer before and after the incubation with *S. aureus*. In all the samples the Hyp concentration is kept equal. The samples after the incubation with cells were centrifuged in order to separate the cells fraction, remaining at the bottom (pellet). The pellet was suspended in the same PBS amount that had before the centrifugation.

The $^1O_2$ phosphorescence is lost in the pellet fraction as did the fluorescence in Figure 3.9, indicating that Hyp was not transferred from the protein to the bacteria. The value of τ_T, indicative of the environment of Hyp, decreased by only 5% reduction as a result of Hyp being slightly more shielded from oxygen when *S. aureus* was present in the sample.

These last two experiments proved that the decrease in the survival fraction showed in Figure 3.8 is because of the Hyp-apoMb that would be located in a close vicinity of the cell membrane, and not due to the Hyp being transferred from the complex to the bacteria.

On the other hand, the Hyp-apoMb complex was also tested against the other two bacteria strains: *E. coli* (gram-negative) and *B. subtilis* (gram-positive) (Figure 3.11). In this case, no similar outcomes were obtained. Neither free Hyp nor the complex were capable of decreasing the

survival fraction in *E. coli* bacteria. The differences in the cell wall morphologies between gram-positive and gram-negative, and the much less permeable cell wall of these last, seems to be the most likely explanation for this negative result.

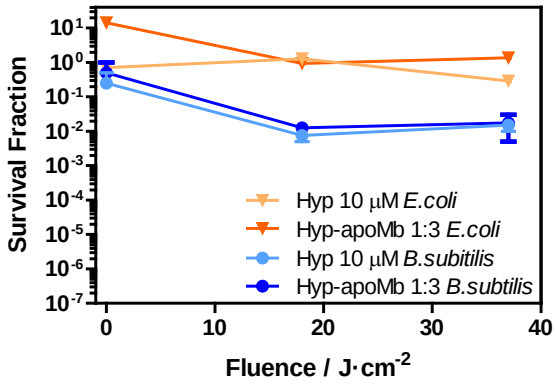

Figure 3.11. Photoinactivation of Hyp and Hyp-apoMb complex with two different light fluences against *E. coli* (triangles) and *B. subtilis* (circles). For both strains, the Hyp concentration is kept equal and the Hyp: apoMb ratio is 1: 3.

The effect on *B. subtilis* was the same for free Hyp as for the complex, inducing two orders of magnitude decrease in the survival fraction. There was a clear difference in the response to the PDT treatment between both gram-positive species (*B. subtilis* and *S. aureus*). One plausible explanation is endospores formation by *B. subtilis* under a stress condition like light treatment. These endospores can mature during the sporulation process and remain dormant for extended periods of time with a remarkable resistance to environmental damages, such as heat, radiation, toxic chemicals or pH extremes. Under favourable environmental conditions, the endospore can restarts the growth during the germination process, which ends in the emergence of a new vegetative cell.

Even though at the beginning of the experiments no endospores could be detected by staining, spores could be found after light exposure. Most probably, while the vegetative cells were killed almost completely during the treatments, formation of endospores lead to the emergence of new vegetative cells in the petri dish, that were counted naturally as live cells, obtaining a high survival fraction.

3.3.3. Hyp-apoMb as a fluorescent probe for super-resolution Stimulated Emission Depletion

The results in this section have been extracted from the PhD thesis of Pietro Delcanale[17] and are included here to facilitate a more complete understanding of the above results. Our colleagues in the group of Prof. Cristiano Viappiani in Italy have studied the suitability of Hyp to perform STED microscopy and tracked the binding sites of Hyp on bacteria incubated with the complex Hyp-apoMb. Hyp is a good candidate for STED microscopy due to its intense fluorescence

emission ($\Phi_F \approx 0.35$)[8,18] and the adequate long-lived excited singlet state (S_1 ~5 ns).[19] To the best of our knowledge this approach has not been reported yet for any PS, but there are some works that reported the observation of stimulated emission of Hyp induced by red light.[19]

First, it was proved that free Hyp and included in the complex undergoes stimulated emission and that this spectral region is not superimposed with the absorption bands of the excited state.

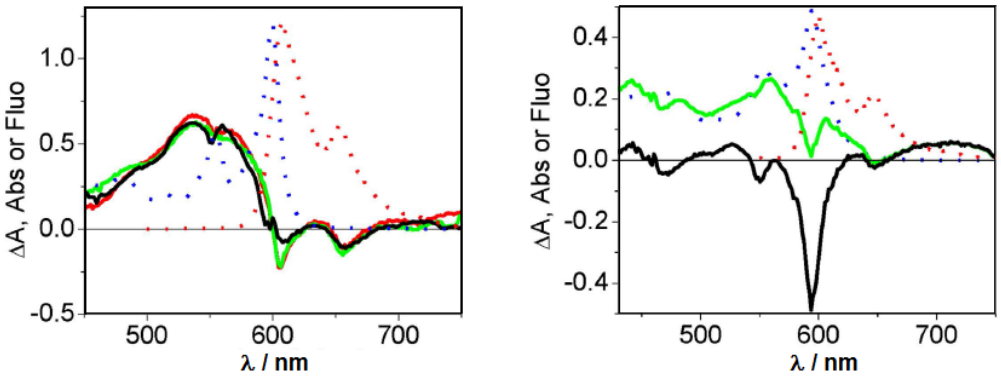

Figure 3.12. Left panel shows the corrected transient absorption spectra (the ground state bleaching is removed) for Hyp in DMSO (120 μM) at 3 ps (black), 10 ps (red), and 100 ps (green). Right panel shows the transient absorption spectra for Hyp-apoMb (120 μM Hyp, 530 μM apoMb) in PBS. The black line is the raw transient absorption spectra, which is corrected subtracting the steady state absorption spectrum (blue dotted line) to retrieve the corrected transient absorption (green) with 1000 ps delay, removing the ground state bleaching. In both graphs, the dotted lines correspond to steady state absorption (blue) and fluorescence emission (red).

In the case of Hyp in DMSO, Figure 3.12 on the left panel shows an extended excited state absorption in the 500-600 nm region, peaked at roughly 550 nm. The negative bands (increased transmitted light) observed at 606 nm and 656 nm were attributed to stimulated emission induced by the probe pulse, which nicely corresponds to those seen in the steady state fluorescence (dotted red line). The different ratio of intensity of these two bands in the steady state and corrected transient absorption spectra is likely due to a self-absorption at ~600 nm occurring in the transient spectra, due to the high concentration of Hyp. Due to this self-absorption at ~600 nm, the wavelength chosen to monitor the stimulated emission was at 647 nm, in the second band. Figure 3.12 on the right panel shows similar results for the complex Hyp-apoMb but with a lower signal-to-noise ratio due to the lower Hyp concentration. Stimulated emission features can nevertheless be recognised at 594 nm and 650 nm, while excited state absorption bands appear broader and weaker in this case, extending to the NIR.

For both samples, the emission of fluorescence is significantly reduced (more than 50% of the initial value) for the higher powers of the STED beam, that is enough to overcome the diffraction-limited resolution. However, the saturation power is lower for Hyp in DMSO than for apoMb-Hyp in water (Figure 3.13).

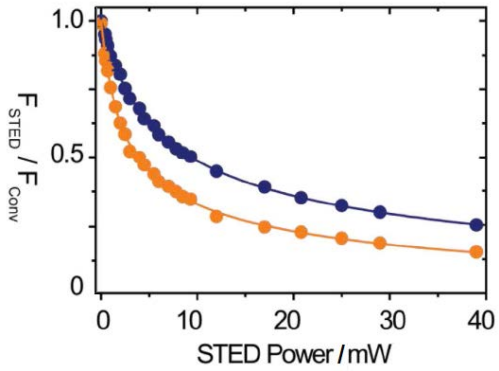

Figure 3.13. Fluorescence depletion curves for Hyp in DMSO (10 µM, orange circles) and apoMb-Hyp in PBS (10 µM Hyp, 30 µM apoMb, blue circles), collected under excitation at 570 nm and detection at 605-670 nm. The STED beam was at 715 nm. Solid lines are the best fit to depletion functions.

The presence of excited state absorption of Hyp-apoMb in the spectral region of the STED beam (Figure 3.12 right panel) is possibly at the origin of the observed saturation parameters (higher saturation power and larger non-saturable fraction) for Hyp-apoMb.

Figure 3.14 shows a comparison of the fluorescence resolution obtained of Hyp-apoMb in *B. subtilis* with a confocal (A) and STED (B) microscopy. There is a clear improvement in the resolution when the image is taken with the STED technique, which allows with a better precision the localisation of the PS. The analysis of the fluorescence emission profile along the cross-section of a cell (Figure 3.14 C) shows the improved resolution by STED microscopy (red line) compared with the confocal microscopy (blue line), which almost maintain the fluorescence intensity along the cross-section. Moreover, the profile for the STED revealed the accumulation of Hyp on the outer bacterial component whose width is on the order of 90 nm, corresponding to the width of the bacterial wall composed of an outer peptidoglycan layer and an inner cell membrane.

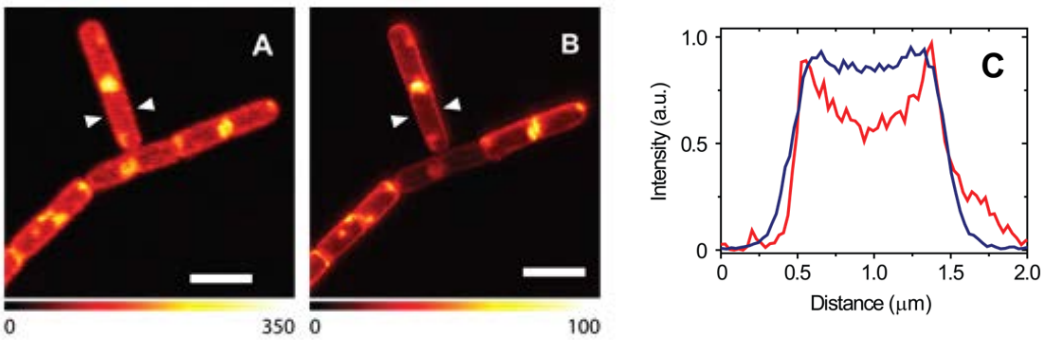

Figure 3.14. Comparison between *B. subtilis* images collected with confocal microscopy (A) and with STED nanoscopy (STED power 30 mW, pixel dwell time 0.1 ms) (B). (C) The blue and the red intensity profiles were measured along the segment connecting the arrows in (A,B) respectively. Scale bars are 2.5 µm.

This fluorescence intensity accumulated above all in the outer membrane seems not to be in disagreement with the fact that Hyp does not release from the protein. Therefore, the fluorescence might be due to the complex, which is placed in the close vicinity or more likely

touching the cell wall membrane. For all these experiments, the amount of protein was in a great excess compared with the Hyp quantity to be sure that the fluorescence comes from the complex and not from free Hyp. It may be concluded after the experiments showed in Figure 3.9 and 3.10 that the fluorescence comes from the Hyp inside the apoMb and not from the Hyp released from the protein.

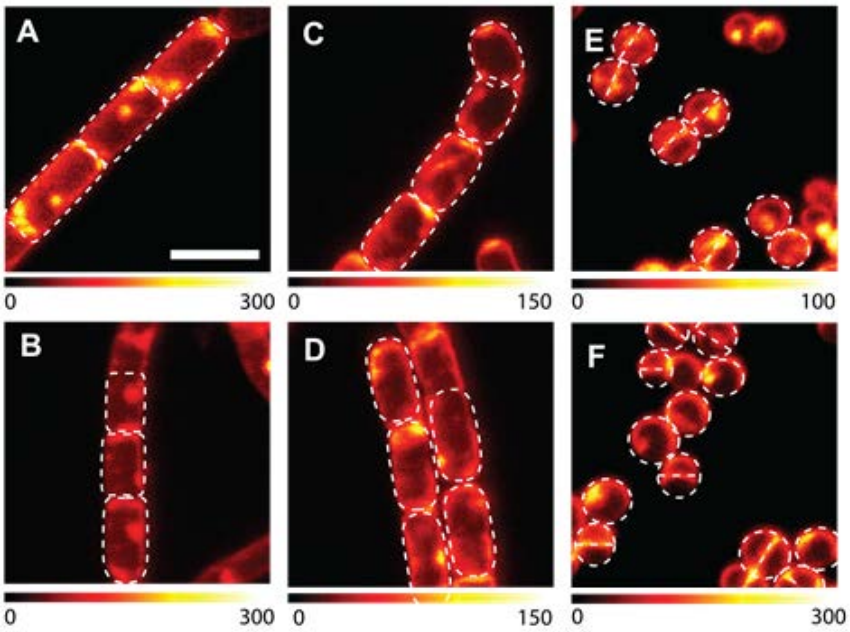

Figure. 3.15. Selected STED images of *B. subtilis* (A,B), *E. coli* (C,D) and *S. aureus* cells (E,F) incubated with Hyp-apoMb (10 µM Hyp, 30 µM apoMb) collected under excitation at 566 nm and detection at 605-670 nm. The STED beam was at 715 nm, power 30 mW and dwell time 0.1 ms (A–D) and 0.05 ms (E,F). White dashed lines are intended as a visual aid to guide the eye along the bacterial shape. Scale bar: 2 µm.

A similar distribution of Hyp on the bacterial cell wall is observed in Figure 3.15 after the incubation of Hyp-apoMb with *S. aureus*, *B. subtilis* and the gram-negative bacteria *E. coli*.

Despite the improving resolution of the images with STED, it is still not possible to assess whether Hyp-apoMb is localised on the external peptidoglycan layer or on the inner plasma membrane of bacteria. However, it is possible to distinguish specific accumulation points of Hyp as judged from the more intense fluorescence observed at the poles of the bacteria and at the central body of the cell. This suggests specific interactions with yet to be identified bacterial components, possibly located inside areas of MreB-dependent wall growth in the case of rod shape bacteria (*B. subtilis* and *E. coli*), of FtsZ dependent wall growth for *S. aureus* or in cytoskeleton components.[20,21] The improved images interestingly allow appreciating details of the division bacteria process whose shape is consistent with the established division mechanisms. *B. subtilis* divides mainly by septation without constriction, resulting in its typically squared off poles (Figures 3.14 and 3.15 A,B).[20] On the contrary, dividing *E. coli* images (Figure 3.15 C,D) show round poles because the gram-negative bacterium divides with a combination

of septum formation and constriction of inner and outer membranes.[22] In the case of *S. aureus*, the septation separates two hemispheres during the cell division.

Finally, it is important to point out that images collected on bacteria incubated with free Hyp in DMSO provide fluorescence distributions which are indistinguishable from those collected and shown with Hyp-apoMb.

3.4. Conclusions

We have investigated the photodynamic activity of the system formed by apoMb (i.e., the myoglobin without the haem group) and Hyp delivered to three different bacterial strains. Since Hyp is largely insoluble and forms aggregates in water, its absorption and above all the fluorescence spectra changes significantly depending on the polarity of its microenvironment. Therefore, these spectral features could be analysed in order to follow the complex formation. Upon addition of apoMb, Hyp in PBS recovered the absorption, increasing the intensity but still with broader bands comparing with those in EtOH. However, when fluorescence emission was exploited, the spectrum became more structured closely resembling that observed in EtOH or DMSO, although a slight red shifted because of the less-polar environment. Together with the fluorescence excitation anisotropy and the binding isotherm, the formation of the Hyp-apoMb complex was proved. All these measurements are in agreement with the computational results, which revealed a binding energy of -9.89 kcal·mol^{-1} of the Hyp to the hydrophobic cavity where normally the haem group is placed. The location and orientation of Hyp in the cavity is very similar to that of haem, leading to a 1:1 complex.

Time-resolved fluorescence measurements indicated again the shielding of Hyp from the aqueous solvent inside the protein matrix and suggests that the photoproperties of Hyp are preserved in the complex. The contribution of short-lived components seen for Hyp in PBS dramatically drops and increase the weight of two longer-lived components likely reflects the coexistence of different Hyp conformers inside the cavity. A decent fluorescence quantum yield of 0.14 ± 0.02 was obtained for the complex in PBS compared with a 0.27 ± 0.02 of Hyp in EtOH.

Of particular interest is the question whether Hyp retains the ability to photosensitise the production of $^1O_2$. The quantum yield measured show a respectable value of 0.14 for apoMb–Hyp in air-saturated solutions, which increased to 0.19 upon oxygen bubbling, comparing with the 0.28 ± 0.05 obtained for Hyp in DMSO. As expected, the quantum yield decreases slightly due to the fact that apoMb scaffold shields Hyp from oxygen to some extent, although not enough to preclude the formation of $^1O_2$.

The bacterial photoinactivation has different outcomes depending on the species used. In the case of *S. aureus*, the complex 1:2 is capable of reducing the CFUs by 5 logs with the lower green light fluence used (18 J·cm^{-2}). Even more interesting is that the complex at equal concentrations of free Hyp showed less dark toxicity. The complex induced a 2 logs decrease in the survival fraction in *B. subtilis*. This clear difference in the response to the PDT treatment between both gram-positive species (*B. subtilis* and *S. aureus*) could be explained by endospores formation upon light treatment. On the other hand, neither the free Hyp nor the complex was capable to decrease the survival fraction in *E. coli* bacteria. The differences in the cell wall morphologies between gram-positive and gram-negative may account for this result.

An experiment was carried out in the presence of *S. aureus*, in which the fluorescence spectrum and the $^1O_2$ transient was measured before and after separating the cells by centrifugation. The fluorescence and $^1O_2$ signals were recovered only in the supernatant fraction after centrifugation. This is an indication that the greater amount of Hyp remained inside the protein cavity and was not transferred to the cell wall.

Finally, STED microscopy provided information about the binding sites of Hyp on bacteria incubated with the Hyp-apoMb complex. Thus, it was found that the complex is accumulated mainly at the cell wall, although the spatial resolution achieved in the present work does not yet allow the identification of the specific wall layer the photosensitizing construct is confined into, nor the identification of the molecular species it is bound to.

In conclusion, the incorporation of Hyp in the apoMb cavity driven by hydrophobic interactions have many advantages: 1) the protein precludes Hyp aggregation and therefore the concomitant negative impact of this effect; 2) the complex still preserves the fluorescence and photosensitising properties of Hyp; 3) this ability of $^1O_2$ production lead to the effective photoinactivation of *S. aureus* with a light dose of 18 J·cm^{-2}; 4) Hyp placed in the protein reduces the dark toxicity compared with free Hyp in *S. aureus* inactivation; and 5) the complex constitutes a biocompatible drug delivery system with theranostics properties for instance.

3.5. References

(1) Planas, O.; Boix-Garriga, E.; Rodríguez-Amigo, B.; Torra, J.; Bresolí-Obach, R.; Flors, C.; Viappiani, C.; Agut, M.; Ruiz-González, R.; Nonell, S. Chapter 9: Newest Approaches to Singlet Oxygen Photosensitisation in Biological Media. In *Photochemistry*; Fasani, E.; Albini, A., Special Periodical Reports; Royal Society of Chemistry, **2015**, 42, 233–278.

(2) Yan, F.; Zhang, Y.; Kim, K. S.; Yuan, H.-K.; Vo-Dinh, T. Cellular Uptake and Photodynamic Activity of Protein Nanocages Containing Methylene Blue Photosensitizing Drug. *Photochem. Photobiol.* **2010**, *86*, 662–666.

(3) Hawkins, M. J.; Soon-Shiong, P.; Desai, N. Protein Nanoparticles as Drug Carriers in Clinical Medicine. *Adv. Drug Deliv. Rev.* **2008**, *60*, 876–885.

(4) Elzoghby, A. O.; Samy, W. M.; Elgindy, N. A. Protein-Based Nanocarriers as Promising Drug and Gene Delivery Systems. *J. Control. Release,* **2012**, *161*, 38–49.

(5) Langer, K.; Balthasar, S.; Vogel, V.; Dinauer, N.; von Briesen, H.; Schubert, D. Optimization of the Preparation Process for Human Serum Albumin (HSA) Nanoparticles. *Int. J. Pharm.* **2003**, *257*, 169–180.

(6) Chen, K.; Preuß, A.; Hackbarth, S.; Wacker, M.; Langer, K.; Röder, B. Novel Photosensitizer-Protein Nanoparticles for Photodynamic Therapy: Photophysical Characterization and in Vitro Investigations. *J. Photochem. Photobiol. B Biol.* **2009**, *96*, 66–74.

(7) Kiesslich, T.; Krammer, B.; Plaetzer, K. Cellular Mechanisms and Prospective Applications of Hypericin in Photodynamic Therapy. *Curr. Med. Chem.* **2006**, *13*, 2189–2204.

(8) López-Chicón, P.; Paz-Cristobal, M. P.; Rezusta, A.; Aspiroz, C.; Royo-Cañas, M.; Andres-Ciriano, E.; Gilaberte, Y.; Agut, M.; Nonell, S. On the Mechanism of Candida Spp. Photoinactivation by Hypericin. *Photochem. Photobiol. Sci.* **2012**, *11*, 1099–1107.

(9) Wagner, U. G.; Müller, N.; Schmitzberger, W.; Falk, H.; Kratky, C. Structure Determination of the Biliverdin Apomyoglobin Complex: Crystal Structure Analysis of Two Crystal Forms at 1.4 and 1.5 A Resolution. *J. Mol. Biol.* **1995**, *247*, 326–337.

(10) Shimoni, E.; Tsfadia, Y.; Nachliel, E.; Gutman, M. Gaugement of the Inner Space of the Apomyoglobin's Heme Binding Site by a Single Free Diffusing Proton. I. Proton in the Cavity. *Biophys. J.* **1993**, *64*, 472–479.

(11) Polverini, E.; Cugini, G.; Annoni, F.; Abbruzzetti, S.; Viappiani, C.; Gensch, T. Molten Globule Formation in Apomyoglobin Monitored by the Fluorescent Probe Nile Red. *Biochemistry,* **2006**, *45*, 5111–5121.

(12) Sire, O.; Alpert, B.; Royer, C. A. Probing pH and Pressure Effects on the Apomyoglobin Heme Pocket with the 2'-(N,N-Dimethylamino)-6-Naphthoyl-4-Trans-Cyclohexanoic Acid Fluorophore. *Biophys. J.* **1996**, *70*, 2903–2914.

(13) Artukhov, V. Y.; Zharkova, O. M.; Morozova, J. P. Features of Absorption and Fluorescence Spectra of Prodan. *Spectrochim. Acta Part A Mol. Biomol. Spectrosc.* **2007**, *68*, 36–42.

(14) Losi, A. Fluorescence and Time-Resolved Photoacoustics of Hypericin Inserted in Liposomes: Dependence on Pigment Concentration and Bilayer Phase. *Photochem. Photobiol.* **1997**, *65*, 791–801.

(15) Wilkinson, F.; Helman, W. P.; Ross, A. B. Quantum Yields for the Photosensitized Formation of the Lowest Electronically Excited State of Molecular Oxygen in Solution. *J. Phys. Chem. Ref. Data,* **1993**, *22*, 113–262.

(16) Lepeshkevich, S. V.; Parkhats, M. V.; Stasheuski, A. S.; Britikov, V. V.; Jarnikova, E. S.; Usanov, S. A.; Dzhagarov, B. M. Photosensitized Singlet Oxygen Luminescence from the Protein Matrix of Zn-Substituted Myoglobin. *J. Phys. Chem. A*, **2014**, *118*, 1864–1878.

(17) Delcanale, P. Protein-Based Nanostructures as Carriers for Photo-Physically Active Molecules in Biosystems, Università degli Studi di Parma, **2017**.

(18) Durán, N.; Song, P. Hypericin and Its Photodynamic Action. *Photochem. Photobiol.* **1986**, *43*, 677–680.

(19) Gai, F.; Fehr, M. J.; Petrich, J. W. Role of Solvent in Excited-State Proton Transfer in Hypericin. *J. Phys. Chem.* **1994**, *98*, 8352–8358.

(20) Margolin, W. Sculpting the Bacterial Cell. *Curr Biol.* **2009**, *19*, R812–R822.

(21) Osborn, M. J.; Rothfield, L. Cell Shape Determination in Escherichia Coli. *Curr. Opin. Microbiol.* **2007**, *10*, 606–610.

(22) Gerding, M. A.; Ogata, Y.; Pecora, N. D.; Niki, H.; De Boer, P. A. J. The Trans-Envelope Tol–Pal Complex Is Part of the Cell Division Machinery and Required for Proper Outer-Membrane Invagination during Cell Constriction in E. Coli. *Mol Microbiol.* **2007**, *63*, 1008–1025.

CHAPTER 4

Hypericin@β-Lactoglobulin

With the aim of assessing the suitability of β-lactoglobulin as a nanocarrier, we have investigated the complex formed with the naturally occurring Hyp at the two hydrophobic cavities located at the interface of the protein dimer. This complex has special interest for antimicrobial applications in the dairy industry as an effective disinfectant for food manufacturing and handling materials. In this chapter, we have investigated the use of DMSO as a co-solvent in the photophysical properties and photo-inactivating action against gram-positive bacteria.

Part of the work described in this chapter was performed at the group of Dipartimento di Scienze Matematiche, Fisiche e Informatiche from the University of Parma (Italy), supervised by Prof. Cristiano Viappini.

4.1. Introduction

The use of PDT for antimicrobial purposes is being even more attractive since the emerging resistance to antibiotics due to their misuse and overuse. The drug-resistant bacteria (i.e., bacteria treated with antibiotics that changes or adapts generating resistance) likely can be transferred to the food chain.[1] This is one of the reasons why aPDT is gaining interest in medical applications for the treatment of localised infections,[2,3] and for decontamination and disinfection processes in the food industry.[4]

The intake of contaminated food with pathogenic microorganisms, or toxic compounds released by microorganisms resulted in what is known as foodborne illness, which is an infection or irritation mainly of the gastrointestinal (GI) tract. The disease-causing microorganisms are most often bacteria, but can also include fungi, viruses and protozoa.[5] Meat, poultry and dairy products are the main source of food borne pathogens particularly *Salmonella*, *Campylobacter*, *Listeria* (*Listeria monocytogenes*) and *Escherichia coli*.[6] Another well-known food-borne pathogen is methicillin-resistant *Staphylococcus aureus* (MRSA) that produces heat-stable enterotoxins during growth on a variety of foods and is an important regional cause of human infection.[7]

Therefore, herein it is presented a system formed by Hyp and a protein as a new alternative strategy for preventing and treating infectious animal diseases of bacterial origin. The antimicrobial photoactivity of Hyp against MRSA, both *in vitro* and *in vivo*, has been recently assessed.[8] Because the effectiveness of Hyp-mediated photodynamic action is heavily dependent on the specific localizing capability of the delivery methodology, proteins appear as particularly interesting delivery agents thanks to their high biocompatibility, bioavailability, and the possibility to select specific proteins suitable to the environment to be targeted. In the current study, we propose the use of βLG, which is the most abundant protein in the whey of cow milk, as a delivery vehicle for antimicrobial photodynamic application of Hyp.[9] βLG is homodimeric protein belonging to the lipocalin family.[10,11] Owing to their ability to bind small hydrophobic molecules, while simultaneously being recognised by cell surface receptors, lipocalins were suggested as potential systems for drug delivery.[10] Whereas some lipocalins possess high ligand specificity, others such as βLG, demonstrate a remarkable versatility in their ligand-binding patterns. Affinity for small molecules is generally intermediate, with dissociation constants (K_d) around 1 μM.

We studied the formation of the complex driven mainly by hydrophobic interactions, besides the binding constant, the spectroscopic and photophysical properties and its ability to

photosensitise $^1O_2$. Since βLG can be coated with DMSO we also evaluated whether a DMSO layer around the protein could provide a better environment for the bound Hyp and improves the photophysical properties. Moreover, the photo-inactivating action of the complex against gram-positive bacteria is also compared between both scenarios: when there is a percentage of DMSO and when there is not. Positive results would establish this system with aPDT applications for the dairy industry as a potential decontamination tool, avoiding the possibility of transferring food-borne pathogens to the food chain.

On the other hand, herein we present the study of the complex constituted between βLG and retinoic acid (RA). It is known that βLG monomer can accommodate several hydrophobic and linear molecules like fatty acids, retinoids, vitamin D, cholesterol or curcumin.[12] Many studies have been published about the binding of retinoids to βLG, but now there still are several contradictions about the binding site, leading one to presume that this would not be an easy task.[13,14] However, many tests are exposed as evidence for the formation of a complex, although the overall difficulty of the system and the poor understanding of the binding sites in the protein, engender the need of further studies.

Finally, we also show preliminary results for the double payload system formed by Hyp and RA in the protein, a novel βLG complex ideal for its use for the acne treatment due to its dual effect. Acne is one of the most common multifactorial chronic inflammatory diseases of the pilosebaceous follicles, which affects approximately 80% adolescents and young adults in 11–30 age group. The pathophysiology of acne involves androgen stimulation inducing sebaceous hyperplasia, altered follicular keratinisation, hormonal imbalance, immune hypersensitivity, and bacterial (*Propionibacterium acnes*) colonisation.[15,16] Hyp and RA separately have been successfully studied for this purpose, thus the complex with both agents suggest at least that will maintain their effects for combating acne. Hyp would be actively decreasing the colonisation of *P. acnes* through PDT, while the mechanism of RA has been widely described in the literature.[17] However, it is worth noting that retinoic acid is not only active for the treatment of acne, but also plays important roles in cell development and differentiation as well as cancer treatment since many types (e.g., lung, prostate, breast, ovarian, bladder, oral, and skin cancers) have been demonstrated to be suppressed.[18]

4.2. Experimental section

4.2.1. Materials

The photoactive molecules rose bengal (RB) and 5,10,15,20-tetrakis(1-methyl-4-pyridinium) porphine tetra(p-toluene-sulfonate) (TMPyP) used as references were purchased from Sigma-Aldrich. The PS Hyp was purchased from HWI Analytik GmbH. β-Lactoglobulin (isoform B) from bovine milk, retinoic acid (tretinoin) powder and Dulbecco's phosphate-buffered saline (PBS x1) were obtained from Sigma Aldrich. All other chemicals were commercially available reagents of at least analytical grade. Milli-Q water (Millipore Bedford, Massachusetts system, resistivity of 18 MΩ cm) was used.

Once the complex PS-protein is prepared it is stored in the fridge kept in the dark. The dialysis tubing cellulose membrane with a cut-off of 12 kDa was bought in Sigma Aldrich. For the microbiological cultures the Tryptic Soy Broth, the Brain Heart Infusion Broth (BHI broth) and the agar-agar were also acquired from Sigma Aldrich.

4.2.2. Binding isotherm

The calculations for the association K_a or dissociation K_d constant for the complex formation follows the same previous scheme of the apoMb complex. However, βLG dimerises and this needs to be taken into account in the chemical equilibrium for the fitting model.

$$\beta LG + \beta LG + Hyp \leftrightharpoons 2\,\beta LG + Hyp \leftrightharpoons Hyp - 2\beta LG$$

Since the dimerisation process is favoured in the conditions and concentrations used and the protein concentration is kept equal during the binding analysis, the model is simplified just for the second part of the equilibrium. The equilibrium binding constant or the association constant is defined as:

$$K_a = \frac{[Hyp - 2\beta LG]}{[2\beta LG]\,[Hyp]}$$

Assuming that unbound Hyp in the aqueous buffer is negligibly fluorescent, the observed fluorescence emission is proportional to the amount of complex Hyp-protein. Following the same mathematical development as that used for apoMb but with the difference that, in this case, the amount of protein is kept constant while the Hyp concentration changes. This allows a simplified analysis of the equilibrium relative to the protein since the dimerisation can be neglected. Then the emitted fluorescence corresponds to the next equation:

$$F^{Hyp,tot} = F^{Hyp,complex} \frac{Ka[2\beta LG]_{tot}[Hyp]_{Tot}}{(1 + K_a[2\beta LG]_{tot})}$$

4.2.3. Modelling studies

The group of Prof. F. Javier Luque at the University of Barcelona (Spain) performed all molecular modelling and dynamics studies. The protein model for the bovine βLG dimer was derived from the X-ray crystallographic structure (PDB entry 1BEB).[19]

Set up and modelling for the complex in aqueous buffer

The structure was refined by including the addition of hydrogen atoms using the xLEAP facility in AMBER12 and the parm99SB force field, removal of nonstandard residues (e.g., sulphate anion), and generation of the disulphide bonds Cys66-Cys160 and Cys106-Cys119. Because the N- and C-terminal segments are not observed in the X-ray structure, N-methylamine and acetyl capping groups were added to the C- and N-terminus, respectively. The binding of Hyp was explored by means of **docking calculations** carried out with GLIDE.[20,21] Default settings are used and the best poses are clustered according to the RMSD between its heavy atoms using a threshold of 2.0 Å and subsequently re-evaluated using the Glide-XP scoring function.

On the other hand, the binding mode derived from docking studies is further checked by means of **Molecular Dynamics** (MD) simulations. In this regard, the simulated system, (i.e., the dimeric protein and the ligand) was solvated on a truncated octahedron box of TIP3P water molecules and the appropriate number of Na^+ counterions was added to neutralise the total charge.[22] The Parm99SB force field was used for the protein,[23] while Hyp was parameterised using the general amber force field in conjunction with RESP (HF/6-31G(d)) charges, and Joung and Cheatham parameters to model the counterions,[24] as implemented in the Antechamber module of AmberTools15 software package.

The final system comprises of around 72000 atoms, including around 22000 water molecules. The geometry of the system is minimised in four steps. First, water molecules are refined through 4500 steepest descent algorithm followed by 10500 steps of conjugate gradient. Then, protein and ligand hydrogen atoms positions are optimised using 500 steps of steepest descent and 4500 of conjugate gradient. Next the ligand, water molecules and counterions are further optimised with 2000 steps of steepest descent and 6000 of conjugate gradient and, finally the whole system is optimised with 2500 steps of steepest descent and 4500 of conjugate gradient. At this point, 3 different replicas are generated by randomly assigning 3 different sets of velocities to the initial coordinates, all fitting a Maxwell distribution for a temperature of 50 K. For each one of the replicas, thermalisation is performed in the NVT ensemble during five 25 ps

steps, using a time step of 1 fs and increasing the temperature from 50 to 298 K. Concomitantly, the inhibitor and the residues in the binding site are restrained during thermalisation using a variable restraint force. Thus, a force constant of 5 kcal·mol^{-1}·Å^{-2} is used in the first stage of thermalisation, and is subsequently decreased by increments of 1 kcal·mol^{-1} Å^{-2} in the next stages. Prior to the production runs, a short MD simulation of 1 ns in the NPT ensemble is conducted in order to allow the system to achieve a stable density value at 1 bar. For each replica, a 50 ns production trajectories is run using SHAKE for bonds involving hydrogen atoms, allowing for a timestep of 2 fs, in conjunction with periodic boundary conditions at constant volume and temperature (298 K; Langevin thermostat with a collision frequency of 3 ps^{-1}), particle mesh Ewald for long-range electrostatic interactions, and a cutoff of 10 Å for nonbonded interactions.

Set up and modelling for the complex in DMSO/water (17% v/v)

The set up of the solvent mixture box follows the procedure reported by Alvarez and Barril,[25] a single molecule of DMSO was built using the Molecular Operating Environment (MOE) and optimised at the HF/6-31G(d) level of theory using Gaussian 09. Partial charges were derived from the optimised structure using the RESP procedure[26,27] and atom types were assigned according to the general amber force field using Antechamber, as it has been done before. The initial DMSO/water (17% v/v) box was obtained by solvating 6 DMSO molecules in a box of 88 TIP3P[22,28] water molecules. Then, was minimised (3500 steps of steepest descent followed by 6400 steps of a conjugate gradient) and thermalised in three steps of 100 ps where the temperature was gradually increased from 50 K to 298 K in the NVT ensemble. Next, the volume of the box was equilibrated under constant pressure and temperature in two stages of 100 ps. Throughout all pre-equilibration stages, the temperature was controlled by using a Langevin thermostat with a collision frequency of 3 ps^{-1}, long-range electrostatics were treated using particle mesh Ewald summation, a cutoff of 4 Å was applied to all non bonded interactions, and SHAKE[29] was employed to constraint all bonds involving hydrogen atoms. All simulations at this stage were performed using the sander module of AmberTools15.

Once the solvent box is well defined, the complex Hyp-2βLG was constructed as it was before, solvated on a truncated octahedron box of TIP3P water molecules and the appropriate number of Na+ counterions. The ff14SB-ildn force field[30] was used for the protein, while Hyp was parameterised exactly as it was without the DMSO. Each system comprised around 60000 atoms, including the protein– ligand complex, 900 DMSO molecules, 14000 water molecules and 9 Na^+ counterions in a simulation box of 625000 Å^3.

The geometry of the system was minimised in five cycles that combined 3500 steps of steepest descent algorithm followed by 6500 of conjugate gradient. Thermalisation was performed in 3 steps of 125 ps, where the temperature was gradually increased from 50 K to 298 K, while the protein and ligands were restrained with a force constant that was concurrently reduced from 1 kcal·mol^{-1}·Å^{-2} to 0.1 kcal·mol^{-1}·Å^{-2}. Prior to the production runs, each system was subjected to a 0.5 ns simulation on the NPT ensemble to equilibrate the density of the system. During the thermalisation and equilibration stages, a timestep of 1 fs was employed using SHAKE to constraint bonds involving hydrogen atoms. The production runs consisted of 250 ns using SHAKE for bonds involving hydrogen atoms, a time step of 2 fs, periodic boundary conditions at constant volume and temperature (298 K; Langevin thermostat with a collision frequency of 3 ps^{-1}), particle mesh Ewald to handle long-range electrostatic interactions, and applying a cutoff of 10 Å to all nonbonded interactions. The sander module was employed for the minimisation stage, while the CUDA accelerated version of PMEMD was used through the heating, equilibration and production stages, with both modules being available in the standard distribution of AMBER15.

4.2.4. Microbial growth and photoinativation process

The microbiological procedure used herein was the same as in the previous chapter. However, in this chapter only two strains were tested: *S. aureus* CECT239 obtained from the Spanish Type Culture Collection (CECT) and *B. subtilis* 168WT, received from Prof. Cristiano Viappiani's group in Parma (Italy). The light source for the photoinactivation experiments was also the same.

4.3. Results and discussion

4.3.1. Complex characterisation in PBS

βLG spontaneously forms homodimers (2βLG) under physiological conditions and under the conditions encountered in milk processing. Therefore, we studied if Hyp can form a stable complex preserving its photosensitising properties.

Modelling studies. βLG forms dimers (2βLG) under conditions close to those encountered physiologically, with a dimerisation constant of K_D = 8.6 μM at pH 7.5.[11,31] βLG is shaped to accommodate small and long chains hydrophobic compounds in its monomeric structure, such as retinol and the aliphatic chains of fatty acids, in the lipocalin-type β-barrel. However, the monomer cavity is too narrow to accommodate Hyp because of its size, which suggests that this compound should bind other pockets. The dimerisation is associated with the antiparallel alignment of two β-strand (residues 147-151) and with the formation of H-bond between them.

The interface between the monomers is also shaped by the AB and CD loops, where residues Asp33 and Arg40 participate in a salt bridge. Inspection of the dimers revealed that Hyp might bind in the two clefts formed at the interface of the monomers in the dimeric complex (Figure 4.1).

The analysis of the best-ranked poses supported the binding of Hyp to the narrow cleft with a relatively large affinity, predicting a binding free energy of −7.4 kcal·mol^{-1}, which is ~2.5 kcal·mol^{-1} more favourable than the binding to the wide cleft (binding free energy of −4.9 kcal·mol^{-1}). This finding is not unexpected, given the hydrophobicity of the compound and the narrow separation between the walls of this cleft, where Hyp is largely occluded from the solvent. Moreover, the binding to the narrow cleft is also stabilised by hydrogen bonds between the hydroxyl groups of the Hyp and backbone carbonyl groups (Lys141, Leu143 and Met145) and the side chains of Asp137 and Glu157. In contrast, binding to the wide cleft leaves one of the two faces of Hyp exposed to the solvent.

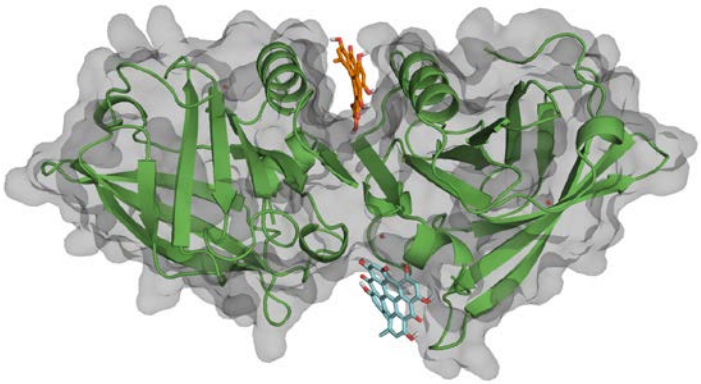

Figure 4.1. Best poses of Hyp bound to the narrow and wide clefts obtained from docking calculations. Hyp is shown as sticks. The orange Hyp is bound in the narrow cleft formed at the bottom of the β-barrel and it extends along the surface of helix 4 and β-strand. While the other Hyp shown in blue is placed in the wide cleft, located at the interface of two helixes and the loops AB and CD, which contains Trp61. The backbone of the dimeric species of βLG is shown in green and the grey area displays the surface of the dimer.[32]

Complex formation in PBS. Binding between Hyp and 2βLG can be monitored through the effects on the absorption spectrum and fluorescence emission, in a similar way that it was done in the previous chapter. As it is already known, Hyp in water shows broad absorption bands and very weak and structureless fluorescence emission.[33] However, when Hyp is dissolved in the presence of 2βLG, its absorption spectrum partially recovers, and most importantly, the fluorescence emission increases substantially and becomes structured. These facts indicate that Hyp is located in a less polar environment than water, as a result of binding to the protein.

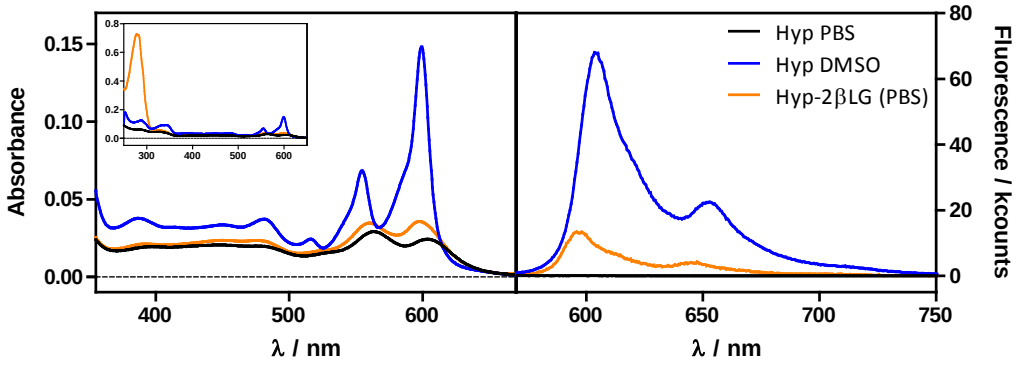

Figure 4.2. Absorption (left panel) and fluorescence emission (right panel) spectra of Hyp 7 μM in PBS (black), DMSO (blue) and in PBS in the presence of 100 μM βLG (2βLG≈ 40 μM, orange).

Binding. Unlike apoMb-Hyp, the self-assembly of the βLG-based nanostructure in aqueous solution results from multiple association equilibria governing the protein dimerisation and the binding of the Hyp at different binding sites, as it has been shown in the docking modelling. However, in order to simplify the analysis and because the protein concentration is kept constant, the dimerisation part of the equilibrium is considered neglected.

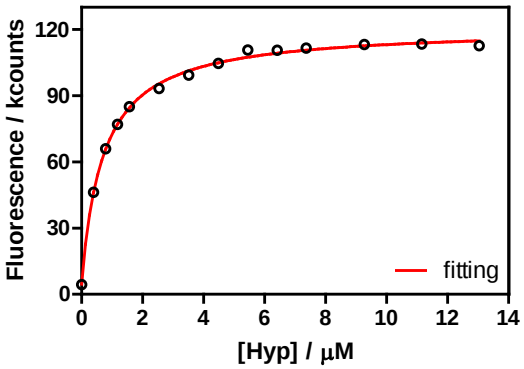

Figure 4.3. Integrated fluorescence emission as a function of total Hyp concentration, fixing the βLG concentration at 100 μM. The red solid line is the result of a fit to the observed emission using a model derived from the binding equilibrium described in the experimental section.

Accordingly, the affinity of Hyp for 2βLG was evaluated by monitoring the fluorescence emission (estimated from the integrated area) as a function of Hyp concentration at βLG = 100 μM (Figure 4.3). Assuming a dimerisation constant, K_D = 8.6 μM^{-1},[11] this corresponds to 2βLG ≈ 40 μM. A model for the binding equilibrium Hyp + 2βLG ⇆ Hyp-2βLG afforded an association constant, K_a = 1.40 ± 0.07 μM^{-1}, corresponding to a dissociation constant, K_d = 0.71 ± 0.03 μM. The resulting K_d is much smaller than the literature constant associated to βLG dimerisation as it was expected because the binding of Hyp to the protein is limited by the fraction of dimeric βLG present.

However, although the complex Hyp-2βLG formed an effective stable complex, its spectral properties and the low fluorescence suggest that Hyp is not fully monomeric when bound to the protein, which prevents the full realisation of its photosensitizing potential. For that reason, the

addition of a fraction of DMSO was thought to help in the photophysical properties and even in the binding of Hyp to the protein.

4.3.2. Photophysical properties with and without DMSO – tuning the solvation surface

Since βLG can be coated with DMSO, this might provide a better environment for the bound Hyp molecules. We studied whether the use of DMSO as a co-solvent improves the photophysical properties of Hyp- βLG, thereby assessing its potential as a photodisinfection agent for materials contaminated with bacteria.

Modelling studies. As previously shown by molecular modelling, Hyp can *a priori* be accommodated in the two clefts formed at the interface of 2βLG. In the narrower cleft, which is shaped by the α-helix that precedes the strand βI, Hyp can be inserted only as a monomer. The other cleft, formed by loops AB and CD which contains Trp61, is wider and might accommodate the binding of dimeric Hyp, and possibly higher order aggregates.

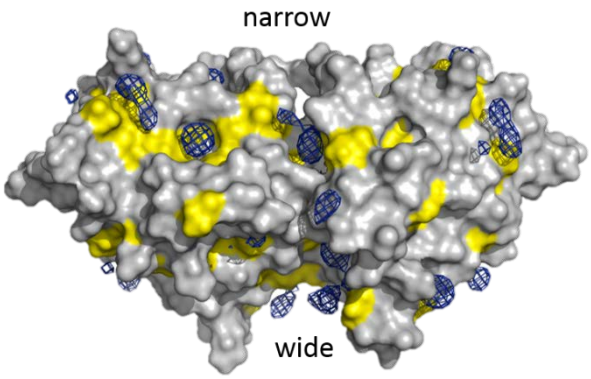

Figure 4.4. Preferential distribution of DMSO molecules around the protein surface of dimeric βLG. Blue isocontours denote a DMSO density of 0.3 g cm^{-3}. Yellow areas denote the surface contribution arising from amino acids with hydrophobic side chains. The location of the narrow and wide clefts at the protein–protein interface is also shown.[34]

It was examined where DMSO preferentially accumulates in the protein through MD simulations. The results on the dimeric βLG in the mixture DMSO/water reveal that DMSO molecules tend to fill specific pockets in hydrophobic patches of the protein surface, including the areas corresponding to the narrow and wide clefts formed at the interface of the interacting monomers (Figure 4.4). This agrees with the experimental finding that at low DMSO concentrations there is a negative preferential binding of DMSO molecules,[35] reflecting the favourable interactions of DMSO with aliphatic and aromatic residues.

Furthermore, mapping of the highly populated binding sites for organic probes is valuable to identify 'hot spots' for the binding of small molecules.[36–39] The distribution of DMSO molecules on the protein surface is consistent with the observation, based on THz spectroscopy, that βLG

is a relatively hydrophobic protein not displaying an extended long-range hydration dynamics,[40] as is observed for other hydrophilic proteins.[41,42]

Figure 4.5 shows the last snapshot collected at the end of a MD simulation. The presence of DMSO neither alters the binding of monomeric Hyp to the narrow cleft nor impedes the binding of Hyp, either as a monomer (A) or a dimer (B), to the wide cleft, where it is stacked against the indole ring of Trp61 (the average distance between the Hyp and indole rings is close to 4.8 Å). Although the present results do not allow us to discern the relative stability of the binding to the two clefts, it is worth noting the large population of DMSO molecules around bound Hyp, especially for the monomeric species in the narrow and wide clefts (blue contour).

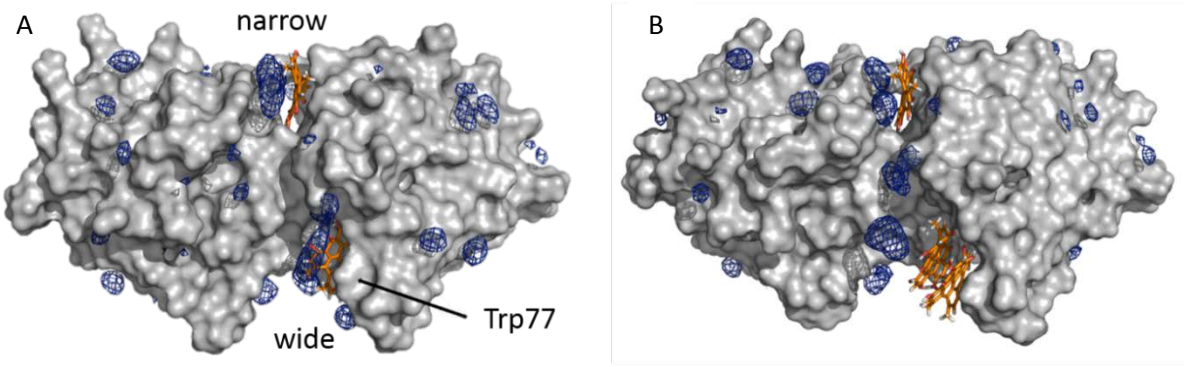

Figure 4.5. Preferential distribution of DMSO molecules around the protein surface of dimeric βLG bound to Hyp molecules as monomers in the narrow cleft, and either (A) monomers or (B) dimers in the wide cleft. Blue isocontours denote a DMSO density of 0.3 g·cm^{-3}. Hyp molecules are shown as orange-based sticks.[34]

Moreover, monomeric Hyp is deeply inserted into the wide cleft, while the larger size of dimeric Hyp leads to a more superficial interaction with the protein. The preferential solvation by DMSO molecules is expected to result in a more effective shielding of bound Hyp from surrounding water molecules, which would stabilise the binding of monomeric Hyp to the protein. This stabilisation of the binding of active Hyp molecules to the protein very probably will improve the photophysical properties.

Hyp and βLG form a stable complex in PBS and in a DMSO:PBS mixture. As shown in Figure 4.2, Hyp in the presence of 2βLG with only PBS as solvent, partially recovered the structured absorption spectrum, with bands centred around 560 nm and 598 nm, along with fluorescence emission (orange lines). Before the addition of a DMSO fraction, we ran an experiment where the fluorescence emission of the tryptophan was measured.

Figure 4.6 plots the Trp residues fluorescence upon addition of DMSO, remaining almost unaffected up to 60% of DMSO when showed an increase in the intensity and a red-shift.

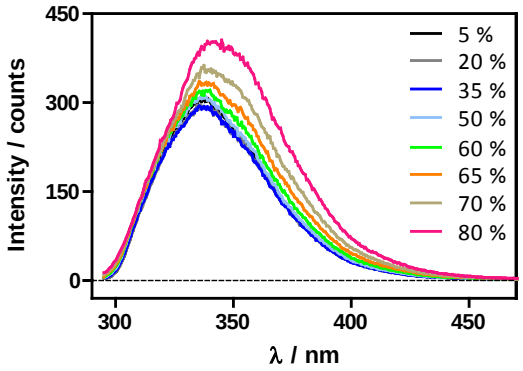

Figure 4.6. Fluorescence emission of the tryptophan (Trp) residues in the βLG upon addition of increasing amounts of DMSO. Excitation at 290 nm.

It seems to be with 50- 60% of DMSO when the protein stars unfolding, which is consistent with the result of Arakawa *et al.*[35] Moreover, with a 50% of DMSO the sample presented bubbles, which is another sign of the protein denaturation.

Different samples were prepared with the same protein and Hyp concentration but with different amount of DMSO in order to monitor how the absorbance change. Figure 4.7 shows this experiment, in particular in the right panel, how the absorbance increases in the two maximums of Hyp. It also revealed that Hyp seems to be monomeric since its fluorescence increases linearly with the amount of DMSO. We chose to work with 20% of DMSO (V_{DMSO} /V_{PBS}), corresponding to ~17% (V_{DMSO}/V_{tot}) because the increased absorbance and fluorescence (data not shown) were considerable and to avoid too much solvent thereafter in the photoinactivation experiments.

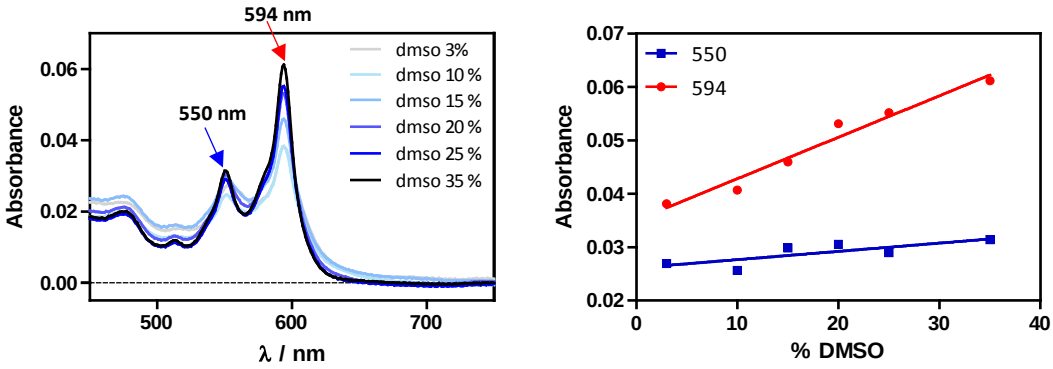

Figure 4.7. Absorbance spectrum (left panel) and the absorbance increase at the maxima of Hyp upon addition of increasing amounts of DMSO (right panel). In all samples the [βLG]= 100 μM and the [Hyp]= 2 μM.

Hence, these results and the modelling calculations suggest that DMSO might stabilise the attachment of monomeric Hyp to the clefts located at the interface of 2βLG. The spectroscopic properties of the complex Hyp-2βLG considerably change in the DMSO:PBS mixture: the absorption spectrum (Figure 4.8 A, orange) is more structured than that in pure PBS (Figure 4.8 A, grey), with absorption bands similar to those observed for Hyp dissolved in pure DMSO (Figure

4.8 A, blue). The intensity of the fluorescence emission is substantially increased as well (Figure 4.8 B, orange).

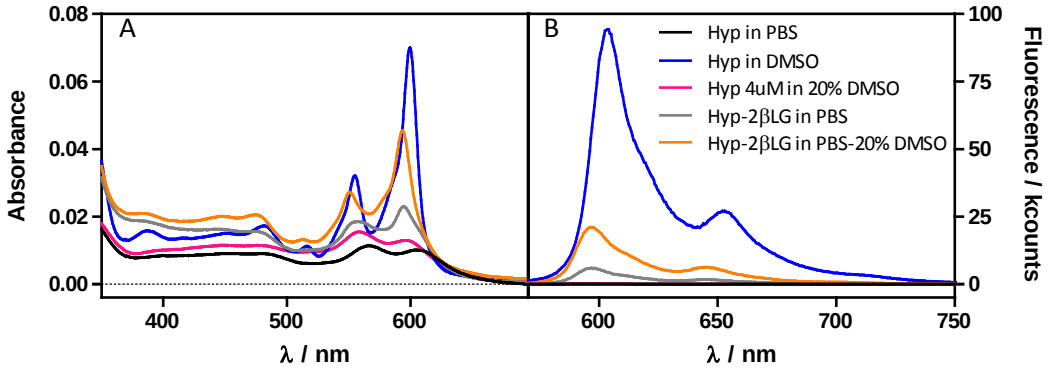

Figure 4.8. Absorption (A) and fluorescence emission (B) spectra of Hyp in differerent samples. The Hyp concentration was 4 μM and that of βLG, when present, was 200 μM. Emission spectra were collected after excitation at 554 nm, T = 20 ºC.

The formation of a stable self-assembled nanostructure in the binary mixtures of PBS and DMSO is confirmed by steady state fluorescence anisotropy and Fluorescence Correlation Spectroscopy (FCS) measurements, both experiments carried out in Parma at the group of Prof. Cristiano Viappiani.

On the one hand, fluorescence anisotropy of Hyp in solution with 2βLG shows a non-zero anisotropy fluorescence excitation spectrum, indicating that the rotational diffusion of the molecule is limited because of the interaction with the protein scaffold (Figure 4.9). However, when a 20% of DMSO is present there is an improved signal-to-noise ratio. In comparison, Hyp dissolved in pure DMSO gives a zero anisotropy spectrum due to the faster rotational diffusion.

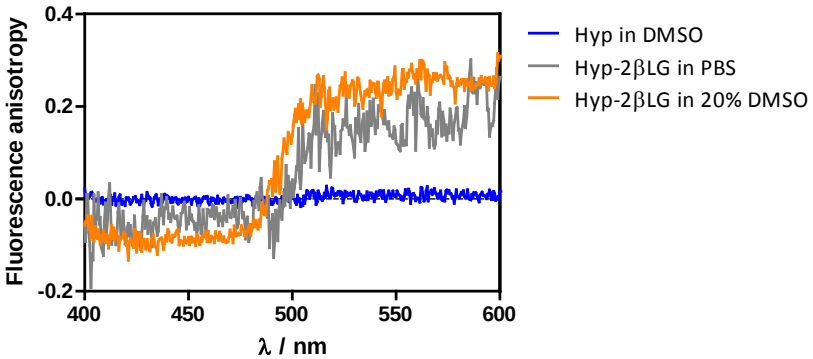

Figure 4.9. Fluorescence anisotropy spectra of Hyp in DMSO (blue), Hyp-2βLG in PBS (grey) and Hyp-2βLG in 20% PBS–DMSO (orange), obtained from excitation spectra (λ_{em} = 620 nm, T = 20 ºC). The Hyp concentration is 4 μM and that of βLG is 200 μM.

On the other hand, FCS is useful determine the diffusion coefficient of molecules taking advantage of the spontaneous thermal fluctuation in the fluorescence emission intensity of the freely diffusing fluorophores in solution.[43,44] Figure 4.10 A shows the cross-correlation function determined for 1 nM Hyp in the presence of 30 μM βLG. The cross-correlation signal is well

described by a model comprising diffusional motion, on the 10 μs – 1 ms time scale, and triplet decay, occurring on the 1–10 μs time scale. The diffusion coefficient of the dominant diffusing species is D = 70 $\mu m^2 \cdot s^{-1}$, consistent with the value expected for Hyp bound to 2βLG. Figure 4.10 B exposes the fluorescence auto-correlation curve obtained for 1 nM Hyp and 36 μM βLG in the presence of a 20% of DMSO, which is well-fitted also by a model comprising molecular diffusion and triplet state decay. The diffusion coefficient of the dominant species is D = 40 $\mu m^2 \cdot s^{-1}$, lower with respect to the pure PBS buffer due to the higher viscosity of the mixture and the different hydrodynamic radius of the DMSO-coated protein.[45,46]

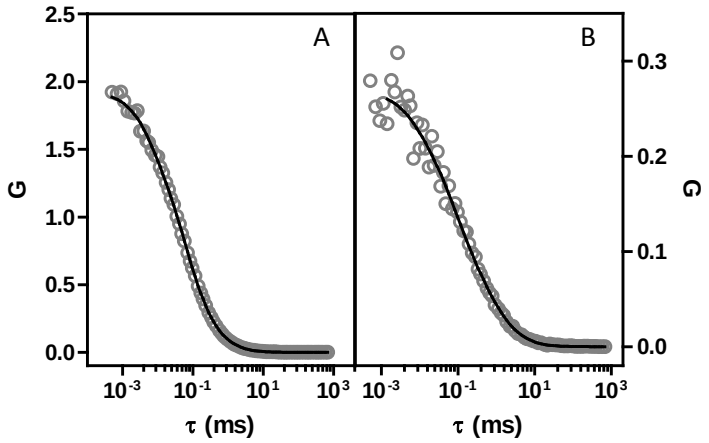

Figure 4.10. Cross correlation functions for 1 nM Hyp in PBS buffer in the presence of 30 μM βLG (A- open circles) and 1 nM Hyp in the mixture PBS–DMSO in the presence of 36 μM βLG (B- open circles). The solid lines are the results of the fit using a model comprising triplet state decay and diffusion. Excitation 475 nm, detection at 670 nm.

A functional nanostructure: photophysical properties are preserved either in PBS or in PBS: DMSO mixture. A key issue for potential applications in photosensitisation-based antimicrobial treatments is that the PS retains the ability to populate the triplet state upon photo-excitation and photosensitise the production of $^1O_2$. The preservation of the fluorescence properties is already a sign that likely the complex will maintain the photophysical properties of Hyp, as it was for the apoMb-Hyp complex. Time-resolved fluorescence emission measurements for Hyp in the presence of 2βLG in PBS afford a biexponential decay with lifetimes (τ_F) of 3.9 ns (35%) and 6.7 ns (65%) (Table 4.1). This is consistent with the co-existence of two populations of Hyp, that likely correspond to the Hyp bound at the two binding sites on 2βLG, as it has been shown by computational methods. The most populated component can be attributed to the Hyp placed in the narrow cleft, where it is better shielded from the solvent and embedded in a less polar environment, and hence is relatively long emission lifetime, even longer than Hyp in DMSO. The minor component can be attributed to Hyp bound at the larger cleft of 2βLG, where the molecule is partially exposed to the solvent and possibly staked to other Hyp, and it is thus characterised by a faster emission lifetime of 3.9 ns. When DMSO is present, the fluorescence

decay fitted with a biexponential relaxation but mainly with one component of 5.6 (80%), which lifetime is identical to the one of the Hyp in DMSO. This is in accordance with the picture derived from MD simulations, where the local environment of the Hyp bound to the protein is coated with DMSO. The minor fast component (lifetime 0.2 ns) have a sub-resolution lifetime and is assigned to scattering.

As shown in Table 4.1, the complex Hyp-2βLG in PBS buffer has a quantum yield for the triplet state formation $\Phi_T = 0.050 \pm 0.002$. The triplet state shows a lifetime decay (τ_T) of around 10 μs, considerably longer than the value obtained for Hyp in DMSO (1.4 μs) and similar to the one reported for Hyp bound to apoMb (11.1 μs), where this relatively long lifetime was attributed to the shielding of Hyp from the solvent by the protein scaffold.[47] Hyp-2βLG photosensitises $^1O_2$ with a yield $\Phi_\Delta = 0.065 \pm 0.010$. The similar Φ_Δ and Φ_T values measured for Hyp-2βLG in PBS buffer indicate that the efficiency of the energy transfer between the triplet state of Hyp and $^3O_2$, leading to the production of $^1O_2$, is close to unity. However, the value retrieved for Φ_Δ is quite low in comparison to the one observed for Hyp in pure DMSO (0.28 ± 0.05) or Hyp bound to apoMb (0.14 ± 0.03). According to MD studies, the reduced fraction of active PS may be due to the preferential binding of Hyp, possibly as an aggregate, to the wide cleft in 2βLG, where it is stacked against Trp61. Moreover, when it is bound to the wide cleft, one face of Hyp is exposed to the aqueous solvent, an interaction which may be detrimental to the photophysics of the compound.

Table 4.1. Principal photophysical parameters of Hyp and Hyp-2βLG in PBS or 20% PBS–DMSO.

Sample	Solvent	τ_F (ns)	Φ_F	τ_T (μs)	Φ_T	τ_Δ (μs)	Φ_Δ
Hyp	DMSO	5.5 ± 0.1 (100%)	0.35 ± 0.02	1.4 ± 0.1	0.35	5.5 ± 0.1	0.28 ± 0.05
Hyp-2βLG	PBS	3.9 (35%) 6.7 (65%)	0.03 ± 0.01	10 ± 2[a] 8.6[b]	0.050 ± 0.002	2.3 ± 0.1	0.065 ± 0.010
Hyp-2βLG	PBS- 20% DMSO	0.2 (20%) 5.6 (80%)	0.06 ± 0.01	8.2 ± 0.4[a] 8.4[b]	0.170 ± 0.002	2.5 ± 0.1	0.12 ± 0.05

[a] Laser flash photolysis; [b] Time-resolved NIR phosphorescence detection

The presence of 20% DMSO induces a nearly, or in some case even more than, two-fold increase in the values of Φ_F, Φ_T, and Φ_Δ, when the 2βLG is present. This increment cannot be attributed to a larger monomeric Hyp molecules unbound to the protein because as it was shown in Figure 4.8 (magenta curve) the spectroscopic features are of an aggregated Hyp with broad and structureless bands close to those seen for Hyp in PBS. Moreover, free Hyp in the mixture DMSO:PBS has an almost undetectable $\Phi_F < 0.001$ and a negligible Φ_T. Therefore, the improvement of the photophysical properties likely comes from a better solvation of Hyp molecules when are bound in the protein scaffold. These results were already expected after

the MD simulations, since DMSO appeared to stabilise the binding of monomeric Hyp to the protein.

Another experiment that would demonstrate that there is no greater affinity of Hyp molecules to 2βLG when DMSO is present is through the analysis of the binding isotherm curve. However, this is tricky since the fluorescence emission upon addition of Hyp not show a clear saturation, indicating the possible presence of additional low-affinity binding sites on the DMSO coated protein (data not shown). Therefore, with this experiment it cannot be concluded whether the presence of DMSO simply induces changes in the local environment of the Hyp molecules, favouring the fluorescence emission, or it also induces an increase in the affinity of the two species. However, looking at the aforementioned results the DMSO forms an effective shield that protects the bound Hyp molecules from water, which offers a better local environment, contributing to its photophysical properties' preservation.

Taken together all the results, the Hyp-2βLG complex can be considered more efficient in the photosensitisation of $^1O_2$ when assembled in a PBS–DMSO mixture, since the concentration of dissolved molecular oxygen in PBS buffer and in the 20% DMSO–PBS mixture can be considered equal.[48]

4.3.3. Bacteria photodynamic inactivation

The enhanced photophysical properties in the presence of DMSO suggest that Hyp-2βLG may have also improved antimicrobial activity. However, as it was shown in the previous chapter, Hyp either alone or in the cavity of the protein, only induces a substantial damage in gram-positive bacteria. Therefore, we focused on gram-positive bacteria photo-damage, evaluating first the cytotoxic potential in *S. aureus*, comparing the effect in PBS or in the binary mixture PBS:DMSO. In addition, after the incubation period, suspensions were centrifuged and the pellet containing the cells was resuspended in an equal volume of solvent (Figure 4.11 lines labelled as pellet), while the supernatant was removed by suction. This washing procedure allows for the removal of the species that are not tightly combined to the cells after the incubation, and thus can be separated by centrifugation.

Figure 4.11 A shows the photoinactivation results in PBS buffer, emphasising that Hyp-2βLG induces a relevant inactivation on *S. aureus*, with a decrease of ~6 logs units in the survival fraction rate upon irradiation with green light (green line). This effect is comparable to the one observed when free Hyp in pure DMSO is added to the bacteria suspension (red line). These results were comparable to those for the washed suspensions; for free Hyp there was still a ~6

logs decrease in the number of CFU (magenta line); and 5 to 6 log units for Hyp-2βLG, with a slight reduction of the dark toxicity (dark green line).

On the contrary, the B panel on Figure 4.11 shows the results of the experiments carried out using the 20% PBS-DMSO mixture as a solvent. Control experiments demonstrated that the presence of DMSO at this concentration is not toxic for these bacteria (orange line). As observed in pure PBS buffer when free Hyp in pure DMSO is added, excellent photoinactivation is obtained with a reduction of 6–7 log units in the survival fraction (red line). No substantial change occurs after washing by centrifugation (magenta line). Surprisingly, the complex Hyp-2βLG considerably reduces its photodynamic action against *S. aureus* in the mixture PBS–DMSO, inducing a decrease in survival fraction of ~3 log units upon irradiation (green line).

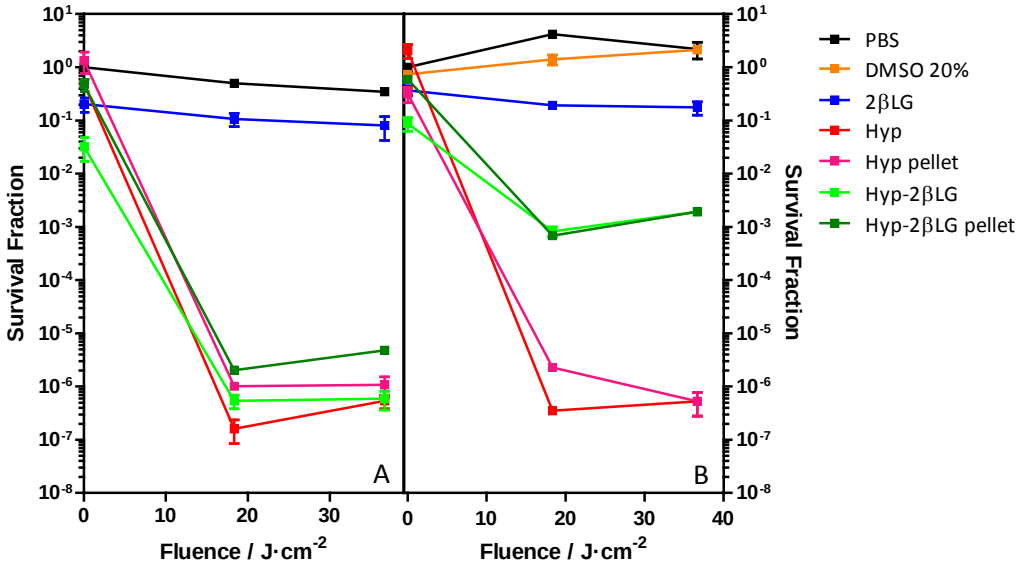

Figure 4.11. Photoinactivation results for *S. aureus* cells in suspension incubated with: 4 μM Hyp and 200 μM βLG. The lines labelled as pellet refers to the resuspended pellet after the wash by centrifugation. The same experiments were performed in a PBS buffered solution (A) and in a 20% PBS–DMSO mixture (B). Controls are made for *S. aureus* suspension in PBS (black), in 20% PBS–DMSO (orange), and incubated with βLG 200 μM (blue).

This result is in apparent contradiction with the measured value of Φ_Δ of the complex, which is about two-fold higher in the mixed solvent PBS–DMSO than in pure PBS. It is worth noting that the different photodynamic activity in the mixed solvent PBS–DMSO does not arise from a reduced photostability of the complex in the mixed solvent as compared to PBS. Exposing Hyp-2βLG to the same light dose as used in the photoinactivation experiments leads to the same level of bleaching of the compound in PBS and in PBS–DMSO (data not shown).

Spectroscopic analysis and some photophysical properties in the presence of *S. aureus*. The comparison of the fluorescence emission spectra in Figure 4.12 can provide some indications about the distribution of Hyp in the presence of *S. aureus* cells. Free Hyp in PBS shows no detectable fluorescence because is largely aggregated in this media (panel A, black). However,

when it was placed in the binary mixture, the fluorescence emission was detectable with a maximum of 593 nm, although still weak (panel B, black). After incubation with bacteria cells, the fluorescence of free Hyp underwent minor but important changes: a slight increase in the emission was observed in pure PBS (panel A, red), while an increase of the emission and a band-shift were observed in the mixture PBS–DMSO (panel B, red, peak at 598 nm). This very likely indicated a re-distribution of Hyp, where Hyp molecules were placed in a different environment than the bulk solvent, provided by the cell. Clearly, the fluorescence when Hyp was incorporated inside the protein cavity (i.e., protected from the PBS buffer) increases (panel A, green), and its emission became more intense in PBS-DMSO, increasing two-fold the intensity (panel B, green). No significant changes in the fluorescence emission of Hyp-2βLG were detected after the incubation with cells neither in PBS (panel A, orange) nor in PBS-DMSO (panel B, orange). This fact likely means that there is not a re-distribution of Hyp molecules, but the vast majority of them are still attached to the protein matrix. Otherwise, if the Hyp would have migrated to the cell surroundings, a change in the fluorescence intensity or a wavelength shift in the maximum would have been expected. However, a big change was observed when this samples incubated whit bacteria were thereafter washed by means of centrifugation, decreasing largely the fluorescence emission until an intensity comparable with the one observed for free Hyp incubated with bacteria. In the washed we removed the supernatant by suction, thus removing the protein that is in suspension and collecting the cells in the pellet. The small but clearly detectable emission spectra of the resuspended pellet (blue line in panels A and B) indicated that an appreciable fraction of Hyp-2βLG was tightly bound to the bacteria. The position of the emission peak for this fraction is very similar in the absence (598 nm) and in the presence of DMSO (597 nm). Nevertheless, the vast majority of Hyp was removed in the supernatant due to the Hyp-2βLG either was not highly bound to the cells or was in suspension not close enough to establish an interaction with cells.

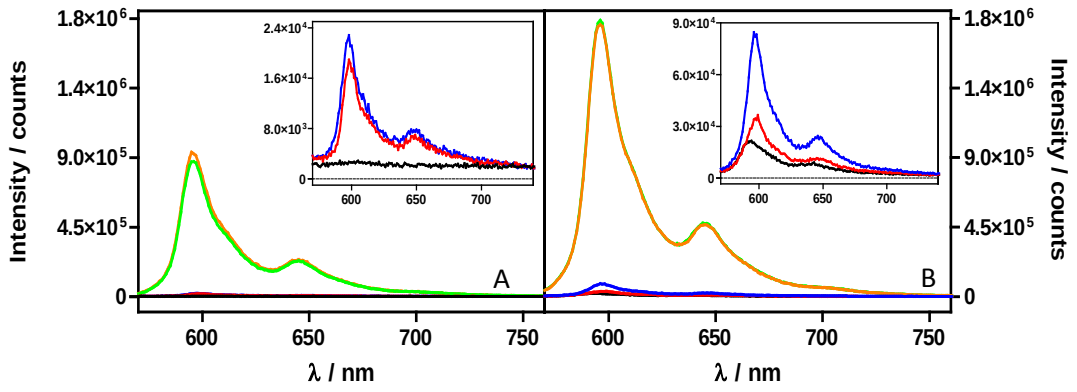

Figure 4.12. Fluorescence emission spectra in PBS buffer (A) and in the 20% PBS–DMSO mixture (B) for Hyp (black), Hyp incubated with *S. aureus* (red), Hyp complexed with 2βLG (green), Hyp complexed with 2βLG incubated with *S. aureus* (orange), Hyp complexed with 2βLG, incubated with *S. aureus* and washed by centrifugation (blue). The Hyp

concentration is 4 μM in all cases and that of βLG, when present, is 200 μM. The insets represent a zoom of the less intense signals. Excitation at 554 nm.

Table 4.2 shows the fluorescence decay lifetime in the absence and presence of *S. aureus* cells. The signals of Hyp alone with cells have an extremely weak fluorescent, hence they are characterised by an intense scattering signal on the shortest time scale (< 0.5 ns). The lifetimes for Hyp alone either in PBS or in the binary mixture are very similar. In 20% DMSO the fluorescence lifetimes with and without cells are the same, but in the steady state fluorescence spectrum there was a red-shift after the incubation with cells, hence likely there was a re-distribution of Hyp which lifetime coincides with the one without *S. aureus* cells.

When *S. aureus* cells were incubated with Hyp-2βLG in PBS, time resolved fluorescence emission from the PS occurs through a biexponential relaxation with similar weights as, and slightly longer lifetimes than, those observed in the absence of bacteria (Table 4.2). This fact indicates that the fluorophore was kept in the same type of environment with or without bacteria, provided by the protein scaffold. We cannot extract more information about the increase of the shorter component when cells were present because of the low signal-to-noise ratio. Similarly, the fluorescence decay observed for *S. aureus* incubated with Hyp-2βLG in PBS–DMSO is essentially the same as that observed for Hyp-2βLG in PBS–DMSO and for Hyp in DMSO (Table 4.2). This suggests that the patches of DMSO coating the hydrophobic areas of the protein surface, persist also when Hyp-2βLG is bound to the bacteria.

Table 4.2. Lifetimes and amplitudes after the analysis of the time resolved fluorescence decays of Hyp and Hyp-2βLG in PBS or 20% PBS–DMSO incubated with *S. aureus* cells.

Sample	Solvent	τ_{F1} (ns)	τ_{F2} (ns)	τ_{F3} (ns)
Hyp	DMSO	-	-	5.5 ± 0.1 (100%)
Hyp + *S. aureus*	PBS	0.2 (48%)	4.2 (52%)	-
Hyp	PBS- 20% DMSO	-	3.5 ± 0.1 (100%)	-
Hyp + *S. aureus*	PBS- 20% DMSO	0.5 (48%)	3.6 (52%)	-
Hyp-2βLG	PBS	-	3.9 (35%)	6.7 (65%)
Hyp-2βLG + *S. aureus*	PBS	-	4.6 (45%)	7.0 (55%)
Hyp-2βLG	PBS- 20% DMSO	0.2 (20%)	-	5.6 (80%)
Hyp-2βLG + *S. aureus*	PBS- 20% DMSO	-	-	5.5 (100%)

Time-resolved $^1O_2$ phosphorescence was measured in an analogous experiment to that of fluorescence emission and, it is also observed that when the samples are washed the $^1O_2$ signal is killed (Figure 4.13). Therefore, this is an additional experiment that allows us to reach the same conclusions: Hyp is kept inside the protein even when the cells are present. The intensity difference in the Hyp-2βLG signals was probably an experimental mistake. Clearly, the amount

of photosensitised $^1O_2$ by Hyp-2βLG is considerably higher when a fraction of DMSO is present, as it has been shown in Table 4.1.

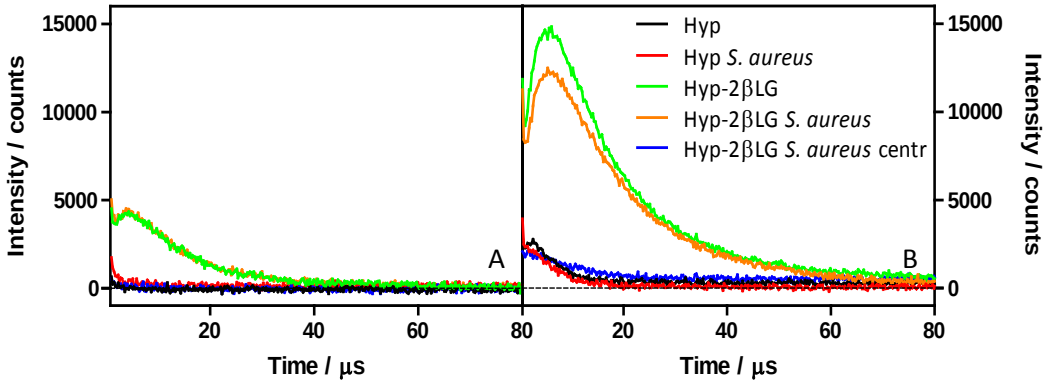

Figure 4.13. NIR phosphorescence emission at 1275 nm in PBS buffer (A) and in the 20% PBS–DMSO mixture (B) for free Hyp alone, incubated with *S. aureus* and the complex Hyp-2LG alone, incubated with *S. aureus* and washed by centrifugation. The Hyp concentration is 4 μM in all cases and that of βLG, when present, is 200 μM.

The lifetime of triplet decay of Hyp-2βLG bound to *S. aureus* is 8 ± 1 μs and 9 ± 1 μs in PBS buffer and in the binary mixture, respectively. Importantly, these values are very similar to those in PBS and PBS–DMSO in the absence of bacteria (Table 4.1). The long lifetime of the triplet state is a further evidence that indicates that Hyp remains bound to the protein carrier since the transfer to the bacterial membrane would lead to a shorter triplet state lifetime (approx. 1–2 μs).

Since experimental evidence suggests that the complex between Hyp and 2βLG remains intact even after binding to *S. aureus*, the different type of interaction of the whole complex Hyp-2βLG coated by DMSO with the cells is most likely the reason for the reduced efficiency in the microbial photoinactivation. In spite of the higher amount of photosensitised $^1O_2$ by Hyp-2βLG, the DMSO coating thus appears to decrease the bioavailability of the photoactive compound. A possible explanation for this fact is that the DMSO patches interfere, or at least modify, the interaction between the complex and the cell wall.

***Bacillus subtilis* photodynamic inactivation.** The complex Hyp-2βLG was also tested against another gram-positive bacteria: *B. subtilis*. In this case, although the concentration of the protein is different, there is still a great excess of protein in order to ensure that Hyp is placed in its clefts. Moreover, we decided to test only the complex in PBS buffer due to the decreased in the photoinactivation effect when a 20% of DMSO is present. The effect on cells is the same of free Hyp and Hyp-2βLG, inducing six orders of magnitude decrease in the survival fraction (Figure 4.14). However, it seems to decrease the dark toxicity when Hyp is inside the protein as it was previously observed for Hyp-apoMb.

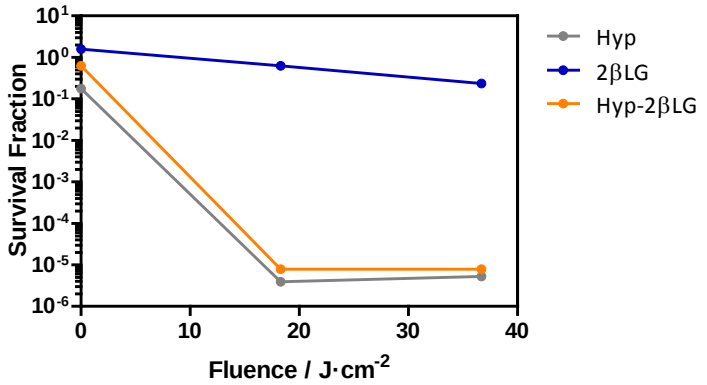

Figure 4.14. Fluence and Hyp-2βLG effects on *B. subtilis* photoinactivation. The concentration of Hyp is 4 μM and the concentration of βLG is 100 μM.

Unlike in the case of Hyp-apoMb complex, this experiment began with vegetative cells but also with endospores. Therefore, at the end of the experiment a spore stain was run in order to know whether the spores had also been killed. The stain distinguished between vegetative cells and endospores. A primary stain (malachite green) was used to stain endospores, which the cells were forced to go into by heating. After decolorising the vegetative cells with water, safranin was used to stain these cells. The results indicated that all the endospores were killed in the case of free Hyp and almost all in the case of the complex. Visual inspection after 1 day more (i.e., after 48 h from the agar seeding in Petri dishes) at 37 ºC did not reveal the growth of new colonies.

4.3.4. Incorporation of retinoic acid to the Hyp-2βLG complex. Study of this multimodal system.

The βLG monomer can accommodate several hydrophobic and linear molecules like fatty acids, retinoids, vitamin D, cholesterol or curcumin.[12] Most of these molecules are placed in the main well-defined binding site in the monomeric unity, where the β-sheets form a flattened and conical barrel, called calyx. In most cases, the complex is stabilised by hydrophobic interactions in the cavity and hydrogen bonding involving the Glu62 and Lys69 at the entrance.[49] However, there are other plausible binding sites like the one in the external surface pocket or in the dimer interface where Hyp is placed.

Some of the molecules that can be bound by βLG are retinoic acid, retinol and other retinoids derivatives.[12,50,51] Many studies have been published about the binding of retinoids to βLG, although there are several contradictions about the binding site and thus it is still under debate.[13,14] Retinol or vitamin A has several isomers, two of these geometric isomers are tretinoin and isotretinoin. The first is the all-*trans* retinoic acid, commercialised under the tradename of Retin-A® for the treatment of acne vulgaris or keratosis pilaris, although it also

has uses against a subtype of leukaemia. Isotretinoin, also known as 13-*cis*-retinoic acid, is also used for acne, but in this case, it is orally administered for a more severe acne under the tradenames of Accutane® or Roaccutane®.[52] Due to the elongated and linear form of the molecule, we chose to work with tretinoin isomer, abbreviated henceforth as RA, which also has fewer side effects in the acne treatment.

Many studies gather several pieces of evidence regarding the binding of RA to βLG with a binding constant (K_d) of ~2 x 10^{-8} M.[50,53,54] Owing to its polyenic structure, RA is quite hydrophobic and then poorly soluble and chemically unstable in water which makes its manipulation difficult. A nice solution is its complexation with βLG, overcoming the solubility problems, increasing the bioavailability and most likely being a potential method to enhance its therapeutic effects.

Acne is one of the most common multifactorial chronic inflammatory diseases of the pilosebaceous follicles, which affects approximately 80% adolescents and young adults in 11–30 age group. The pathophysiology of acne involves androgen stimulation inducing sebaceous hyperplasia, altered follicular keratinisation, hormonal imbalance, immune hypersensitivity, and bacterial (*Propionibacterium acnes*) colonisation.[15,16] Not only are many studies about tretinoin (RA) alone against acne, whose effectiveness is well documented; but also in formulations with novel delivery systems that improve its tolerability against this disease. For instance, Retin-A Micro (0.1% gel) contains RA trapped within porous copolymer microspheres or Avita, where RA is incorporated within a polyoylprepolymer. Each of these formulations releases RA slowly within the follicle and onto the skin surface, which in turn reduces irritancy with the same efficacy.[55,56]

There are no reports describing the formation of a βLG complex with a double payload of RA and Hyp. Such a multimodal complex could be ideally used for the acne treatment, because of the successful results of Hyp's activity against acne. The complex will carry two agents with different biological effects and targets. On the one hand, Hyp would be actively decreasing the colonisation of Propionibacterium acnes (*P. acnes*) through PDT, as demonstrated by Larissa *et al*.[17] This anaerobic gram-positive bacterium is the main responsible for the inflammatory manifestations in acne. On the other hand, RA has a clear participation in combating these skin disorders as has been previously mentioned.

Study of the monomeric βLG-RA complex. Although tretinoin is more stable than other *cis* isomers, it is very susceptible to degradation under daylight by oxidation of the conjugated double bonds. However, some studies confirm that retinol is protected against enzymatic oxidation, heating and irradiation when it is complexed with βLG.[57,58] Figure 4.15 shows the

normalised absorbance in three different polar solvents, with maxima at 336 nm, 340 nm and 353 nm in PBS, EtOH and DMSO, respectively. A red shift is observed for an aprotic solvent such as DMSO. Moreover, RA is slightly fluorescent in EtOH, but not in DMSO (data not shown).

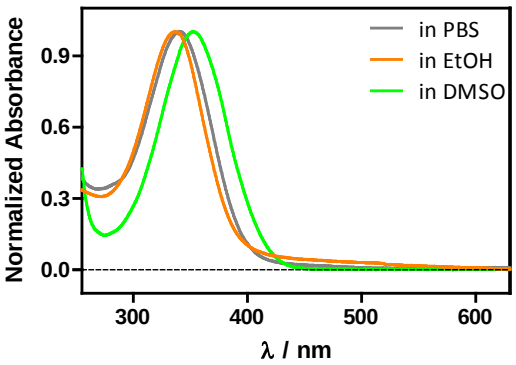

Figure 4.15. Normalised absorption spectrum of 1 μM RA in PBS, EtOH and DMSO.

RA, though not readily soluble in water, shows a structured band when it is added from an EtOH stock in low concentrations and the spectrum is measured immediately (Figure 4.15, grey). As it is known, free RA in certain organic solvents, but overall in aqueous solution, is markedly unstable. The absorption decays within minutes to a few hours, depending on the solvent, temperature, light, and other factors, resulting into a complex mixture of products.[57] The degradation of RA in water (A) and in EtOH (B) is shown in Figure 4.16, recording the absorbance spectra as a function of time. The degraded species or most likely the aggregated RA molecules showed a completely different band, with two maxima at ~345 nm and ~436 nm, this last maximum is gradually shifted to the red over time.

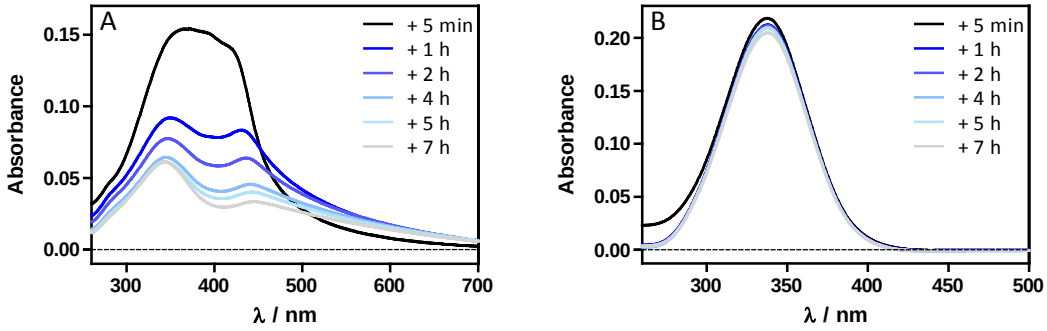

Figure 4.16. Absorption spectra of 1.7 μM RA as a function of time in A) water and B) EtOH.

However, RA in βLG seems to be stable by comparison with free RA as judged by spectral criteria, since the profile of the aggregated species was not observed when the protein is present, even after 4 h. This is itself an evidence of a RA-βLG interaction, likely where RA is partially or totally protected from the aqueous solvent due to the good stability. Probably the absorbance would decay only after protein denaturation. Figure 4.17 shows the absorption spectra of a fixed amount of RA titrated with increasing protein concentrations, presenting two maxima: one at

280 nm and other at ~350 nm assigned to the protein and to RA, respectively. The important feature of the spectrum is the red-shift when βLG was added. It appears to imply that there is an interaction, most likely arising from binding of RA to βLG as many aforementioned articles. The protein concentration goes from 0 to 100 μM. The affinity seems reasonably high, as the spectral shift is complete already at 10 μM βLG (i.e., after the second addition of βLG).

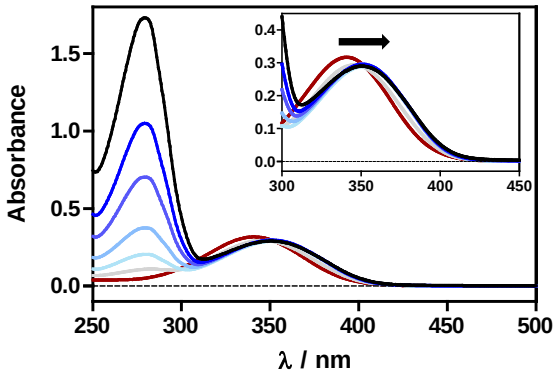

Figure 4.17. Absorption spectra of the RA-βLG complex upon addition of increasing amounts of protein, from 0 to 100 μM. The concentration of RA was fixed at 6 μM. The inset shows a zoom in the RA absorbance.

Moreover, Figure 4.18 shows how the band of the aggregated RA in water is partially recovered, forming a well-structure band at 355 nm upon addition of βLG. The shoulder centred at 430 nm is likely due to the still free RA, which disappears almost completely when there is an excess of protein. Once again, the radical change of the absorption spectra when βLG is present revealed the existence of a ligand-protein interaction.

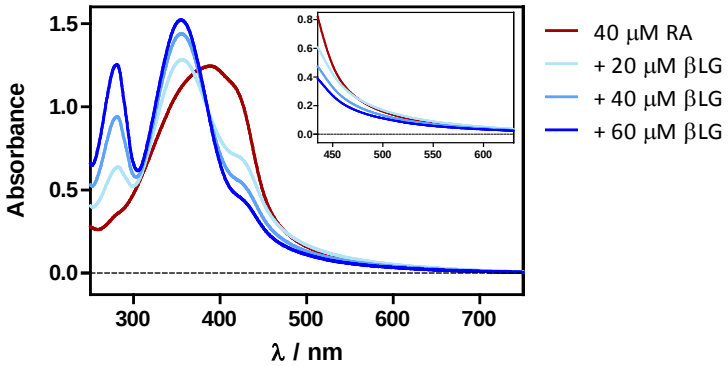

Figure 4.18. βLG addition effect on the absorption spectrum of free RA in PBS. The inset shows a zoom in from the last part of the spectrum from 440 to 630 nm, observing a decrease in the scattering upon protein addition.

In order to prove the binding and determine the binding affinity of RA to βLG, fluorescence quenching was measured. Fluorescence quenching is the decrease of the quantum yield of fluorescence from a fluorophore induced by a variety of molecular interactions with a quencher molecule.[59] Based on spectral overlap, Förster resonance energy transfer (FRET) is expected to occur between Trp-residues as donors and the RA ligand as acceptor. The βLG monomer contains two Trp residues at positions 19 and 61, Trp19 is in an apolar environment within the

central hydrophobic β-barrel or calyx, while Trp61 is part of an external loop, partly exposed, and its fluorescence might be partially quenched by the proximity of the Cys66-Cys160 disulphide bond (Figure 4.19).[60] Therefore, it is possible to use FRET from the intrinsic Trp fluorescence (Trp61 and Trp19) in βLG as a tool to study the interaction of RA with the protein.

Some of the studies available in the literature suggest that RA is bound to an external surface pocket located between the β-barrel and the α-helix, where Phe136 and Lys141 stabilised the interaction.[13] However, other modelling calculations studies, confirmed that Trp19 is the one involved in the energy transfer analysis, which is deep inside of the calyx, and can then interact with Lys70.[54,61] Moreover, a nice study by Cho *et al.* supports this last theory.[14] These authors prepared four different mutants replacing the four amino acids with play a role in the interaction with RA. The mutant that shows a marked decrease in its binding is the one lacking the Lys70, which allowed to conclude that RA binding must be within the calyx.

Figure 4.19. Representation of the main amino acids of βLG monomer involves in the interaction with RA. RA is represented in purple sticks in one of the possible binding sites. Orange sticks represent some of the Lys, in blue the two Trp present in the protein, in green Phe136 which may interact with RA when it is in the surface pocket and in yellowish-green colour is represented the two Cys forming the disulphide bond next to Trp61.

In the titration shown in Figure 4.17, FRET cannot be easily observed because the dimerisation process is mixed up with the binding process, and besides the absorbance at 280 nm is way too high to allow any reliable conclusion. Therefore, we repeated the titration of a fixed amount of 15 μM βLG at increasing RA concentrations at pH 7.4 (Figure 4.20). The band in the absorption spectrum centred at 355 nm increases upon addition of RA without the appearance of the shoulder at 430 nm even when the concentration of RA and βLG is the same. However, it is worth noting that at 435 nm the absorbance grows because of the scattering, probably due to some free RA molecules forming aggregates.

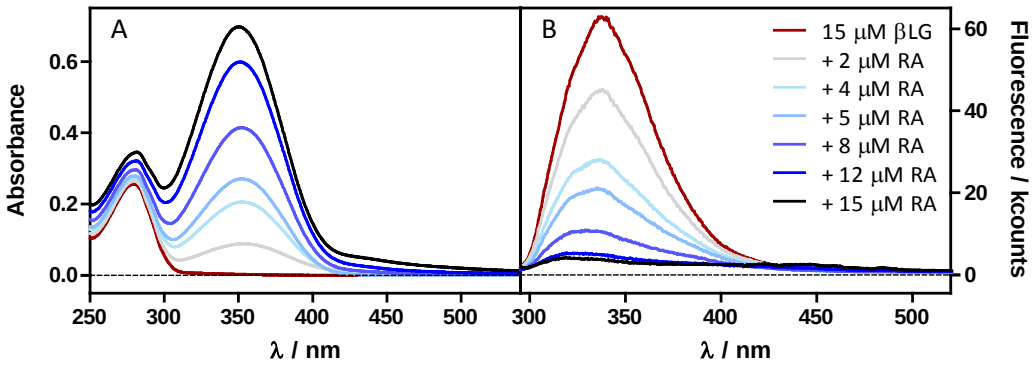

Figure 4.20. Absorption (A) and fluorescence emission (B) spectra of RA-βLG mixtures at increasing RA concentrations (between 0 and 15 μM). The βLG concentration was fixed at 15 μM. Emission spectra are collected after excitation at 280 nm to avoid the direct excitation of RA.

Because the acceptor is not fluorescent, the fluorescence emission will decrease with increasing concentrations of RA due to the quenching of Trp (panel B). The fluorescence emission of βLG alone had a maximum close to 340 nm, which indicated that excitation at 280 nm elicited the fluorescence of Trp residues mainly, and that the contribution of tyrosine residues in the 305-315 nm range (possible since βLG has four Tyr residues), was low and did not display a peak. However, it is possible that the shoulder that appeared after the addition of RA is due to the fluorescence of these Tyr residues, which is most prominent with 4 or 5 μM of RA when there is already an extended quenching of the Trp fluorescence (Figure 4.21). The shoulder at ~315 nm is best appreciated with logarithmic scale in Figure 4.21.

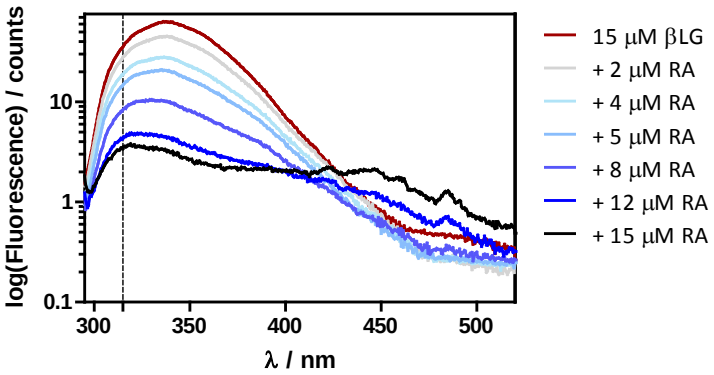

Figure 4.21. The same fluorescence emission spectrum of RA-βLG mixtures that is shown in the previous Figure, but in a logarithmic scale.

The results confirm the binding of RA to the βLG monomer since the fluorescence decreased by 26% and 88% after addition of 2 μM and 15 μM RA, respectively. Nevertheless, the high absorbance of RA in the range where Trp emits may lead, and most likely does, to simple absorption by RA of photons emitted by Trp. Notwithstanding, FRET is indeed taking place at the same time.

This energy transfer process could be directly monitored measuring the fluorescence lifetime of Trp in the RA-βLG complex, since FRET causes the lifetime of the donor (τ_D) to decrease.

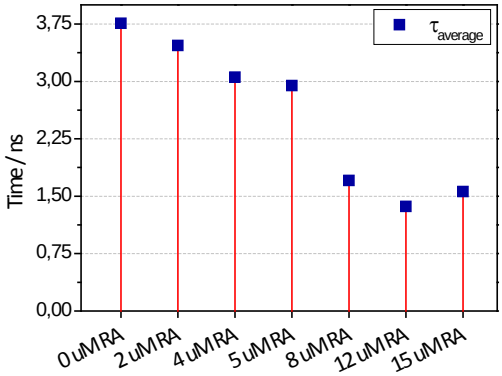

Figure 4.22. Evolution diagram of the fluorescence lifetime at increasing RA concentrations (between 0 and 15 μM). The βLG concentration was fixed at 15 μM. Excitation at 280 nm, detection at 340 nm.

The fluorescence decay revealed two components, likely attributable to Trp 19, since Trp 61 is quenched by the proximity of the Cys66-Cys160 disulphide bond.[62,63] However, one of the components was nearly at the edge of the detection limit. Taking into account that Trp residues in many proteins present a multi-exponential decay[64,65] and the difficult issue of assigning the lifetimes to individual Trps, we opted for analysing the average lifetime (Figure 4.22). The average lifetime decreases steadily down to 59% upon addition of RA, which indicates quenching, most likely by a FRET mechanism.

Study of the dimeric βLG-RA complex. On the other hand, the same experiments were carried out with a dimeric concentration of βLG, kept constant at 60 μM. The experiments were done using a 0.2 cm-pathway cuvette in order to avoid or diminish the inner filter effects.

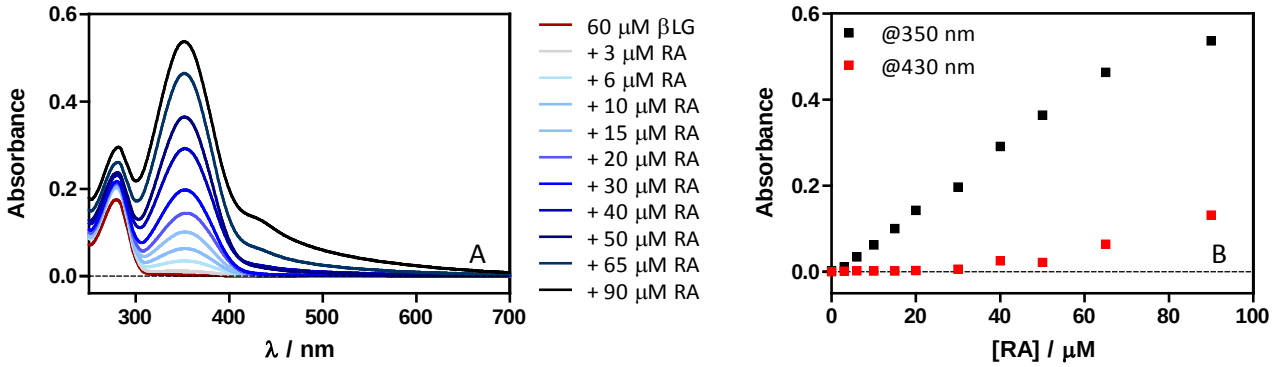

Figure 4.23. (A) Absorption spectra of RA-βLG mixtures at increasing RA concentrations (between 0 and 90 μM). The βLG concentration was fixed at 60 μM. (B) Evolution of the absorption at 350 and 430 nm upon addition of RA.

Figure 4.23 shows the titration of a fixed amount of 60 μM βLG by increasing RA concentrations at pH 7.4. The results were similar to those observed at 15 μM βLG. Nevertheless, a new band appeared at 430 nm at RA concentrations above 50 μM. As can be observed in panel B, the band at 350 nm (i.e., the maximum of RA absorption) shows a linear growth, while the band at 430 nm begins to increase only above 40 μM of RA. This fact indicates that RA starts to aggregate only when the binding is complete and the protein is saturated.

The fluorescence emission is shown in Figure 4.24 after correction by the dilution factor and the inner filter effect at 280 nm. As aforementioned, Trp61's fluorescence might be partially quenched in the native structure by the nearby disulphide bond, and thus it can be assumed that the main fluorophore is Trp19.[66] The graph in logarithmic scale (panel B) helps differentiate the transitions.

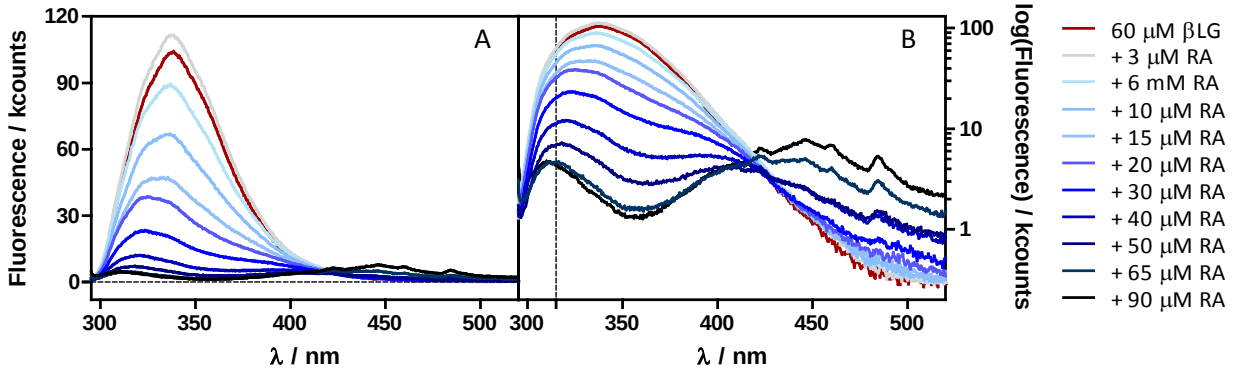

Figure 4.24. Fluorescence emission spectra of RA-βLG mixtures at increasing RA concentrations (between 0 and 90 μM) in a linear (A) and logarithmic scale (B). The βLG concentration was fixed at 60 μM. Excitation at 280 nm.

As can be observed in panel B, the maximum at 335 nm shifts to the blue as RA is increased. Two of the plausible explanations are: 1) there is a conformational change of Trp likely due to the interaction between RA and βLG or 2) the maximum of Trp contribution is quenched and then the band of the Tyr residues (i.e., with a maximum t 310-315 nm) results more prominent, leading to a blue-shift. The conformational change of Trp suggested in the first hypothesis could also be caused by protein denaturation due to the excess of EtOH in the sample (i.e., the EtOH is added since the RA stock is in this media). However a titration of the protein alone with increasing amounts of EtOH did not induce the same features (data not shown), which rules out this possibility.

The results unambiguously indicate that binding of RA to the protein occurs, although the binding site could not be assigned. The extent of quenching is difficult to quantify because of the inner filter effect and the direct excitation of RA at 280 nm at least for the higher RA concentrations. This last option could also explain the appearance of a new fluorescence band at ~450 nm for RA concentration above 30 μM (panel B, Figure 4.24), due to the formation of RA aggregates outside the protein matrix (fluorescence spectrum of RA in water not shown). This is in agreement with the onset of the absorption band at 430 nm (Figure 4.18 and 4.23).

Figure 4.25 shows the average fluorescence lifetime of Trp as a function of the RA concentration. It is worth noting that the average fluorescence lifetime at zero RA concentration (2.1 ns) is much shorter than that observed at 15 μM (3.8 ns, Figure 4.22) According to Ahmadi *et al.*[67] the micro-environment of Trp residues may be altered when protein dimers are formed, which

seems to be the case in our system. Moreover, the fluorescence is quenched by RA to a lesser extent than at 15 μM, which is also consistent with the change of Trp microenvironment induced by the formation of dimers.

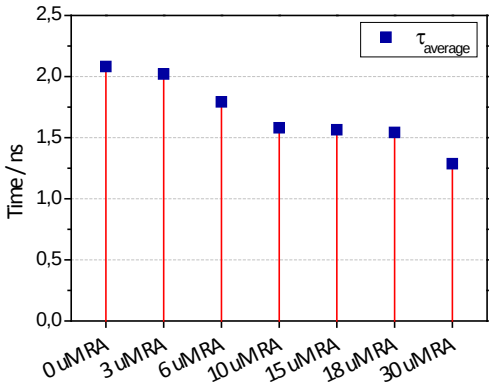

Figure 4.25. Evolution diagram of the fluorescence lifetime at increasing RA concentrations (between 0 and 30 μM). The βLG concentration was fixed at 60 μM. Excitation at 280 nm, detection at 340 nm.

Although the present results do not allow us to either discern the site of RA binding to the protein or quantify the efficiency of the quenching process, the existence of an interaction between βLG and RA has been unambiguously demonstrated by spectroscopic experiments. This agrees with previous reports in the literature, although given the complexity of the system it is not surprising that even today the topic is under debate.

Study of the addition of RA upon the Hyp-2βLG complex. The study of the double payload complex may bring a new insight into the system since the properties and characteristics of Hyp-2βLG system have already been established.

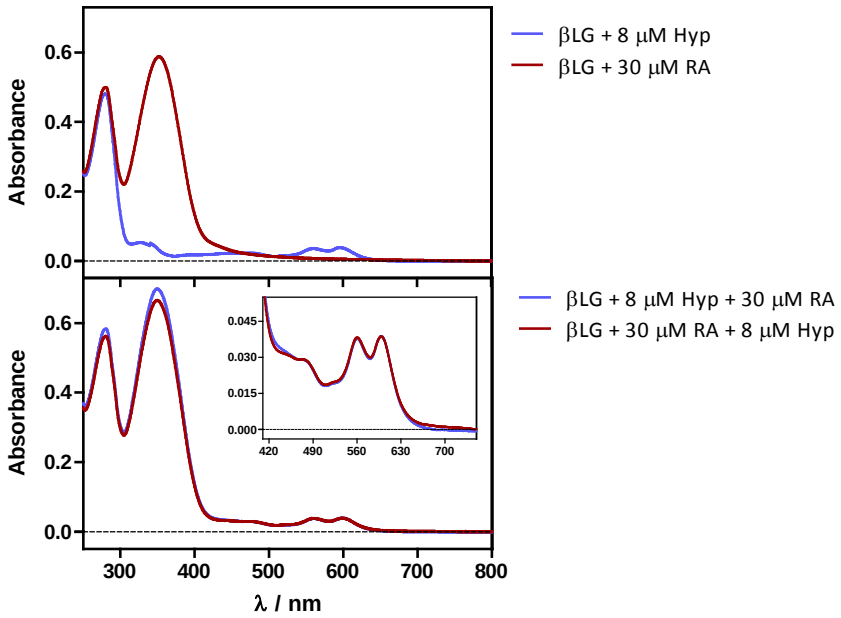

Figure 4.26. Absorption spectra of Hyp-RA-βLG mixtures, obtaining after different addition's orders. Upon 60 μM of βLG, first was added 8 μM of Hyp and secondly 30 μM of RA (blue line). On the other case, upon the same amount of protein (60 μM of βLG), first was added 30 μM of RA and secondly 8 μM of Hyp (red line).

The study of the RA-βLG complex in the monomeric and dimeric protein suggested that the binding site is the same in both conditions and it is not largely hindered in the dimer. Therefore, the order of addition between RA and Hyp should render the same results, since it has been demonstrated that Hyp does not bind to the monomeric pocket. Figure 4.26 shows the absorption spectra of the Hyp-RA-βLG complex prepared in different orders. An excess amount of Hyp was used for the experiment in order to ensure that Hyp was in both pockets of the dimer (Figure 4.5).

Figure 4.27 shows the fluorescence emission of the Hyp-RA complex built in different orders. There are no substantial differences either in absorption or in fluorescence depending on the RA and Hyp addition's order.

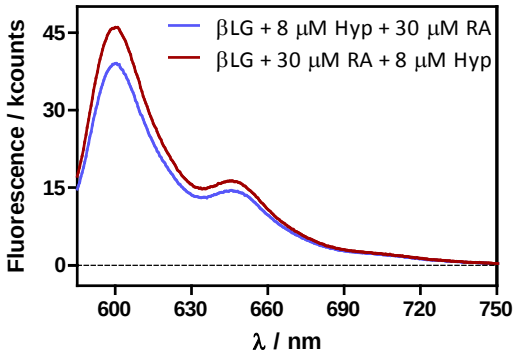

Figure 4.27. Fluorescence emission spectrum of Hyp-RA-βLG complex constituted in different addition's orders. Upon 60 μM of βLG, first was added 8 μM of Hyp and secondly 30 μM of RA (blue line). On the other case, upon the same amount of protein (60 μM of βLG), first was added 30 μM of RA and secondly 8 μM of Hyp (red line).

Therefore, for further experiments, the chosen order was to first prepare the protein-Hyp complex and then study the titration with increasing amounts of RA. Figure 4.28 shows the results of such study using 1 μM Hyp and 60 μM βLG, the same ratio used in section 4.3.1, for which mostly all the Hyp molecules are located in the highest affinity cavity (i.e., in the narrow cleft) of the protein dimer.

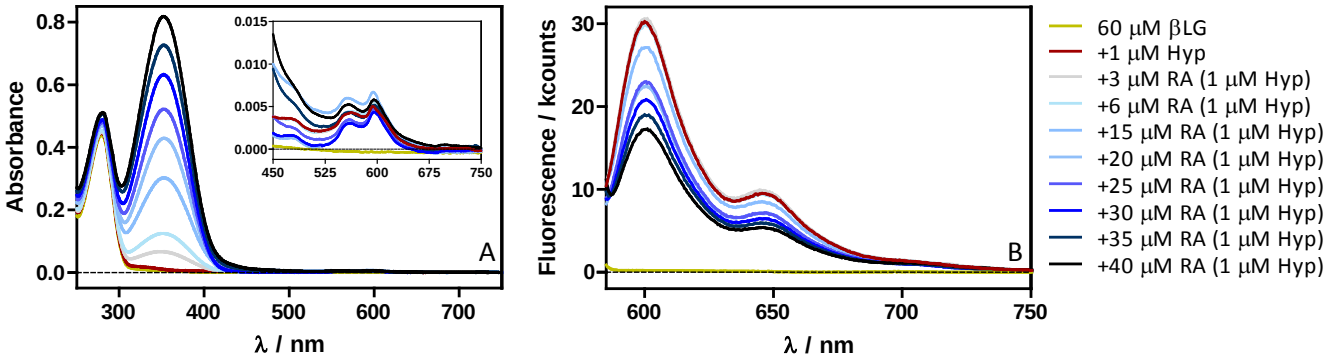

Figure 4.28. Absorption (A) and fluorescence emission (B) spectra of Hyp-RA-βLG mixtures at increasing RA concentrations (between 0 and 40 μM). The βLG and Hyp concentration were fixed at 60 and 1 μM, respectively. Emission spectra were collected after excitation at 554 nm.

It is worth noting that the difference in the absorbance at 554 nm is mostly due to some scattering and not to light absorption by RA (Figure 4.28, panel A). Surprisingly, the fluorescence of Hyp after excitation at 554 nm decreased upon addition of RA, which suggests some sort of quenching (panel B). An alternative explanation in terms of an inner filter effect by RA (plausible because the absorbance at 554 increases upon addition of RA) was safely ruled out after correcting the fluorescence intensity by the fraction of light absorbed by RA. Fluorescence quenching is the decrease of the quantum yield of fluorescence from a fluorophore induced by variety molecular interactions with quencher molecule, such as excited-state reaction, molecules rearrangement, energy transfer, ground state complex formation and collision quenching.[68] The different mechanisms of quenching are usually classified as either dynamic quenching or static quenching. Dynamic or collisional quenching refers to a process that the fluorophore and the quencher come into contact during the transient existence of the excited state. Static quenching refers to fluorophore–quencher complex formation.[69] In general, dynamic and static quenching can be distinguished by the difference of their fluorescence, or by their different dependence on temperature and viscosity.[59]

In order to elucidate the process which was taken part, the fluorescence quenching data were analysed by Stern-Volmer plots (Figure 4.28).

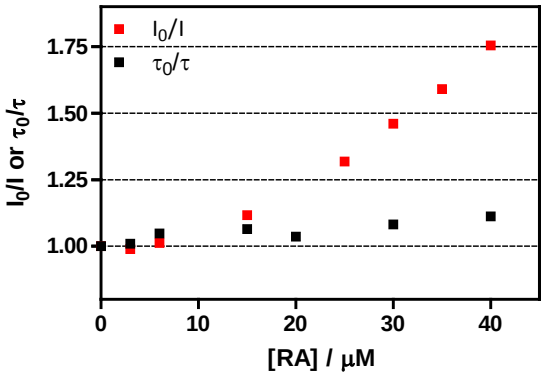

Figure 4.29. Stern-Volmer plot of the fluorescence intensities ratio or excited state lifetimes of the Hyp-βLG complex in the absence (I_0 or τ_0) and presence of different RA concentrations.

The Stern-Volmer relationship for dynamic quenching is given by Eq. 4.1:

$$\frac{I_0}{I} = 1 + K_D Q \qquad \text{Eq. 4.1}$$

where I_0 and I are the fluorescence intensities of Hyp in the absence and presence of RA, respectively, Q is the concentration of RA and K_D is the dynamic Stern-Volmer quenching constant, related to the lifetime of the fluorophore. According to this equation, a linear relationship is expected in case of simple dynamic quenching. This is indeed the case when the Stern-Volmer plot is constructed from average fluorescence lifetimes (Figure 4.29). However,

the intensity data show a non-linear relationship with an upward curvature, indicating that in addition to collisional dynamic quenching non-luminescent aggregates are also formed (static quenching). An alternative explanation could be that RA forms aggregated, which would also lead to a non-linear Stern-Volmer plot.[70] However, this explanation is inconsistent with the linear plot observed using lifetimes.

The titration experiments were repeated for two higher concentrations of Hyp, namely 4 and 8 μM, maintaining the same βLG concentration and the same order of addition (Figure 4.30).

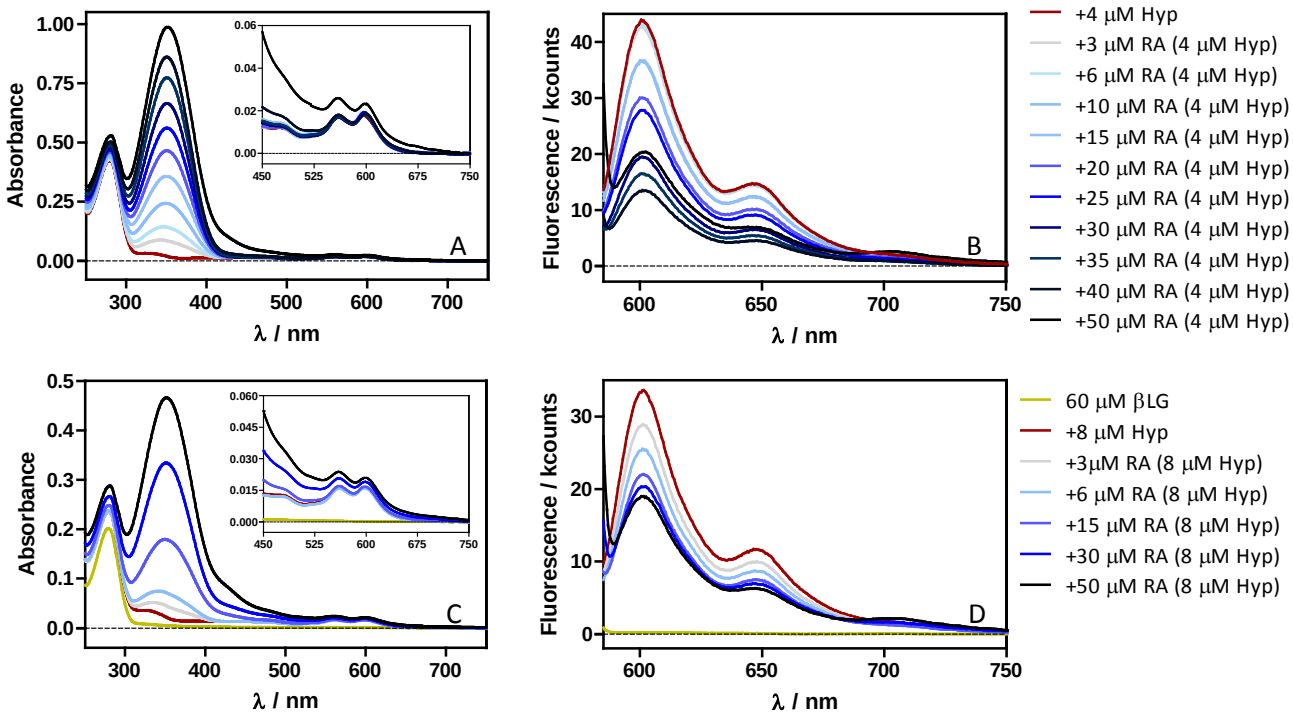

Figure 4.30. Absorption (A,C) and fluorescence emission (B,D) spectra of Hyp-RA-βLG mixtures at increasing RA concentrations (between 0 and 50 μM). The βLG was fixed at 60 and Hyp concentration was 4 μM for panel A and B, and 8 μM for panel C and D. Emission spectra were collected after excitation at 554 nm.

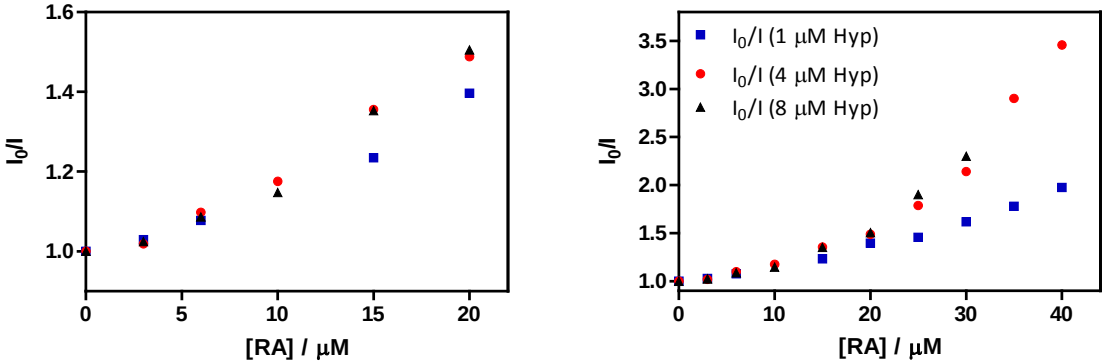

Figure 4.31. Stern-Volmer plot of Hyp-βLG complex with different Hyp concentrations (1, 4 and 8 μM) upon addition of increasing RA concentrations. Left panel shows until 20 μM of RA, whereas right panel shows until 40 μM RA.

Figure 4.31 shows the corresponding Stern-Volmer plots for three different Hyp concentrations. The curves present a first lineal part until 20 μM of RA (left panel), when either a static or

dynamic quenching process is dominant. Both processes may be competitive when the concentration is higher than 20 μM RA and the Stern-Volmer exhibits a nonlinear dependence (right panel). This increasingly upward trend is much more evident for 4 and 8 μM than for the lower Hyp concentration. Therefore, we decided to restrict the fit to the linear region in order to find the K_D using Eq. 4.1. The values found were independent of Hyp concentration, namely K_D = 2.3 x 10^4, 2.4 x 10^4 and 2.3 x 10^4 M^{-1}, for 1, 4 and 8 μM Hyp, respectively.

The value of static quenching constant, K_S, was obtained fitting the whole set of date with Eq. 4.2:

$$\frac{I_0}{I} = 1 + (K_D + K_S)[Q] + K_D K_S [Q]^2 \qquad \text{Eq. 4.2}$$

where K_S is the static fluorescence quenching constant and it is related to the critical concentration of the quencher above which the static quenching occurs. A plot was constructed showing (I_0/I-1)/ [Q] versus [Q] (not shown). A linear relationship was observed, from which K_S was determined to be 1.6 x 10^4, 4.9 x 10^4 and 4.6 x 10^4 M^{-1}, for 1, 4 and 8 μM Hyp, respectively. The increase in K_S at higher concentration of Hyp is consistent with the binding of two Hyp molecules by the βLG dimer at high Hyp concentrations.

Although it is difficult to elucidate the mechanistic details of the quenching, it is clear that both dynamic and static quenching occur.

A final study was done in order to assess whether RA can migrate from the protein to bacteria cells. An assay was carried out taking advantage of the facts that Hyp sticks to the protein and its fluorescence is quenched by RA. We reasoned that RA migration would restore the fluorescence of Hyp in the protein. This is exactly what was observed as shown Figure 4.32, where the fluorescence emission of Hyp-RA-βLG complexes containing 20 and 40 μM RA was recorded in the absence and presence of *S. aureus* bacteria.

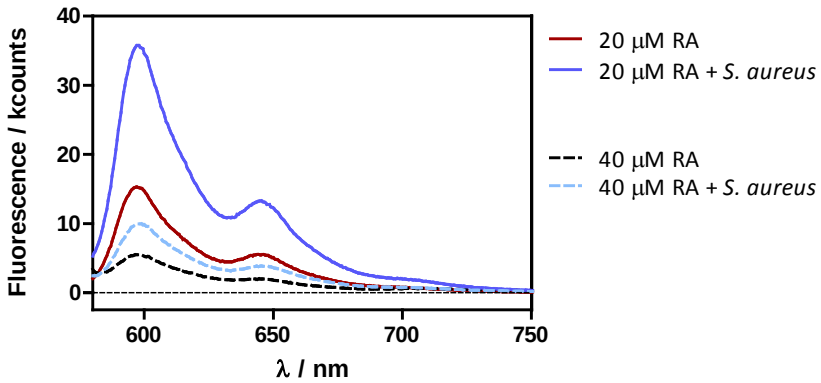

Figure 4.32. Fluorescence emission spectrum of Hyp-RA-βLG complex keeping constant the βLG and Hyp concentration at 60 μM and 8 μM, respectively. Additionaly, 20 μM (red line) or 40 μM (black segmented line) of RA was added. Blue lines shows the fluorescence emission upon addition of *S. aureus* cells for both complexes.

For both complexes, the fluorescence increased in the presence of cells, indicating that RA quenching process was no longer taking place. It is worth noting that the final fluorescence intensity was not the same for the complexes, indicating that RA was not completely removed from the complex, at least for the highest concentration.

Quenching process of the excited states of Hyp by RA was also studied by LFP. Figure 4.33 shows the time-resolved triplet absorption transients at 520 nm of Hyp-βLG complexes adding different amounts of RA and comparing with the transients in the presence of *S. aureus* cells.

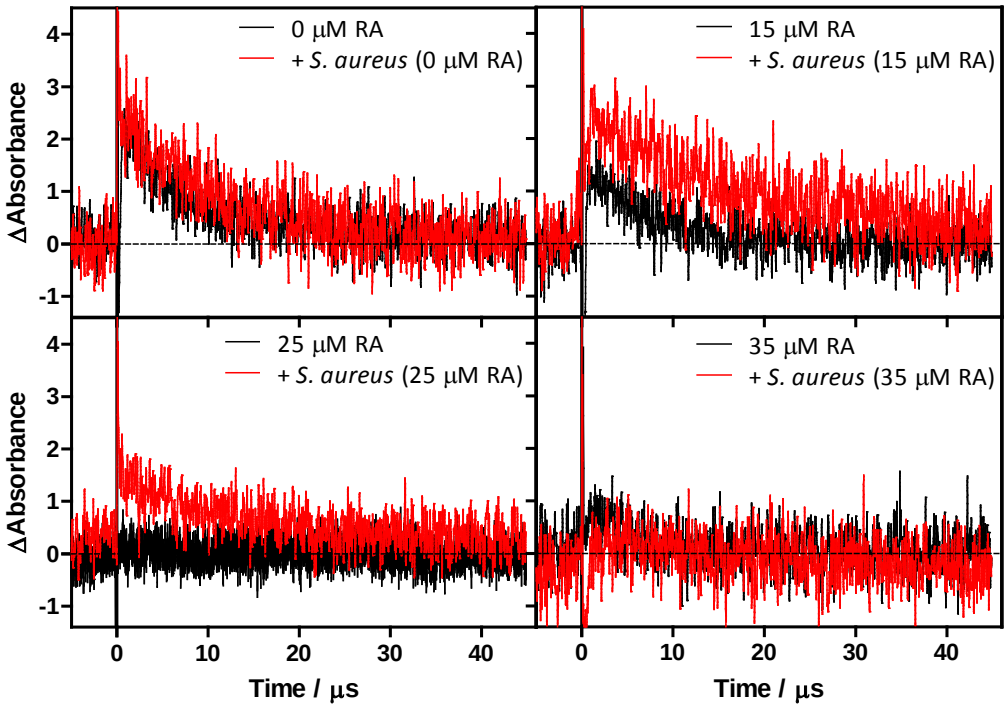

Figure 4.33. Time-resolved triplet absorption transients at 520 nm of Hyp-βLG complexes (60 μM of βLG and 15 μM of Hyp) with different RA concentrations (black transients). Each spectrum was compared with the complex in the same conditions but after 30 min of incubation with *S. aureus* cells (red transients). Transients were acquired after the excitation at 532 nm, 100 shots and with a T/div scale of 5 μs.

By comparing the black transients (without cells) in the four panels, it may be concluded that the production of triplet hypericin is quenched upon addition of RA. This is consistent with (and a consequence of) the quenching of fluorescence (i.e., of the singlet state, which is the precursor of the triplet state). Upon addition of cells, no change was observed in the absence of RA, consistent with Hyp remaining in the protein. When the complex contained RA, recovery of the triplet signal was observed, consistent with the migration of RA to the cells. Recovery was total at low RA concentration but only partial at higher concentrations, in agreement with the fluorescence studies.

To summarise, it has been successfully demonstrated that Hyp, RA and βLG form a ternary complex, the structure and stoichiometry of which depends on the concentrations of the two

ligands. Moreover, the fact that the Hyp photophysical properties are silenced (i.e., quenched) by RA while not in contact with bacteria, makes this system very attractive for the treatment of bacterial infections as it is photochemically unreactive until it is close to the target.

4.4. Conclusions

Hyp successfully binds to the milk whey protein βLG at the two hydrophobic cavities located at the interface of the protein homodimer, which can confer water-solubility and biocompatibility to the PS. The Hyp-2βLG system preserves the photophysical properties of the natural Hyp, although the presence of the wide cleft, capable of accommodating more than one PS molecule, and the partial exposure of bound Hyp to the aqueous environment, in general, lower and worsen the photophysical properties. Taking advantage of the known peculiar solvation properties of βLG, we show that it is possible to coat the dimeric protein with the co-solvent DMSO, which provides a better environment for the bound Hyp molecules and disrupts the Hyp aggregates. While this increases fluorescence, triplet, and singlet oxygen yields, it turns out that the presence of DMSO is detrimental to antibacterial treatments. Surprisingly, the complex resulted to be more effective against *S. aureus* cells when there is no DMSO. This most likely arises from a change in the interaction between Hyp-2βLG and the cellular constituents, which prevents the DMSO coated nanostructure from reaching more photosensitive regions in the bacterial wall. It has been demonstrated that the nanostructured complex has an interesting potential in dairy industry processes. It has been suggested to be introduced as an effective disinfectant for food manufacturing and handling materials.

The second part of the chapter demonstrated the formation of a complex between βLG and RA. RA seems to be placed close to the Trp19 cavity as demonstrated by a FRET process between this Trp and RA. The study of the RA-βLG complex in the monomeric and dimeric protein suggested that the binding site is the same in both conditions and it is not largely hindered in the dimer.

Finally, the double payload system formed by Hyp and RA bound to the protein was studied. Surprisingly, the fluorescence of Hyp was quenched by RA, which renders a photochemically safe delivery nanosystem. Both types of quenching (dynamic and static) were demonstrated to occur. The photophysical properties of the Hyp-βLG complex were restored in the presence of S. aureus bacteria due to the transfer of RA from the protein complex to the cells, which suggests a strong potential for the treatment of bacterial infections with this dual RA-Hyp system.

4.5. References

(1) *Guide to Prudent Use of Antimicrobial Agents in Dairy Production. Federation Internationale Du Lait-International Dairy Federation (IDF)*, **2013**.

(2) Dai, T.; Huang, Y. Y.; Hamblin, M. R. Photodynamic Therapy for Localized Infections- State of the Art. *Photodiagnosis Photodyn. Ther.* **2009**, *6*, 170–188.

(3) Kharkwal, G. B.; Sharma, S. K.; Huang, Y. Y.; Dai, T.; Hamblin, M. R. Photodynamic Therapy for Infections: Clinical Applications. *Lasers Surg. Med.* **2011**, *43*, 755–767.

(4) Luksiene, Z.; Brovko, L. Antibacterial Photosensitization-Based Treatment for Food Safety. *Food Eng. Rev.* **2013**, *5*, 185–199.

(5) WHO | Food safety http://www.who.int/mediacentre/factsheets/fs399/en/ (accessed Sep 19, 2017).

(6) Akbar, A.; Anal, A. K. Food Safety Concerns and Food-Borne Pathogens, Salmonella, Escherichia Coli and Campylobacter. *Fuuast J. Biol.* **2011**, *1*, 5–17.

(7) Doyle, M. E.; Ellin Doyle, M.; Hartmann, F. A.; Wong, A. C. L. *White Paper on Sources of Methicillin-Resistant Staphylococcus Aureus (MRSA) and Other Methicillin-Resistant Staphylococci: Implications for Our Food Supply?*, **2011**.

(8) Nafee, N.; Youssef, A.; El-Gowelli, H.; Asem, H.; Kandil, S. Antibiotic-Free Nanotherapeutics: Hypericin Nanoparticles Thereof for Improved in Vitro and in Vivo Antimicrobial Photodynamic Therapy and Wound Healing. *Int. J. Pharm.* **2013**, *454*, 249–258.

(9) Flower, D. R.; North, A. C.; Sansom, C. E. The Lipocalin Protein Family: Structural and Sequence Overview. *Biochim. Biophys. Acta,* **2000**, *1482*, 9–24.

(10) Åkerström, B.; Borregaard, N.; Flower, R.; Salier, J. P. *Lipocalins*; Landes Bioscience: Austin, TX, **2006**.

(11) Mercadante, D.; Melton, L. D.; Norris, G. E.; Loo, T. S.; Williams, M. A. K.; Dobson, R. C. J.; Jameson, G. B. Bovine β-Lactoglobulin Is Dimeric under Imitative Physiological Conditions: Dissociation Equilibrium and Rate Constants over the pH Range of 2.5-7.5. *Biophys. J.* **2012**, *103*, 303–312.

(12) Le Maux, S.; Bouhallab, S.; Giblin, L.; Brodkorb, A.; Croguennec, T. Bovine β-Lactoglobulin/fatty Acid Complexes: Binding, Structural, and Biological Properties. *Dairy Sci. Technol.* **2014**, *94*, 409–426.

(13) Lange, D. C.; Kothari, R.; Patel, R. C.; Patel, S. C. Retinol and Retinoic Acid Bind to a Surface Cleft in Bovine Beta-Lactoglobulin: A Method of Binding Site Determination Using Fluorescence Resonance Energy Transfer. *Biophys. Chem.* **1998**, *74*, 45–51.

(14) Cho, Y.; Batt, C. A.; Sawyer, L. Probing the Retinol-Binding Site of Bovine β-Lactoglobulin. *J. Biol. Chem.* **1994**, *269*, 11102–11107.

(15) Sinha, P.; Srivastava, S.; Mishra, N.; Yadav, N. P. New Perspectives on Antiacne Plant Drugs: Contribution to Modern Therapeutics. *Biomed Res. Int.* **2014**, *2014*, 301304.

(16) Sparavigna, A.; Tenconi, B.; De Ponti, I.; La Penna, L. An Innovative Approach to the Topical Treatment of Acne. *Clin. Cosmet. Investig. Dermatol.* **2015**, *8*, 179–185.

(17) Larissa, S. A.; Perussi, J. R. Effectiveness of Hypericin in Decreasing the Population of Propionibacterium Acnes. *Photodiagnosis Photodyn. Ther.* **2015**, *12*, 355.

(18) Chen, M.-C.; Hsu, S.-L.; Lin, H.; Yang, T.-Y. Retinoic Acid and Cancer Treatment. *BioMedicine,* **2014**, *4*, 22.

(19) Brownlow, S.; Morais Cabral, J. H.; Cooper, R.; Flower, D. R.; Yewdall, S. J.; Polikarpov, I.; North, A. C.; Sawyer, L. Bovine Beta-Lactoglobulin at 1.8 A Resolution-Still an Enigmatic Lipocalin. *Structure,* **1997**, *5*, 481–495.

(20) Friesner, R. A.; Banks, J. L.; Murphy, R. B.; Halgren, T. A.; Klicic, J. J.; Mainz, D. T.; Repasky, M. P.; Knoll, E. H.; Shelley, M.; Perry, J. K.; *et al.* Glide: A New Approach for Rapid, Accurate Docking and Scoring. 1. Method and Assessment of Docking Accuracy. *J. Med. Chem.* **2004**, *47*, 1739–1749.

(21) Halgren, T. A.; Murphy, R. B.; Friesner, R. A.; Beard, H. S.; Frye, L. L.; Pollard, W. T.; Banks, J. L. Glide: A New Approach for Rapid, Accurate Docking and Scoring. 2. Enrichment Factors in Database Screening. *J. Med. Chem.* **2004**, *47*, 1750–1759.

(22) Jorgensen, W. L.; Chandrasekhar, J.; Madura, J. D.; Impey, R. W.; Klein, M. L. Comparison of Simple Potential Functions for Simulating Liquid Water. *J. Chem. Phys.* **1983**, *79*, 926–935.

(23) Wang, J.; Wolf, R. M.; Caldwell, J. W.; Kollman, P. A.; Case, D. A. Development and Testing of a General Amber Force Field. *J. Comput. Chem.* **2004**, *25*, 1157–1174.

(24) Joung, I. S.; Cheatham, T. E. Molecular Dynamics Simulations of the Dynamic and Energetic Properties of Alkali and Halide Ions Using Water-Model-Specific Ion Parameters. *J. Phys. Chem. B,* **2009**, *113*, 13279–13290.

(25) Alvarez-Garcia, D.; Barril, X. Relationship between Protein Flexibility and Binding: Lessons for Structure-Based Drug Design. *J. Chem. Theory Comput.* **2014**, *10*, 2608–2614.

(26) and, T. F.; Kollman*, P. A. Application of the RESP Methodology in the Parametrization of Organic Solvents. **1998**.

(27) Bayly, C. I.; Cieplak, P.; Cornell, W.; Kollman, P. A. A Well-Behaved Electrostatic Potential Based Method Using Charge Restraints for Deriving Atomic Charges: The RESP Model. *J. Phys. Chem.* **1993**, *97*, 10269–10280.

(28) Price, D. J.; Brooks, C. L. A Modified TIP3P Water Potential for Simulation with Ewald Summation. *J. Chem. Phys.* **2004**, *121*, 10096–10103.

(29) Miyamoto, S.; Kollman, P. A. Settle: An Analytical Version of the SHAKE and RATTLE Algorithm for Rigid Water Models. *J. Comput. Chem.* **1992**, *13*, 952–962.

(30) Maier, J. A.; Martinez, C.; Kasavajhala, K.; Wickstrom, L.; Hauser, K. E.; Simmerling, C. ff14SB: Improving the Accuracy of Protein Side Chain and Backbone Parameters from ff99SB. *J. Chem. Theory Comput.* **2015**, *11*, 3696–3713.

(31) Dufour, E.; Genot, C.; Haertlé, T. β-Lactoglobulin Binding Properties during Its Folding Changes Studied by Fluorescence Spectroscopy. *Biochim. Biophys. Acta,* **1994**, *1205*, 105–112.

(32) Rodríguez-Amigo, B.; Delcanale, P.; Rotger, G.; Juárez-Jiménez, J.; Abbruzzetti, S.; Summer, A.; Agut, M.; Luque, F. J.; Nonell, S.; Viappiani, C. The Complex of Hypericin with β-Lactoglobulin Has Antimicrobial Activity with Potential Applications in Dairy Industry. *J. Dairy Sci.* **2015**, *98*, 89–94.

(33) Miškovský, P.; Jancura, D.; Sánchez-Cortés, S.; Kočišová, E.; Chinsky§, L. Antiretrovirally Active Drug Hypericin Binds the IIA Subdomain of Human Serum Albumin: Resonance Raman and Surface-Enhanced Raman Spectroscopy Study. *J. Am. Chem. Soc.* **1998**, *120*, 6374–6379.

(34) Delcanale, P.; Rodriguez Amigo, B.; Juárez-Jiménez, J.; Luque, J.; Abbruzzetti, S.; Agut, M.; Nonell, S.; Viappiani, C. Tuning the Local Solvent Composition at a Drug Carrier Surface: Effect of Dimethyl Sulfoxide/water Mixture on the Photofunctional Properties of Hypericin-β-Lactoglobulin. *J. Mater. Chem. B,* **2017**, *5*, 1633–1641.

(35) Arakawa, T.; Kita, Y.; Timasheff, S. N. Protein Precipitation and Denaturation by Dimethyl Sulfoxide. *Biophys. Chem.* **2007**, *131*, 62–70.

(36) Mattos, C.; Ringe, D. Locating and Characterizing Binding Sites on Proteins. *Nat. Biotechnol.* **1996**, *14*, 595–599.

(37) Liepinsh, E.; Otting, G. Organic Solvents Identify Specific Ligand Binding Sites on Protein Surfaces. *Nat. Biotechnol.* **1997**, *15*, 264–268.

(38) English, A. C.; Groom, C. R.; Hubbard, R. E. Experimental and Computational Mapping of the Binding Surface of a Crystalline Protein. *Protein Eng.* **2001**, *14*, 47–59.

(39) Alvarez-Garcia, D.; Barril, X. Molecular Simulations with Solvent Competition Quantify Water Displaceability and Provide Accurate Interaction Maps of Protein Binding Sites. *J. Med. Chem.* **2014**, *57*, 8530–8539.

(40) Vondracek, H.; Dielmann-Gessner, J.; Lubitz, W.; Knipp, M.; Havenith, M. THz Absorption Spectroscopy of Solvated β-Lactoglobulin. *J. Chem. Phys.* **2014**, *141*, 22D534.

(41) Ebbinghaus, S.; Kim, S. J.; Heyden, M.; Yu, X.; Heugen, U.; Gruebele, M.; Leitner, D. M.; Havenith, M. An Extended Dynamical Hydration Shell around Proteins. *Proc. Natl. Acad. Sci. U. S. A.* **2007**, *104*, 20749–20752.

(42) Ebbinghaus, S.; Meister, K.; Born, B.; DeVries, A. L.; Gruebele, M.; Havenith, M. Antifreeze Glycoprotein Activity Correlates with Long-Range Protein−Water Dynamics. *J. Am. Chem. Soc.* **2010**, *132*, 12210–12211.

(43) Magde, D.; Elson, E.; Webb, W. W. Thermodynamic Fluctuations in a Reacting System—measurement by Fluorescence Correlation Spectroscopy. *Phys. Rev. Lett.* **1972**, *29*, 705–708.

(44) Haustein, E.; Schwille, P. Fluorescence Correlation Spectroscopy: Novel Variations of an Established Technique. *Annu. Rev. Biophys. Biomol. Struct.* **2007**, *36*, 151–169.

(45) Cowie, J. M. G.; Toporowski, P. M. Association in the Binary Liquid System Dimethyl Sulphoxide -Water. *Can. J. Chem.* **1961**, *39*, 2240–2243.

(46) LeBel, R. G.; Goring, D. A. I. Density, Viscosity, Refractive Index, and Hygroscopicity of Mixtures of Water and Dimethyl Sulfoxide. *J. Chem. Eng. Data,* **1962**, *7*, 100–101.

(47) Comas-Barceló, J.; Rodríguez-Amigo, B.; Abbruzzetti, S.; Rey-Puech, P. del; Agut, M.; Nonell, S.; Viappiani, C. A Self-Assembled Nanostructured Material with Photosensitising Properties. *RSC Adv.* **2013**, *3*, 17874–17879.

(48) Miyamoto, H.; Yampolski, Y.; Young, C. L.; Yampol'skii, Y.; Young, C. IUPAC-NIST Solubility Data Series. 103. Oxygen and Ozone in Water, Aqueous Solutions, and Organic Liquids. *J. Phys. Chem. Ref. Data,* **2014**, *43*, 33102.

(49) Loch, J. I.; Bonarek, P.; Polit, A.; Riès, D.; Dziedzicka-Wasylewska, M.; Lewiński, K. Binding of 18-Carbon Unsaturated Fatty Acids to Bovine β-lactoglobulin—Structural and Thermodynamic Studies. *Int. J. Biol. Macromol.* **2013**, *57*, 226–231.

(50) Kontopidis, G.; Holt, C.; Sawyer, L. The Ligand-Binding Site of Bovine β-Lactoglobulin: Evidence for a Function? *J. Mol. Biol.* **2002**, *318*, 1043–1055.

(51) Kontopidis, G.; Holt, C.; Sawyer, L. β-Lactoglobulin: Binding Properties, Structure, and Function. *J. Dairy Sci.* **2004**, *87*, 785–796.

(52) Layton, A. The Use of Isotretinoin in Acne. *Dermatoendocrinol.* **2009**, *1*, 162–169.

(53) Acta, B. Spectroscopic Characterization of β-Lactoglobulin-Retinol Complex. *Biochim. Biophys. Acta,* **1980**, *5*, 28–42.

(54) Zsila, F.; Bikádi, Z.; Simonyi, M. Retinoic Acid Binding Properties of the Lipocalin Member β-Lactoglobulin Studied by Circular Dichroism, Electronic Absorption Spectroscopy and Molecular Modeling Methods. *Biochem. Pharmacol.* **2002**, *64*, 1651–1660.

(55) Rathi, S. K. Acne Vulgaris Treatment: The Current Scenario. *Indian J. Dermatol.* **2011**, *56*, 7–13.

(56) Lai, F.; Pireddu, R.; Corrias, F.; Fadda, A. M.; Valenti, D.; Pini, E.; Sinico, C. Nanosuspension Improves Tretinoin Photostability and Delivery to the Skin. *Int. J. Pharm.* **2013**, *458*, 104–109.

(57) Futterman, S.; Heller, J. The Enhancement of Fluorescence and the Decreased Susceptibility to Enzymatic Oxidation of Retinol Complexed with Bovine Serum Albumin, β-Lactoglobulin, and the Retinol-Binding Protein of Human Plasma. *J. Biol. Chem.* **1972**, *247*, 5168–5172.

(58) Hattori, M.; Watabe, A.; Takahashi, K. β-Lactoglobulin Protects β-Ionone Related Compounds from Degradation by Heating, Oxidation, and Irradiation. *Biosci. Biotech. Biochem.* **1995**, *59*, 2295–2297.

(59) Lakowicz, J. R. *Principles of Fluorescence Spectroscopy*; Third Edit.; Springer: Maryland, USA, **2006**.

(60) Liang, L.; Subirade, M. β-Lactoglobulin/Folic Acid Complexes : Formation, Characterization, and Biological Implication. *J. Phys. Chem. B,* **2010**, *114*, 6707–6712.

(61) Dufour, E.; Marden, M. C.; Haertlé, T. β-Lactoglobulin Binds Retinol and Protoporphyrin IX at Two Different Binding Sites. *FEBS Lett.* **1990**, *277*, 223–226.

(62) Portugal, C. A. M.; Crespo, J. G.; Lima, J. C. Anomalous "unquenching" of the Fluorescence Decay Times of β-Lactoglobulin Induced by the Known Quencher Acrylamide. *J. Photochem. Photobiol. B Biol.* **2006**, *82*, 117–126.

(63) Albani, J. R.; Vogelaer, J.; Bretesche, L.; Kmiecik, D. Tryptophan 19 Residue Is the Origin of Bovine β-Lactoglobulin Fluorescence. *J. Pharm. Biomed. Anal.* **2014**, *91*, 144–150.

(64) Lakowicz, J. R. Time-Resolved Protein Fluorescence. In *Principles of Fluorescence Spectroscopy*; Springer, **2006**; 577–606.

(65) Albani, J.-R. Sub-Structures Formed in the Excited State Are Responsible for Tryptophan Residues Fluorescence in β-Lactoglobulin. *J. Fluoresc.* **2011**, *21*, 1683–1687.

(66) Creamer, L. K. Effect of Sodium Dodecyl Sulfate and Palmitic Acid on the Equilibrium Unfolding of Bovine β-Lactoglobulin. *Biochemistry,* **1995**, *34*, 7170–7176.

(67) Khorsand, A. S.; Mahmoodian, M. M.; P., M.; Reza, S. M.; Chamani, J. A Comparison Study of the Interaction between β - Lactoglobulin and Retinol at Two Different Conditions : Spectroscopic and Molecular Modeling Approaches. *J Biomol Struct Dyn,* **2014**, *33*, 1880–1898.

(68) Lindon, J. C.; Tranter, G. E.; Koppenaal, D. W. *Encyclopedia of Spectroscopy and Spectrometry*; Third Edit. **2016**.

(69) Tan, M.; Liang, W.; Luo, X.; Gu, Y. Fluorescence Spectroscopy Study on the Interaction between Evodiamine and Bovine Serum Albumin. *J. Chem.* **2012**, *2013*, 1–6.

(70) Bejoymohandas, K. S.; George, T. M.; Bhattacharya, S.; Natarajan, S.; Reddy, M. L. P. AIPE-Active Green Phosphorescent Iridium (III) Complex Impregnated Test Strips for the Vapor-Phase Detection of 2,4,6-Trinitrotoluene (TNT). *J. Mater. Chem. C,* **2014**, *2*, 515–523.

CHAPTER 5

Liposomes with Protoporphyrin IX and CPT-11 as a drug delivery system with dual therapeutic activity in cancer

Liposomes with their high loading capacity and their flexibility to accommodate different agents either hydrophilic or hydrophobic came into focus as valuable carriers for their use in PDT combined therapies. This chapter describes the development of a liposomal formulation containing PpIX and the chemotherapeutic drug CPT-11. The photophysical properties and their effect *in vitro* against cancer cells were assessed in order to prove the effectiveness of the dual therapy in comparison with the individual treatments.

The work described in this chapter has been carried out in collaboration with the group of Dr. Angeles Villanueva at the Universidad Autónoma de Madrid. (Spain).

5.1. Introduction

Despite being one of the first DDS used and studied, liposomes are still a common resource because of the many opportunities they offer. These spherical vesicles can be formulated in different sizes, composition, charge and lamellarity, which ultimately modulate their ability to incorporate drugs, thereby increasing the efficacy and reducing the side effects and toxicity of the encapsulated agent.[1] Moreover, liposomes are non-toxic *per se*, flexible, biocompatible, completely biodegradable, and non-immunogenic for systemic and non-systemic administrations.[2]

Despite extraordinary advances over the last decade, cancer chemotherapy still has two major limitations: the low selectivity of the drugs, leading to serious side effects, and the emergence of resistance, which limits the effectiveness of the drugs. Because such limitations affect increasingly larger segments of the population as it grows older, alternative approaches and strategies must be sought that could positively impact on these issues. PDT is a particular form of chemotherapy in which light is used to activate a photosensitising drug, which confines the therapeutic effect to the illuminated region. Several characteristics make it particularly attractive: the safety of photosensitising drugs in the absence of light, the absence of clear resistance mechanisms due to its multitargeted action, and the absence of severe side effects, which enable virtually unlimited repeat treatments. PDT has not yet reached the necessary development to become first-choice treatment except for a very small number of indications. However, during the last years it has been considered a perfect treatment modality to use in combination with chemotherapy. Combination therapies are a current cornerstone of cancer therapy, either combining similar drugs that work on different targets (e.g., co-administration of two chemotherapeutic agents), or combining drugs whose mechanisms of action go through completely different pathways (e.g., co-administration of a chemotherapeutic agent and a PS). This chapter will focus on this last scenario.

PDT in combination with conventional and approved antineoplastic drugs may overcome some of the limitations of chemotherapy, without overlapping toxicities. The advantages of combining both modalities are that they target different key signals transduction pathways and should be more efficient in destroying cancer cells, eluding the cellular resistance mechanisms. Indeed, few reports and preclinical studies show that the combined treatment allow the reduction of the dosage of individual drugs and consequently the lessening of important side effects, while the overall efficacy is preserved or even increased.[3–7]

Furthermore, the recent advances in nanotechnology enable the incorporation of various pharmaceutical components in a single nanoplatform, which facilitates the selective delivery of the drug and the PS to the same cell and with the optimum ratio. Moreover, encapsulation in nanocarriers can significantly improve the accumulation of the therapeutic agent in the target tumour tissue through the EPR effect and protect both agents from their inactivation in the biological environment.[8] Liposome size, surface charge, and bilayer fluidity can be modulated by handling properly bilayer lipid composition and by choosing suitable preparation conditions, which determines the behaviour of the vector both *in vitro* and *in vivo*. The control of the physical parameters can be responsible for improving the efficacy of the encapsulated drug. Thus, liposomes with rigid bilayers are, for instance, more stable *in vivo* because the penetration and adsorption of blood opsonins to their surface becomes hindered. Consequently, the use of rigid liposomes decreases their uptake by the reticuloendothelial system, resulting in a decrease of their clearance from the bloodstream, solving the problem of the small circulation half-life of conventional liposomes.[9] Knowledge of how the lipid composition affects their properties as a DDS is a cornerstone in order to yield the perfect carrier.

Therefore, herein we present a dual liposome system that co-encapsulates PpIX as the PDT agent and irinotecan (CPT-11) as the chemotherapeutic drug. This system has been characterised and compared with the properties of its unimodal counterparts (i.e., liposomes that encapsulate only one agent). Moreover, we studied the photophysical properties and their $^1O_2$ production. The cell studies, most of them carried out at the Universidad Autónoma de Madrid by the group of Dr. Angeles Villanueva, provided us with the cell viability results and the study of the cell morphology. Also for cell studies, unimodal and bimodal liposome preparations were studied and compared. Moreover, two different scenarios were constructed to reflect the importance of administering both agents in the same vehicle: unimodal liposomes given in combination or bimodal liposomes which contain both agents in the same carrier. Finally, the optimised system was functionalised and covalently linked to a monoclonal antibody for active targeting.

5.2. Experimental section

5.2.1. Materials

The phospholipids *L*-α-distearoyl-phosphathidylcholine (DSPC), *L*-α-dioleoyl-phosphathidyl-serine (sodium salt) (DOPS), and cholesterol (CHOL) were purchased from Avanti Polar Lipids (Birmingham, USA). Irinotecan hydrochloride trihydrate (CPT-11) was acquired from Afine Chemicals Limited (Hangzhou, China), with a purity grade of ≥ 99%. PpIX was obtained from Frontier Scientific (Lancashire, United Kingdom). *D,L*-lactic acid was purchased from Sigma-

Aldrich Chemical Co. (St. Louis, MO, USA). Tetrahydrofuran HPLC grade without stabiliser (THF), the solvent in which the liposomes were disrupted, was acquired from Scharlab (Barcelona, Spain). *Meso*-tetraphenylporphyrin (TPP), quinine sulphate monohydrate and Rose Bengal (RB), used as references, were acquired from Sigma-Aldrich Chemical Co. (St. Louis, MO, USA). All other chemicals were commercially available reagents of at least analytical grade. Milli-Q water (Millipore Bedford, Massachusetts system, resistivity of 18 MΩ cm) was used.

The dialysis tubing cellulose membrane with a cut-off of 12-14 kDa was purchased from Sigma Aldrich. Polyester Chromafil® filters from Macherey-Nagel (Düren, Germany) were used for sterilising the formulations with a pore size of 0.20 μm and a diameter of 25 mm.

5.2.2. Preparation of unimodal and bimodal liposomes

Intermediate unilamellar liposomes (IUVs) were prepared by microemulsification method, using a ternary mixture of DSPC:DOPS:CHOL in a molar ratio of 65:35:30. In order to obtain the unimodal liposomes, the appropriate amount of CPT-11 or PpIX were added to the ternary lipid mixture, maintaining the lipid:drug molar ratio at 7.5:1 or 150:1, respectively. Separately, the bimodal liposomes were prepared to add both agents to the ternary lipid mixture keeping the previously mentioned lipid:drug molar ratio. The mixture of lipids and drug(s) were dissolved in the minimum amount of chloroform, together with a small amount of methanol to obtain a clear solution. The organic solvents were evaporated by rotary evaporation yielding a thin lipid film on the sides of a round bottom flask. Formulations containing PpIX prior to $CHCl_3$ evaporation were kept protected from light during 1 h in order to facilitate the contact lipids/PS. The dried film was maintained overnight in a vacuum desiccator with P_2O_5 to remove all the solvent traces. The multilamellar vesicles (MLV) were formed by hydrating the film with the appropriate volume of 10 mM (pH 4.4) lactate buffer to a final lipid concentration of 10 mg/mL. MLVs dispersions remained during 15 min in a thermostatic bath, with a temperature set above the T_m. Then, the mixture was vortexed during 30 min, alternating periods of 30 s in the bath and 30 s vortexing. At this point, MLVs dispersions were frozen (liquid N_2) and thawed (water bath) five times, bath-sonicated for 15 min at $T > T_m$ and, finally, microemulsified (EmulsiFlex B3 device, Avestin, Ottawa, Canada). Microemulsification was carried out by pumping the fluid 10 cycles through the interaction chamber at 110 kPa.

Control blank liposomes (i.e., liposomes without encapsulated drugs) were prepared in the same way but without the addition of PpIX or CPT-11. All liposome preparations were sterilised by filtration with a 0.20 μm diameter filter and stored in the dark at 4 ºC.

5.2.3. Liposome characterisation

Determination of the total CPT-11 and PpIX content

THF was added to a known aliquot of liposome suspension (liposome aliquot/THF; 1:50 v/v), in order to disrupt the bilayer and release the loading. The vials were closed, stirred and heated above the T_m for 30 min, which enabled a quick rupture of the bilayers.

The concentration of both PpIX and CPT-11 was quantified spectrophotometrically by using calibration curves obtained under the same conditions. PpIX was quantified by fluorescence emission (Spex-Fluoromax 4, Horiba Jobin Yvon, Edison, NJ) at λ_{max} 632 nm (λ_{exc} 504 nm), whereas the CPT-11 was quantified by absorbance measurements (Varian Cary 6000i, Varian Inc., Palo Alto, CA) at λ_{max} 368 nm.

In the case of bimodal liposomes, the PpIX concentration was also evaluated by fluorescence at λ_{max} 632 nm (λ_{exc} 504 nm), while CPT-11's determination was more elaborate because both agents absorb at 368 nm. Thus, the content of CPT-11 was determined by measuring the total absorbance at 368 nm and subtracting the absorbance of PpIX.

Determination of the non-encapsulated PpIX and CPT-11 fraction

The fraction of non-encapsulated CPT-11 was quantified by filtration and centrifugation with Centricon YM-10 Filter Devices (EMD Millipore Corporation, Billerica, Massachusetts), which have hydrophilic cellulose membranes that allow molecules < 10 kDa pass through. An aliquot of 200 μL of the liposome suspension was introduced in these devices and was centrifuged at 14,000g for 30 min at 4 ºC (refrigerated centrifuge 3-30KS, Sigma, Osterode am Harz, Germany). The filtrate was resuspended in 10 mM lactate buffer and the absorbance was measured at 369 nm and compared with its calibration curve (0.002–0.01 mg/mL). The percentage encapsulation and drug concentration were obtained from the difference between total and non-entrapped CPT-11.

On the other hand, the fraction of non-encapsulated PpIX was determined by centrifugation of a known aliquot of liposomes at 5000 rpm during 10 min (refrigerated centrifuge 3-30KS, Sigma, Osterode am Harz, Germany). Non-encapsulated PpIX forms aggregates in the external aqueous buffer and precipitates, accumulating in the pellet during centrifugation, unlike IUVs. Once the supernatant was removed, the pellet was resuspended in a known volume of THF and then its fluorescence was measured and compared with its calibration curve (0.0001–0.001 mg/mL, slits 3) at λ_{max} 632 nm (λ_{exc} 504 nm). The percentage encapsulation and drug concentration were calculated from the difference between total and non-entrapped PpIX.

Determination of the lipid content

The amount of lipids in the liposome suspensions was measured following Stewart's method.[10] This methodology is based on the formation of a reddish complex between the phospholipid and ammonium ferrothiocyanate, which is soluble in chloroform. Calibration curves for each lipid composition (0.01–0.1 mg lipid) were obtained. Chloroform and ammonium ferrothiocyanate (1:1, v/v, usually 2 mL) were added to 10-12 μL aliquots of the sample in order to form this colorimetric complex. The organic phase, extracted after vortexing and centrifugation 2000 rpm during 20 min (centrifuge Nüve NF 400R, Ankara, Turkey), was used to select the absorbance maximum. Measurements were carried out in a Beckman DU40 spectrophotometer (Beckman Coulter, Inc., Fullerton, California), reading at 465 nm. The lipid concentration was ultimately determined by comparison with the calibration curve.

Vesicle Size and ζ potential

The size and size distribution of liposomes were determined by photon correlation spectroscopy (PCS), while the ζ-potential were measured using laser Doppler electrophoresis. In both cases, the instrument was a Zetasizer Nano-ZS (Malvern Instruments Ltd, Malvern, UK) equipped with an optic unit containing a 4 mW He-Ne laser (Spectra Physics, Santa Clara, USA) and an electrophoresis cell. The device was calibrated with standard carboxy-modified polystyrene latex samples. Measurements were performed at 25 ºC and λ_{exc}= 633 nm, using liposomal suspensions containing ~0.2 mg lipid/mL of 10 mM, pH 4.4, lactate buffer.

Control of the liposome suspensions stability

The stability of liposomes during storage was controlled by measuring their size over time. In addition, absorbance spectra were collected to monitor whether any turbidity or scattering increased over storage time.

Drug loading and entrapment efficiency calculation

Drug loading (DL) and entrapment efficiency (EE) of the PS and the chemotherapeutic drug were calculated as follows:

$$DL\ \%\ (w/w) = \frac{mass\ of\ drug/PS\ encapsulated\ (mg)}{mass\ of\ lipids\ (mg)} \cdot 100$$

$$EE\ \%\ (w/w) = \frac{mass\ of\ drug/PS\ encapsulated\ (mg)}{mass\ of\ drug/PS\ theoretically\ encapsulated\ (mg)} \cdot 100$$

The theoretical value of drug encapsulated was the total drug concentration measured and quantified before the sterilisation by filtration in order to know which percentage is lost.

5.2.4. Cell cultures

The tumour epithelial HeLa cells (human cervix adenocarcinoma, ATCC CCL-2) were purchased from American Type Culture Collection (USA). Cells were grown as monolayer attached cultures in DMEM supplemented with 10% (v/v) Fetal Calf Serum (FCS), 50 U/mL penicillin and 50 μg streptomycin/mL (whole media), all acquired from Thermo Fisher Scientific (Merck Millipore, Billerica, MA, USA). Cells were cultured under a 5% CO_2 atmosphere plus 95% air at 37 ºC, and maintained in a SteriCult 200 (Hucoa- Erloss, Madrid, Spain) incubator. Depending on the experiment, cells were seeded in 25 cm^2 flasks (F25) or in 24-well plates with or without 10 mm square coverslips. Subconfluent cell cultures were used with a cell density of at least 3000 cell/cm^2 72 h before starting the experiments. The cell density was assessed with a Bürker counting chamber. All the plastic materials were purchased from Corning (Nueva York, EE UU).

Photodynamic treatments in vitro

Cells seeded in 24-well plates (with or without coverslip) or F25 flasks, depending on subsequent processing, received photodynamic treatments with either the PpIX unimodal liposomes or the bimodal liposomes with CPT-11. Accordingly, cells were incubated for 24 h with 2.5 μM PpIX liposome suspension in lactate buffer, washed three times with medium (not serum supplemented) and maintained in whole medium during irradiation and post-treatment time. Irradiations were performed by means of a red light-emitting diode (LED Par 64, Showtec; Shoreham, UK) device (λ= 633 ± 9 nm) with a fluence rate of 7 $mW \cdot cm^{-2}$. Cells were irradiated for 4.5 min, corresponding to total light dose of 2 $J \cdot cm^{-2}$ (total light dose ($J \cdot cm^{-2}$)= fluence rate ($W \cdot cm^{-2}$) x treatment time (s)). Either immediately or at different times after irradiation different methodological protocols were performed. Besides, experiments were carried out by incubation with the corresponding blank or empty liposomes or the loaded liposomes without irradiation (dark toxicity), in order to examine possible cytotoxic effect exercised by the lipid or the PS.

Cell viability studies

Dark- and photo-toxicity was assessed by the MTT colorimetric assay 24 h after treatments. This method evaluates the number of viable cells based on the mitochondrial activity, involving a reduction of the MTT to its insoluble formazan, a purple colour compound only soluble in organic solvents. Immediately prior to use, a stock solution of dimethylthiazolyl-diphenyl-tetrazolium bromide (MTT, Sigma-Aldrich, 1 mg/mL) in PBS was prepared and sterilised by filtration. Five hundred microliters of this MTT solution (50 μg/mL MTT in whole medium) was added to each culture dish without coverslip. Cells were incubated for 3 h, then the reduced formazan was extracted with 500 μL DMSO and the absorbance was measured at 542 nm in a SpectraFluor

spectrophotometer (Tecan Group Ltd, Männedorf, Switzerland). Cell survival was expressed as the percentage of absorption of treated cells in comparison with that of control cells. Data corresponded to mean values±standard deviation (SD) from at least two different experiments.

Morphological studies

Morphological changes were assessed at different times after incubation and irradiation in the case of PpIX and bimodal liposomes, by neutral red (NR) staining observed using bright field or differential interference contrast (DIC) microscopies. For NR staining, cells grown in square coverslips were fixed with methanol at -20 ºC for 5 min and then stained (Panreac Quimica; 0.1% solution in distilled water, 2 min). After washing and air drying, preparations were mounted in DePeX (Serva, Heidelberg, Germany). Cells were also observed under DIC microscopy using an inverted microscope, without being processed, to avoid possible morphological artefacts. These studies reveal the morphological alterations that characterise the main cell death mechanisms.

Optical microscopy

Routine observation of the cell cultures during their maintenance and the effect of the different treatments were done with an inverted microscope Olympus CKX1 (Tokyo, Japan). Living cells were captured with an inverted microscope Leica DMI 6000B equipped with a Leica DFC420 C digital camera (Leica) and images were processed using the Photoshop CS5 software (Adobe Systems, USA).

Statistical calculations

For statistical calculations, one-way ANOVA with post-hoc Tukey Kramer Multiple Comparisons test was used. P values < 0.05 (*), < 0.01 (**), and < 0.001 (***) were considered as statistically significant. The software GraphPad Prism (GraphPad Software, La Jolla, CA, USA) were used for the analysis.

5.2.5. Preparation of trastuzumab-conjugated bimodal liposomes

The monoclonal antibody (mAb) used is Trastuzumab (Herceptin®, ~148 kDa, abbreviated henceforth as TZ), a recombinant humanised IgG1 monoclonal antibody with high affinity for the extracellular part of HER2 receptor. It was approved by the FDA in 1998 for therapy against metastatic breast cancers overexpressing the HER2 receptors.[11] TZ was purchased from Carbosynth (Berkshire, UK). When it was received, the sample was diluted in PBS pH 7.4 and aliquoted in small volumes (each vial contained 20 mg/mL) and stored frozen. The lipid L-α-distearoyl-phosphoethanolamine-N- [maleimide(polyethylene glycol)-2000] (ammonium salt) (DSPE-PEG_{2000}-Mal) was acquired from Tebu-bio (Barcelona, Spain). The minitrap Sephadex G25 column was acquired from GE Healthcare Life Sciences (Barcelona, Spain).

Preparation of maleimide-functionalised liposomes

IUVs were prepared by microemulsification method as it was previously described, but using a quaternary mixture of DSPC:DOPS:CHOL:DSPE-PEG_{2000}-Mal in a molar ratio of 65:35:30:2. The DSPE-PEG lipid represented a 1.5% of the total lipid. The dried film was also hydrated with 10 mM (pH 4.4) lactate buffer to a final lipid concentration of 10 mg/mL. The protocol continued as was described above. These liposomes were prepared 1 day before the reaction with the thiolated TZ, to avoid undesirable reactions with the free maleimide group.

Antibody thiolation

The mAb were thiolated using Traut's reagent (2-iminothiolane) at a Traut's:TZ molar ratio of 16:1. Traut's reagent solution was prepared immediately before its use, dissolved in 50 mM phosphate buffer at pH 8 to a concentration of 2 mg/mL. TZ and Traut's reagent were mixed together in the same buffer and incubated at RT in the dark for 1.5 h under argon atmosphere. The antibody was purified by dialysis (MW cut off 12000-14000) in phosphate buffer with 0.11 M NaCl and 10 mM EDTA to pH 6 to remove the non-reacted Traut's reagent. The thiolated TZ was prepared just before addition of the liposomes.

Conjugation of thiolated TZ to bimodal liposomes

Thiolated TZ and bimodal liposomes were mixed in a glass vial at a DSPE-Mal:TZ molar ratio of 10:1. The air phase was replaced with argon, the bottle capped, and the reaction was let overnight at RT in the dark under gentle stirring. After overnight conjugation, the immunoliposomes were purified using size exclusion chromatography Sephadex column G-25, eluted with the same phosphate buffer at pH 6.

5.3. Results and discussion

5.3.1. Physicochemical characterisation

The co-encapsulation of Irinotecan (CPT-11) and PpIX in liposomes was studied. CPT-11 is an antineoplastic agent belonging to the family of topoisomerase I inhibitors that arrest the synthesis of DNA and possess strong antitumor activity. This molecule of the camptothecins' family is converted to its 100-fold more active metabolite SN-38 by a human carboxylesterase (hCE), primarily in the liver, but also in tumours.[12] Contrary to its metabolite, CPT-11 is quite soluble in water because of the positive charge of its piperidine group (pKa ~11, Figure 5.1). Despite CPT-11 already being a first-line drug approved for the treatment of a variety of human tumours (e.g., colorectal, lung and gynaecological cancers) there are some limitations that hamper its broader use as a free molecule.[12] For instance, the chemical instability of the lactone

ring, which opens to the inactive carboxylate form at physiological pH, requires protecting the molecule from the external environment to maximise its pharmacological potential (Figure 5.4). In addition, severe side effects have also been reported, limiting its application.[12] Therefore, encapsulating CPT-11 in liposomes is a potential strategy to overcome these drawbacks. Indeed, FDA approved a liposome formulation of irinotecan (Onivyde®) for the treatment of metastatic pancreatic cancer in October 2015, which was later granted by the EU agency.[1]

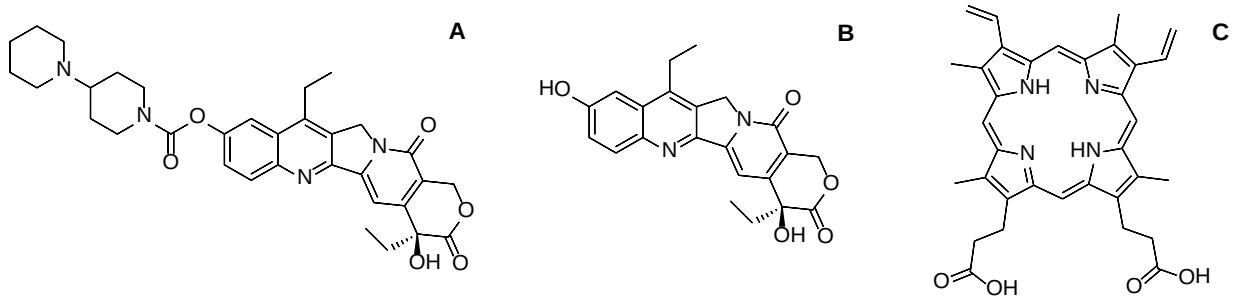

Figure 5.1. Chemical structures of the antineoplastic agent, CPT-11 and the PS, PpIX used in this chapter. CPT-11 (A) and its active metabolite, SN-38 (B) and one of most known porphyrins, PpIX (C).

On the other hand, the PS chosen as partner was PpIX, one of the most common porphyrins in nature. It is usually coordinated with iron atoms forming the prosthetic group of several proteins. PpIX is a highly coloured pigment that is hardly soluble under physiological conditions due to the two negative charges conferred by the propionic acid groups (Figure 5.1). The poor solubility in water strongly limits their free administration in aqueous environments, and therefore its encapsulation in nanocarriers arises as a convenient strategy.

The spectroscopic characteristics of these free drugs are shown in Figure 5.2. The absorption and fluorescence spectra of CPT-11 in water show maxima at 368 nm and 430 nm, respectively. PpIX shows a Soret band absorption at 411 nm and four Q bands at about 505, 540, 580 and 632 nm in THF. The fluorescence spectra peaks at 632 nm.

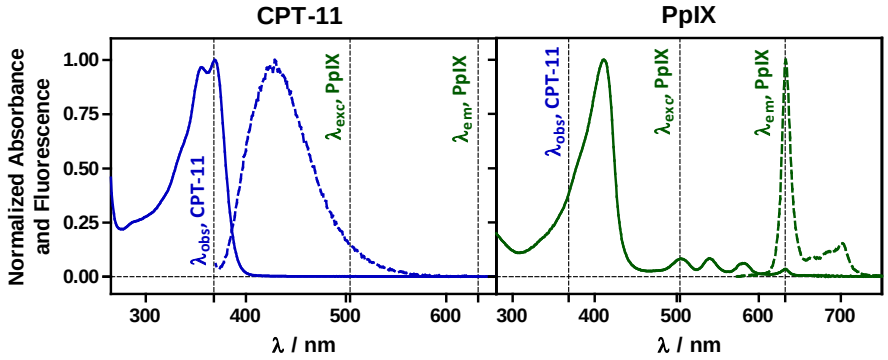

Figure 5.2. Absorption (solid line) and fluorescence emission (dashed line) spectra of CPT-11 (blue) and PpIX (green) solutions, in buffer at pH 4.4 and THF, respectively. In vertical dashed lines are pointed the wavelengths used for the measurements of the entrapment efficiencies either for CPT-11 or PpIX.

As depicted in Figure 5.3, PpIX aggregates in water, which results in a completely structureless bands in absorption and in a much weaker and broader fluorescence emission (Figure 5.3).[13] Encapsulation of PpIX in liposomes restores the photophysical properties of the monomeric form, which is itself a clear advantage.[14,15]

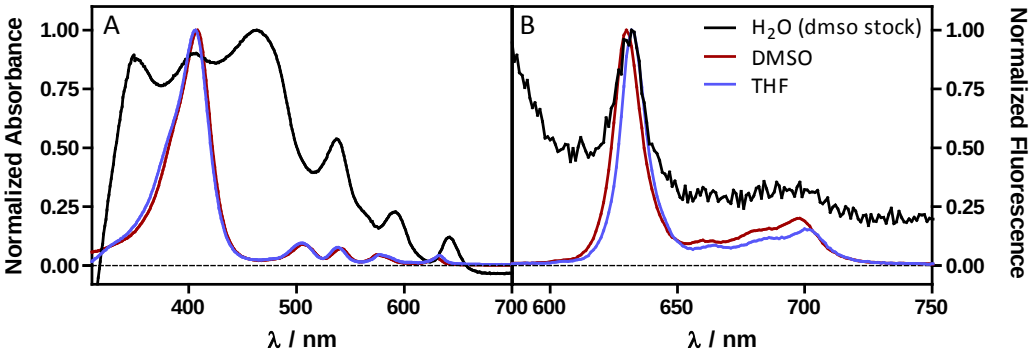

Figure 5.3. Normalised absorption (A) and fluorescence emission (B) spectra of PpIX in different media. In water, PpIX forms strong aggregates that almost lose the spectroscopic characteristics.

The lipid formulation for the encapsulation of CPT-11 by extrusion has already been optimised in the group, turning out to be DSPC:DOPS:CHOL (65:35:30 molar ratio).[16,17] DSPC is a synthetic phosphatidylcholine with two saturated fatty acids chains of C18, which give rigidity to the bilayer and increase the gel-to-liquid phase transition (T_m). Moreover, the absence of unsaturated bonds prevents the possible oxidative reactions, which can cause permeability changes and ultimately destabilise the liposome bilayer. In addition, the double bonds create spaces among the tightly packed tails.[18] Consequently, the more unsaturated lipids the bilayer contains, the more permeable the bilayer becomes. Therefore, a 65% of DSPC yielded a tight package bilayer and together with a high T_m, quite stable over time. For all these reasons, this lipid avoids the slow leakage outside the bilayer when the formulation includes an amphiphilic drug such as irinotecan.

CHOL molecules are localised in the bilayer with its hydroxyl group facing the water phase. Thus, it usually increases the rigidity of the bilayer, modifying its molecular packing. CHOL provides a rigid structure that makes the lipid bilayer more condense as compared with pure phospholipids above the T_m. However, below the T_m, CHOL induces the opposite effect , because it intercalates in the gel phase lipid, creating certain disorders.[18]

Finally, the incorporation of DOPS in the lipid bilayer is of utter importance since the negative charge of the C18 monounsaturated phosphatidylserine lipid interacts with the positive charge of the encapsulated CPT-11 and helps keep the drug inside. Moreover, the double bonds and the low T_m (-11 ºC) slightly increase the permeability of the bilayer to the desired degree. All in all, the systems provides optimal efficiencies for the encapsulation of the hydrophobic PpIX.

Irinotecan, as well as its active metabolite SN-38, undergoes a pH-dependent equilibrium, consisting of an opening lactone ring at pH above 6.8, producing the inactive carboxylate form. Consequently it becomes more hydrophobic with $logP_{o/w}$ values ranging from -0.684 at pH 4.4 to 1.087 at pH 7.4 (Figure 5.4).[17] Moreover, in its carboxylate form, the molecule turns out to be a zwitterion, losing the interaction with the DOPS lipids in the bilayer and its biological activity. Altogether, keeping the buffer at pH 4.4 is crucial for the proper drug encapsulation.

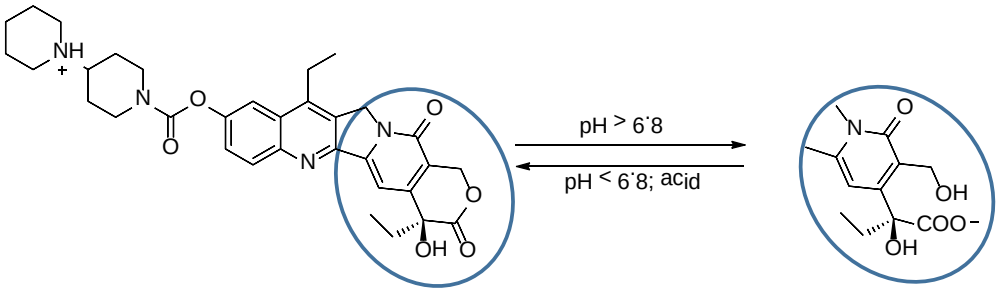

Figure 5.4. pH-dependant equilibrium of CPT-11. The biologically active form of the lactone is opened when the pH is neutral/basic.

Regarding the lipid composition DSPC:DOPS:CHOL (65:35:30) there are no antecedents of the double encapsulation of both CPT-11 and PpIX, taking into account the chemical differences between both molecules. Table 5.1 summarises all the attempts tested for the liposome formation with the lipid composition aforementioned.

Table 5.1. Some physicochemical characteristics of the different conditions tested. All the formulations have the same lipid composition DSPC:DOPS:CHOL (63:35:30) and the same lipid concentration of ~10 mg/mL.

Formulation	Lipid:Drug[a]	Method	EE %	Z-ave (nm)	Notes
1	CPT-11 7.5:1	Extrusion	85	153 ± 13	already described
2	PpIX 100:1	Extrusion	52	155	PS retained in the filters
3	PpIX 100:1	Microemulsification 110 kPa 10 cycles	95	126	Size and PI[d] higher than the following
4	PpIX 100:1	Microemulsification 110 kPa 10 cycles	98	101	1 h lipids/PS before the film formation
5	CPT-11 7.5:1	Microemulsification 150 kPa 10 cycles	86	293	High PI[d] and second small population
6	CPT-11 7.5:1	Microemulsification 110 kPa 25 cycles	85	189	both are similar
7	CPT-11 7.5:1	Microemulsification 110 kPa 10 cycles	86	179	
8	CPT-11 7.5:1 PpIX 50:1	Microemulsification 110 kPa 10 cycles	84 56	214	separated film[b]
9	CPT-11 7.5:1 PpIX 50:1	Microemulsification 110 kPa 10 cycles	75 96	153	combined film[c]

a Referred to the molar ratio

b The separated film was done as follows: 1. First the film of the half amount of lipids + CPT-11 was hydrated with buffer and then with this suspension was hydrated the second film, which was done with the remaining amount of lipids + PpIX.

c The combined film was done with both agents (PpIX and CPT-11) at the same time.

d Polydispersity Index

Due to the high hydrophobicity of PpIX, the method was modified to achieve homogenous sized liposomes since a great amount of PS was retained in the polycarbonate filters of the extruder (formulation # 2). In the case of CPT-11, the best conditions set in the emulsiflex were 110 kPa and 10 cycles (formulation # 7, Figure 5.5 A), as it was for PpIX. It is worth noting that keeping the suspension of PpIX in $CHCl_3$ for 1 h (protected from light) facilitates the contact lipid/PS during the film formation. This procedure afforded an easier film hydration and a smaller size's population size (formulation # 4, Figure 5.5 A), leading to an optimal protocol for the further bimodal formulations.

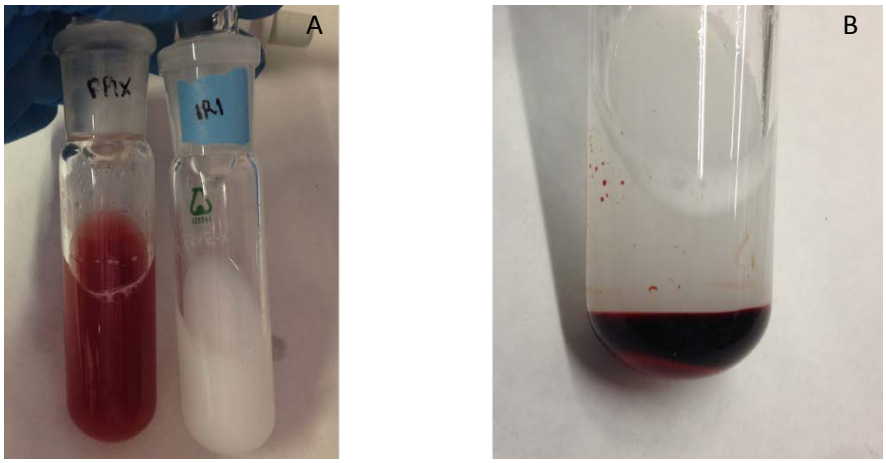

Figure 5.5. Photography of the unimodal preparations after the film hydration (A) and the separated film preparation when the PpIX dried film is hydrated with the CPT-11 and half of the lipids suspension (B).

A passive method of encapsulation in liposomes consists of the concomitant introduction of the PS, the drug and lipids. Clearly, the preparation of a unique film (formulation # 9) by a passive method resulted in a much better encapsulation of the PpIX compared to entry #8, where two different films were prepared separately with each drug and then mixed (Figure 5.5 B). The low PpIX encapsulation observed in formulation # 8 suggests that CPT-11 molecules were partially intercalated in the bilayer, hindering the later PpIX incorporation.

The ratio between PS and drug inside bimodal liposomes was prepared according to the IC_{50} values found previously in PpIX and CPT-11 unimodal liposomes (Figure 5.15). Blank liposomes (i.e., without the encapsulation of any drug) were always prepared as controls. Table 5.2 summarises the most important physicochemical characteristics for either bimodal or unimodal formulations, including blank liposomes.

Table 5.2. Physicochemical characteristics of blank, unimodal and bimodal liposomes with CPT-11 and PpIX loaded. The lipid composition was DSPC:DOPS:CHOL 65:35:30.

Encapsulated drug	Z-ave (nm)[a]	PI[b]	ζ-pot (mV)[c]	DL % (w/w)[d]	EE % (w/w)[e]	[CPT-11] (mM)[f]	[PpIX] (μM)[f]	[lipid] (mg·mL^{-1})
-	96 ± 12	0.23 ± 0.04	-59 ± 4	-	-	-	-	7.3 ± 0.2
CPT-11	189 ± 17	0.19 ± 0.10	-58 ± 7	12.5 ± 5.1	82 ± 9	1.26 ± 0.23	-	6.8 ± 0.6
PpIX	93 ± 10	0.23 ± 0.03	-59 ± 6	0.5 ± 0.1	98 ± 3	-	65 ± 14	7.2 ± 0.5
both	169 ± 18	0.19 ± 0.03	-57 ± 3	11.1 ± 1.1 0.5 ± 0.1	85 ± 7 89 ± 7	1.21 ± 0.09 -	- 63 ± 9	7.5 ± 0.3

a Particle size measured as Z average mean
b Polydispersity Index
c Zeta-potential
d Bulk encapsulated drug concentration in the liposomes suspension
Values reported are the mean ± SD (standard deviation) of at least three independent experiments

The encapsulation of CPT-11 resulted in an increase in liposome size but with a lower polydispersity index compared to those formulations without this drug. Although the size was somewhat higher, probably because the methodology of vesicle homogenisation was changed, the entrapment efficiency was in agreement with previous observations.[16] When PS was encapsulated, the size and the polydispersity were comparable with blank liposomes' values, the former being remarkably smaller than those formulations with CPT-11. The zeta-potential was maintained constant in all formulations, which indicates that the agents were mainly inside the liposome, without interfering with the external surface charge of the lipid bilayer. The negative charged surface endows the liposomes with a greater stability in suspension, avoiding the aggregation due to the repulsion between charges. In all cases, the entrapment efficiency was above 80% (looking at the average values), being slightly lower for the CPT-11 formulations. For these particular CPT-11 formulations, most of the drug was lost in the sterilisation process, by filtration through 0.20 μm filters, necessary for further cellular assays. Thus, the CPT-11 non-encapsulated after the filtration was <5% in all cases. It is worth noting that for the evaluation of lipid concentration at 465 nm, the absorption of PpIX did not interfere at these concentrations.

Figure 5.6. Photograph of one of the batches with the four formulations from left to right are: blank liposomes, CPT-11 unimodal, PpIX unimodal and bimodal liposomes.

Figure 5.6 shows the appearance of the four optimised preparations. The blank and PpIX liposomes were quite translucent, indicative of a smaller size, while the preparations that contain CPT-11 had a rather milky appearance.

One of the most attractive characteristics of this lipid formulation is its T_m at 46.0 ± 1.3,[16] which is above the physiological temperature (40 – 44 ºC). The choice of the lipids and their molar ratio in the formulation allows the control and modulation of their T_m and can render structures stable enough at physiological temperature. Remarkably, when T_m is not too far from the physiological temperature, the cargo release could be triggered by hyperthermia. Therefore, these liposomes could be considered temperature-sensitive liposomes (TSL), which could allow the release in anatomical regions subjected to local hyperthermia such as cancer tumours.[19]

Formulation stability. Liposomes are thermodynamically unstable colloidal systems and they tend to aggregate over time. Factors that can affect the degree of aggregation include temperature, ionic strength and surface charge.[20] Additionally, unsaturated fatty acids are prone to undergo oxidative reactions, which can cause permeability changes within the liposome bilayer. Interactions of drugs with phospholipids also alter the chemical stability, hence the stability profile of a single drug may be entirely different from its liposome preparation stability profile.[21] Ultimately, liposomes tend to fuse and grow into bigger vesicles, which is a thermodynamically more favourable state. Fusion and breakage of liposomes on storage also poses a critical problem, leading to drug leakage from the vesicles. Therefore, it is essential to develop stability protocols, such as visual appearance and size distribution, which are important parameters to evaluate physical stability.

Taking into account all these considerations, the lipid formulation developed is quite stable. The high zeta-potential (> 30 mV negative or positive) of these liposomes which tend to repeal each other, provides an additional stability in solution. However, the ideal stabilisation method is lyophilisation since the dry state increases the shelf-life of the final product.[22] These formulations, once lyophilised, can be stored at room temperature for an extended time. Unfortunately, lyophilisation of these preparations causes the loss of approximately 20% of CPT-11 entrapment and the increase in the liposome size.

Figure 5.7 shows size and zeta-potential evolution diagrams over time. The size of blank and PpIX liposomes was remarkably stable for eight weeks after preparation. Whereas both preparations with CPT-11 increased their size at the third week.

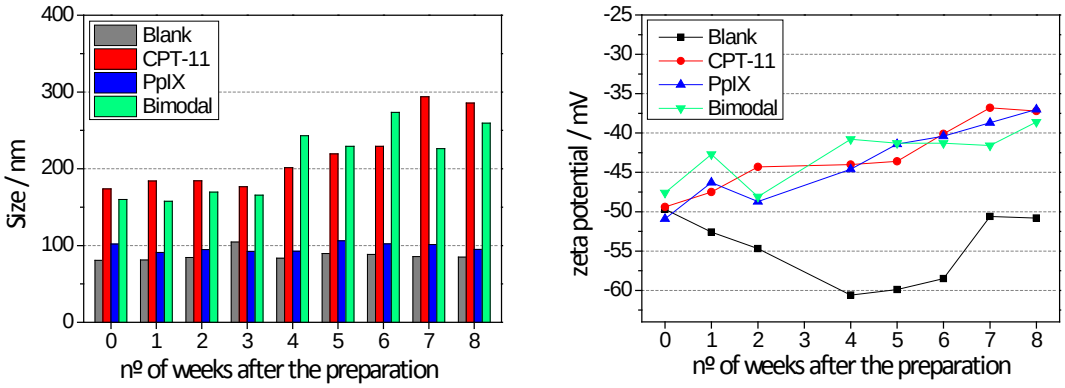

Figure 5.7. Size (Z-average mean, left panel) and zeta-potential (right panel) evolution diagrams over the time of the four liposome formulations.

The zeta-potential increased slowly over time for all the formulations that contained a drug, either the antineoplastic agent or the PS (Figure 5.7, right panel). It remained almost stable until the second week of their preparation. The bimodal and the CPT-11 unimodal formulations showed a considerably less negative zeta-potential after 7-8 weeks from their preparation, most likely because of a positively charged CPT-11 leakage. Curiously, blank liposomes exhibited an initial zeta-potential decreased (increased in the negative scale) that ultimately returned to the early values. On the other hand, the physical stability of vesicles can also be assessed by measuring the absorbance at 450 nm over time, which is also known as the suspension turbidity (Figure 5.8).

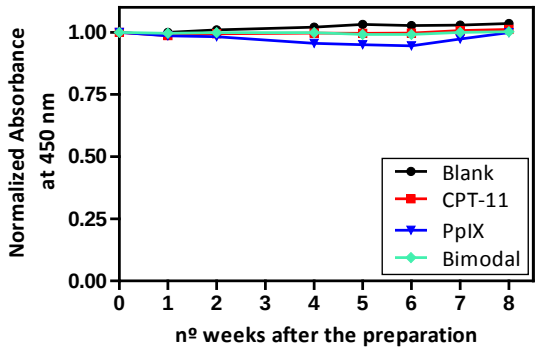

Figure 5.8. Normalised absorbance at 450 nm over the time of the four liposome preparations.

The turbidity of the four preparations was remarkably stable for eight weeks after preparation. In contrast to the CPT-11 size increase shown in the evolution diagram, we did not observe any considerable change in the turbidity measures. These results suggest that liposomes do not form large aggregates over that period of time, which are the main cause of the scattering increase.

5.3.2. Spectroscopic and photophysical properties

The absorption spectrum of the bimodal preparation presents the typical bands of both agents, although it is difficult to observe the Q-bands of PpIX and the double maxima band of the CPT-11 due to the scattering of the vesicles (Figure 5.9). The spectra of both agents in solution are also shown as a comparison.

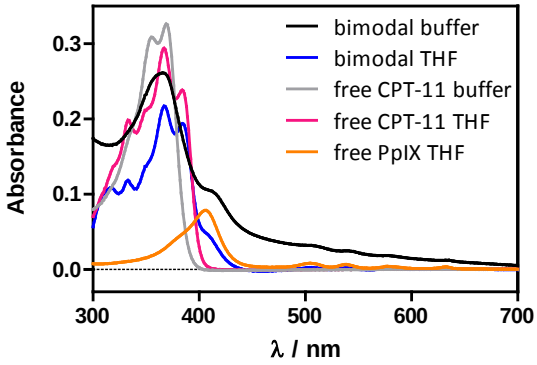

Figure 5.9. Absorption spectrum of the bimodal liposomes, both in buffer and once they have been disrupted in THF (1:50; liposomes aliquot:THF). The spectra of both agents in solution are also shown for comparison.

More details could be extracted from the fluorescence spectra of the liposomes, again either in buffer or in THF, when they were disrupted. Figure 5.10 shows the fluorescence spectra of the unimodal liposomes; panel A presents the CPT-11 region and panel B the PpIX region. As was expected, CPT-11 inside the liposome showed exactly the same profile as when in free aqueous solution. This phenomenon was completely different when the liposomes were disrupted in THF. It is worth noting that PpIX inside the liposomes shows a monomeric fluorescence profile but with a 3 nm shift to the red, in comparison with free PpIX in THF. The red-shift is likely indicative of a more hydrophobic environment.

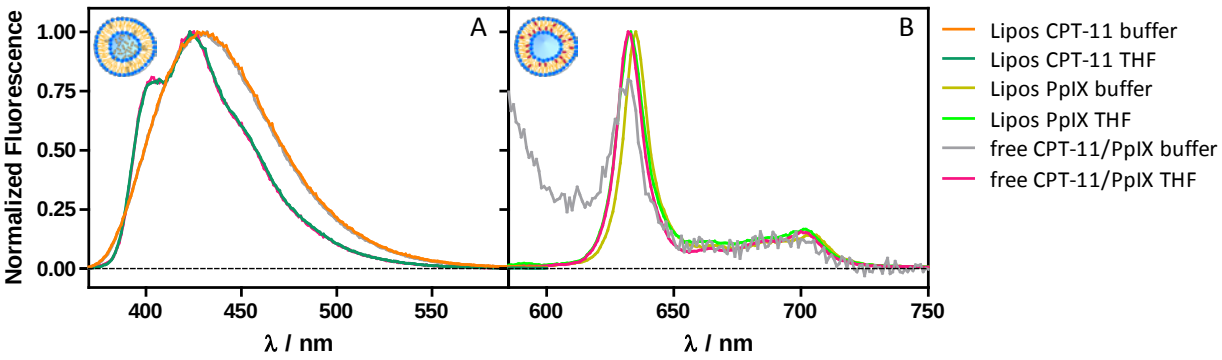

Figure 5.10. Fluorescence emission spectra of the CPT-11 (A) and PpIX (B) unimodal liposomes. Free drugs in solution spectra are shown for comparison. The λ_{exc} for CPT-11 was set at 360 nm and at 504 nm in the case of PpIX.

Figure 5.11 shows the same spectra but for the bimodal liposomes. The scenario presented the exact same characteristics for both agents as in their unimodal counterparts.

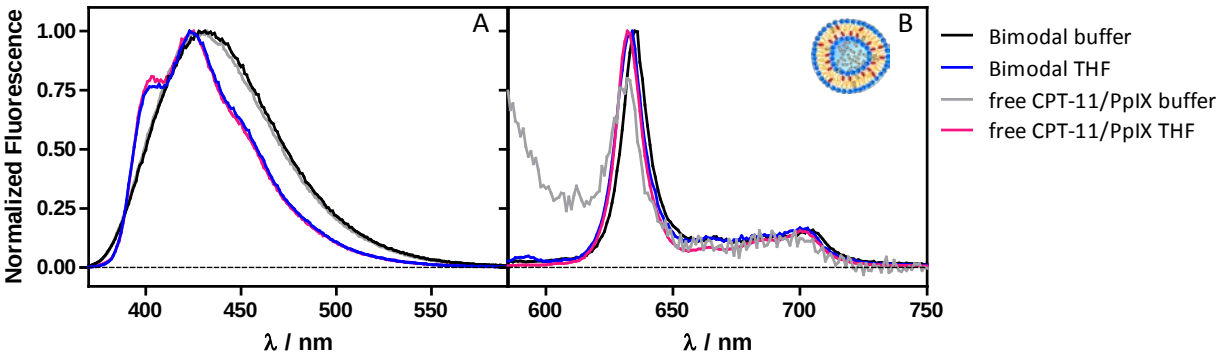

Figure 5.11. Fluorescence emission spectra of the bimodal liposomes, showing the CPT-11 (A) and PpIX (B) spectral region. Free drugs in solution spectra are given for comparison. The λ_{exc} for CPT-11 was set at 360 nm and at 504 nm in the case of PpIX.

The fluorescence and $^1O_2$ quantum yields (Φ_F and Φ_Δ) were determined by comparing the signals for a set of sample and reference solutions in order to avoid scattering problems, as discussed in section 2.2.2. Figure 5.12 shows the absorbance and fluorescence emission spectra of the samples, indicating the λ_{exc} for the measurement of Φ_F and Φ_Δ and their respective fluorescence references. In all cases, the absorbance spectra of diluted blank liposomes were also recorded for scattering subtraction.

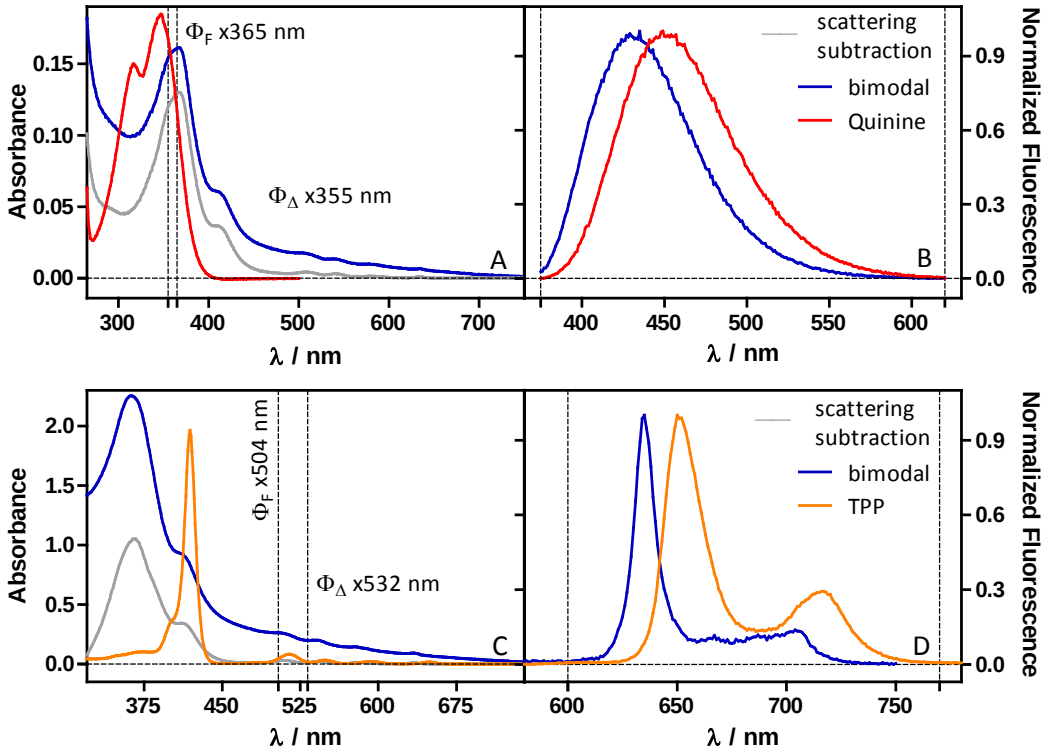

Figure 5.12. Absorption (A and C) and fluorescence emission (B and D) spectra of bimodal liposomes (blue line) and their respective references for the Φ_F measurement. The grey line correspond to the scattering correction absorption of the liposomes. The vertical dashed lines in the absorption spectra indicate the excitation wavelength used for the determination of Φ_F and Φ_Δ. The references used were quinine in H_2SO_4 0.5M (red line) and TPP in toluene (orange line) for CPT-11 and PpIX, respectively.

Fluorescence decay kinetics in liposomes revealed only one component for CPT-11 and two components for PpIX (Figure 5.13, Table 5.3), indicating two different populations of the excited

singlet state of PpIX (^{1}PpIX*) in the vesicles. The time constant for CPT-11 liposomes was exactly the same as in buffer solution (3.5 ns), which clearly indicates that CPT-11 inside the vesicles was exposed to the aqueous core. Likewise, PpIX showed two components, the main one with a lifetime slightly higher than in THF (11.6 ns), indicating that the environment of PpIX in the bilayer was more hydrophobic than THF. The second component (~4.3 ns) can be assigned to a minor population of aggregated PpIX molecules inside the bilayer.

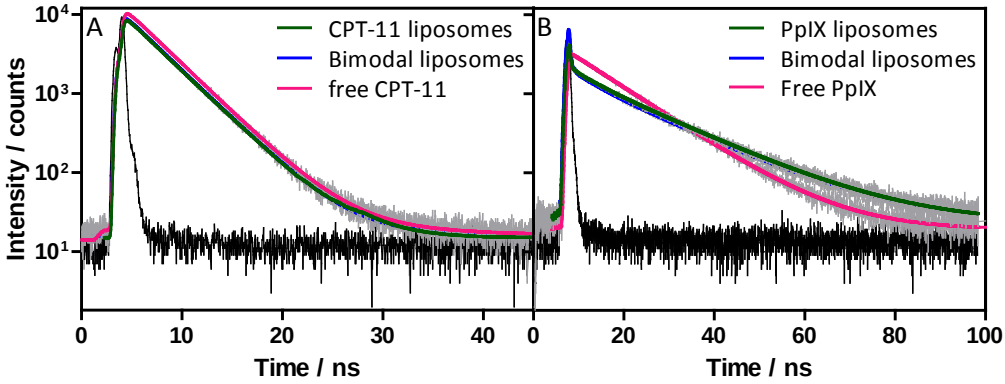

Figure 5.13. Time-Resolved Fluorescence decays of unimodal and bimodal liposomes in lactate buffer, showing CPT-11 (A) and PpIX (B) spectroscopic region. Panel A: λ_{exc} 375 nm, λ_{obs} 430 nm and panel B: λ_{exc} 502 nm, λ_{obs} 700 nm. The black line corresponds to instrumental response factor (IRF).

PpIX was encapsulated at a concentration ~20-fold lower than CPT-11. As the steady state fluorescence emission revealed, the PpIX seems to be completely monomeric inside the bilayer. On the other hand, CPT-11 presents lower Φ_F than in the aqueous buffer probably due to self-quenching processes caused by the high local concentration.

Table 5.3. Fluorescence quantum yields and fluorescence lifetimes, with their relative amplitudes, of CPT-11 and PpIX loaded in liposomes in lactate buffer. The respective values of both agents free in solution are also presented.

Sample	Solvent	λ_{exc} (λ_{obs}) / nm	τ_1 / ns (A%)	τ_2 / ns (A%)	Φ_F[a]
free CPT-11	buffer	375 (430)	3.5 (99.9%)	24.7 (0.1%)	0.62 ± 0.01
CPT-11 liposomes	buffer		3.5 ± 0.1 (100%)	-	0.44 ± 0.08
Bimodal liposomes	buffer		3.5 ± 0.1 (100%)	-	0.38 ± 0.06
free PpIX	THF	502 (700)	11.6 (100%)	-	0.13 ± 0.01
PpIX liposomes	buffer		16.6 ± 0.1 (79.7%)	4.1 ± 0.2 (20.3%)	0.18 ± 0.04
Bimodal liposomes	buffer		16.2 ± 0.5 (71.3%)	4.6 ± 0.3 (28.7%)	0.19 ± 0.05

a Φ_F was found at λ_{exc} 365 nm and 504 nm for CPT-11 and PpIX, respectively, as it is shown in Figure 5.12. Results are the mean ± SD of at least two independent experiments.

Quenching the drugs triplet state with oxygen led to the production of the cytotoxic species $^1O_2$ as unequivocally demonstrated by the observation of the specific NIR phosphorescence of this species at 1275 nm. The temporal profile of the signals (S_t, Figure 5.14) shows the typical rise-

and-decay function that characterises $^1O_2$ kinetics (Eq. 2.3). The signals at different oxygen concentrations are presented, allowed an unequivocal assignation of the triplet, because of the fact that the presence of oxygen quenches the triplet state. Surprisingly, CPT-11 shows a clear transient of $^1O_2$ production, although with a lower signal-to-noise ratio due to the lower Φ_Δ compared with PpIX.

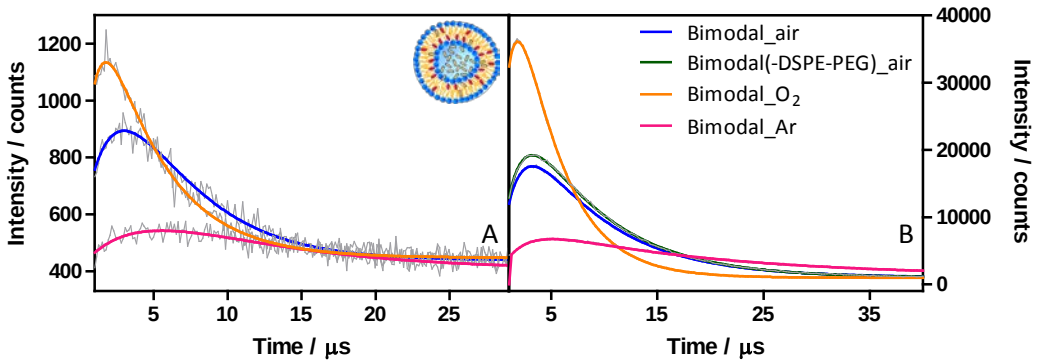

Figure 5.14. Time-resolved $^1O_2$ phosphorescence at different oxygen concentrations in aqueous suspensions of bimodal liposomes. Panel A shows the CPT-11 signals after the λ_{exc} at 355 nm, and panel B the PpIX signals after the λ_{exc} at 532 nm. In addition, panel B shows an extra liposome formulation coated with a 1.5% of a PEG_{2000} lipid (dark green line), which would be ultimately used for the target moiety coupling.

Data analysis (Table 5.4) of the signals presented in Figure 5.14 confirmed the assignment of the triplet and $^1O_2$ populations in bimodal liposomes.

Table 5.4. Time constants of $^1O_2$ luminescence of bimodal liposomes under different oxygen concentrations.

Sample	λ_{exc} / nm	Atmosphere	τ_T / µs	τ_Δ / µs
Bimodal Liposomes	355	air	5.6	1.8
		O_2	2.8	2.0
		Ar	11.2	2.1
Bimodal-DSPE-PEG_{2000}	532	air	7.3	1.7
Bimodal Liposomes		air	7.5	1.7
		O_2	3.9	1.2
		Ar	17.2	1.7

Table 5.5. Time constants of $^1O_2$ luminescence and Φ_Δ of unimodal and bimodal liposomes. Data of the free CPT-11 and free PpIX in lactate buffer and in THF, respectively are shown as reference. CPT-11 was excited at 355 nm, while PpIX at 532 nm and $^1O_2$ phosphorescence was recorded at 1275 nm.

Sample	Solvent	λ_{exc} / nm	τ_T / µs	τ_Δ / µs	Φ_Δ
free CPT-11	buffer	355	2.6	3.9	0.31 ± 0.04
CPT-11 liposomes	buffer		5.2 ± 0.5	2.0 ± 0.3	0.05 ± 0.01
Bimodal liposomes	buffer		5.0 ± 0.5	1.9 ± 0.6	0.13 ± 0.03
free PpIX	THF	532	0.3	21.3	0.56[23,a]
PpIX liposomes	buffer		6.4 ± 0.3	2.3 ± 0.1	0.63 ± 0.05
Bimodal liposomes	buffer		7.7 ± 0.4	1.7 ± 0.1	0.15 ± 0.02

a Value found in literature in PBS with Triton X-100.
Results are the mean ± SD of at least two independent experiments, except for the free drugs in solution.

Finally, data analysis of the time constant of $^1O_2$ luminescence and the $^1O_2$ quantum yield of the unimodal and bimodal liposomes are shown in Table 5.5.

The fact that the τ_Δ of CPT-11 was slightly lower in liposomes than in free solution pointed out that $^1O_2$ was a bit quenched before its decay. Because of the amphiphilic nature of CPT-11, this is located partially in the lipid bilayer with the piperidine group exposed to the aqueous core of the liposome. This might be the major population of CPT-11 molecules in liposomes due to the single fluorescence lifetime collected. Whereas other CPT-11 molecules, the minority, could also be found in the intraliposomal region interacting electrostatically with DOPS lipids, improving the formulating stability. Thus, most likely the newly formed $^1O_2$ is quenched by the lipids of the surroundings. Triplet excited states of the encapsulated drugs showed longer lifetime values than in homogeneous solution, which indicates that oxygen was somewhat hampered in the liposomes. Therefore, the Φ_Δ was reduced for both liposome formulations in comparison with their quantum yield in buffer solution (Φ_Δ = 0.31). This reduction was attributed not only, but mainly, to CPT-11 interactions caused by the high local concentration, but also to the slightly low local oxygen concentration inside this system. This last hypothesis can be further supported by the longer τ_T lifetime. The Φ_Δ reduction was more relevant in the unimodal liposomes, and although there is not a clear explanation, the presence of both drugs in the same system might somewhat reduce the CPT-11 interactions, reverting in an increase in the quantum yield. No other remarkable differences in the reported values were observed between unimodal and bimodal liposomes, regarding the CPT-11 observation.

Concerning the PpIX observation at 532 nm, the τ_Δ was very similar to those found for CPT-11, regardless of the λ_{exc}, denoting that $^1O_2$ might easily escape from inside the liposome and diffuse out to the aqueous medium during its lifetime.[24] This is supported by the fact that the $^1O_2$ diffusion length is about 0.4 μm in pure lipids and 0.2 μm in water. Taking into account that the diameter of liposomes is about 0.1 μm, $^1O_2$ can diffuse back and forth over the liposome.[25] Triplet excited states of the encapsulated PS showed longer lifetime values than in homogeneous THF solution, which indicates that oxygen was slightly hampered in the liposomes, just as in the previous scenario. However, the $^1O_2$ quantum yield is remarkably different in the unimodal compared to the bimodal liposomes. One plausible explanation is that the presence of the CPT-11, which is also placed in the bilayer, facilitates PpIX aggregation, due to the high local concentration of drugs in the bilayer, and thus considerably decreasing the Φ_Δ. While in the case of unimodal PpIX liposomes, the PS can be well-accommodated in the monomeric form, and even increase the Φ_Δ above the value in solution found in the literature.

5.3.3. Cell viability studies

The results of this section were obtained by Dr. Angeles Villanueva and Dr. Ana Lázaro at the Universidad Autónoma de Madrid and are included here to facilitate the interpretation of results.

HeLa cells were incubated in the dark with various concentrations of CPT-11 and PpIX unimodal liposomes for 24 h. Afterwards, cells with PpIX liposomes were exposed to 2 J·cm^{-2} of red light and cell viability was assessed 24 h after the treatment in the case of PpIX liposomes and after the incubation for CPT-11 liposomes (Figure 5.15). These results allowed the assessment of the half-maximal inhibitory concentration (IC_{50}), the most widely used and informative measure of a drug's efficacy. It indicates how much drug is needed to inhibit a biological process by half, in this case, that causes a 50% reduction in cell viability.

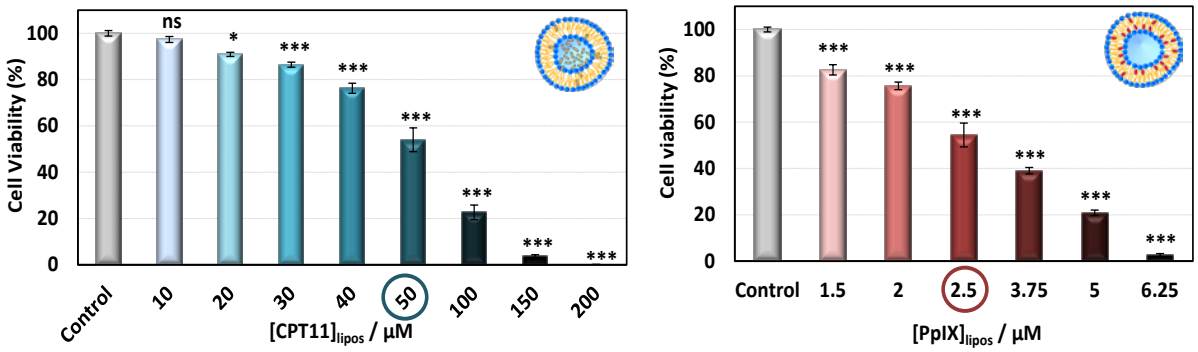

Figure 5.15. Cell viability or cell survival (expressed in percentage) after incubation with unimodal PpIX and CPT-11 liposomes at various concentrations. Evaluation of the cell viability through the colorimetric MTT assay that was carried out 24 h after the incubation. In the case of PpIX liposomes, the cells were exposed to red light irradiation (2 J·cm^{-2}) before the MTT assay.

The optimal concentrations were 50 µM for CPT-11 and 2.5 µM for PpIX liposomes, the ratio being PpIX:CPT-11 1:20, which is of utter importance for the co-encapsulation of both agents in the bimodal liposomes.

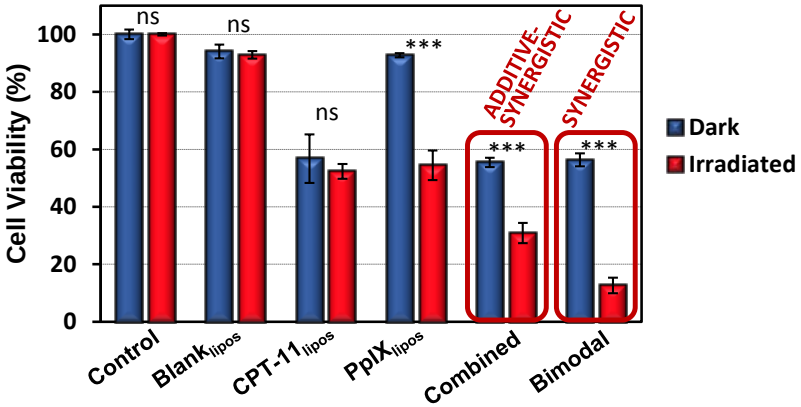

Figure 5.16. Cell viability after the treatment with unimodal and bimodal liposomes in dark and after the light exposed conditions (2 J·cm^{-2}). The samples were analysed 24 h after the different treatment through the MTT assay. (ns: not significant)

Once the optimal concentrations were found, the cell viability was assessed following the protocol above (MTT assay) after 24 h from the treatment, comparing unimodal liposomes, unimodal combination given at the same time and bimodal liposomes (Figure 5.16).

The irradiation of control cells did not produce any considerable differences in the cell viability in the experimental conditions. Blank liposomes showed a slight decrease in cell viability, probably due to the high concentration of lipids in the cell in order to achieve the IC_{50} of CPT-11, which is particularly high. The CPT-11 unimodal liposomes did not show a different effect neither in the dark, nor after the red light irradiation. It has been proven that the CPT-11 administered in liposomes has significantly decreased cell viability compared to the CPT-11 delivered in solution.[26–29] Moreover, recent reviews have highlighted important advantages of liposomal formulations of chemotherapeutic agents, with an increased efficacy and reduced toxicity compared to un-entrapped drugs in cancer therapy.[30,31] PpIX unimodal liposomes were not cytotoxic in the dark (viability of 92.7%), while after the PDT treatment, the viability decreased remarkably.

The analysis of combined treatments was evaluated according to the method written by Valeriote and Lin:[32]

Synergism: $[A + B] < [A] \times [B]$

Additivity: $[A + B] = [A] \times [B]$

where [A] and [B] represent the cell viability for the individual treatment of compounds A and B (CPT-11 and PpIX), whereas [A + B] represents the cell viability for the combined treatment, either the administration of the bimodal liposomes or the unimodals combined (labelled in the graph as combined).

Both the combination of unimodals and the bimodal liposomes in dark conditions showed the same effect as CPT-11. However, upon irradiation the cell viability decreased considerably, leading to an additive-synergistic effect for the combination of both unimodal liposomes and to a clear synergistic effect for the bimodal liposomes. Therefore, the fact that both agents were encapsulated in the same carrier may imply a more effective therapy.

5.3.4. Subcellular localisation and morphological changes

The results of this section were obtained by Dr. Angeles Villanueva and Dr. Ana Lázaro at the Universidad Autónoma de Madrid.

Figure 5.17 shows the subcellular localisation of the unimodal liposomes 24 h after the incubation by confocal microscopy and its overlapping with DIC.

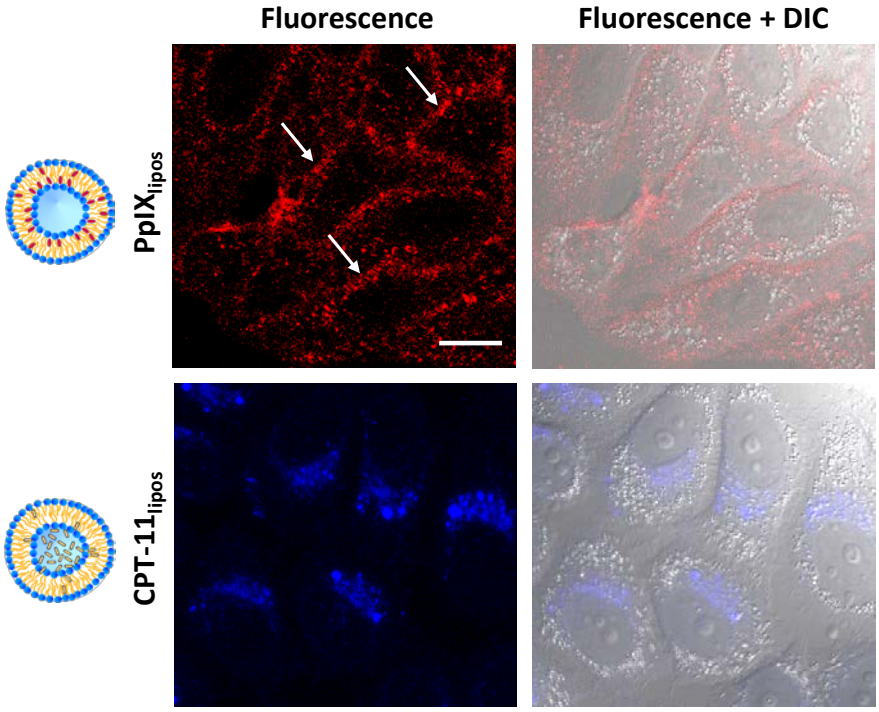

Figure 5.17. Subcellular localisation of the PS/drug administered individually in liposomes. The samples were analysed 24 h after incubation by confocal microscopy (left panels) and merged with DIC (right panels). The arrows show the intracellular limits of the cells. Scale bar= 10 µm.

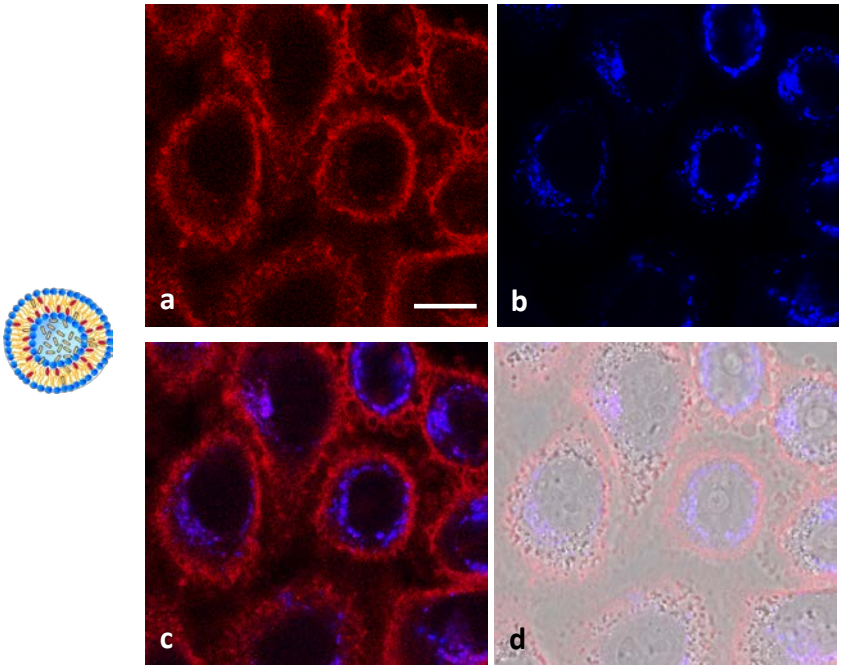

Figure 5.18. Subcellular localisation of the PS/drug administered simultaneously in bimodal liposomes. The samples were analysed 24 h after incubation by confocal microscopy looking at the PpIX's fluorescence (a), the CPT-11's fluorescence (b), the merging of both fluorescences (c) and finally merging with DIC microscopy (d). Scale bar= 10 µm.

PpIX, when administered in unimodal liposomes, was distributed all over the cytoplasm with a special accumulation in the vicinity of intracellular limits indicated in the figure with arrows. It was practically absent in the nuclei. CPT-11, when given as a unimodal liposome, was distributed diffusely as a granular pattern all over the cell, either in the nuclei or in the cytoplasm, but with a major concentration in what appeared to be the Golgi apparatus and lysosomes.

Figure 5.18 shows an equivalent scenario for the drugs administered together in the bimodal liposomes. The subcellular localisation was similar to those obtained for the unimodal liposomes, demonstrating that the entrance route to the cell and accumulation places were similar for both types of liposomes.

Figure 5.19 shows the cellular morphology after 12 h from incubation with liposomes (except for control sample) and the PDT treatment, by direct visualisation with DIC and after the neutral red (NR) staining.

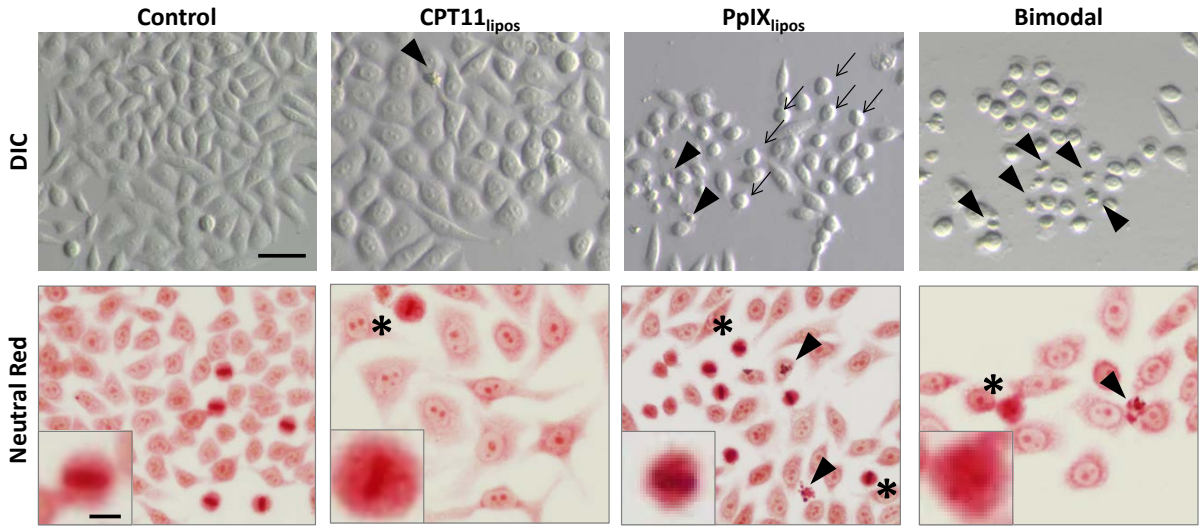

Figure 5.19. Morphological changes of HeLa cells after the treatments in phase contrast or DIC and after NR staining. The cells were incubated with unimodal or bimodal liposomes and visualised directly by DIC microscopy after 12 h from irradiation or after 24 h from the NR staining. The arrowheads point out apoptotic cells, the asterisks some altered metaphases and arrows cells in division. Scale bar = 25 μm and 5 μm in the metaphase zoom.

The treatment with CPT-11 or PpIX in HeLa cells resulted in different cellular morphologies revealed by DIC and NR for general morphology. CPT-11 produced an increase in the cellular size, resulting in larger and flatter cells than the control ones. It is worth noting that there were fewer cells in division, and the few metaphases were altered because of the increased size and the appearance of fragmented chromosomes not properly aligned in the equatorial plate (Figure 5.19, asterisk or zoom). Moreover, some typical apoptotic features can be appreciated in DIC images, such as rounded morphology with chromatin condensed and fragmented, and packed into apoptotic bodies (Figure 5.19, arrowhead). The fact that CPT-11 liposomes triggered the

apoptotic pathway as the main mechanism in HeLa cells death was supported by indirect immunofluorescence staining of diffuse green cytoplasmic fluorescence for Bax around the blue nuclear emission by H-33258.[29]

PpIX liposomes produced an increase in number of cells in division, resulting in a higher number of metaphases (round-shaped cells), possibly because of a metaphase arrest (Figure 5.19, asterisks). Moreover, many cells had undergone apoptosis 12 h after PDT, as deduced again from cell shrinkage, chromatin condensation and nuclear fragmentation. In the NR image after 24 h, it seems that cells in the temporal metaphase arrest resulted in some normal metaphases, but the majority presented altered features, better seen in the zoom of the metaphase, where the chromosomes were not aligned as it happened for CPT-11 treatment. Contrary to CPT-11 treatment, PpIX did not produce a cellular size increased.

The treatment with bimodal liposomes resulted in a combination of individual effects on both PpIX and CPT-11.

For a better understanding of some cell death mechanisms, the cells were also observed under light microscopy (phase contrast or DIC) 10 days after treatment (Figure 5.20). An inverted microscope was used, without being processed, to avoid possible morphological artefacts.

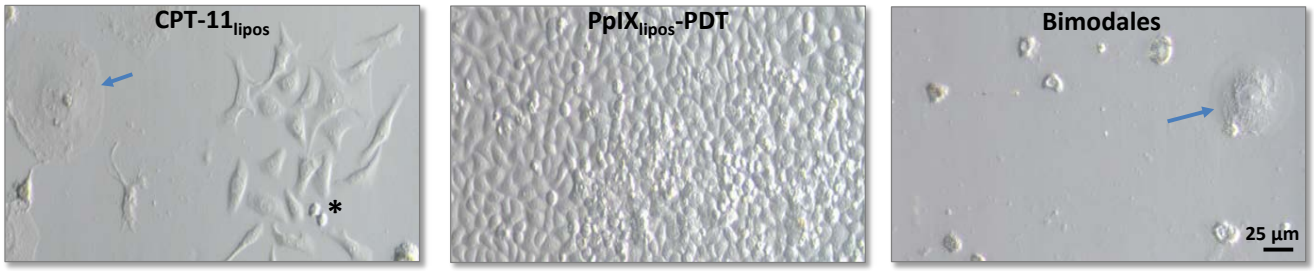

Figure 5.20. Morphology of HeLa cells under light microscopy (DIC) 10 days after the different treatment using an inverted microscope. Scale bar = 25 µm. Blue arrows show the senescent cells, confirmed by the β-galactosidase assay.

10 days after the CPT-11 liposomes treatment, scarce cells can survive producing large and flat cells (blue arrow) which, after the positive result of β-galactosidase assay (after five days from treatment, data not shown), were proven to be senescent cells. Furthermore, some resistant cells were seen with a similar size to the control cells that proliferate. The image of PDT treatment with PpIX liposomes after 10 days shows many attached cells, therefore the cells that survived continued proliferating. In the case of bimodal liposomes treatment, there was a huge amount of dead cells through apoptosis and the scarce, still living cells were senescent (blue arrow). Through β-galactosidase assay, fewer senescent cells were seen in the case of bimodal liposomes compared to those exposed to CPT-11 liposomes (data not shown).

5.3.5. Active targeting with Herceptin®

A great deal of effort has been made over the years to develop liposomes that have targeting vectors attached to the bilayer surface. Although all particles reach the target site (e.g., tumour) via passive targeting (EPR effect), the addition of ligands to the particles does not increase the amount that reach the target. But ligand-mediated targeting does increase the receptor-mediated uptake of particles by the target cells themselves, depending on factors such as: vasculature permeability; tumour penetrability; antigen density; ligand affinity; binding site barrier.[30] Targeting efficiency is related to receptor density at the cell surface.

Numerous procedures for the conjugation of antibodies to liposomes have been developed.[33–36] Briefly, there are four categories defined by the particular functionality of the antibody being modified, namely amine modification, carbohydrate modification, disulphide modification, and noncovalent conjugation.[37] Clearly, the most useful procedure involved the modification of the antibody and a lipid in the liposome with crosslinkers, which, when activated, react with each other to form a permanent covalent link. One of the most widely used approaches has been the reaction of sulfhydryl groups with maleimide groups, because it is relatively clean, fast and efficient.[37,38] Therefore, this was the approach used but, because the frequency of sulfhydryl occurrence is usually low, we decided to thiolate the primary amines first, with 2-iminothiolane (Traut's reagent, Figure 5.21).

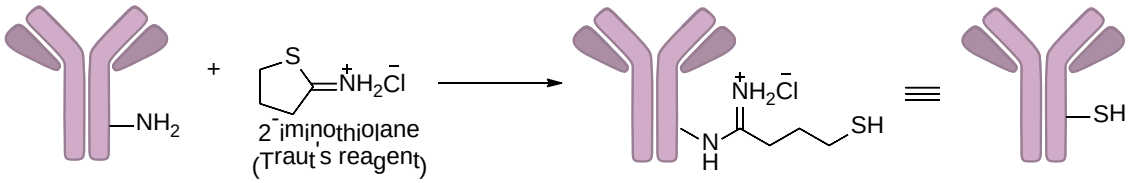

Figure 5.21. Scheme of the TZ's thiolation reaction with Traut's reagent (2-iminothiolane).[39]

Traut's reagent is fully water-soluble and reacts with primary amines in a pH range from 7-10, despite the fact that the imidothioester is not highly stable in solution.[39] One advantage of using this reagent is that the modification in the mAb preserves the positive charge of the original amine. After the reaction in 50 mM phosphate buffer at pH 8, the thiolation degree was not assessed because of the small reaction volume. Moreover, in the purification dialysis, EDTA was added to avoid the oxidation and formation of disulphide crosslinks of the sulfhydryl groups. EDTA chelate metal ions that together with the oxygen removed during the reactions prevent metal-catalysed oxidation of sulfhydryls.[39]

Targeted liposomes are obtained either by incorporation of mAb-lipid conjugates during liposome preparation or by incorporation of lipids with reactive groups during liposome

preparation and subsequent mAb coupling. The last alternative usually renders better results.[40] A major problem in the preparation of protein-liposome conjugates is the tendency of the conjugates to crosslink, resulting in the formation of large aggregates that are cleared rapidly in vivo. The crosslinking effect is intrinsic to all reactions involving multivalent ligands and can be controlled by reducing the number of reactive functions on the liposome or antibody (for example, reducing the degree of thiolation, or by reducing the initial protein/lipid ratio).[37] Another recurrent solution is to use PEG-lipids to control the crosslinking reactions. Access to the liposome surface in the presence of PEG-lipids is strongly affected by size; consequently, single antibodies may penetrate the polymer cloud and react at the surface but the much larger antibody-PEGylated liposome conjugates will not, because of steric interactions between the PEG-lipids incorporated into the membranes. Typically, 1-2% PEG-lipids (PEG molecular weight 2000) in our antibody-conjugated formulations are used, in order to control aggregation but still retain reasonable binding and coupling efficiency.[41,42] Taking advantage of the fact that there is a commercial lipid with a maleimide terminal group, we ran the synthesis of liposomes with a 1.5% of DSPE-PEG_{2000}-Mal of the total lipid (Figure 5.22).

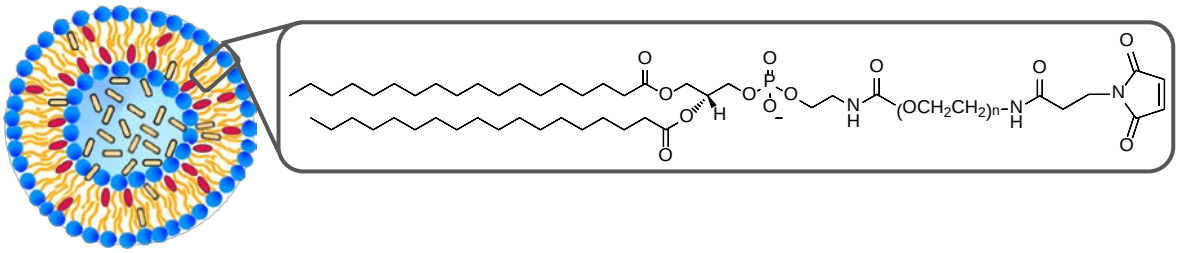

Figure 5.22. Bimodal liposome representation that contains a 1.5% of DSPE-PEG_{2000}-Mal for further reaction with the free thiol groups of TZ.

The scheme reaction between the thiolated TZ and liposomes is shown in Figure 5.23, where the free maleimide group of the liposomes reacts with the sulfhydryl on the protein, obtaining a stable conjugate with a thioether bond. This conjugation efficiency is highly dependent on the pH of the conjugation mixture, yielding good results between 6.5-7.5, although the reaction favours primary amines in a more alkaline pH. However, the pH-dependent equilibrium of the CPT-11 strongly limited the pH work conditions. Different conditions of this reaction were tested, changing the pH and the ionic strength of the buffer or the molar ratio of DSPE-Mal:TZ. However, the best conditions were obtained by the coupling reaction in phosphate buffer at pH 6 with 0.11 M NaCl, whereby considerably increased ionic strength (higher osmolarity) and pH can help maintain the CPT-11 in the active form inside the bilayer. The lactone of CPT-11 opens at pH above 6.8 approximately (Figure 5.4), therefore at pH 6 there is still a great portion of CPT-11 molecules that should be in the active form, having a positive charge that interacts with the negatively charged DOPS lipid.

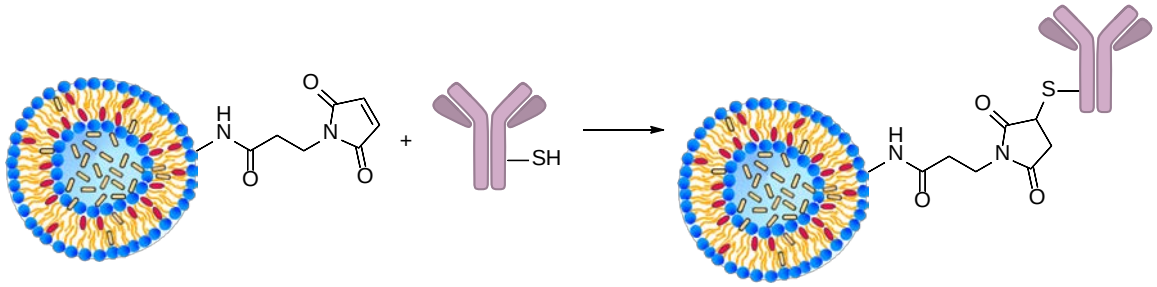

Figure 5.23. Scheme of the coupling reaction between the activated bimodal liposomes and the thiolated TZ, yielding stable thioether linkages.

After the conjugation and purification through the SEC G-25 column, the fractions were analysed by absorbance and fluorescence spectroscopy (Figure 5.24 and 5.25).

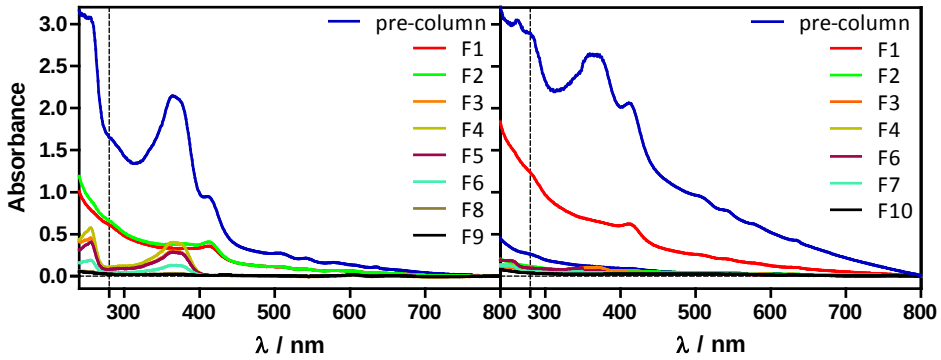

Figure 5.24. Absorption spectra of the fractions collected from the Sephadex G-25 column. The left panel shows the purification fractions after the reaction with 50 mM phosphate buffer and 0.15 M NaCl at pH 8. The right panel shows the purification fractions after the reaction with 50 mM phosphate buffer and 0.11 M NaCl at pH 6.

The absorbance analysis of the fractions collected, clearly showed that CPT-11 was outside the liposomes in the fractions where the protein was not present. In the left panel, CPT-11 was mostly collected in fractions F4 and F5 when the reaction was carried out at pH 8 with irinotecan in carboxylate form. In the right panel at pH 6, mainly with the active form of the compound, the absorbance does not clearly show the presence of irinotecan. Besides the pH difference of the buffers in the coupling reaction, the liposome concentration in the right panel was clearly higher. For a further confirmation that CPT-11 was outside the liposomes, the fractions shown in the right panel were also analysed by fluorescence.

Figure 5.25 shows the fluorescence of Trp residues of the protein, CPT-11 and PpIX of each collected fraction. While for Trp and PpIX the higher fluorescence was registered in fractions F1 and F2, for CPT-11 it was fractions F4 and F6 which had higher signals.

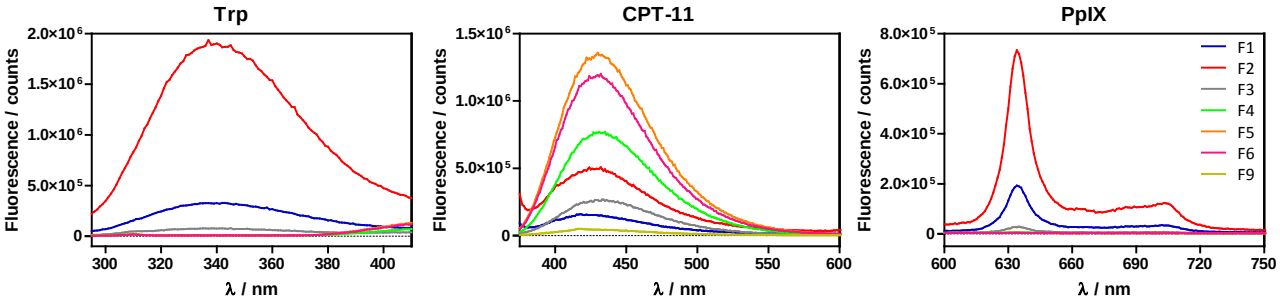

Figure 5.25. Fluorescence emission spectra of Trp, CPT-11 and PpIX in the fractions collected from the Sephadex G-25 column, when the reaction was carried out at pH 6 with 50 mM phosphate buffer and 0.11 M NaCl. The λ_{exc} was 280, 365 and 504 nm for Trp, CPT-11 and PpIX, respectively.

Therefore, although there appear to be fractions with liposomes linked to TZ (fraction F1 and F2), the large majority of CPT-11 molecules were diffused outside the liposomes. According to the CPT-11 fluorescence on fractions F1 and F2 and when interpolated in the calibration curve, only 20% still remained inside the liposomes. The concentration gradient achieved with the increased osmolarity of the buffer was not enough to maintain the drug inside the bilayer. At pH lower than 6, TZ begins to be unstable. Taking everything into consideration, the covalent linkage of the bimodal liposomes to TZ was in detriment of the good results obtained until now. There seems to be a strong pH limitation between the stability of the antibody and the co-encapsulation of both PS and CPT-11 inside the bilayer, which led us to conclude the study at this stage.

5.4. Conclusions

We have investigated the photodynamic activity of the dual system PpIX and CPT-11 delivered to cancer cells using an optimised liposomal formulation. Additionally, we have prepared unimodal liposomes loaded separately with each drug to compare their photophysical properties.

Liposomes of DSPC:DOPS:CHOL 65:35:30, prepared by a microemulsification method, had a diameter of around 95 nm that grew to 175 nm when they contained CPT-11. In all cases, the liposomes had a pronounced negative zeta-potential and an entrapment efficiency above 80%. It is worth noting that the molar ratio of both drugs was maintained in bimodal liposomes, according to the IC_{50} relationship.

The unique fluorescence lifetime of CPT-11 revealed a preferential location in contact with the aqueous core of liposomes. Moreover, the fluorescence spectrum showed the same profile as the CPT-11 in buffer solution, which was in agreement with the previous observation. CPT-11 self-quenching is denoted by the lower Φ_F value in comparison with free drug in solution. Surprisingly, CPT-11 was able to photosensitise $^1O_2$ when excited at 355 nm. The relatively low Φ_Δ is in agreement with the self-quenching as well, reasonably explained by the high local concentration.

Absorption and fluorescence spectra, as well as fluorescence quantum yields of PpIX inside the liposomes, indicated that it was not appreciably aggregated in the lipid bilayer. However, a minor fluorescence component is likely explained by the existence of some PpIX aggregated molecules. On the other hand, the presence of highly concentrated CPT-11 could facilitate the PpIX self-aggregation, which can also account for the remarkable decrease of Φ_Δ in bimodal liposomes. However, the low Φ_Δ value did not affect the PDT efficiency of this formulation, which was in agreement with the PpIX release as confocal images proved.

Interestingly, the treatment with bimodal liposomes rendered a combined effect of both PpIX and CPT-11. The analysis of cells 10 days after the treatment resulted in a huge amount of dead cells through apoptosis, and the scarce, still living cells were senescent. Through β-galactosidase assay, fewer senescent cells were seen in the case of bimodal liposomes compared to those exposed to CPT-11 liposomes.

Finally, the results obtained for the covalent conjugation of the TZ antibody to the bimodal liposomes were discouraging. There seems to be a strong pH limitation between the mAb stability and the co-encapsulation of both PS and CPT-11 inside the bilayer.

Taking everything into consideration, the results presented here showed the development of a dual therapy DDS, targeting different cellular/molecular pathways. As we previously expected, the combined therapy in cancer may be more efficient in destroying cancer cells and in eluding the cellular resistance mechanisms. It has already been confirmed that the combination of phototherapy and chemotherapy, when carefully planned, has been shown to be an effective tumour treatment option pre-clinically and clinically. Chemotherapy can enhance the efficacy of PDT by targeting surviving cancer cells or by inhibiting regrowth of damaged tumour blood vessels.[45]

We have proved that phospholipid-cholesterol liposomes possess optimum properties for the encapsulation of both PpIX and CPT-11. Although the development of new anticancer DDSs have undergone a spectacular increase over the last years,[7,44–46] to our knowledge, it is the first time that deep research has been carried out using bimodal liposomes with PpIX and CPT-11. We also demonstrated that there was a clear improvement in the cytotoxic effect in cells when the bimodal liposomes were administered instead of the combination of unimodal liposomes. Moreover, given the clinical expectations of the individual therapies, this combination is easily translatable for clinical uses, reducing doses and lessening noxious side effects. Nevertheless, several studies *in vivo* need to be done before its clinical use, in order to ensure the positive results and effectiveness of this combined therapy. Furthermore, deeper studies should be carried out for the effective active targeting of this system.

Finally, no studies were done with unimodal liposomes related to administrations at different times in order to know whether the previous administration of the PS or the chemotherapeutic drug results in an improvement in the effectiveness. In that case, one of the liposomes would be administered first and after a certain incubation time, the other liposomes will be delivered.

5.5. References

(1) Bulbake, U.; Doppalapudi, S.; Kommineni, N.; Khan, W. Liposomal Formulations in Clinical Use: An Updated Review. *Pharmaceutics,* **2017**, *9*, 1–33.

(2) Akbarzadeh, A.; Rezaei-Sadabady, R.; Davaran, S.; Joo, S. W.; Zarghami, N.; Hanifehpour, Y.; Samiei, M.; Kouhi, M.; Nejati-Koshki, K. Liposome: Classification, Preparation, and Applications. *Nanoscale Res. Lett.* **2013**, *8*, 102.

(3) Marise De Freitas, L.; Serafim, R. B.; Ferreira De Sousa, J.; Moreira, T. F.; Tavares, C.; Santos, D.; Baviera, A. M.; Valente, V.; Soares, C. P.; Fontana, C. R. Photodynamic Therapy Combined to Cisplatin Potentiates Cell Death Responses of Cervical Cancer Cells. *BMC Cancer,* **2017**, *17*, 1–12.

(4) Zhou, L.; Wei, S.; Ge, X.; Zhou, J.; Jiang, H.; Li, F.; Shen, J. Combination of Chemotherapy and Photodynamic Therapy Using Graphene Oxide as Drug Delivery System. *J. Photochem. Photobiol. B.* **2014**, *135*, 7–16.

(5) Ke, M.-R.; Chen, S.-F.; Peng, X.-H.; Zheng, Q.-F.; Zheng, B.-Y.; Yeh, C.-K.; Huang, J.-D. A Tumor-Targeted Activatable Phthalocyanine-Tetrapeptide-Doxorubicin Conjugate for Synergistic Chemo-Photodynamic Therapy. *Eur. J. Med. Chem.* **2017**, *127*, 200–209.

(6) Ruiz-González, R.; Milán, P.; Bresolí-Obach, R.; Stockert, J.; Villanueva, A.; Cañete, M.; Nonell, S. Photodynamic Synergistic Effect of Pheophorbide a and Doxorubicin in Combined Treatment against Tumoral Cells. *Cancers (Basel).* **2017**, *9*, 18.

(7) Huang, H. C.; Mallidi, S.; Liu, J.; Chiang, C. Te; Mai, Z.; Goldschmidt, R.; Ebrahim-Zadeh, N.; Rizvi, I.; Hasan, T. Photodynamic Therapy Synergizes with Irinotecan to Overcome Compensatory Mechanisms and Improve Treatment Outcomes in Pancreatic Cancer. *Cancer Res.* **2016**, *76*, 1066–1077.

(8) Khdair, A.; Chen, D.; Patil, Y.; Ma, L.; Dou, Q. P.; Shekhar, M. P. V; Panyam, J. Nanoparticle-Mediated Combination Chemotherapy and Photodynamic Therapy Overcomes Tumor Drug Resistance. *J Control Release J Control Release January,* **2010**, *25*, 137–144.

(9) Kong, G.; Dewhirst, M. W. Hyperthermia and Liposomes. *IInt J Hyperth.* **1999**, *15*, 345–370.

(10) Stewart, J. C. Colorimetric Determination of Phospholipids with Ammonium Ferrothiocyanate. *Anal. Biochem.* **1980**, *104*, 10–14.

(11) Tripathy, D. Targeted Therapies in Breast Cancer. *Breast J.* **2005**, *11*, S30–S35.

(12) Tobin, P.; Clarke, S.; Seale, J. P.; Lee, S.; Solomon, M.; Aulds, S.; Crawford, M.; Gallagher, J.; Eyers, T.; Rivory, L. The in Vitro Metabolism of Irinotecan (CPT-11) by Carboxylesterase and Beta-Glucuronidase in Human Colorectal Tumours. *Br. J. Clin. Pharmacol.* **2006**, *62*, 122–129.

(13) Hu, J.; Allen, R.; Rozinek, S.; Brancaleon, L. Experimental and Computational Characterization of Photosensitized Conformational Effects Mediated by Protoporphyrin Ligands on Human Serum Albumin. *Photochem. Photobiol. Sci.* **2017**, *16*, 694–710.

(14) Ding, H.; Sumer, B. D.; Kessinger, C. W.; Dong, Y.; Huang, G.; Boothman, D. A.; Gao, J. Nanoscopic Micelle Delivery Improves the Photophysical Properties and Efficacy of Photodynamic Therapy of Protoporphyrin IX. *J Control Release,* **2011**, *151*, 271–277.

(15) Singh, S.; Aggarwal, A.; Bhupathiraju, N. V. S. D. K.; Arianna, G.; Tiwari, K.; Drain, C. M. Glycosylated Porphyrins, Phthalocyanines, and Other Porphyrinoids for Diagnostics and Therapeutics. *Chem. Rev.* **2015**, *115*, 10261–10306.

(16) Casadó, A.; Sagristá, M. L.; Mora, M. Formulation and in Vitro Characterization of Thermosensitive Liposomes for the Delivery of Irinotecan. *J. Pharm. Sci.* **2014**, *103*, 3127–3138.

(17) Casadó, A.; Giuffrida, M. C.; Sagrist??, M. L.; Castelli, F.; Pujol, M.; Alsina, M. A.; Mora, M. Langmuir Monolayers and Differential Scanning Calorimetry for the Study of the Interactions between Camptothecin Drugs and Biomembrane Models. *Biochim. Biophys. Acta - Biomembr.* **2016**, *1858*, 422–433.

(18) Monteiro, N.; Martins, A.; Reis, R. L.; Neves, N. M. Liposomes in Tissue Engineering and Regenerative Medicine. *J. R. Soc. Interface,* **2014**, *11*.

(19) Baronzio, G. F.; Gramaglia, A.; Baronzio, A.; Freitas, I. Influence of Tumor Microenvironment on Thermoresponse. In *Hyperthermia in Cancer Treatment: A Primer*; Springer US: Boston, MA, **2006**, 67–91.

(20) Liposomes as Sterile Preparations and Limitations of Sterilisation Techniques in Liposomal Manufacturing. *Asian J. Pharm. Sci.* **2013**, *8*, 88–95.

(21) Laouini, A.; Jaafar-Maalej, C.; Limayem-Blouza, I.; Sfar, S.; Charcosset, C.; Fessi, H. Preparation, Characterization and Applications of Liposomes: State of the Art. *J. Colloid Sci. Biotechnol.* **2012**, *1*, 147–168.

(22) Çağdaş, M.; Sezer, A. D.; Bucak, S. Liposomes as Potential Drug Carrier Systems for Drug Delivery. In *Application of Nanotechnology in Drug Delivery*, **2014**, 1–50.

(23) Redmond, R. W.; Gamlin, J. N. A Compilation of Singlet Oxygen Yields from Biologically Relevant Molecules. *Photochem. Photobiol.* **1999**, *70*, 391–475.

(24) Fu, Y.; Kanofsky, J. R. Singlet Oxygen Generation from Liposomes: A Comparison of Time-Resolved 1270 Nm Emission with Singlet-Oxygen Kinetics Calculated from a One Dimensional Model of Singlet-Oxygen Diffusion and Quenching. *Photochem. Photobiol.* **1995**, *62*, 692–702.

(25) Molnár, A.; Dědic, R.; Svoboda, A.; Hála, J. Spectroscopic Study of Singlet Oxygen Photogeneration by Lipophilic Photosensitiser in Liposomes. *J. Lumin.* **2008**, *128*, 783–785.

(26) Ramsay, E.; Alnajim, J.; Anantha, M.; Zastre, J.; Yan, H.; Webb, M.; Waterhouse, D.; Bally, M. A Novel Liposomal Irinotecan Formulation with Significant Anti-Tumour Activity: Use of the Divalent Cation Ionophore A23187 and Copper-Containing Liposomes to Improve Drug Retention. *Eur. J. Pharm. Biopharm.* **2008**, *68*, 607–617.

(27) Wei, H.; Song, J.; Li, H.; Li, Y.; Zhu, S.; Zhou, X.; Zhang, X.; Yang, L. Active Loading Liposomal Irinotecan Hydrochloride: Preparation, in Vitro and in Vivo Evaluation. *Asian J. Pharm. Sci.* **2013**, *8*, 303–311.

(28) Carnevale, J.; Ko, A. H. MM-398 (Nanoliposomal Irinotecan): Emergence of a Novel Therapy for the Treatment of Advanced Pancreatic Cancer. *Futur. Oncol.* **2016**, *12*, 453–464.

(29) Casadó, A.; Mora, M.; Sagristà, M. L.; Rello-Varona, S.; Acedo, P.; Stockert, J. C.; Cañete, M.; Villanueva, A. Improved Selectivity and Cytotoxic Effects of Irinotecan via Liposomal Delivery: A Comparative Study on Hs68 and HeLa Cells. *Eur. J. Pharm. Sci.* **2017**, *109*, 65–77.

(30) Allen, T. M.; Cullis, P. R. Liposomal Drug Delivery Systems: From Concept to Clinical Applications. *Adv. Drug Deliv. Rev.* **2013**, *65*, 36–48.

(31) Perche, F.; Torchilin, V. P. Recent Trends in Multifunctional Liposomal Nanocarriers for Enhanced Tumor Targeting. *J. Drug Deliv.* **2013**, *2013*, 705265.

(32) Valeriote, F.; Lin, H. Synergistic Interaction of Anticancer Agents: A Cellular Perspective. *Cancer Chemother. reports,* **1975**, *59*, 895–900.

(33) Heath, T. D. and Martin, F. J. The Development and Application of Protein-Liposome Conjugation Techniques. *Chem. Phys. Lipids,* **1986**, *40*, 347–358.

(34) Hashimoto, Y.; Endoh, H.; Sugawara, M. Chemical Methods for the Modification of Liposomes with Proteins or Antibodies. In *Liposome Technology*; CRC Press: Boca Raton, FL, **1993**, 3, 41–49.

(35) Leserman, L. D.; Machy, P.; Barbet, J. Covalent Coupling of Monoclonal Antibodies and Protein A to Liposomes: Specific Interaction with Cells in Vitro and in Vivo. In *Liposome Technology*; CRC Press: Boca Raton, FL, **1993**, 29–40.

(36) Torchilin, V. P. Immobilization of Specific Proteins on Liposome Surface: Systems for Drug Targeting. In *Liposome Technology*; CRC Press: Boca Raton, FL, **1993**, 75–90.

(37) Ansell, S. M.; Harasym, T. O.; Tardi, P. G.; Buchkowsky, S. S.; Bally, M. B.; Cullis, P. R. Antibody Conjugation Methods for Active Targeting of Liposomes. In *Drug Targeting*; Humana Press: New Jersey, **2000**, 25, 51–68.

(38) Golkar, N.; Tamaddon, A. M.; Samani, S. M. Effect of Lipid Composition on Incorporation of Trastuzumab-PEG-Lipid into Nanoliposomes by Post-Insertion Method: Physicochemical and Cellular Characterization. *J. Liposome Res.* **2015**, *26*, 1–13.

(39) Hermanson, G. T.; Hermanson, G. T. Chapter 4 - Homobifunctional Cross-linkers. In *Bioconjugate Techniques*, **2008**, 234–275.

(40) Hermanson, G. T.; Hermanson, G. T. Chapter 22 - Preparation of Liposome Conjugates and Derivatives. In *Bioconjugate Techniques*, **2008**, 858–899.

(41) Klauber, T. C. B.; Laursen, J. M.; Zucker, D.; Brix, S.; Jensen, S. S.; Andresen, T. L. Delivery of TLR7 Agonist to Monocytes and Dendritic Cells by DCIR Targeted Liposomes Induces Robust Production of Anti-Cancer Cytokines. *Acta Biomater.* **2017**, *53*, 367–377.

(42) Sofou, S.; Enmon, R.; Palm, S.; Kappel, B.; Zanzonico, P.; Mcdevitt, R.; Scheinberg, D. A.; Sgouros, G. Large Anti-HER2/neu Liposomes for Potential Targeted Intraperitoneal Therapy of Micrometastatic Cancer. *J Liposome Res.* **2010**, *20*, 330–340.

(43) Brezova, V.; Valko, M.; Breza, M.; Morris, H.; Telser, J.; Dvoranova, D.; Kaiserova, K.; Varecka, L.; Mazur, M.; Leibfritz, D. Role of Radicals and Singlet Oxygen in Photoactivated DNA Cleavage by the Anticancer Drug Camptothecin: An Electron Paramagnetic Resonance Study. *J. Phys. Chem. B* **2003**, *107*, 2415–2425.

(44) Brezová, V.; Dvoranová, D.; Zúbor, V.; Breza, M.; Mazúr, M.; Valko, M. Photochemical Properties of Camptothecin in the Presence of copper(II) Ions: The Role of Radicals as Prospective Species in Photodynamic Therapy. *Mol. Biotechnol.* **2007**, *37*, 48–51.

(45) Luo, D.; Carter, K. A.; Miranda, D.; Lovell, J. F. Chemophototherapy: An Emerging Treatment Option for Solid Tumors. *Adv. Sci.* **2017**, *4*, 1–24.

(46) Peng, C.-L.; Lai, P.-S.; Lin, F.-H.; Yueh-Hsiu Wu, S.; Shieh, M.-J. Dual Chemotherapy and Photodynamic Therapy in an HT-29 Human Colon Cancer Xenograft Model Using SN-38-Loaded Chlorin-Core Star Block Copolymer Micelles. *Biomaterials* **2009**, *30*, 3614–3625.

CHAPTER 6

Liposomes with Protoporphyrin IX and Doxorubicin as a drug delivery system with dual therapeutic activity in cancer

With the same aim as the previous chapter of assessing the improved effectiveness of the dual therapy in comparison with the individual treatments, we have also prepared a second liposomal formulation. The liposomes containing PpIX and the chemotherapeutic drug doxorubicin have been studied, evaluating their physicochemical characteristics, photophysical properties and photobiological activity. Moreover, their covalent conjugation with an active targeting moiety, such as a monoclonal antibody, was also considered.

The work described in this chapter has been carried out in collaboration with the group of Dr. Angeles Villanueva at the Universidad Autónoma de Madrid. (Spain).

6.1. Introduction

Doxorubicin (Dox) is the best known and most widely used member of the anthracycline antibiotic group of anticancer agents, originally isolated from *Streptomyces peucetius var. caesius*.[1] It was first introduced in the 1970s and has since been widely used as a main first line anticancer drug because of its broad reactivity spectrum and its excellent antineoplastic activity against a multitude of human cancer diseases.[2] For instance, leukaemia, lymphomas, breast, uterine, ovarian, and lung cancers.[3–5] The mechanism of action has been extensively investigated. Dox is a DNA-intercalating agent and a topoisomerase II inhibitor.[6] Moreover, it is also known to form free radicals, which produce lipid peroxidation and can damage DNA with double and single strand breaks and cause lesions in the bases.[7] However, the clinical use of Dox is hampered by acute and subacute side effects such as vomiting, bone marrow suppression, alopecia and drug-induced dose-limiting irreversible cardiotoxicity and myelosuppression, which may lead to congestive heart failure and death in worst cases.[8] An approach to ameliorating Dox-related toxicity is to use drug carriers, which engender a change in the pharmacological distribution of the drug, resulting in a reduction of drug levels in the heart. Nowadays, there are some approved Dox-liposome formulations such as Doxil in USA and Caelyx and Myocet in Canada and Europe, which were approved in 1999 by the FDA and in 2000 by the European Medicines Evaluation Agency (EMA).[9]

Therefore, with regard to the prior chapter, the goal is to use PDT in combination with Dox in liposomes, reducing the drug dose and looking for additive or synergetic effects. Herein, we present a dual liposome system that co-encapsulates PpIX as the PDT agent and Dox, using a completely different lipid formulation from chapter 5. This system has been characterised and compared with the properties of its unimodal counterpart (i.e., liposomes that only encapsulate one agent). Moreover, we studied the photophysical properties and their $^1O_2$ production. The cell studies, most of them carried out at the Universidad Autónoma de Madrid by the group of Dr. Angeles Villanueva, provided us with the cell viability results and the study of the cell death mechanisms. Also for cell studies, unimodal and bimodal liposomes were studied and compared. Moreover, two different scenarios were constructed to reflect the importance of administering both agents in the same vehicle: unimodal liposomes given in combination or bimodal liposomes which already contain both agents in the same carrier. Finally, the optimised system was functionalised and covalently linked to a monoclonal antibody through a pegylated lipid for active targeting. Preliminary results in two cell lines, with positive and negative overexpression of HER-2 receptors, are presented in order to evaluate the improved selectivity.

6.2. Experimental section

6.2.1. Materials

The phospholipid egg *L*-α-phosphatidylcholine (EPC), with a purity grade of a 95%, and cholesterol (CHOL) were purchased from Avanti Polar Lipids (Birmingham, USA). Doxorubicin hydrochloride (Dox) was acquired from Apollo Scientific (Manchester, United Kingdom) with a purity grade of > 99%. The PS protoporphyrin IX (PpIX) was obtained from Frontier Scientific (Lancashire, United Kingdom). The citric acid monohydrate and sodium carbonate anhydrous were purchased from Panreac (Barcelona, Spain). Tetrahydrofuran (THF) HPLC grade without stabiliser, the solvent in which the liposomes were disrupted, was acquired from Scharlab (Barcelona, Spain). *Meso*-tetraphenylporphyrin (TPP) and Rose Bengal (RB) used as references, were acquired from Sigma-Aldrich Chemical Co. (St. Louis, MO, USA). All other chemicals were commercially available reagents of at least analytical grade. Milli-Q water (Millipore Bedford, Massachusetts system, resistivity of 18 MΩ cm) was used.

The dialysis tubing cellulose membrane with a cut-off of 12 kDa was purchased from Sigma Aldrich. Polyester Chromafil® filters from Macherey-Nagel (Düren, Germany) were used for sterilising the formulations with a pore size of 0.20 μm and a diameter of 25 mm.

6.2.2. Preparation of unimodal and bimodal liposomes

Intermediate unilamellar liposomes (IUVs) were prepared by microemulsification method, using a binary mixture of EPC:CHOL in a molar ratio of 7:3. Contrary to the methodology of chapter 5, the PS was first encapsulated by a passive method, whereas Dox was encapsulated using active loading methods once the liposomes were already formed.

In order to obtain blank or PpIX unimodal liposomes, the binary mixture of lipids and the appropriate amount of PpIX were dissolved in the minimum amount of chloroform, together with a small amount of methanol to obtain a clear solution. The PS was added to the binary lipid mixture, maintaining the lipid:PpIX molar ratio at 25:1 The organic solvents were evaporated by rotary evaporation yielding a thin lipid film on the sides of a round bottom flask. Formulations containing PpIX prior to $CHCl_3$ evaporation were kept protected from light during 1 h in order to facilitate the contact lipids/PS. From now on, the protocol followed to obtain size homogenously IUVs was the same of section 5.2.3, but hydrating the film with the appropriate volume of 300 mM (pH 4.0) citrate buffer to a final lipid concentration of 20 mg/mL. Microemulsification was also carried out by pumping the fluid 10 cycles through the interaction chamber at 110 kPa, as was previously reported.

Dox was then encapsulated in blank or PpIX liposomes in response to a transmembrane pH gradient, thus obtaining the Dox unimodal and bimodal liposomes. Briefly, the pH of the liposome suspension, initially at pH 4.0, was raised to pH 7.8 with 0.5 M Na_2CO_3. In this step, the lipid and PpIX concentration were diluted by almost half (lipid:PpIX molar ratio of 50:1 aprox.), creating a pH gradient across the vesicles, acidic inside and slightly basic outside. An aqueous solution of Dox was subsequently heated to 60 ºC for 5 min, and then added dropwise to a preheated (60 ºC) vial of liposomes suspension, adding the appropriate amount of Dox to achieve a lipid:Dox molar ratio of 250:1. This mixture was incubated under intermittent gentle shaking for 20 min. at 60 ºC. All liposomes preparations were sterilised by filtration with a 0.20 μm diameter filter and stored in the dark at 4 ºC.

6.2.3. Liposome characterisation

Determination of the total Dox and PpIX content

THF was added to a known aliquot of liposome suspension (liposome aliquot/THF; 1:50 v/v) in order to disrupt the bilayer and release the loading. The vials were closed, stirred and heated above the T_m for 30 min, which enabled a quick rupture of the bilayers.

The concentration of both PpIX and Dox was quantified spectrophotometrically by using calibration curves obtained under the same conditions. PpIX was quantified by fluorescence emission (Spex-Fluoromax 4, Horiba Jobin Yvon, Edison, NJ) at λ_{max} 632 nm (λ_{exc} 504 nm), whereas the Dox was also quantified by fluorescence at λ_{max} 588 nm (λ_{exc} 470 nm).

In the case of bimodal liposomes, the Dox concentration was also evaluated by fluorescence at λ_{max} 588 nm (λ_{exc} 470 nm), while PpIX's determination was more elaborate because both agents emit at 632 nm if excited at 504 nm. Thus, the PpIX's content was determined by measuring its fluorescence at 690 nm upon excitation at 632 nm and comparing with a calibration curve obtained under the same conditions.

Determination of the non-encapsulated PpIX fraction or the encapsulated fraction of Dox

The fraction of non-encapsulated PpIX was determined as described in section 5.2.3. Size exclusion chromatography was used to separate free Dox from liposome-encapsulated molecules. A PD-10 desalting column (disposable PD 10 Desalting Columns, GE Healthcare Bio-Sciences AB, Uppsala, Sweden) containing Sephadex G-25 was used, which allows a rapid separation of high molecular weight substances from low molecular weight ones, namely the Dox fraction in the extra-liposomal media. A known aliquot of liposome suspension was added to the PD-10 column and eluted with a mixture of citrate buffer with the necessary amount of

Na_2CO_3 0.5 M until a pH 7.8 was reached (the same media as that of the liposome suspensions). The liposome band was collected in a graduated cylinder in order to measure the volume. From this diluted suspension, a known aliquot was taken and placed in vials, then the appropriate amount of THF was added in order to disrupt the bilayer and release the loading (liposome aliquot/THF; 1:50 v/v). The quantification at this point followed the protocol aforementioned for the Dox total content.

Determination of the lipid content

The amount of lipids in the liposome suspensions was measured following the Stewart's method, detailed in section 5.2.3.[10]

Vesicle Size and ζ potential

The equipment and followed protocol was the same as that described in section 5.2.3.

Control of the liposome suspensions stability

The stability of liposomes during storage was controlled by measuring their size over time. Moreover, absorbance spectra were collected to monitor any turbidity or scattering increase over storage time.

Drug loading and entrapment efficiency calculation

Drug loading (DL) and entrapment efficiency (EE) of the PS and the chemotherapeutic drug were calculated as follows:

$$DL\ \%\ (w/w) = \frac{mass\ of\ drug/PS\ encapsulated\ (mg)}{mass\ of\ lipids\ (mg)} \cdot 100$$

$$EE\ \%\ (w/w) = \frac{mass\ of\ drug/PS\ encapsulated\ (mg)}{mass\ of\ drug/PS\ theoretically\ encapsulated\ (mg)} \cdot 100$$

The theoretical value of drug encapsulated was the total drug concentration measured and quantified before the sterilisation by filtration in order to know which percentage is lost.

6.2.4. Cell cultures

The tumour epithelial HeLa cells (human cervix adenocarcinoma, ATCC CCL-2) and BT-474 cells (ATCC HTB-20) were purchased from American Type Culture Collection (USA). Cells were grown as monolayer attached cultures in DMEM supplemented with 10% (v/v) fetal bovine serum (FBS), 50 U/mL penicillin and 50 µg streptomycin/mL (whole media), all acquired from Thermo Fisher Scientific (Merck Millipore, Billerica, MA, USA). Cells were cultured under a 5% CO_2

atmosphere plus 95% air at 37 ºC, and maintained in a SteriCult 200 (Hucoa- Erloss, Madrid, Spain) incubator. Depending on the experiment, cells were seeded in 25 cm^2 flasks (F25) or in 24-well plates with or without 10-mm square coverslips. Subconfluent cell cultures were used with a cell density of at least 3000 cell/cm^2 72 h before starting the experiments. The cell density was assessed with a Bürker counting chamber. All the plastic materials were purchased from Corning (Nueva York, EE UU).

Photodynamic treatments in vitro

Cells seeded in 24-well plates (with or without coverslip) or F25 flasks, depending on subsequent processing, received photodynamic treatments with either the PpIX unimodal liposomes or the bimodal liposomes with Dox. Accordingly, cells were incubated for 24 h with 2.5 μM PpIX liposome suspension in aqueous buffer, washed three times with medium (not serum supplemented) and maintained in whole medium during irradiation and post-treatment time. Irradiations were performed by means of a red light-emitting diode (LED Par 64, Showtec; Shoreham, UK) device (λ= 633 ± 9 nm) with a fluence rate of 7 $mW \cdot cm^{-2}$. Cells were irradiated for 4.5 min, corresponding to total light dose of 2 $J \cdot cm^{-2}$ (total light dose ($J \cdot cm^{-2}$)= fluence rate ($W \cdot cm^{-2}$) x treatment time (s)). Either immediately or at different times after irradiation different methodological protocols were performed, carrying out the MTT 24 or 72 h after the treatments. Besides, experiments were done by incubation with the corresponding blank or empty liposomes or the loaded liposomes without irradiation (dark toxicity), in order to examine possible cytotoxic effect exercised by the lipid or the PS.

Cell viability studies

Dark- and photo-toxicity was assessed by the MTT colorimetric assay 24 and 48 h after treatments. This method evaluates the number of viable cells based on the mitochondrial activity, involving a reduction of the MTT to its insoluble formazan, a purple colour compound only soluble in organic solvents. Immediately prior to use, a stock solution of dimethylthiazolyl-diphenyl-tetrazolium bromide (MTT; Sigma-Aldrich, 1 mg/mL) in PBS was prepared and sterilised by filtration. Five hundred microliters of this MTT solution (50 μg/mL MTT in whole medium) was added to each culture dish without coverslip. Cells were incubated for 3 h, then the reduced formazan was extracted with 500 μL DMSO and the absorbance was measured at 542 nm in a SpectraFluor spectrophotometer (Tecan Group Ltd, Männedorf, Switzerland). Cell survival was expressed as the percentage of absorption of treated cells in comparison with that of control cells. Data corresponded to mean values ± SD from at least four different experiments.

Morphological studies

Morphological changes were assessed at different times after incubation and PDT in the case of PpIX and bimodal liposomes, by differential interference contrast (DIC) microscopy. An inverted microscope was used to analyse the samples at different times without being processed, to avoid possible morphological artefacts. These studies consist on the morphological alterations' analysis that characterises the main cell death mechanisms.

Optical microscopy

Routine observation of the cell cultures during their maintenance and the effect of the different treatments were done with an inverted microscope Olympus CKX1 (Tokyo, Japan). Living cells were captured with an inverted microscope Leica DMI 6000B equipped with a Leica DFC420 C digital camera (Leica) and images were processed using the Photoshop CS5 software (Adobe Systems, USA).

Statistical calculations

For statistical calculations one-way ANOVA with post-hoc Tukey Kramer Multiple Comparisons test were used. P values < 0.05 (*), < 0.01 (**), and < 0.001 (***) were considered as statistically significant. The software R Development Core Team, a language and environment for statistical computing (R Foundation for Statistical Computing, Vienna, Austria) were used for the analysis.

6.2.5. Preparation of trastuzumab-conjugated liposomes

Trastuzumab (Herceptin®, ~148 kDa, abbreviated henceforth as TZ) was purchased from Carbosynth (Berkshire, UK) and was stored aliquoted at -20 ºC. The lipids DSPE-PEG_{2000}-Mal and L-α-distearoyl-phosphoethanolamine-N- [methoxy (polyethylene glycol)-2000] (ammonium salt) (DSPE-PEG_{2000}) were acquired from Tebu-bio (Barcelona, Spain). The Sepharose CL-6B was acquired from Sigma-Aldrich Chemical Co. (St. Louis, MO, USA) with a bead diameter of 40- 165 μm and a separation range of 10- 4000 kDa.

Preparation of maleimide-functionalised liposomes

IUVs were prepared by microemulsification method as was previously described, but using a ternary mixture of EPC:CHOL:DSPE-PEG_{2000}-Mal in a molar ratio of 7:3:0.16. The DSPE-PEG lipid represented a 1.6% of the total lipid. With this lipid, blank liposomes and bimodal liposomes were prepared, in the latter case using the same lipid:drug molar ratio of 25:1 and 250:1 for PpIX and Dox, respectively. Moreover, bimodal liposomes with a PEG-lipid but without the Mal termination (DSPE-PEG_{2000}) were also prepared as a control. The dried film was also hydrated

with 300 mM (pH 4.0) citrate buffer to a final lipid concentration of 20 mg/mL. The protocol continued as was described above. These liposomes were prepared 1 day before the reaction with the thiolated TZ, to avoid undesirable reactions with the free maleimide group.

Antibody thiolation

The mAb were thiolated using Traut's reagent (2-iminothiolane) at a Traut's:TZ molar ratio of 16:1. Traut's reagent solution was prepared immediately before its use, dissolved in 50 mM phosphate buffer at pH 8 to a concentration of 2 mg/mL. TZ and Traut's reagent were mixed together in the same buffer and incubated at RT in the dark for 1.5 h under argon atmosphere. The antibody was purified by dialysis (MW cut off 12000-14000) in an aqueous mixture of pH 7.8. This aqueous mixture was equal to the extraliposomal medium, thus to a certain amount of 300 mM citrate buffer at pH 4 the necessary amount of 500 mM sodium carbonate was added until reach the pH 7.8. 10 mM EDTA was also added to remove the non-reacted Traut's reagent. The thiolated TZ was prepared just before addition of the liposomes.

Conjugation of thiolated TZ to bimodal liposomes

Thiolated TZ and bimodal liposomes were mixed in a glass vial at a DSPE-Mal:TZ molar ratio of 10:1, and following the exact procedure detailed in chapter 5, subsection 5.2.5. However, the purification was carried out through size exclusion chromatography using Sepharose CL-6B that was eluted with the same aqueous mixture at pH 7.8.

6.3. Results

6.3.1. Physicochemical characterisation

Dox is an amphipathic molecule that possesses a water-insoluble aglycone group, the adriamycinone, and a water-soluble sugar named daunosamine. However, the molecule is considered hydrophilic at physiological pH since it presents a positive charge on the sugar moiety (Figure 6.1). The most lipophilic molecular form of Dox is dominant at moderately alkaline pH, between 8.2 and 10.2, the pK_a values of the amine and the phenol in position 11 respectively. The hydrophilicity of Dox is also dependent on the drug concentration, since beyond a concentration of 30 μM Dox molecules less hydrophilic dimers are prone to form (stacking effect), which precipitate in aqueous solution. The pH increase (i.e., of the neutral form percentage) is in favour of the stacking phenomenon.[8,11]

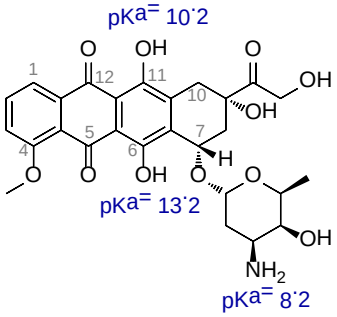

Figure 6.1. Chemical structure of Dox, a well-known chemotherapeutic drug of the anthracycline family.[8]

There are two proposed mechanisms by which doxorubicin acts in cancer cells: 1) intercalation into DNA and disruption of topoisomerase-II-mediated DNA repair and 2) generation of free radicals which lead to damage in cellular membranes, DNA and proteins. In brief, Dox is oxidised to a semiquinone, an unstable metabolite, which is converted back to Dox in a process that releases ROS. These species can lead to lipid peroxidation, membrane and DNA damage, oxidative stress, and trigger apoptotic pathways to cell death. Alternatively, Dox may interact with DNA by intercalation and inhibition of macromolecular biosynthesis, arresting the progression of topoisomerase II and breaking the DNA chain for replication.[1] However, although this overall mechanism is well-known, there are still some mechanistic details under discussion.

On the other hand, the PS chosen as partner was PpIX, as in the previous chapter. The spectroscopic characteristics of these free drugs are shown in Figure 6.2.

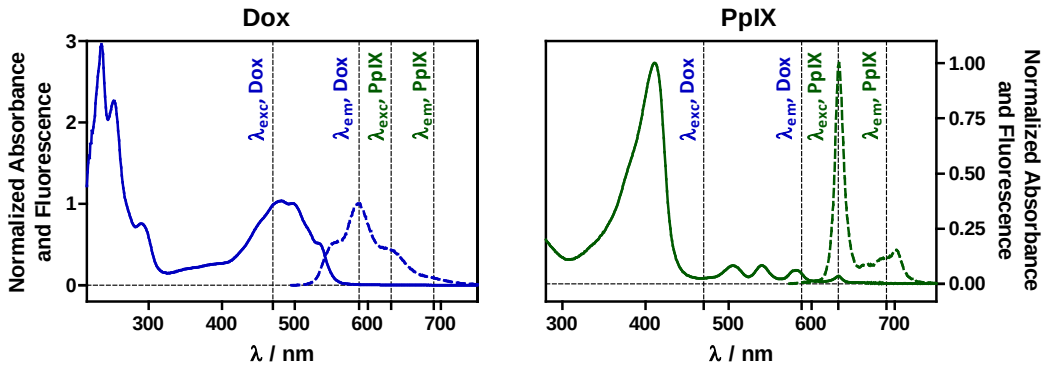

Figure 6.2. Absorption (solid line) and fluorescence emission (dashed line) spectra of Dox (blue) and PpIX (green) solutions, in water pH 7.8 and THF, respectively. The vertical dashed lines show the wavelengths used for the measurements of the entrapment efficiencies either for Dox or PpIX.

The absorption and fluorescence spectra of Dox in water shows maxima at 480 nm and 588 nm, respectively. PpIX shows a Soret band absorption at 411 nm and four Q bands at about 505, 540, 580 and 632 nm in THF. The fluorescence spectrum peaks at 632 nm. The fluorescence overlap of both agents makes the individual characterisation tricky. Therefore, we decided to follow Dox at 588 nm where PpIX does not emit, and excite PpIX at 632 nm because at ~580 nm (a Q band maximum) there was still a low absorption from Dox.

In the case of Dox, any group variation on the chromophore ultimately leads to changes in the absorption and fluorescence spectra. One clear example is the pH change, since the deprotonation of the phenol group in basic conditions leads to a red-shift absorbance and a dramatic decrease in the fluorescence emission (Figure 6.3).[8]

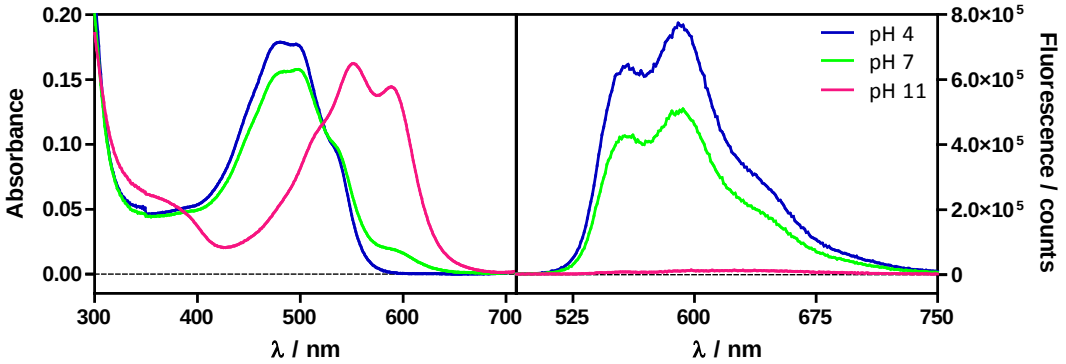

Figure 6.3. Absorption (A) and fluorescence emission (B) spectra of Dox at different pHs.

It is also known that these changes in the spectroscopic properties go along with a change of colour.[8] Dox appears orange at pH 4, orange-reddish at pH 7, violet at pH 11 and blue at pH 13 or above (Figure 6.4).

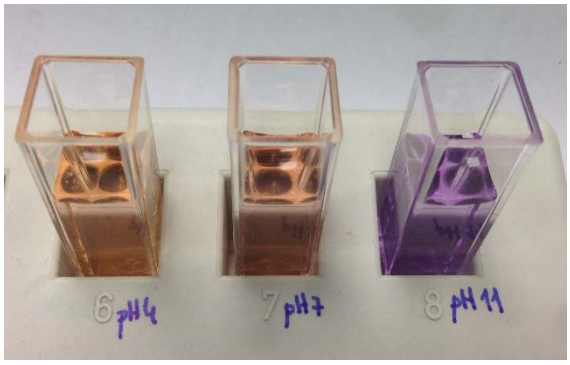

Figure 6.4. Dox colour change with pH, appearing orange at pH 4, orange reddish at pH 7 and violet at pH 11.

As mentioned above, one approach to ameliorating Dox-related toxicity is to use drug carriers. One possible DDS for Dox are liposomes. Indeed, currently there are some approved Dox-liposome formulations such as Doxil, Caelyx (these two in pegylated form) or Myocet (non-pegylated form). Many advantages have already been confirmed such as higher drug levels in tumour tissue with Doxil® than with free Dox in multiple cancer models.[12,13] Moreover, the Dox-induced cardiotoxicity, one of typical side effect of free Dox treatment, is reduced when the drug is encapsulated in any carrier.[14–16] Doxil/Caelyx liposomal formulation are composed of hydrogenated soya phosphatidylcholine, CHOL and PEG-modified phosphatidylethanolamine (55:40:5 molar ratio), whereas Myocet is composed of egg phosphatidylcholine (EPC) and CHOL (55:45 molar ratio).

For Dox encapsulation in liposomes passive trapping methods are not efficient, obtaining maximum yields of 80% and low drug-to-lipid ratios.[8] On the contrary, active trapping procedures are highly efficient, which is based on the addition of Dox to pre-formed liposomes through a trans-bilayer ion gradient. These different loading techniques are usually driven by the use of pH-, manganese-, sulphate- or citrate- gradients. All of these concepts follow one principle, namely that the free Dox base diffuses inside the liposome in response to one of these gradients. Furthermore, once Dox is inside the vesicles, it suffers a modification which inhibits the membrane re-permeation, resulting in accumulation of the drug inside the liposomes.[2] In our case, the transmembrane gradient was caused by a pH- and concentration- gradient, being acidic in the interior and slightly basic in the external bilayer of the liposomes. The core of the liposomes contained citrate buffer 300 mM at pH 4, whereas the external pH was adjusted, after the PpIX or blank liposomes were pre-formed, to 7.8 with 500 mM Na_2CO_3. This concentration and pH gradient helps maintain the drug inside the bilayer. The non-protonated Dox would then diffuse into the vesicles, where the lower pH causes the Dox protonation. The positively-charged Dox can no longer cross the bilayer and is therefore trapped inside. New extra-liposomal and non-protonated Dox can further diffuse into the liposomes due to the gradient. Therefore, a "proton pool" inside the liposomes is necessary as a driving force for Dox loading.

In the previous chapter, the importance of the lipid composition was already mentioned. The lipid formulation chosen was EPC:CHOL 7:3, according to the approved lipid formulations and some published articles.[2,17] On the one hand, natural EPC lipid is a further purification of total egg extract, thus it is still a mixture of unsaturated fatty acid chains, mainly of phosphatidylcholine (95.5%) and egg sphingomyelin (SM, 0.5%), with mostly 16:0 and 18:1 fatty acids. The EPC lipid results in a low T_m of -15 ºC when it is pure. Phosphatidylcholine is the major membrane phospholipid in eukaryotic cells, which constitutes a flexible bilayer increasing its permeability. In general, longer acyl chains like C18 tend to release the payload less rapidly than C14 short acyl chains. On the other hand, CHOL decreases the fluidity and permeability of the bilayer a bit at temperatures above the T_m, limiting the cargo rapid leakage. Indeed, CHOL is a common constituent of liposomal Dox formulations due to its ability to modulate membrane permeability and biological stability.[8] Ultimately, a fluid and permeable membrane is needed to facilitate the Dox molecules diffusion across the bilayers. Table 6.1 summarises all the conditions tested with this lipid formulation EPC:CHOL 7:3.

Table 6.1. Some physicochemical characteristics of the different conditions tested. All the formulations have the same lipid composition EPC:CHOL (7:3) and the same initial lipid concentration of 20 mg/mL.

Formulation	Lipid:Drug[a]	Method	EE %	Z-ave (nm)[a]	Notes
1	Dox 5:1	Extrusion	98	173	-
2	Dox 5:1	Microemulsification 110 kPa 10 cycles	n/m	n/m	Encapsulation of solid Dox. A significant part of Dox precipitates outside[17]
3	Dox 5:1	Microemulsification 110 kPa 10 cycles	98	161	Encapsulation of a Dox solution. The precipitate of the prior formulation was not seen
4	PpIX 50:1	Microemulsification 110 kPa 10 cycles	87	145	1 h lipids/PS before the film formation
5	Dox 250:1 PpIX 50:1	Microemulsification 110 kPa 10 cycles	89 99	149	Prepare the PpIX liposomes and then encapsulate Dox through a pH gradient

a Referred to the molar ratio

First, the extrusion method was tested in order to assess whether Dox was retained in polycarbonate filters and well encapsulated through the gradient aforementioned (formulation # 1). Good results were obtained for a lipid:drug molar ratio of 5:1. Therefore, since the final goal was the bimodal PpIX+Dox preparation, the microemulsification method was also tested. No changes were expected because the liposomal suspension that goes through the emulsiflex had previously undergone the Dox encapsulation procedure. We also tested two different ways of adding Dox for its encapsulation: 1) in powder or 2) in a concentrated solution (formulations # 2 and 3). The addition of Dox powder resulted in poor encapsulation, as judged by visual inspection, since most of the drug remained outside the bilayer forming a precipitate (formulation # 2). Conversely, when Dox was added in solution, high entrapment efficiencies were achieved with good visual results.

Regarding PpIX encapsulation, entry # 4 tested the lipid composition as an optimum formulation for its entrapment. Good entrapment results were obtained maintaining the incubation time PpIX/lipids prior to form the dried film, as was done in the previous chapter. This lipid composition results in higher liposomes size compared to the ones obtained in chapter 5.

Finally, a first test was carried out with the dual drug/PS encapsulation maintaining the ratio between IC_{50} Dox:PpIX 1:5, according the IC_{50} experiments with free drugs (Figure 6.14). The dilution step during the adjustment of the external pH must be considered in the formulation designed. For this reason, formulation # 5 did not reach the correct ratio between Dox and PpIX. Further tests lessening the PpIX:lipid molar ratio were also carried out without improving the outcomes. Therefore, in this dual formulation the limiting factor is the PS encapsulation. However, some physicochemical characteristics of Dox liposomes with a lower lipid:drug molar ratio are presented in Table 6.2.

Table 6.2. Physicochemical characteristics of blank and Dox unimodal liposomes, with lower lipid:drug molar ratio than in the bimodal formulations. The lipid composition was EPC:CHOL 7:3.

Encapsulated drug	Z-ave (nm)[a]	PI[b]	ζ-pot (mV)[c]	DL % (w/w)	EE % (w/w)	[Dox] (mM)[d]
-	190 ± 41	0.39 ± 0.06	-7 ± 6	-	-	-
Dox	162 ± 26	0.21 ± 0.04	-3 ± 1	17.7 ± 0.1	99 ± 0	2.40 ± 0.02

a Particle size measured as Z average mean
b Polydispersity Index
c Zeta-potential
d Bulk encapsulated drug concentration in the liposomes suspension
Values reported are the mean ± SD of two independent experiments

Figure 6.5 shows the appearance of these concentrated Dox liposomes.

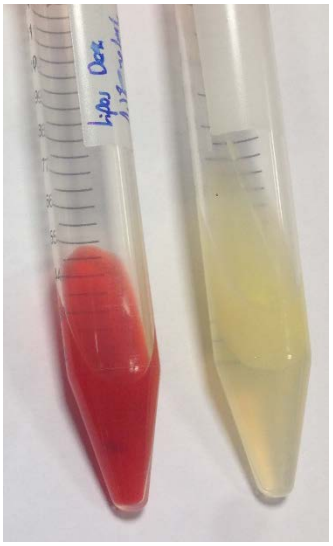

Figure 6.5. Photograph of blank and concentrated Dox liposomes.

It is worth noting that the dilution process necessary to change the external pH is the reason why the lipid concentration at the beginning of the synthesis was 20 mg/mL. Blank liposomes (i.e., without the encapsulation of any drug) were always prepared as controls. Table 6.3 summarises the most important physicochemical characteristics for the optimised preparations either bimodal or unimodal formulations, including blank liposomes.

Table 6.3. Physicochemical characteristics of blank, unimodal and bimodal liposomes with Dox and PpIX loaded. The lipid composition was EPC:CHOL 7:3.

Encapsulated drug	Z-ave (nm)[a]	PI[b]	ζ-pot (mV)[c]	DL % (w/w)	EE % (w/w)	[Dox] (μM)[d]	[PpIX] (μM)[d]	[lipid] (mg·mL^{-1})
-	136 ± 21	0.25 ± 0.06	-4 ± 1	-	-	-	-	11.7 ± 1.0
Dox	153 ± 31	0.38 ± 0.14	-4 ± 1	0.7 ± 0.2	95 ± 4	148 ± 21	-	10.4 ± 0.4
PpIX	132 ± 21	0.37 ± 0.08	-9 ± 1	3.6 ± 0.1	91 ± 8	-	721 ± 77	11.3 ± 0.6
both	124 ± 32	0.28 ± 0.10	-9 ± 2	0.7 ± 0.1 3.3 ± 0.2	95 ± 3 90 ± 9	137 ± 22 -	- 685 ± 73	11.6 ± 0.6

a Particle size measured as Z average mean
b Polydispersity Index
c Zeta-potential
d Bulk encapsulated drug concentration in the liposomes suspension
Values reported are the mean ± SD of at least three independent experiments

Adding Dox to liposomes resulted in an increase in their size and polydispersity index. At the time when PpIX was encapsulated, the size was comparable to the value of blank liposomes but with higher polydispersity as well. On the other hand, the size and polydispersity of bimodal liposomes were remarkably smaller than those of the other formulations, since the co-encapsulation of both drugs somehow stabilises the preparation. In principle, PpIX and Dox do not disturb each other since PpIX is accommodated in the bilayer and Dox in the aqueous core. The zeta-potential was near-neutral in all formulations, somewhat more negative for those formulations that contained PpIX. This fact indicated that a small fraction of PpIX molecules might be in the external part of the bilayer. The overall zeta-potential was slightly negative in all formulations due to a small percentage of *L*-*α*-phosphatidylserine in the commercial EPC. It has been published that neutral PEGylated Dox liposomes show many advantages in comparison with their cationic counterparts: a superior therapeutic activity, a drop in the antitumor efficacy and low tumour accumulation.[18] Moreover, Allen *et al*. stated that near-neutral surface charge increases the circulation half-life of liposomes, which are more stable than negatively-charged liposomes when they are injected into the blood circulation.[19] In all cases, the entrapment efficiency was above 90% (looking at the average values), being slightly lower for PpIX formulations. For these particular formulations, most of the drug was lost in the sterilisation process by filtration through 0.20 μm filters. Thus, the non-encapsulated PpIX was <3% after filtration in all cases.

Figure 6.6 shows the appearance of the four optimised preparations, presenting similar turbidity by visual inspection.

Figure 6.6. Photograph of one of the batches with the four formulations from left to right are: Dox unimodal and PpIX unimodal liposomes, bimodal liposomes and blank liposomes.

Formulation stability. As in the previous chapter, the stability of the liposomal suspensions was studied assessing the evolution of their size, zeta-potential and turbidity over time. The mostly unsaturated nature of the lipid formulation and the near-neutral zeta-potential, which have no force to prevent the particles flocculating, would suggest a low stability. Nevertheless, the size

and zeta-potential evolution diagrams over time, lead to the opposite conclusion (Figure 6.7). The size of all preparations was remarkably stable for eleven weeks after preparation. Only blank liposomes showed some disperse values.

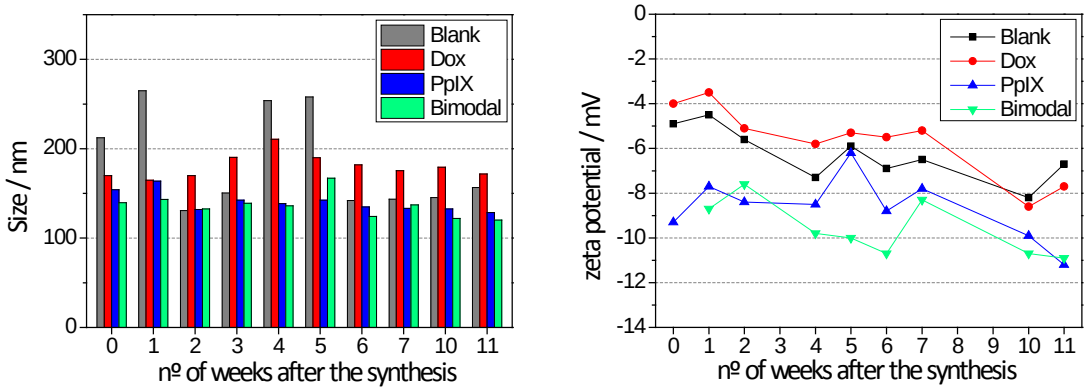

Figure 6.7. Size (Z-average mean, left panel) and zeta-potential (right panel) evolution diagrams over time of the four liposome preparations.

Likewise, the zeta-potential was surprisingly stable for all preparations during the first seven weeks, and then decreased by a mere -3 mV.

Vesicles physical stability can also be assessed by measuring the absorbance at 450 nm over time (Figure 6.8).

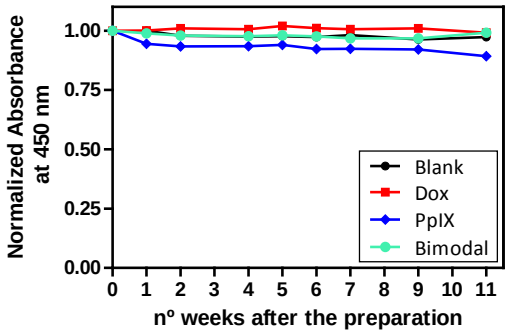

Figure 6.8. Normalised Absorbance at 450 nm over time of the four liposomes preparations.

The turbidity of the four preparations was remarkably stable for eleven weeks after preparation. This is in agreement with the size-evolution over time. The suitability of lyophilisation was also tested, but unfortunately, the rehydratation of the lyophilised powder resulted in a considerable size increase in the vesicles and a low Dox entrapment.

6.3.2. Spectroscopic and photophysical properties

The absorption spectrum of Dox unimodal liposomes shows strong scattering, hindering the Dox absorption bands, which could be better appreciated once disrupted in THF (Figure 6.9,A). Figure 6.9 B shows the bimodal absorption in buffer and THF, presenting an undistinguishable Dox

absorption due to its lower concentration in the vesicles. The typical bands of PpIX, including the Q-bands, could however be well distinguished.

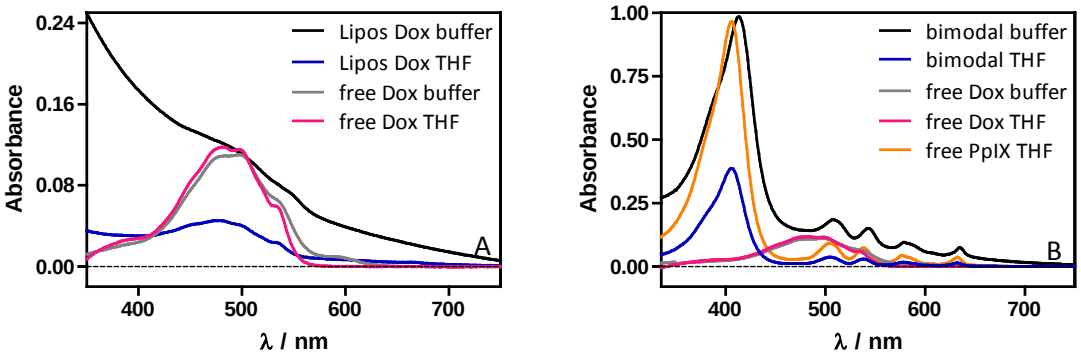

Figure 6.9. Absorption spectra of Dox unimodal (A) and bimodal (B) liposomes, including their absorption in aqueous solution at pH 7.8 and once they were disrupted in THF (1:50; liposomes aliquot:THF). The spectra of both agents in solution are given for comparison. Buffer stands for the mixture of citrate buffer and sodium carbonate until reaching pH 7.8.

Figure 6.10 shows the fluorescence spectra of the unimodal and bimodal liposomes; panel A presents the Dox region and panel B the PpIX region. Dox in either unimodal or bimodal liposomes shows the same fluorescence spectrum but with a difference in the relation between maxima in comparison with free Dox. This fact likely indicates that a fraction of Dox was partially aggregated. Once the liposomes were disrupted in THF, the spectra show the same profile as for free Dox in this media. Conversely, PpIX shows a structured fluorescence spectrum even in aqueous suspension, which indicates that the molecules are localised in the bilayer without forming aggregates. In PpIX unimodal liposomes, the emission band showed well-structured bands upon excitation at 504 nm (data not shown). Once again, the spectrum peak was 3- 4 nm shifted to the red, compared with free PpIX in THF, as already described in chapter 5.

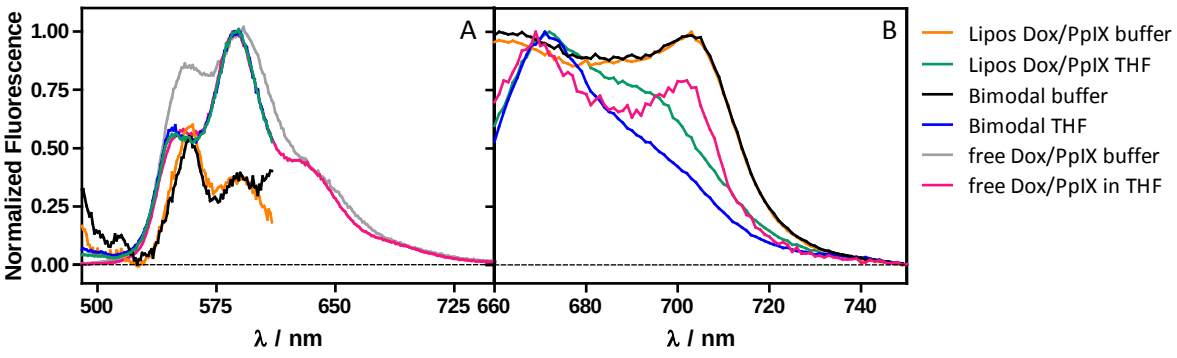

Figure 6.10. Fluorescence emission spectra of the Dox (A) and PpIX (B) unimodal and bimodal liposomes. Free drugs in solution spectra are given for comparison. The λ_{exc} for Dox was set at 470 nm and at 632 nm in the case of PpIX. Buffer stands for the mixture of citrate buffer and sodium carbonate until reaching pH 7.8.

The determination of fluorescence and $^1O_2$ quantum yield (Φ_F and Φ_Δ) were determined as described in chapter 5. Figure 6.11 shows the absorbance and fluorescence emission spectra of

the unimodal liposomes. In all cases, the absorbance spectra of diluted blank liposomes were also recorded for scattering subtraction.

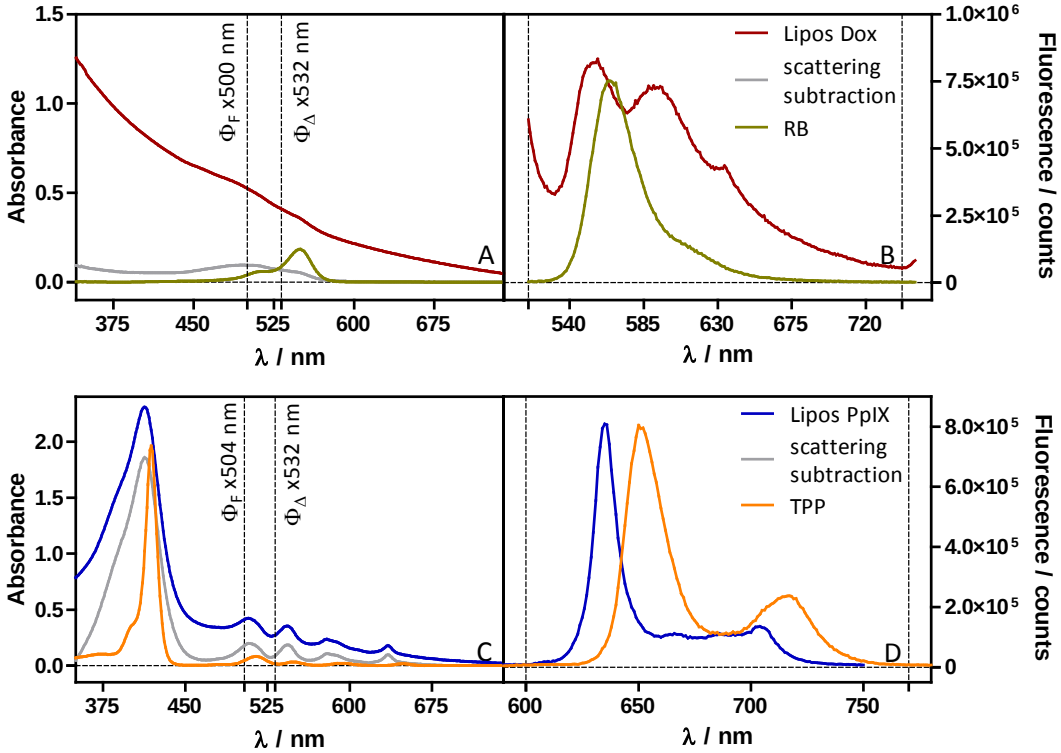

Figure 6.11. Absorption (A and C) and fluorescence emission (B and D) spectra of Dox unimodal liposomes (dark red line), PpIX unimodal liposomes (blue line) and their references for the Φ_F measurement. The grey lines correspond to the scattering corrected absorption of the liposomes. The vertical dashed lines in the absorption spectra indicate the excitation wavelength used for the determination of Φ_F and Φ_Δ. The references used were RB in water (dark green line) and TPP in toluene (orange line) for Dox and PpIX, respectively.

It was not possible to determine Φ_F for the bimodal liposomes due to the overlap of emission spectra between Dox and PpIX.

Fluorescence decay kinetics for bimodal liposomes revealed two components for Dox inside the liposomes and two components for PpIX as well (Figure 6.12, Table 6.4), indicating two different populations of the excited singlet state in the vesicles. The main component for Dox unimodal liposomes showed the same lifetime as in aqueous solution (1.0 ns), which clearly indicates that the largest fraction was in the aqueous core. However, both in unimodal and in bimodal preparations, another component was detected, likely due to a fraction of aggregated Dox molecules. Likewise, PpIX showed two components, the main one with a lifetime slightly higher than in neat THF solution (11.6 ns), indicating that the environment of PpIX in the bilayer was more hydrophobic than THF. The second component (~5 ns) can be assigned to a minor population of PpIX aggregates inside the bilayer.

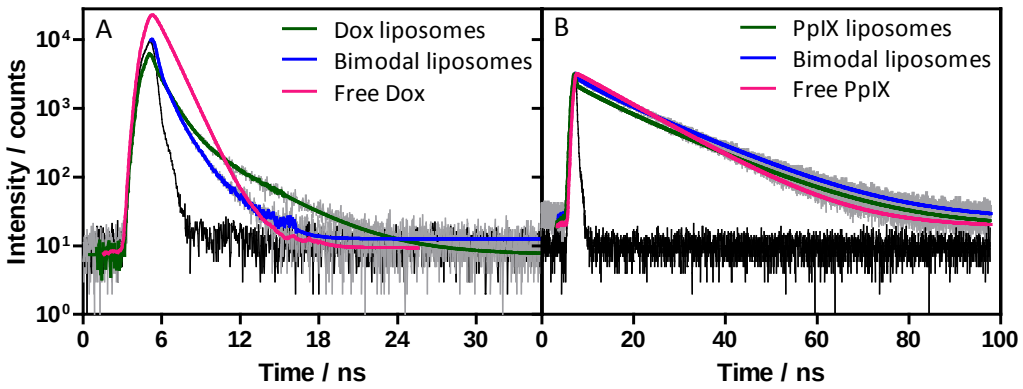

Figure 6.12. Time-Resolved Fluorescence decays of unimodal and bimodal liposomes in aqueous suspension at pH 7.8, showing Dox (A) and PpIX (B) spectroscopic region. Panel A: λ_{exc} 502 nm, λ_{obs} 558 nm and panel B: λ_{exc} 502 nm, λ_{obs} 700 nm. The black line corresponds to instrumental response factor (IRF).

Table 6.4. Fluorescence quantum yields, fluorescence lifetimes with their relative amplitudes of the Dox and PpIX loaded in liposomes in aqueous suspension. The respective values of both agents in free solution are also presented as reference.

Sample	Solvent	λ_{exc} (λ_{obs}) / nm	τ_1 / ns (A%)	τ_2 / ns (A%)	Φ_F[a]
free Dox	aqueous pH 7.8	502 (500)	1.0 (100%)	-	0.04 ± 0.01
Dox liposomes	aqueous pH 7.8		1.0 ± 0.2 (83.9%)	3.8 ± 0.5 (16.1%)	0.04 ± 0.04
Bimodal liposomes	aqueous pH 7.8		0.6 ± 0.1 (77.9%)	1.9 ± 0.5 (22.1%)	-
free PpIX	THF	502 (700)	11.6 (100%)	-	0.13 ± 0.01
PpIX liposomes	aqueous pH 7.8		15.9 ± 0.4 (77.6%)	6.9 ± 0.1 (22.4%)	0.13 ± 0.02
Bimodal liposomes	aqueous pH 7.8		15.2 ± 0.6 (79.4%)	4.6 ± 0.7 (20.6%)	-

a Φ_F was found at λ_{exc} 500 nm and 504 nm for Dox and PpIX, respectively, as it is shown in Figure 6.11.
Results are the mean ± SD of at least two independent experiments.

The aforementioned hypothesis that the largest population of the agents was in a monomeric state was confirmed by Φ_F measurements. Dox and PpIX in liposomes showed the same Φ_F than their references in aqueous solution and in THF, respectively.

Dox is well-known to produce a variety of ROS but its efficiency of $^1O_2$ photosensitisation is low (Φ_Δ= 0.03 in EtOH)[20]. Indeed, the signals collected from Dox liposomes cannot be adjusted due to the imperceptible $^1O_2$ transient, which was under the detection limit. The temporal profile of the $^1O_2$ signals at 1275 nm is presented for PpIX liposomes (unimodal and bimodal preparations, Figure 6.13). Variation of oxygen concentration allowed an unequivocal assignation of the lifetimes to the triplet state of the PS and to $^1O_2$, because only the triplet state is quenched by oxygen (Table 6.5).

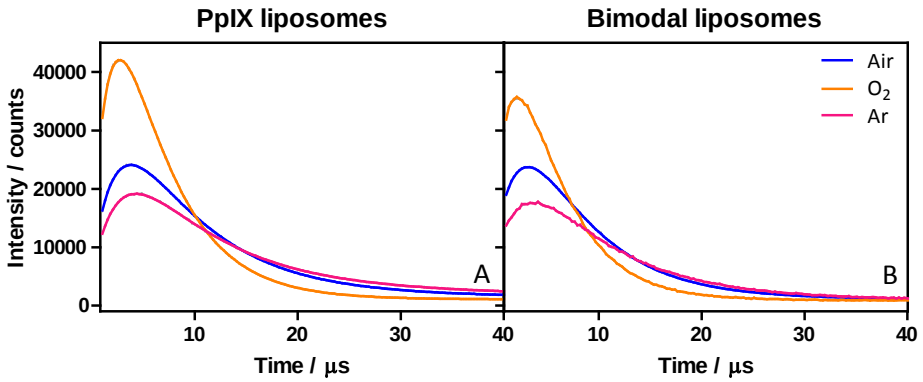

Figure 6.13. Time-resolved $^1O_2$ phosphorescence under different oxygen concentration in aqueous suspensions of PpIX unimodal (A) and bimodal (B) liposomes. The λ_{exc} was at 532 nm in both cases.

Data analysis (Table 6.5) of the signals presented in Figure 6.13 confirmed the assignment of the triplet and $^1O_2$ populations in bimodal liposomes.

Table 6.5. Time constants of $^1O_2$ luminescence of PpIX unimodal and bimodal liposomes under different oxygen concentration.

Sample	Atmosphere	τ_T / µs	τ_T / µs	τ_Δ / µs
PpIX Liposomes	air	6.7	52.5	2.5
	O_2	4.8	22.0	1.9
	Ar	7.7	29.8	2.8
Bimodal Liposomes	air	6.2	26.2	2.6
	O_2	3.2	6.2	2.5
	Ar	7.4	23.6	2.9

Data fitting yielded two triplet lifetimes, which indicates that the PS was localised in two different areas of the lipid bilayer. On the contrary, $^1O_2$ decay was monoexponential, with a lifetime of ~2.5 µs in the H_2O-based suspension. Although a biexponential decay of $^1O_2$ might have been expected due to the presence of two independent PS-triplet species, the monoexponential decay indicates a single decay pathway for both populations. This fact suggests that, in this system, $^1O_2$ decays predominantly in the external aqueous medium and not in lipid phase (12.2 µs)[21] in agreement with the kinetic model proposed by Lee and Rodgers[22]. The overall conclusion is that $^1O_2$ can escape easily from the liposomes and diffuse into the external aqueous phase during its lifetime.[23,24]

The time constants of $^1O_2$ luminescence and production quantum yields of the unimodal and bimodal liposomes are shown in Table 6.6. Two triplet lifetimes were registered, the longest one with a maximum 3% relative amplitude and the ~6.5 µs component, the latter being equal to the one found in chapter 5. The Φ_Δ of PpIX in liposomes is in good agreement with literature value in PBS with Triton X-100.

Table 6.6. Time constants of $^1O_2$ luminescence and Φ_Δ of unimodal and bimodal liposomes. Data of the free Dox and free PpIX in aqueous solution and in THF, respectively are shown as reference. Both were excited at 532 nm and $^1O_2$ phosphorescence was recorded at 1275 nm.

Sample	Solvent	$\tau_{T,1}$ / µs	$\tau_{T,2}$ / µs	τ_Δ / µs	Φ_Δ
free Dox	water	-	-	-	0.01[20]
Dox liposomes	aqueous pH 7.8	-	-	-	-
Bimodal liposomes	aqueous pH 7.8	-	-	-	-
free PpIX	THF	0.3	-	21.3	0.56[a]
PpIX liposomes	aqueous pH 7.8	6.6 ± 0.2	17.5 ± 8.3	2.6 ± 0.1	0.55 ± 0.07
Bimodal liposomes	aqueous pH 7.8	6.4 ± 0.1	38.7 ± 19.5	2.7 ± 0.1	0.53 ± 0.02

a Value found in literature in PBS with Triton X-100.
Results are the mean ± SD of at least two independent experiments, except for the free drugs in solution.

6.3.3. Cell viability studies

The results of this section were obtained by Dr. Angeles Villanueva and Mrs Andrea Tabero at the Universidad Autónoma de Madrid and are included here to facilitate the interpretation of results.

HeLa cells were incubated in the dark with different free Dox and PpIX concentrations for 18 h. Afterwards, cells with PpIX were exposed to 2 J·cm^{-2} of red light and cell viability was assessed 24 h after the treatment (in the case of PpIX) and after the incubation (for Dox; Figure 6.14). These results allowed the assessment of the half-maximal inhibitory concentration (IC_{50}), which indicates how much drug is needed to cause a 50% reduction in cell viability.

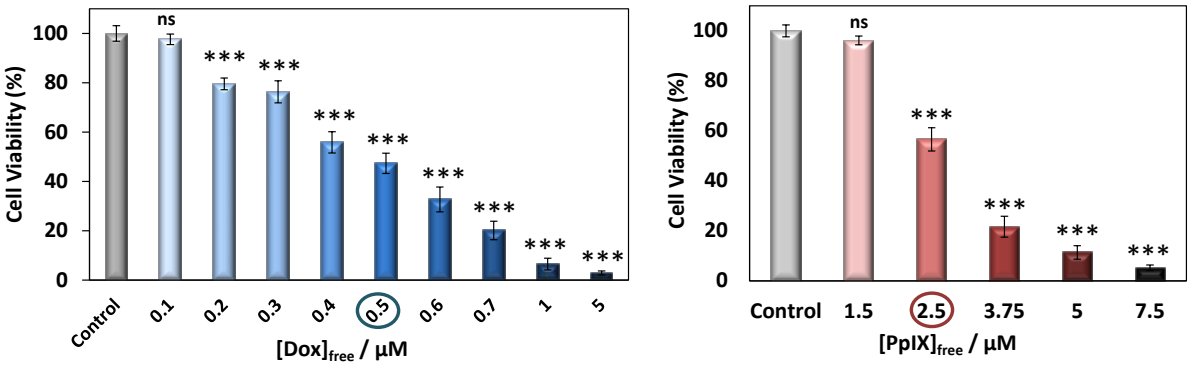

Figure 6.14. Cell viability or cell survival (expressed in percentage) 18 h after incubation with free PpIX and free Dox at various concentrations. Evaluation of the cell viability through the colorimetric MTT assay that was carried out 24 h after the incubation. In the case of PpIX, the cells were exposed to red light irradiation (2 J·cm^{-2}) before the MTT assay. (ns: not significant)

The optimal IC_{50} concentrations of free drugs were extrapolated for liposome concentrations, which were 0.5 µM for Dox and 2.5 µM for PpIX, the ratio being Dox:PpIX 1:5. Once the optimal concentrations were found, the cell viability was assessed following the protocol above (MTT assay) 24 and 72 h after the treatment, comparing unimodal liposomes, unimodal combination and bimodal liposomes (Figure 6.15).

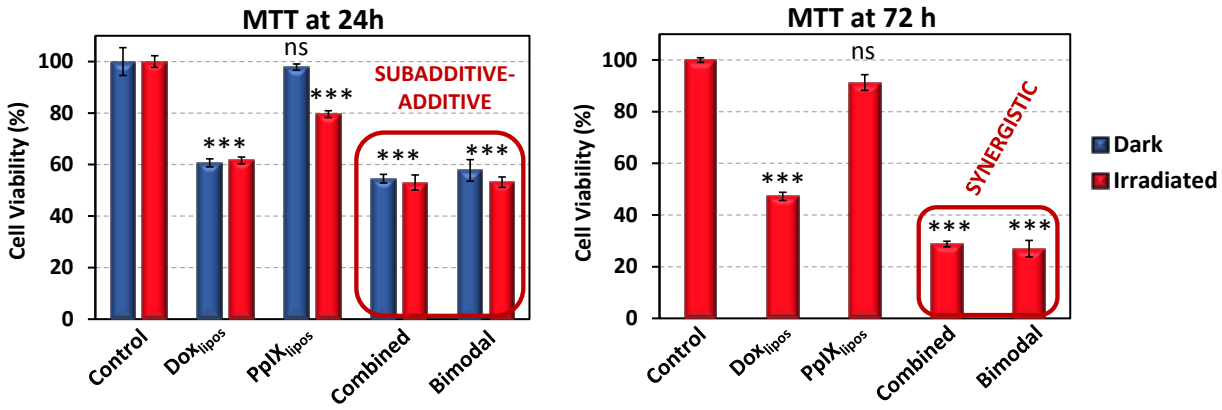

Figure 6.15. Cell viability 24 h (left panel) and 72 h (right panel) after PDT treatment (2 J·cm^{-2}) with unimodal and bimodal liposomes.

The irradiation of control cells did not produce any considerable differences in the cell viability in the experimental conditions. Blank liposomes, despite not showing the data, did not present any decrease in cell viability. The Dox unimodal liposomes showed a 15% reduction when the MTT was carried out 72 h after the irradiation. On the contrary, PpIX liposomes reduced their effect on time and cell viability increased by 12% when samples were analysed 72 h after the treatment. PpIX unimodal liposomes were not cytotoxic in dark conditions (viability of 92.7%), while after the PDT treatment the viability slightly decreased.

The analysis of combined treatments were evaluated according to the method written by Valeriote and Lin, as was done in chapter 5:[25]

Synergism: [A + B] < [A] x [B]

Additivity: [A + B] = [A] x [B]

Subadditivity: [A] x [B] < [A + B] < [A], when [A] < [B]

where [A] and [B] represent the cell viability for the individual treatment of compounds A and B (Dox and PpIX), whereas [A + B] represents the cell viability for the combined treatment, either the administration of the bimodal liposomes or the unimodals combined (referred in the graph as combined).

The MTT carried out 24 h after treatment showed that the cell viability of the combined formulations slightly decreased, leading to a subadditive-additive effect. While the analysis of MTT at 72 h presented a remarkable reduction in the combined cell viability, yielding a synergistic effect. Unlike CPT-11+PpIX liposomes, this system did not present any difference between the combined treatments. Therefore, the fact that both agents were encapsulated in the same carrier does not seem to imply a greater effect.

As we have described in chapter 5, the morphological changes of PpIX liposomes 10 days after treatment resulted in many resistant cells which continue proliferating under our experimental

conditions. These resistant cells also appeared at the 72 h MTT for PpIX liposomes. However, with the combined and bimodal system these living cells did not proliferate, demonstrating the effectiveness of the combined therapy. The ultimate cell viability values for unimodals combined and bimodal liposomes were 28.8% and 27.0%, respectively.

6.3.4. Subcellular localisation and morphological changes

The results of this section were obtained by Dr. Angeles Villanueva and Mrs Andrea Tabero at the Universidad Autónoma de Madrid.

Figure 6.16 shows the subcellular localisation of the unimodal liposomes 18 h after incubation by confocal microscopy and its overlapping with DIC. PpIX, when administered in liposomes, was distributed with a special accumulation in the vicinity of the plasma membrane. In the case of unimodal liposomes, Dox was mainly distributed in the nuclei although it can also be observed as a dotted pattern in the perinuclear region.

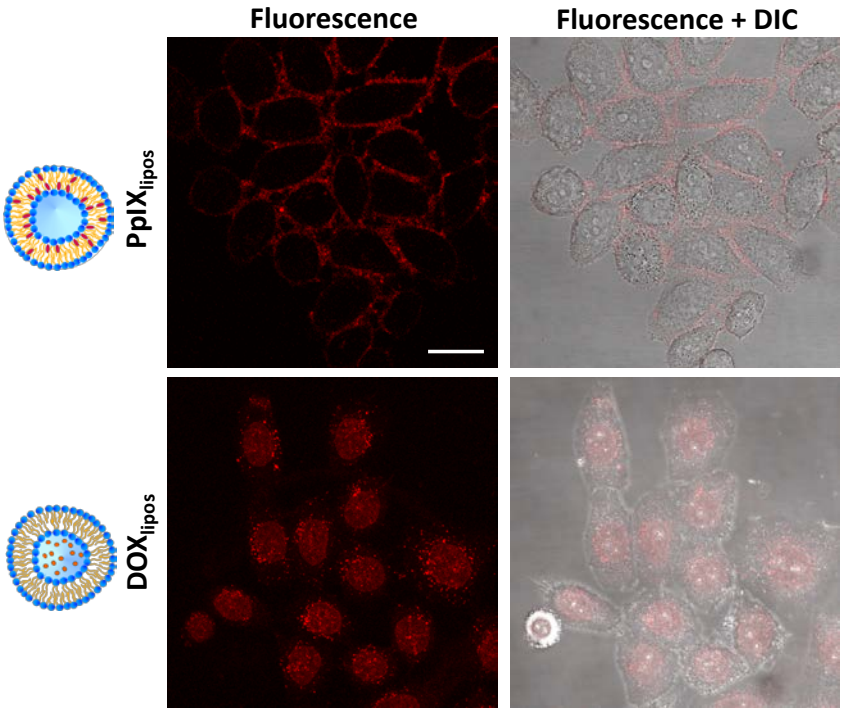

Figure 6.16. Subcellular localisation of the PS/drug administered individually in liposomes. The samples were analysed 18 h after incubation by confocal microscopy (left panels) and the merging with DIC (right panels). Scale bar= 15 μm.

The localisation of PS/drug in the bimodal liposomes was not assessed because of the overlapping of both absorbance and fluorescence. However, most likely the PS/drug are localised in the same cellular regions, since the carrier is the same. This was exactly what we saw in chapter 5, whereby no clear differences were detected between unimodal and bimodal liposomes.

Another feature of a good DDS is the enhancement of the drug accumulation in the diseased tissue. Some uptake experiments were carried out by flow cytometry, showing that PpIX and Dox signals had a higher intensity when they were encapsulated in liposomes. It may be caused by a higher accumulation rate or by a slower release from the cell in comparison with the administration of the free drugs (data not shown).

The treatment with Dox or PpIX liposomes in HeLa cells resulted in different cellular morphologies revealed 24 h from incubation (Dox liposomes) and PDT treatment (PpIX and combined liposomes) by DIC (Figure 6.17).

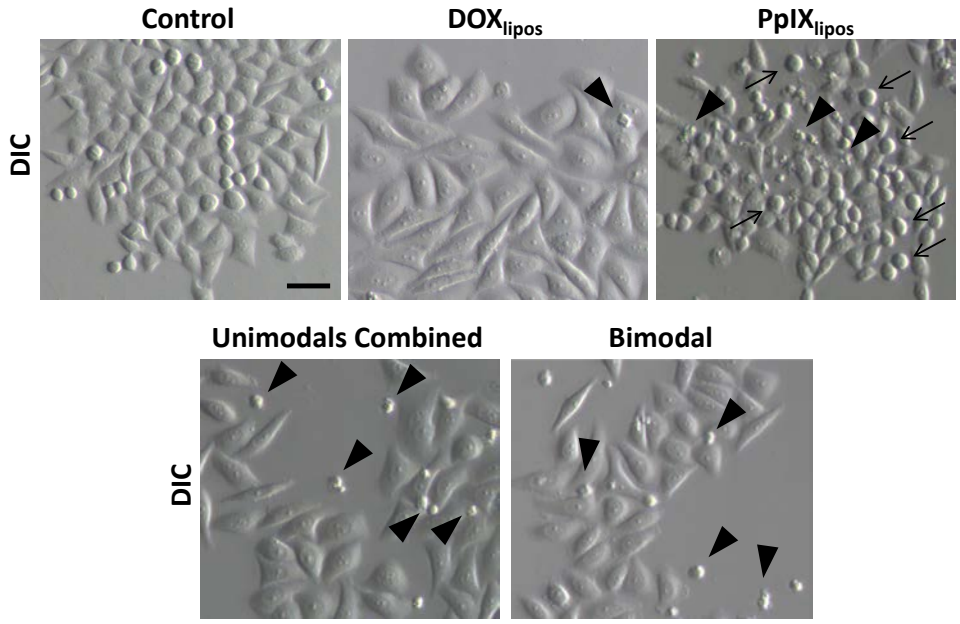

Figure 6.17. Morphological changes of HeLa cells after the treatments in phase contrast or DIC. The cells were incubated with unimodal, unimodals combined or bimodal liposomes and visualised directly 24 h after irradiation. The arrowheads point out apoptotic cells and arrows, cells in division. Scale bar = 25 μm.

Dox produced an increase in the cellular size, resulting in larger and flatter cells than the control ones. It is worth noting that there were practically no cells in division, and the few metaphases were probably altered as it happened for CPT-11 liposomes. Moreover, cells with some typical apoptotic features can be observed in a low percentage. Some of these features are the rounded morphology with chromatin condensed and fragmented, and packed into apoptotic bodies (Figure 6.17, arrowhead). The fact that Dox liposomes trigger the apoptotic pathway as the main mechanism in HeLa cells death is supported by many articles, principally when it is in combination with PDT.[16,18,26,27]

PpIX liposomes produced an increase in number of cells in division, resulting in a higher number of metaphases (round-shape cells, Figure 6.17, arrows), possibly because of a metaphase arrest. Moreover, many cells had undergone apoptosis 24 h after PDT, as deduced again from cell

shrinkage, chromatin condensation and nuclear fragmentation (Figure 6.17, arrowhead). Contrary to Dox treatment, PpIX did not produce an increase in cellular size.

The combined treatment, either the bimodal liposomes or the combination of unimodals, produced similar effects. Any combined treatment resulted in a combination of individual effects of both PpIX and Dox. Therefore, an increase in the cellular size was observed, inherent in Dox treatment, and many apoptotic cells.

6.3.5. Active targeting with Herceptin®

The active targeting process followed the same protocol that was previously described in chapter 5 (subsection 5.3.5). Briefly, TZ was thiolated with 2-iminothiolane in the same 50 mM phosphate buffer at pH 8. Moreover, bimodal or blank liposomes were prepared adding 1.6% of the pegylated Mal-terminated lipid (DSPE-PEG_{2000}-Mal), in a molar ratio EPC:CHOL:DSPE-PEG_{2000}-Mal 7:3:0.16. Blank liposomes were also prepared as control. Theoretically, in the reaction with thiolated TZ and functionalised liposomes, the free maleimide group of the surface reacts with the sulfhydryl on the protein, obtaining a stable conjugate with a thiother bond. This reaction was carried out overnight, protected from light, under Ar atmosphere and in the same aqueous mixture at pH 7.8. In addition, another batch of bimodal liposomes was also prepared but with DSPE-PEG_{2000}, which does not bear the maleimide group, and hence the TZ binding is prevented.

After the conjugation and purification through a Sepharose CL-6B column, the fractions were analysed by absorbance and fluorescence spectroscopy.

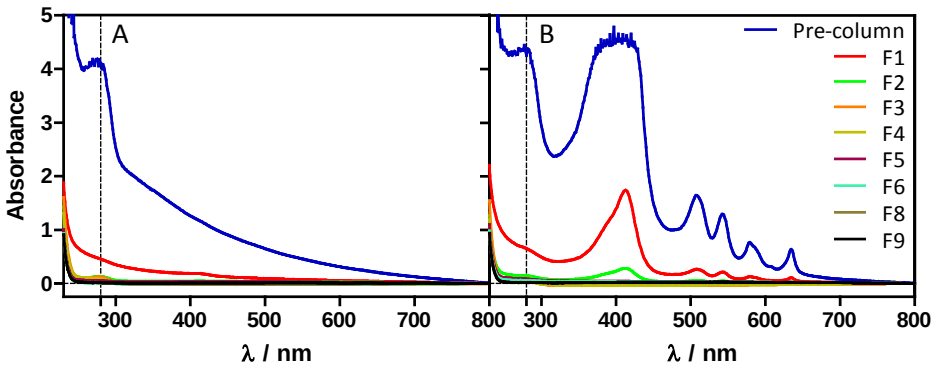

Figure 6.18. Absorption spectra of the fractions collected from the Sepharose CL-6B column of actively targeted blank liposomes (A) and actively targeted bimodal liposomes (B). The column was eluted with the same extraliposomal medium at pH 7.8.

The absorbance analysis of the fractions collected clearly showed that blank targeted-liposomes were in F1, the one which contains liposomes and protein. While in the case of bimodal targeted-liposomes were in F1 and F2 (Figure 6.18). The fractions of both samples were also analysed by

fluorescence in order to ascertain that Trp, PpIX and Dox were in each fraction (Figure 6.19 and 6.20).

Figure 6.19 shows the fluorescence of Trp residues (from the antibody) of each collected fraction in the sample of blank liposomes. Although the highest amount of protein was collected in F2 and F3, a significant fluorescence was also registered in F1, where the liposomes scattering were also observed by absorbance. This light dispersion could also be noted at the beginning of the fluorescence F1 signal.

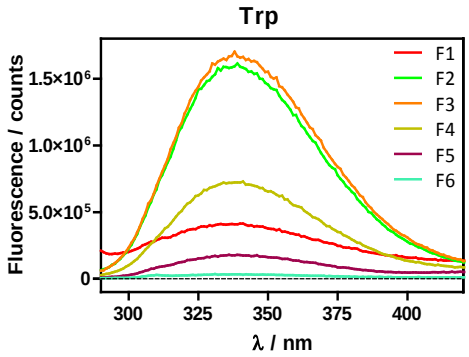

Figure 6.19. Fluorescence emission spectrum of Trp residues of each collected fraction in the sample of blank liposomes. The λ_{exc} was 280 nm.

Something similar occurred with the sample of bimodal liposomes. The highest intensity signal of Trp residues was seen in F3 and F4 fractions, which did not have liposomes (i.e., PpIX or Dox's fluorescence were not detected, Figure 6.20). However, F2 still had fluorescence coming from PpIX, Dox and Trp residues, thus it was the fraction selected for further cell tests.

It is worth noting that fluorescence coming from the PS/drug were in the same fractions and roughly with the same intensity. This fact is indicative of both agents being trapped in liposomes, in contrast to what happened in chapter 5.

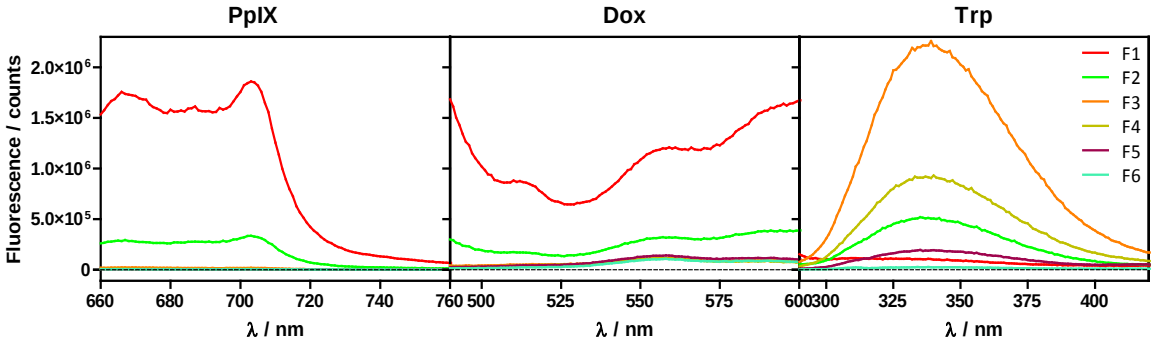

Figure 6.20. Fluorescence emission spectra of PpIX, Dox and Trp, in the fractions collected from the Sepharose CL-6B column for the sample of bimodal liposomes. The λ_{exc} was 280, 470 and 632 nm for Trp, Dox and PpIX, respectively.

The PS/drug concentration was quantified after the TZ covalently bound reaction, and fortunately, the ratio Dox:PpIX 1:5 was maintained. Moreover, the lipid concentration was also assessed through the normal procedure. The concentration of the conjugated Herceptin were

roughly estimated using the extinction coefficient in aqueous suspension (ε_{280nm} = 225,000 $M^{-1} \cdot cm^{-1}$)[28] and with the scattering absorbance subtraction. The contribution of Dox at 280 nm was not considered due to the low concentration in the sample. The TZ concentration was around 0.8 μM.

These results are preliminary, and thus further experiments need to be carried out in order to optimise the conjugation reaction between the TZ and the functionalised liposomes. Some conditions such as the reaction time or the equivalent ratio TZ:DSPE-PEG_{2000}-Mal should be modified in order to improve the conjugation yield.

Before the biological evaluation of these systems, the liposomes were characterised before and after the TZ conjugation to ensure similar size and zeta-potential.

Table 6.7. Size and zeta-potential characterisation of blank and bimodal liposomes before and after the TZ conjugation reaction.

Formulation	Encapsulated drug	Z-ave (nm)[a]	PI[b]	ζ-pot (mV)[c]
Liposomes-PEG-Mal	-	144	0.28	-13
Liposomes-PEG-Mal	PpIX + Dox	141	0.26	-11
Liposomes-PEG	PpIX + Dox	155	0.39	-11
Liposomes-PEG-TZ	-	153	0.68	-7
Liposomes-PEG-TZ	PpIX + Dox	158	0.62	-9

a Particle size measured as Z average mean
b Polydispersity Index
c Zeta-potential
Values reported from one experiment

All liposomes with the pegylated lipid (either DSPE-PEG_{2000}-Mal or DSPE-PEG_{2000}) showed a negative zeta-potential around -12 ± 1 mV, which supposed a reduction of 3 mV on average compared to those without these lipids. This reduction was due to the negatively-charged pegylated lipid, although it just represents 1.6% of the total lipid. Likewise, when the pegylated liposomes were conjugated with TZ, the zeta-potential slightly increased. This measurement provides information about the conjugation since TZ has an isoelectric point (pI) of 8.5,[29,30] with an overall cationic nature at pH 7.8. Therefore, the slight increase in zeta-potential value supported the successful TZ conjugation with liposomes. On the other hand, the hydrodynamic diameter of liposomes with PEG increased around 20 nm compared to those without DSPE-PEG_{2000}. However, once the liposomes were conjugated with TZ, the size increased 13 nm on average for both conjugated liposomes, which nicely corresponds with the TZ size.[31]

The bimodal immunoliposomes were tested against HER2-positive breast cancer cells (BT-474) and HER2-negative cell line (HeLa). The p185HER2 (human epidermal growth factor receptor 2) receptor is upregulated in human cancers of several histology (breast, ovarian, and prostate)

with a low basal expression in normal tissues, it allows cancer-specific delivery with HER2 monoclonal antibody conjugation.[18] Focusing on breast cancer, approximately the 20% of cases are HER2-positive, and indeed are more aggressive and tend to reoccur more often than HER2-negative.[30]

Many reports describe the better drug accumulation normally because of an increased receptor-mediated internalisation in tumours and a higher therapeutic efficacy over untargeted nanocarriers.[32–34]

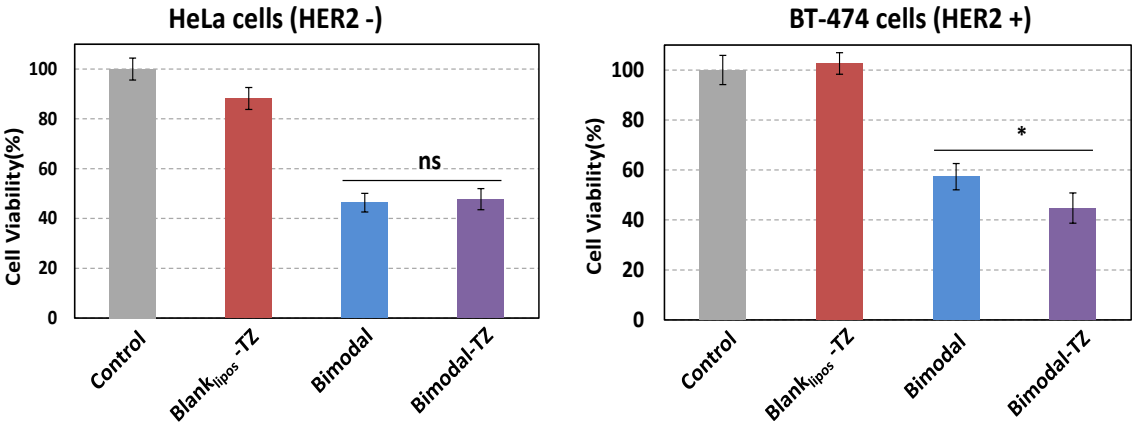

Figure 6.21. Cell viability of two different cell lines (HER2 negative and positive) with TZ-conjugated blank liposomes, TZ-conjugated bimodal liposomes and non-targeted bimodal liposomes. The MTT was carried out 24 h after the light treatment (2 J·cm^{-2}). (ns: not significant)

Two cancer lines (HeLa and BT-474) were used to investigate the anticancer actions of the formulations. HeLa cells are a HER-negative, while BT-474 is a breast cancer line HER2-positive. Therefore, a comparative evaluation of cytotoxicity against these cell lines could provide a good understanding of the contribution of TZ in targeting HER2-positive breast cancers. Cytotoxicity measures were assessed 24 h after incubation and irradiation (2 J·cm^{-2}), comparing bimodal liposomes with and without the linked TZ (Figure 6.21). At the same drug concentration as before (corresponding to 0.45 μM Dox and 2.5 μM PpIX), BT-474 cell viability after 24 h of treatment was 57.3% and 44.7% for bimodal and TZ-linked bimodal liposomes, respectively. The results indicated that TZ-linked liposomes were slightly more cytotoxic ($p > 0.05$) than the non-actively targeted liposomes. This may be due to the interaction between TZ and HER2 receptors in these cells, which makes internalisation of TZ-bimodal liposomes through receptor-mediated endocytosis somewhat more efficient. However, TZ-bimodal liposomes did not cause significant higher cytotoxicity than the non-targeted liposomes in HeLa cells. HeLa cell viability after 24 h of treatment was 46.4% and 47.8% for non-targeted and TZ-linked bimodal liposomes.

After treatments with targeted and non-targeted liposomes at different times, changes in cell morphology and a decrease in the number of viable BT-474 (HER2-positive) cells were observed (Figure 6.22).

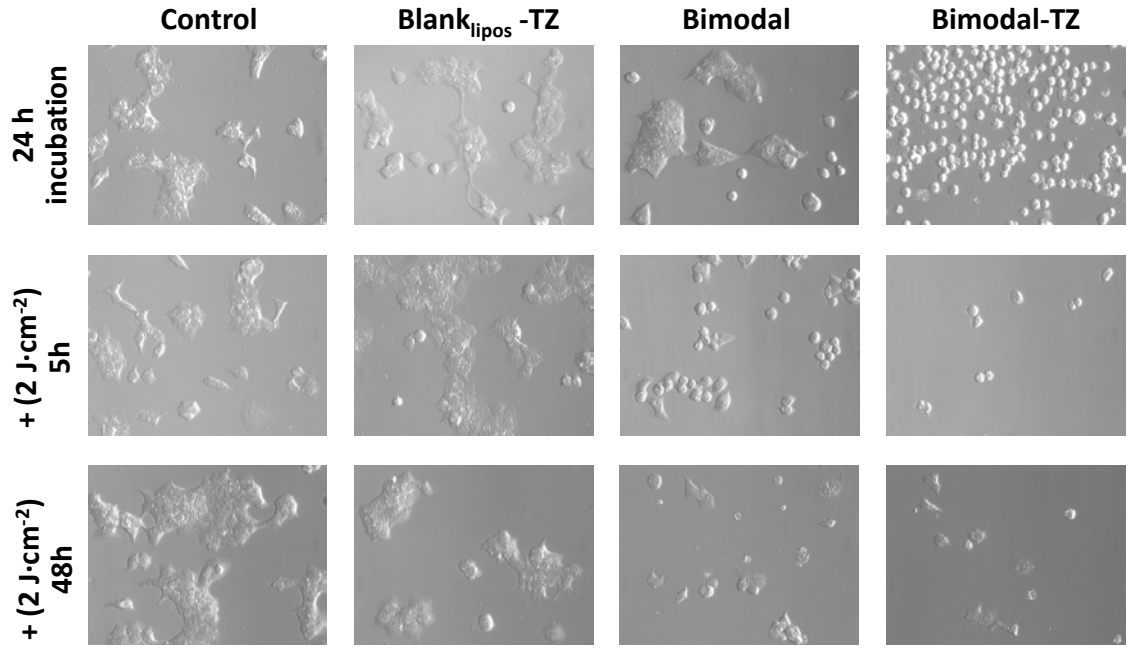

Figure 6.22. Morphological changes of BT-474 cells at different times after the light treatment with DIC microscopy. The cells were incubated with TZ-conjugated blank liposomes, TZ-conjugated bimodal liposomes and non-targeted bimodal liposomes visualised 24 h after the incubation, 5 h and 48 h after the light irradiation.

Blank-conjugated liposomes did not show any significant toxicity, but in comparison with control cells there was a lower cell proliferation. Bimodal-conjugated liposomes showed a high toxicity even before the irradiation, most likely because of the Dox effect, perceiving a clear apoptotic morphology. Moreover, most of the cells after the PDT activity lost their adhesion to the culture substrate. Conversely, non-targeted liposomes were somewhat cytotoxic before the light treatment, but especially once irradiated. However, 48 h after the treatment there were still some cells with a viable morphology.

On the other hand, the changes in cell morphology after treatments with targeted and non-targeted liposomes at different times in HeLa (HER2-negative) cells were also observed (Figure 6.23).

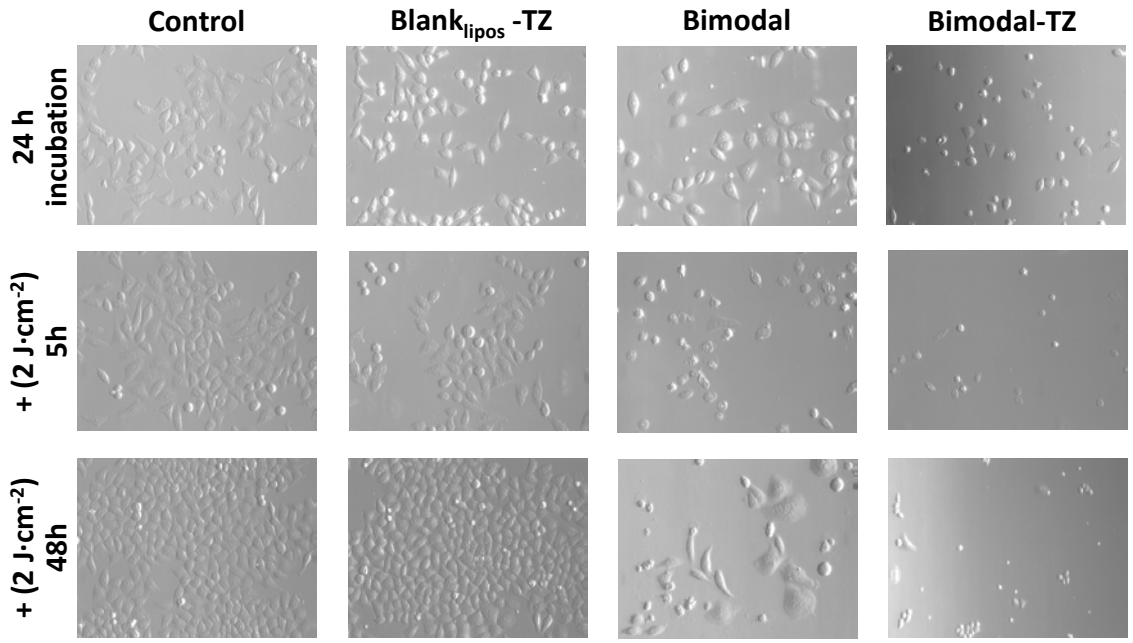

Figure 6.23. Morphological changes of HeLa cells at different times after the light treatment with DIC microscopy. The cells were incubated with TZ-conjugated blank liposomes, TZ-conjugated bimodal liposomes and non-targeted bimodal liposomes visualised 24 h after the incubation, 5 h and 48 h after the light irradiation.

Once again, blank-conjugated liposomes did not show any significant toxicity and they seem not to affect the cellular growth, clearly perceived 48 after treatment in comparison with control cells. Bimodal-conjugated liposomes showed some toxicity before the irradiation. However, some apoptotic features were observed 5 h after irradiation, but still some viable cells were detected latter on. Non-targeted liposomes also presented some live cells after the light treatment.

All in all, the main cell death mechanism observed with bimodal liposomes was apoptosis. Although the results presented must be considered preliminary and further experiments need to be done in order to assess this effect, some promising outcomes were obtained. On the one hand, almost no alive cell remained after the treatment with targeted-liposomes. On the other hand, the presence of many viable cells were observed with a non-targeted liposome treatment, demonstrating some additional effects when the TZ was covalently bound.

6.4. Conclusions

We have investigated the photodynamic activity of the dual system PpIX and Dox delivered to cancer cells using an optimised liposomal formulation. Additionally, we have prepared unimodal liposomes loaded separately with each drug to compare their photophysical properties.

Liposomes of EPC:CHOL 7:3, prepared by a microemulsification method, had a diameter of around 130 nm that grew to 150 nm approximately when they contained Dox. In all cases, the liposomes had a near-neutral zeta-potential and an entrapment efficiency above 90%. It is worth

noting that in bimodal liposomes the molar ratio of both drugs was kept according to the IC_{50} relationship, being 1:5 Dox: PpIX. The results of the turbidity and size measurements over time were remarkably stable for all formulations.

The unique fluorescence lifetime of Dox revealed a preferential location in contact with the aqueous core of liposomes, which was in agreement with the Φ_F value. Fluorescence decay kinetics indicated two different populations of the excited singlet state in the vesicles. The main component had the same lifetime as the reference in aqueous solution (1.03 ns), and the other component likely due to a fraction of aggregated Dox molecules. The $^1O_2$ signals could not be adjusted due to the imperceptible transient which is under the detection limit.

PpIX, even in aqueous suspension, showed a structured fluorescence profile which was indicative that the molecules were well-accommodated in the bilayer. Fluorescence decay lifetimes showed a second component that likely corresponds to a minor population (20%) of PpIX aggregated molecules. The value of Φ_Δ was equal in both unimodal and bimodal liposomes or even higher than the literature value in solution, which means a low or non-existent self-aggregation.

The dual activity of Dox and PpIX liposomes was evaluated *in vitro* against HeLa cells by the MTT cell viability assay, carried out 24 h and 72 h after the treatment. The results obtained for the combination of Dox and PpIX were slightly diverse compared to those obtained for the CPT-11 and PpIX combination. Unimodal PpIX liposomes upon light rendered a low cell viability decrease, which is responsible for the small differences between dark and irradiated samples. However, both the combined unimodals and the bimodal liposomes considerably decreased the cell viability 72 h after the treatment. The resistant cells after PDT treatment (also observed in chapter 5) which continue proliferating under our experimental conditions, clearly cannot live after the combined treatment. This proved the effectiveness of the combined therapy, yielding a synergistic effect for unimodals combined and bimodal liposomes. However, the overall effect achieved was slightly minor to the one observed with bimodal liposomes in chapter 5 (a decrease of 27.0% in cell viability compared to a 13% cell viability with CPT-11 and PpIX). Furthermore, contrary to what happened in chapter 5, this formulation did not show a different effect between the combination of unimodals combination and the bimodal liposomes.

Finally, the results obtained for the TZ-covalent conjugation to the bimodal liposomes, although preliminary, were encouraging. However, further experiments need to be done in order to ensure the results presented. A better explanation of the outcomes could probably be further discussed in some months.

Taking everything into consideration, the results presented here showed the development of a dual therapy system, targeting different cellular/molecular pathways. We proved that phospholipid-cholesterol liposomes possess optimum properties for the encapsulation of both PpIX and Dox. We also demonstrated that there is a clear improvement in the cytotoxic effect in cells when the combined liposomes, either bimodal liposomes or a combination of unimodals, are administered.

6.5. References

(1) Thorn, C. F.; Oshiro, C.; Marsh, S.; Hernandez-Boussard, T.; McLeod, H.; Klein, T. E.; Altman, R. B. Doxorubicin Pathways: Pharmacodynamics and Adverse Effects. *Pharmacogenet. Genomics,* **2011**, *21*, 440–446.

(2) Fritze, A.; Hens, F.; Kimpfler, A.; Schubert, R.; Peschka-Süss, R. Remote Loading of Doxorubicin into Liposomes Driven by a Transmembrane Phosphate Gradient. *Biochim. Biophys. Acta* **2006**, *1758*, 1633–1640.

(3) Weiss, A.; den Bergh, H. van; Griffioen, A. W.; Nowak-Sliwinska, P. Angiogenesis Inhibition for the Improvement of Photodynamic Therapy: The Revival of a Promising Idea. *Biochimica et Biophysica Acta - Reviews on Cancer*, **2012**, *1826*, 53–70.

(4) Skeel, R. T.; Khleif, S. N. *Handbook of Cancer Chemotherapy*; 8th ed.; Lippincott Williams & Wilkins Handbook Series: PA, USA, **2011**.

(5) Minotti, G.; Menna, P.; Salvatorelli, E.; Cairo, G.; Gianni, L. Anthracyclines: Molecular Advances and Pharmacologic Developments in Antitumor Activity and Cardiotoxicity. *Pharmacol. Rev.* **2004**, *56*, 185–229.

(6) Osheroff, N.; Corbett, A. H.; Robinson, M. J. Mechanism of Action of Topoisomerase II-Targeted Antineoplastic Drugs. *Adv. Pharmacol.* **1994**, *29B*, 105–126.

(7) Doroshow, J. H. Role of Hydrogen Peroxide and Hydroxyl Radical Formation in the Killing of Ehrlich Tumor Cells by Anticancer Quinones. *Proc Natl Acad Sci USA,* **1986**, *83*, 4514–4518.

(8) Abraham, S. A.; Waterhouse, D. N.; Mayer, L. D.; Cullis, P. R.; Madden, T. D.; Bally, M. B. The Liposomal Formulation of Doxorubicin. In *Methods in enzymology*; **2005**; 391, 71–97.

(9) Pisano, C.; Cecere, S.; Di Napoli, M. Clinical Trials with Pegylated Liposomal Doxorubicin in the Treatment of Ovarian Cancer. *J Drug Deliv.* **2013**, *2013*, 12.

(10) Stewart, J. C. Colorimetric Determination of Phospholipids with Ammonium Ferrothiocyanate. *Anal. Biochem.* **1980**, *104*, 10–14.

(11) Munnier, E.; Tewes, F.; Cohen-Jonathan, S.; Linassier, C.; Douziech-Eyrolles, L.; Marchais, H.; Soucé, M.; Hervé, K.; Dubois, P.; Chourpa, I. On the Interaction of Doxorubicin with Oleate Ions: Fluorescence Spectroscopy and Liquid-Liquid Extraction Study. *Chem Pharm Bull.* **2007**, *55*, 1006–1010.

(12) Hau, P.; Fabel, K.; Baumgart, U.; Rümmele, P.; Grauer, O.; Bock, A.; Dietmaier, C.; Dietmaier, W.; Dietrich, J.; Dudel, C.; *et al.* Pegylated Liposomal Doxorubicin-Efficacy in Patients with Recurrent High-Grade Glioma. *Cancer,* **2004**, *100*, 1199–1207.

(13) Anders, C. K.; Adamo, B.; Karginova, O.; Deal, A. M.; Rawal, S.; Darr, D.; Schorzman, A.; Santos, C.; Bash, R.; Kafri, T.; *et al.* Pharmacokinetics and Efficacy of PEGylated Liposomal Doxorubicin in an Intracranial Model of Breast Cancer. *PLoS One,* **2013**, *8*, e61359.

(14) Rahman, A. M.; Yusuf, S. W.; Ewer, M. S. Anthracycline-Induced Cardiotoxicity and the Cardiac-Sparing Effect of Liposomal Formulation. *Int. J. Nanomedicine,* **2007**, *2*, 567–583.

(15) Gill, S. E.; Savage, K.; Wysham, W. Z.; Blackhurst, D. W.; Winter, W. E.; Puls, L. E. Continuing Routine Cardiac Surveillance in Long-Term Use of Pegylated Liposomal Doxorubicin: Is It Necessary? *Gynecol. Oncol.* **2013**, *129*, 544–547.

(16) Zakaria, S.; Gamal-Eldeen, A. M.; El-Daly, S. M.; Saleh, S. Synergistic Apoptotic Effect of Doxil(R) and Aminolevulinic Acid-Based Photodynamic Therapy on Human Breast Adenocarcinoma Cells. *Photodiagnosis Photodyn. Ther.* **2014**, *11*, 227–238.

(17) Mayer, L. D.; Tai, L. C. L.; Ko, D. S. C.; Masin, D.; Ginsberg, R. S.; Cullis, P. R.; Bally, M. B. Influence of Vesicle Size, Lipid Composition, and Drug-to-Lipid Ratio on the Biological Activity of Liposomal Doxorubicin in Mice. *Cancer Res.* **1989**, *49*, 5922–5930.

(18) Perche, F.; Torchilin, V. P. Recent Trends in Multifunctional Liposomal Nanocarriers for Enhanced Tumor Targeting. *J. Drug Deliv.* **2013**, *2013*, 705265.

(19) Allen, T. M.; Cullis, P. R. Liposomal Drug Delivery Systems: From Concept to Clinical Applications. *Adv. Drug Deliv. Rev.* **2013**, *65*, 36–48.

(20) Ruiz-González, R.; Milán, P.; Bresolí-Obach, R.; Stockert, J.; Villanueva, A.; Cañete, M.; Nonell, S. Photodynamic Synergistic Effect of Pheophorbide a and Doxorubicin in Combined Treatment against Tumoral Cells. *Cancers (Basel).* **2017**, *9*, 18.

(21) Ehrenberg, B.; Anderson, J. L.; Foote, C. S. Kinetics and Yield of Singlet Oxygen Photosensitized by Hypericin in Organic and Biological Media. *Photochem. Photobiol.* **1998**, 135–140.

(22) Lee, P. C.; Rodgers, M. A. J. Singlet Molecular Oxygen in Micellar Systems. 1. Distribution Equilibriums between Hydrophobic and Hydrophilic Compartments. *J. Phys. Chem.* **1983**, *87*, 4894–4898.

(23) Fu, Y.; Kanofsky, J. R. Singlet Oxygen Generation from Liposomes: A Comparison of Time-Resolved 1270 Nm Emission with Singlet-Oxygen Kinetics Calculated from a One Dimensional Model of Singlet-Oxygen Diffusion and Quenching. *Photochem. Photobiol.* **1995**, *62*, 692–702.

(24) Baier, J.; Maier, M.; Engl, R.; Landthaler, M.; Baumler, W. Time-Resolved Investigations of Singlet Oxygen Luminescence in Water, in Phosphatidylcholine, and in Aqueous Suspensions of Phosphatidylcholine or HT29 Cells. *J. Phys. Chem. B,* **2005**, *109*, 3041–3046.

(25) Valeriote, F.; Lin, H. Synergistic Interaction of Anticancer Agents: A Cellular Perspective. *Cancer Chemother. reports,* **1975**, *59*, 895–900.

(26) Khdair, A.; Chen, D.; Patil, Y.; Ma, L.; Dou, Q. P.; Shekhar, M. P. V; Panyam, J. Nanoparticle-Mediated Combination Chemotherapy and Photodynamic Therapy Overcomes Tumor Drug Resistance. *J Control Release J Control Release January,* **2010**, *25*, 137–144.

(27) Luo, D.; Carter, K. A.; Miranda, D.; Lovell, J. F. Chemophototherapy: An Emerging Treatment Option for Solid Tumors. *Adv. Sci.* **2017**, *4*, 1–24.

(28) Bhattacharyya, S.; Wang, S.; Reinecke, D.; Kiser, W.; Kruger, R. A.; DeGrado, T. R.; DeGrado, T. R. Synthesis and Evaluation of near-Infrared (NIR) Dye-Herceptin Conjugates as Photoacoustic Computed Tomography (PCT) Probes for HER2 Expression in Breast Cancer. *Bioconjug. Chem.* **2008**, *19*, 1186–1193.

(29) Barua, S.; Yoo, J.-W.; Kolhar, P.; Wakankar, A.; Gokarn, Y. R.; Mitragotri, S. Particle Shape Enhances Specificity of Antibody-Displaying Nanoparticles. *Proc. Natl. Acad. Sci. U. S. A.* **2013**, *110*, 3270–3275.

(30) Kulhari, H.; Pooja, D.; Shrivastava, S.; Kuncha, M.; Naidu, V. G. M.; Bansal, V.; Sistla, R.; Adams, D. J. Trastuzumab-Grafted PAMAM Dendrimers for the Selective Delivery of Anticancer Drugs to HER2-Positive Breast Cancer. *Sci. Rep.* **2016**, *6*, 23179.

(31) Pabari, R. M.; Ryan, B.; Ahmad, W.; Ramtoola, Z. Physical and Structural Stability of the Monoclonal Antibody, Trastuzumab (Herceptin®), Intravenous Solutions. *Curr. Pharm. Biotechnol.* **2013**, *14*, 220–225.

(32) Kirpotin, D. B.; Drummond, D. C.; Shao, Y.; Shalaby, M. R.; Hong, K.; Nielsen, U. B.; Marks, J. D.; Benz, C. C.; Park, J. W. Antibody Targeting of Long-Circulating Lipidic Nanoparticles Does Not Increase Tumor Localization but Does Increase Internalization in Animal Models. *Cancer Res.* **2006**, *66*, 6732–6740.

(33) Yang, T.; Choi, M.-K.; Cui, F.-D.; Lee, S.-J.; Chung, S.-J.; Shim, C.-K.; Kim, D.-D. Antitumor Effect of Paclitaxel Loaded PEGylated Immunoliposomes against Human Breast Cancer Cells. *Pharm. Res.* **2007**, *24*, 2402–2411.

(34) Laginha, K. M.; Moase, E. H.; Yu, N.; Huang, A.; Allen, T. M. Bioavailability and Therapeutic Efficacy of HER2 scFv-Targeted Liposomal Doxorubicin in a Murine Model of HER2-Overexpressing Breast Cancer. *J. Drug Target.* **2008**, *16*, 605–610.

CHAPTER 7

General discussion

A general discussion of the entire work presented along the previous chapters as well as a brief discussion about the future research in the combined therapies and photodynamic therapy is comprised in this chapter.

7.1 General discussion and future perspectives

The results presented along the previous chapters can be considered as an overview of drug delivery systems development in PDT, and in some cases used in combination with other therapies (Figure 7.1).

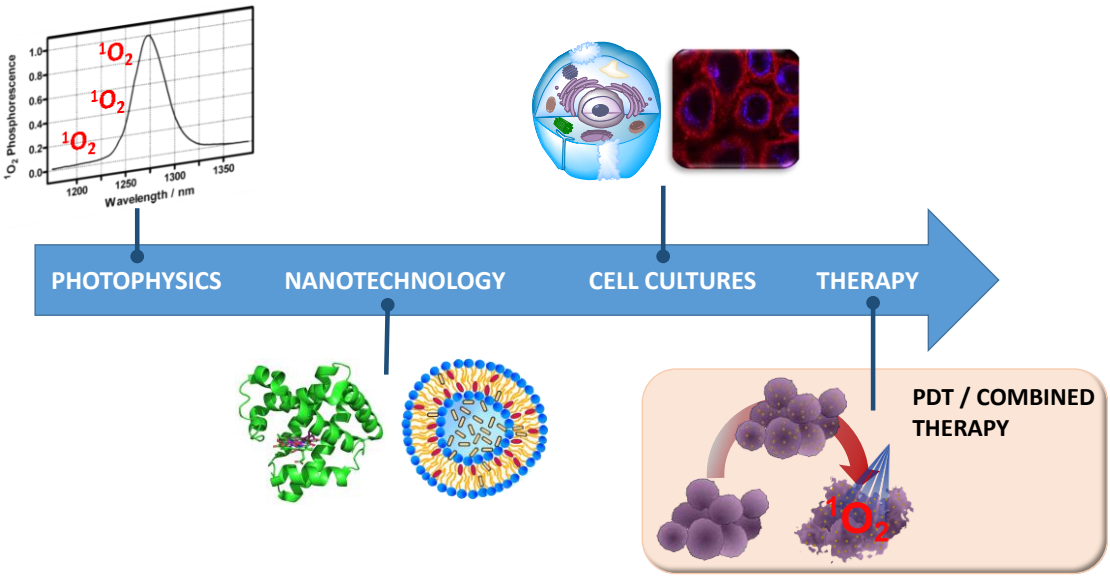

Figure 7.1. Brief overview of the fields studied during this thesis.

The work presented deals mainly with the study of two different biodegradable and biocompatible nanocarriers as DDSs. Nanotechnology applied in nanomedicine has been exploited during many years, offering many advantages in several diseases treatments. Even today, is a current important research topic with a high impact on the scientific community.[1] Nanostructures for drug delivery as the ones presented in this thesis offer many advantages:

- Improve the stability of hydrophobic drugs (most of the PSs) rendering them suitable for administration.
- Improve the biodistribution and pharmacokinetics, resulting in improved efficacy.
- Reduce adverse effects as a consequence of favoured accumulation at target sites.
- Decrease the toxicity by using biocompatible nanomaterials.

Specifically, two different blocks can be distinguished in the thesis with completely diverse applications: proteins used for aPDT purposes and liposomes for the *in vitro* treatment against cancer cells. As a first approximation, we have explored the role of both drug and PS and the nanocarrier itself for a better understanding on the physicochemical and photophysical properties. We also have pursued the adequacy of biodegradable nanoplatforms in their activity *in vitro*, which we have realized that many times there is not a direct correlation between higher Φ_Δ and more effective cell photoinactivation.

Regarding the protein nanocarriers, we have successfully demonstrated the formation of two Hyp stable complexes with apoMb and βLG. In both cases, Hyp spontaneously binds the protein cavity mainly driven by simply hydrophobic interactions. In apoMb, Hyp binds in the well-defined hydrophobic pocket where the haem group is normally placed. Whereas in βLG, Hyp binds into the clefts formed at the interface between monomers, more favourable in the narrow cleft where the PS is largely occluded from the solvent. Both complexes still preserved the Hyp fluorescence, thus can be considered as a nanovehicle in theranostics applications, although this possibility has not been further considered. Moreover, it has been assessed the photosensitising properties of Hyp yielding a respectable value of Φ_{Δ}= 0.13 approximately in both proteins, in the case of βLG coated with DMSO. This ability of $^1O_2$ production led to an effective photoinactivation of *S. aureus* with a light fluence of 18 J·cm^{-2} for Hyp-apoMb (Figure 7.2, B). Conversely, Hyp-2βLG complex only induced a relevant *S. aureus* inactivation with the same light fluence in the absence of DMSO. These results demonstrates that the improved photophysical properties of the delivery system are not necessarily translated into more effective photoinactivation of bacterial cells, as it has been aforementioned. Indeed, in this particular case, the increase observed in fluorescence, triplet, and singlet oxygen yielded in the presence of DMSO, turned out to be detrimental to the antibacterial treatment. This most likely arises from a change in the interaction between Hyp-2βLG and the cellular constituents, which prevents DMSO coated nanostructure from reaching more photosensitive regions in the bacterial wall (Figure 7.2, C).

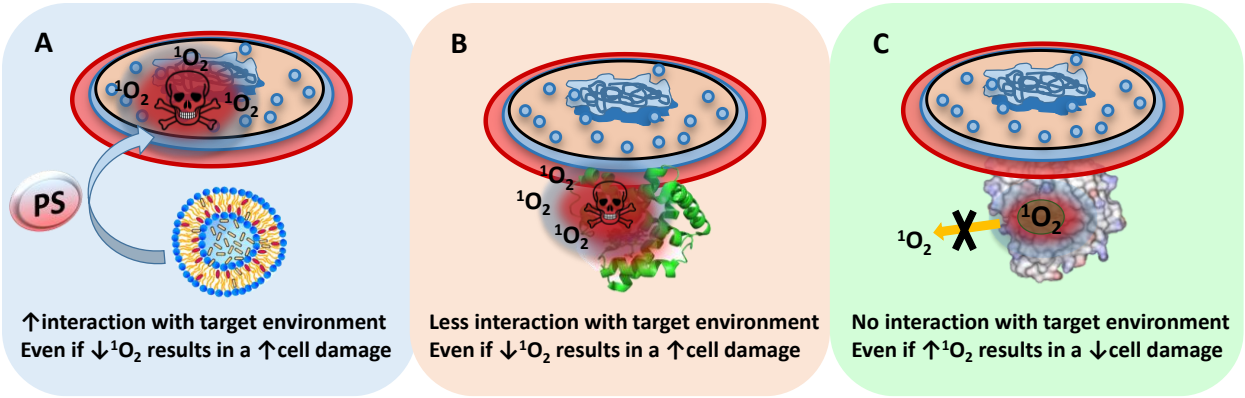

Figure 7.2. Three possible scenarios that demonstrate that high $^1O_2$ production are not translated into more effective photoinactivation. Scenario A is related to liposomes activity, B to Hyp-apoMb and Hyp-2βLG in PBS activity and C to Hyp-2βLG in the presence of DMSO, because the patches of this solvent persist when the complex is bound to bacteria cell, preventing that $^1O_2$ reaches photosensitive regions in bacteria walls.

Likewise, a decrease of 6 log units in the number of *B. Subtilis* CFUs upon irradiation was induced by the Hyp-2βLG complex. It is worth noting that in most cases a slight reduction of the dark Hyp toxicity was achieved with protein complexes.

As many experimental evidences suggested, Hyp remained inside the protein cavity even after the incubation with bacteria cells, which likely means that was all the nanosystem the one responsible for the efficient photoinactivation (Figure 7.2, B and C).

It has been demonstrated that both pharmacologically active Hyp compounds precludes its aggregation and efficiently photoinactivate *S. aureus* bacteria upon green light exposure. The overall efficiency is the result of a combination of suitable photosensitisation yield and interaction with the target environment. Specifically, Hyp-2βLG complex has an interesting potential in dairy industry processes, which has been suggested to be introduced as an effective disinfectant for food manufacturing and handling materials since the protein is widely found in the whey of cow milk.

The second cornerstone in the thesis was to explore the PDT combination with other therapies. PDT is an excellent therapeutic partner because is largely non-toxic in the absence of light. In the field of antimicrobials and antifungals, there are only a few reports on the combination of traditional treatments with aPDT. Unfortunately, little is known about the protocols used and only some reports can bring light to the dark.[2,3] As a first attempt, the double payload system formed by Hyp and RA bound to the βLG protein was studied. First, the formation of a complex between βLG and RA, which seems to be placed close to the Trp19 cavity has been successfully demonstrated. Surprisingly, the fluorescence of Hyp was quenched by RA, which rendered a photochemically innocuous delivery nanosystem. Both types of quenching (dynamic and static) were demonstrated to occur. Even more interesting was that the photophysical properties of Hyp-βLG complex were restored in the presence of *S. aureus* bacteria due to the transfer of RA from the protein complex to the cells. This fact suggests a strong potential for the treatment of bacterial infections. This dual encapsulation of a PS with a conventional drug against acne can be exploited as a system for combined therapy which targets different cellular pathways, increasing the chances of combating the disease.

The second main block of the thesis is related to the work with liposomes as nanocarriers for combined therapy. In this particular case, liposomes where chosen as nanovehicles for both PS and chemotherapeutic drug due to allows the encapsulation of high payloads of either hydrophilic or hydrophobic agents.[4] Moreover, these nanocarriers can be accumulated preferentially at tumour, inflammatory and infectious sites by virtue of the enhanced permeability and retention (EPR) effect.

Two different formulations has been optimised for this purpose, encapsulating PpIX and two different drugs, CPT-11 in the first formulation and Dox in the second one. The bimodal formulations with both agents entrapped and their unimodal counterparts, having each drug loaded in separate liposomes, have been evaluated in both cases. The photophysical properties allowed us to confirm that PpIX loaded into the vehicles was photochemically active, and both PS and drug were mainly in the monomeric form. Surprisingly, the CPT-11 ability to photosensitise $^1O_2$ when was excited at 355 nm was measured. Just a few articles demonstrated that upon UVA excitation the camptothecin (i.e., the irinotecan active core) was able to produce singlet oxygen and free radicals.[5,6]

The dual activity of CPT-11 or Dox and PpIX delivered in liposomes was evaluated *in vitro* against HeLa cancer cells. In the case of CPT-11 and PpIX, cell viability decreased considerably after the treatment with the combination of both unimodal liposomes, which led to an additive-synergistic effect. Whereas after the treatment with bimodal liposomes, the effect observed was clearly synergistic compared to the individual treatments. Therefore, the fact that both agents were encapsulated in the same carrier may imply a more effective therapy, ensuring that the dual therapy took place in the same cell or surroundings. On the one hand, the fact that Φ_Δ of PpIX was remarkably higher for the unimodal liposomes did not affect the PDT efficacy of the bimodal formulation, because of, as confocal studies proved, PpIX was internalised by cells mostly without the vehicle (Figure 7.2, A). For this system, the conjugation with the active targeting vector was not achieved.

The results obtained for the combination of Dox and PpIX were slightly diverse. Unimodal PpIX liposomes upon light rendered a low cell viability decrease, which was responsible for the small differences between dark and irradiated samples. However, both the combined unimodals and the bimodal liposomes considerably decreased the cell viability assessed by the MTT analysis carried out 72 h after the treatment. For this particular system, the active targeting vector was successfully attached to the liposome surface through a covalently linked between the free maleimide group of the liposomes and the sulfhydryl group on the protein. The bimodal immunoliposomes were slightly more cytotoxic ($p > 0.05$) than the non-actively targeted liposomes, despite being preliminary results.

The advantages of combining both chemotherapeutic and PDT modalities are that they target different key signals transduction pathways and should be more efficient in destroying cancer cells, eluding the cellular resistance mechanisms (Figure 7.3).[7] Indeed, few reports and preclinical studies show that the combined treatment allows a reduction of the dosage of

individual drugs and consequently a lessening of important side effects, while the overall efficacy is preserved or even increased.[8–12]

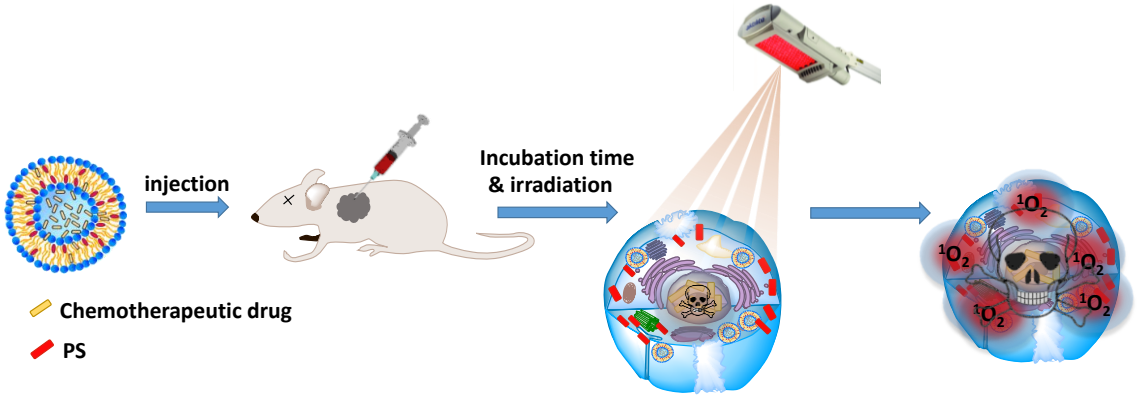

Figure 7.3. Schematic illustration of the steps followed with a dual drug delivery system through a combined therapy. After being injected, the nanocarrier is uptake by cells (better selectively by tumour cells).While the chemotherapeutic drug is already active (in the nucleus), the PS needs the light irradiation to generate ROS species and cause cell death. The result is the targeting of different cellular/molecular pathways which produce a high cell damage eluding the cellular resistance mechanisms.

Furthermore, the high Φ_F of the PpIX could be considered for theranostics purposes and be useful for diagnose and treat diseases in one step.

Altogether, the results presented in this thesis proof the importance of the PS localization for a better effective PDT treatment, which results in a combination of suitable photosensitisation yield and interaction with the target environment. Moreover, the combined therapy requires knowledge of different fields, such as cell culture and nanotechnology in order to successfully rationalise a good combined therapy nanostructure. In this way, we have developed two nanoplatforms that show promising results as nanocarriers for combined therapy. The liposomes with the dual payload overcome resistance and improve the effectiveness of the individual treatments.

Many advances has still been done in DDSs in a way to obtain more controllable drug release nanostructures such as stimulus-responsive carriers, or introducing a $^1O_2$-sensitive linker which trigger the release.[13–15] The other major hurdle of DDSs is the demand of a better selectivity over malignant tissue thus in recent years most of them has been actively targeted.[10]

7.2 References

(1) Obaid, G.; Broekgaarden, M.; Bulin, A.-L.; Huang, H.-C.; Kuriakose, J.; Liu, J.; Hasan, T. Photonanomedicine: A Convergence of Photodynamic Therapy and Nanotechnology. *Nanoscale,* **2016**, *8*, 12471–12503.

(2) Chibebe Junior, C.; Sabino, C. P.; Tan, X.; Junqueira, J. C.; Wang, Y.; Fuchs, B. B.; Jorge, A. O.; Tegos, G. P.; Hamblin, M. R.; Mylonakis, E.; *et al.* Selective Photoinactivation of Candida Albicans in the Non- Vertebrate Host Infection Model Galleria Mellonella Selective Photoinactivation of Candida Albicans in the Non-Vertebrate Host Infection Model Galleria Mellonella. *BMC Microbiol.* **2013**, *13*, 1471–2180.

(3) Morton, C. O.; Chau, M.; Stack, C. In Vitro Combination Therapy Using Low Dose Clotrimazole and Photodynamic Therapy Leads to Enhanced Killing of the Dermatophyte Trichophyton Rubrum. *BMC Mcrobiology,* **2014**, *14*, 1471–2180.

(4) Khdair, A.; Chen, D.; Patil, Y.; Ma, L.; Dou, Q. P.; Shekhar, M. P. V; Panyam, J. Nanoparticle-Mediated Combination Chemotherapy and Photodynamic Therapy Overcomes Tumor Drug Resistance. *J Control Release J Control Release January,* **2010**, *25*, 137–144.

(5) Brezova, V.; Valko, M.; Breza, M.; Morris, H.; Telser, J.; Dvoranova, D.; Kaiserova, K.; Varecka, L.; Mazur, M.; Leibfritz, D. Role of Radicals and Singlet Oxygen in Photoactivated DNA Cleavage by the Anticancer Drug Camptothecin: An Electron Paramagnetic Resonance Study. *J. Phys. Chem. B,* **2003**, *107*, 2415–2425.

(6) Brezová, V.; Dvoranová, D.; Zúbor, V.; Breza, M.; Mazúr, M.; Valko, M. Photochemical Properties of Camptothecin in the Presence of copper(II) Ions: The Role of Radicals as Prospective Species in Photodynamic Therapy. *Mol. Biotechnol.* **2007**, *37*, 48–51.

(7) Postiglione, I.; Chiaviello, A.; Palumbo, G. Enhancing Photodynamic Therapy Efficacy by Combination Therapy: Dated, Current and Oncoming Strategies. *Cancers (Basel).* **2011**, *3*, 2597–2629.

(8) Marise De Freitas, L.; Serafim, R. B.; Ferreira De Sousa, J.; Moreira, T. F.; Tavares, C.; Santos, D.; Baviera, A. M.; Valente, V.; Soares, C. P.; Fontana, C. R. Photodynamic Therapy Combined to Cisplatin Potentiates Cell Death Responses of Cervical Cancer Cells. *BMC Cancer,* **2017**, *17*, 1–12.

(9) Zhou, L.; Wei, S.; Ge, X.; Zhou, J.; Jiang, H.; Li, F.; Shen, J. Combination of Chemotherapy and Photodynamic Therapy Using Graphene Oxide as Drug Delivery System. *J. Photochem. Photobiol. B.* **2014**, *135*, 7–16.

(10) Ke, M.-R.; Chen, S.-F.; Peng, X.-H.; Zheng, Q.-F.; Zheng, B.-Y.; Yeh, C.-K.; Huang, J.-D. A Tumor-Targeted Activatable Phthalocyanine-Tetrapeptide-Doxorubicin Conjugate for Synergistic Chemo-Photodynamic Therapy. *Eur. J. Med. Chem.* **2017**, *127*, 200–209.

(11) Ruiz-González, R.; Milán, P.; Bresolí-Obach, R.; Stockert, J.; Villanueva, A.; Cañete, M.; Nonell, S. Photodynamic Synergistic Effect of Pheophorbide a and Doxorubicin in Combined Treatment against Tumoral Cells. *Cancers (Basel).* **2017**, *9*, 18.

(12) Huang, H. C.; Mallidi, S.; Liu, J.; Chiang, C. Te; Mai, Z.; Goldschmidt, R.; Ebrahim-Zadeh, N.; Rizvi, I.; Hasan, T. Photodynamic Therapy Synergizes with Irinotecan to Overcome Compensatory Mechanisms and Improve Treatment Outcomes in Pancreatic Cancer. *Cancer Res.* **2016**, *76*, 1066–1077.

(13) Saravanakumar, G.; Lee, J.; Kim, J.; Kim, W. J. Visible Light-Induced Singlet Oxygen-Mediated Intracellular Disassembly of Polymeric Micelles Co-Loaded with a Photosensitizer and an Anticancer Drug for Enhanced Photodynamic Therapy. *Chem. Commun.* **2015**, *51*, 9995–9998.

(14) Wan, H.; Zhang, Y.; Zhang, W.; Zou, H. Robust Two-Photon Visualized Nanocarrier with Dual Targeting Ability for Controlled Chemo-Photodynamic Synergistic Treatment of Cancer. *ACS Appl. Mater. Interfaces,* **2015**, *7*, 9608–9618.

(15) Ng, D. K. P.; Wong, R.; Fong, W.-P.; Lo, P.-C. Encapsulating pH-Responsive Doxorubicin-Phthalocyanine Conjugates in Mesoporous Silica Nanoparticles for Combined Photodynamic Therapy and Controlled Chemotherapy. *Chem. - A Eur. J.* **2017**.

CHAPTER 8

Conclusions

Conclusions

1. A stable hypericin-apomyoglobin complex has been successfully assembled. It preserves the photophysical and photosensitising properties of hypercicin, effectively photoinactivates *S. aureus* bacteria upon exposure to visible light, and shows lower dark toxicity than free Hyp.

2. A complex between β-lactoglobulin and hypericin has been constructed and successfully used to photoinactivate gram-positive bacteria. Coating its surface with DMSO considerably improves its photophysical properties, yet detracting from its antibacterial activity. This biocompatible complex has potential in dairy industry processes as an effective disinfectant for food manufacturing and handling materials.

3. A ternary complex between retinoic acid, hypericin and β-lactoglobulin has been assembled and characterised. Retinoic acid quenches the excited states of hypericin, rendering a photochemically innocuous complex. However, in the presence of *S. aureus* bacteria, retinoic acid is transferred from the protein to cells and the photosensitising properties of the complex are restored. This ternary nanosystem may be of interest for the combined treatment of bacterial infections.

4. A liposomal formulation has been developed that encapsulates both protoporphyrin IX and irinotecan with high efficiency and high drug payloads. The photophysical properties and singlet oxygen production ability of encapsulated protoporphyrin IX remain close to those in solution, facilitating its photodynamic activity. This dual drug formulation shows a synergistic killing effect against HeLa cancer cells. This dual nanosystem may be of interest for the combined treatment of cancer.

5. A liposomal formulation has also been developed that encapsulates both protoporphyrin IX and doxorubicin, also with high efficiency and high drug payloads. The photophysical properties and singlet oxygen production ability of encapsulated protoporphyrin IX remain close to those in solution, facilitating its photodynamic activity. This dual drug formulation shows a synergistic killing effect against HeLa cancer cells, however at later times than the protoporphyrin IX-irinotecan formulation. This dual nanosystem may therefore be also of interest for the combined treatment of cancer.

List of abbreviations

aPDT	Antimicrobial photodynamic therapy
ApoMb	Apomyoglobin
AUC	Area under the curve
CHOL	Cholesterol
CPT-11	Irinotecan
DDS	Drug delivery system
DIC	Differential interference contrast
DL	Drug loading
DMSO	Dimethyl sulfoxide
DOPS	L-α-dioleoyl-phospathidylserine
Dox	Doxorubicin
DSPC	L-α-distearoyl-phospathidylcholine
DSPE	L-α-distearoyl-phosphoethanolamine
EE	Entrapment efficiency
EPC	Egg L-α-phosphatidylcholine
EPR	Enhanced and permeability retention effect
ER	endoplasmic reticulum
EtOH	Ethanol
FDA	Food and drug administration
Hyp	Hypericin
IC_{50}	Half-maximal inhibitory concentration
IUV	Intermediate unilamellar liposome
LFP	Laser flash photolysis
mAb	Monoclonal antibody
Mb	Myoglobin
MLV	Multilamellar vesicles
NIR	Near-infrared radiation
NP	Nanoparticle
PDT	Photodynamic therapy

PEG	Poly-(ethylene glycol)
PpIX	Protoporphyrin IX
PS	Photosensitiser
RA	Retinoic acid (Tretinoin)
ROS	Reactive oxygen species
STED	Stimulated emission depletion
THF	Tetrahydrofuran
T_m	Phase transition temperature
Trp	Tryptophan
TZ	Trastuzumab
UV	Ultraviolet
βLG	β-lactoglobulin
$^1O_2$	Singlet oxygen
$^3O_2$	Molecular oxygen
λ	Wavelength
Φ_F	Fluorescence quantum yield
Φ_Δ	Singlet oxygen quantum yield
τ_Δ	Singlet oxygen lifetime
τ_T	Photosensitizer's triplet lifetime
τ_T	Fluorescence emission lifetimes

List of publications

Papers

- Delcanale, P.; **Rodríguez-Amigo, B.**; Juárez-Jiménez, J.; Luque, F. J.; Abbruzzetti, S.; Agut, M.; Nonell, S.; Viappiani, C. *Tuning the local solvent composition at a drug carrier surface: the effect of dimethyl sulfoxide/water mixture on the photofunctional properties of hypericin*-β-*lactoglobulin complexes*. J. Mater. Chem. B, 2017, *5*, 1633. DOI: 10.1039/c7tb00081b.
- Delcanale, P.; Montali, C.; **Rodríguez-Amigo B.**; Abbruzzetti, S.; Bruno, S.; Bianchini, P.; Diaspro, A.; Agut, M.; Nonell, S.; Viappiani, C. *Zinc-substituted myoglobin is a naturally occurring photoantimicrobial agent with potential applications in food decontamination*. J. Agric. Food Chem. 2016, *64*, 8633. DOI: 10.1021/acs.jafc.6b03368.
- Delcanale P.; Pennacchietti, F.; Maestrini, G.; **Rodríguez-Amigo B.**; Bianchini, P.; Diaspro, A.; Iagatti, A.; Patrizi, B.; Foggi, P.; Agut, M.; Nonell, S.; Abbruzzetti, S.; Viappiani, C. *Subdiffraction localization of a nanostructured photosensitizer in bacterial cells*. Scientific Reports, 2015, *5*. DOI: 10.1038/srep15564.
- **Rodríguez-Amigo, B.**; Delcanale, P.; Rotger, G.; Juárez-Jiménez, J.; Abbruzzetti, S.; Summer, A.; Agut, M.; Luque, F. J.; Nonell, S.; Viappiani, C. *The complex of hypericin with* β-*lactoglobulin has antimicrobial activity with potential Applications in dairy industry*. J. Dairy Sci., 2015, *98*, 1, 89. DOI: 10.3168/jds.2014-8691.
- Comas-Barceló, J.; **Rodríguez-Amigo, B.**; Abbruzzetti, S.; del Rey-Puech, P.; Agut, M.; Nonell, S.; Viappiani, C. A self-assembled nanostructured material with photosensitising properties. RSC advances, 2013, 3, 17874. DOI: 10.1039/c3ra42609b.

Book chapters

- Hally, C.; **Rodríguez-Amigo, B.**; Bresolí-Obach, R.; Planas, O.; Nos, J.; Boix-Garriga, E.; Ruiz-González R.; Nonell, S.; *Photodynamic Therapy*. In Theranostics and Image Guided Drug Delivery; Thanou, A. Ed.; Royal Society of Chemistry: Cambridge, 2017. ISBN: 978-178-2624-66-0. Accepted
- **Rodriguez-Amigo, B.**; Planas, O; Torra, J; Bresolí-Obach, R.; Ruiz-González, R.; Nonell, S.; Chapter 2: *Photosensitisers for Photodynamic Therapy: State of the Art and Perspectives*. In Photodynamic Medicine: From Bench to Clinic; Kostron, H.; Hasan, T., Eds.; Royal Society of Chemistry, 2016, 1, 23-62. ISBN: 978-1-78262-451-6.

- Boix-Garriga, E.; **Rodriguez-Amigo, B.**; Planas, O.; Nonell S.; Chapter 2: *Properties of Singlet Oxygen*. In Singlet Oxygen: Applications in Biosciences and Nanosciences, Volume 1; Flors C.; Nonell, S., Eds. Royal Society of Chemistry, 2016, 1, 23-46. ISBN: 978-1-78262-038 -9.
- Planas, O.; Boix-Garriga, E.; **Rodriguez-Amigo, B.**; Torra, J.; Bresolí-Obach, R.; Flors, C.; Viappiani, C.; Agut, M.; Ruiz-González, R.; Nonell S.; Chapter 9: *Newest approaches to singlet oxygen photosensitisation in biological media*. In Photochemistry: Volume 42; Fasani, E.; Albini, A., Eds.; Photochemistry; Royal Society of Chemistry, 2015, 42, 233-278. ISBN: 978-1- 84973-956-6.

Communications in congresses

- Rodríguez-Amigo, B.; Lázaro-Carrillo, A.; Tabero, A.; Villanueva, A.; Cañete, M.; Stockert, J. C.; Sagristà, M. L.; Mora, M.; Nonell, S. *Chemotherapy and singlet oxygen: a deadly tandem*. XXXVI Reunión Bienal de la Real Sociedad Española de Química (RSEQ), Sitges (Spain), 25-29 June, 2017.
- **Rodríguez-Amigo, B.**; Delcanale, P.; Juárez-Jiménez, J.; Abbruzzetti, S.; Summer, A.; Agut, M.; Luque, F. J.; Nonell, S.; Viappiani, C. *The use of* β*-LG protein as nanocarrier for the natural photosensitizer hypericin. Influence of DMSO as a co-solvent in the photophysical and photoinactivation properties*. 16th Congress of the European Society for Photobiology, Aveiro (Portugal), August 31 – September 4, 2015.
- **Rodríguez-Amigo, B.**; Rotger, G.; Agut, M.; Juárez-Jiménez, J.; Delcanale, P.; Abbruzzetti, S.; Viappiani, C.; Luque, F. J.; Nonell, S. *Proteins as nanocarriers for the natural hydrophobic photosensitiser hypericin*. 25th IUPAC Symposium on Photochemistry, Bordeaux (France), 13-18 July, 2014.

Additional papers are at different stages of publication

- **Rodríguez-Amigo, B.**; Delcanale, P.; Abbruzzetti, S.; Viappiani, C.; Nonell, S. *A double payload complex between Hypericin and Tretinoin in the* β*-lactoglobulin protein*. Manuscript in preparation.